An implicit spline-based method with PDE-based regularization for the construction of complex geological models

Ayoub Belhachmi

UNIVERSITÉ CÔTE D'AZUR | ÉCOLE DOCTORALE SCIENCES FONDAMENTALES ET APPLIQUÉES

THÈSE DE DOCTORAT

Une méthode implicite pour la construction des modèles géologiques complexes via une interpolation à l'aide des splines et une régularisation basée sur les équations aux dérivées partielles.

Ayoub Belhachmi
Inria, Aromath, d'Université Côte d'Azur

Présentée en vue de l'obtention du grade de docteur en **Mathématiques** d'Université Côte d'Azur.
Dirigée par : **Bernard Mourrain**
Co-encadrée par : **Azeddine Benabbou**
Soutenue le : **16/01/2024**

Devant le jury, composé de :
Bernard Mourrain, DR, Inria Sophia Antipolis – Méditerranée.
Azeddine Benabbou, Phd, SLB Schlumberger Services Pétroliers Montpellier.
Boniface Nkonga, Pr, Université de Nice Sophia-Antipolis.
Géraldine Morin, Pr, IRIT - N7 - Toulouse INP Université de Toulouse.
Guillaume Caumon, Pr, RING, ENSG-GeoRessources, Université de Lorraine.
Colin Daly, Phd, SLB Schlumberger Oilfield UK.

An implicit Spline-based method with PDE-based regularization for the construction of complex geological models.

Une méthode implicite pour la construction des modèles géologiques complexes via une interpolation a l'aide des splines et une régularisation basée sur les équations aux dérivées partielles.

Ayoub Belhachmi

Le jury est composé de :

Président
Boniface Nkonga, Professeur, Université de Nice Sophia-Antipolis.

Rapporteurs
Géraldine Morin, Professeure, IRIT - N7 - Toulouse INP Université de Toulouse.
Guillaume Caumon, Professeur, RING, ENSG-GeoRessources, Université de Lorraine.

Examinateurs
Colin Daly, Docteur, SLB Schlumberger, Oilfield UK.
Bernard Mourrain, Directeur de recherche, INRIA Sophia Antipolis-Méditerranée.

Invités
Azeddine Benabbou, Docteur, SLB Schlumberger Services Pétroliers Montpellier.

Résumé

La construction d'un géomodèle numérique est une étape clé dans l'étude et l'exploration du sous-sol. Ces modèles sont construits à partir de données sismiques ou de puits, qui forment un ensemble de points de données associés à des valeurs correspondant à leurs âges géologiques. Cette tâche consiste à construire une fonction implicite, également appelée fonction stratigraphique, qui interpole cet ensemble de points de données. Souvent, les données disponibles sont rares et bruitées, ce qui rend cette tâche difficile, principalement pour les réservoirs où les structures géologiques sont complexes avec plusieurs discontinuités. Pour résoudre ce problème, le problème d'interpolation est généralement complété par un terme de régularisation qui impose un comportement régulier de la fonction implicite. Dans cette thèse, nous proposons une nouvelle méthode pour calculer la fonction stratigraphique qui représente les couches géologiques dans des contextes arbitraires. Dans cette méthode, les données sont interpolées par des splines Powell-Sabin C^1 quadratiques par morceaux et la fonction peut être régularisée via de nombreuses énergies de régularisation. La méthode est discrétisée en éléments finis sur un maillage triangulaire conforme aux failles géologiques. Par rapport aux méthodes d'interpolation classiques, l'utilisation de splines quadratiques par morceaux présente deux avantages majeurs. Premièrement, une meilleure approximation des surfaces stratigraphiques présentant de fortes courbures. Deuxièmement, une réduction de la résolution du maillage, tout en générant des surfaces plus lisses et plus régulières.

La régularisation de la fonction est la composante la plus difficile de toute approche de modélisation implicite. Souvent, les méthodes classiques produisent des modèles géologiques incohérents, en particulier pour les données présentant de fortes variations d'épaisseur, et des effets de bulles sont généralement observés. Pour résoudre ce problème, nous introduisons deux nouvelles énergies de régularisation liées à deux EDPs fondamentales, sous leur forme générale avec des coefficients variants spatialement. Ces EDPs sont l'équation de diffusion anisotrope et l'équation de flexion d'une plaque mince anisotrope. Dans la première approche, le tenseur de diffusion est introduit et adapté de manière itérative aux variations et à l'anisotropie des données. Dans la seconde, le tenseur de rigidité est adapté de manière itérative aux variations et à l'anisotropie des données. Nous démontrons l'efficacité des méthodes proposées en $2D$, spécifiquement sur des coupes transversales de modèles géologiques avec des réseaux de failles complexes et des couches géologiques présentant des variations d'épaisseur.
Mots-clés: Modélisation implicite - Modélisation structurelle - Fortes variations d'épaisseur - Splines - EDP anisotrope - Interpolation.

Abstract

The construction of a geological numerical model is a key step in the study and exploration of the subsurface. These models are constructed from seismic or well data, which consist of data points associated with values corresponding to their geological ages. This task involves constructing an implicit function, known also as stratigraphic function, which interpolates this set of data points. Often the available data are sparse and noisy, which makes this task difficult, mainly for reservoirs where the geological structures are complex with distinct discontinuities and unconformities. To address this, the interpolation problem is typically supplemented with a regularization term that enforces a regular behaviour of the implicit function. In this thesis, we propose a new method to compute the stratigraphic function that represents geological layers in arbitrary settings. In this method, the data are interpolated by piecewise quadratic C^1 Powell-Sabin splines and the function can be regularized via many regularization energies. The method is discretized in finite elements on a triangular mesh conforming to the geological faults. Compared to classical interpolation methods, the use of piecewise quadratic splines has two major advantages. First, a better handling of stratigraphic surfaces with strong curvatures. Second, a reduction in mesh resolution, while generating surfaces of higher smoothness and regularity.

The regularization of the function is the most difficult component of any implicit modeling approach. Often, classical methods produce inconsistent geological models, in particular for data with high thickness variation, and bubble effects are generally observed. To handle this problem, we introduce two new regularization energies that are linked to two fundamental PDEs, in their general form with spatially varying coefficients. These PDEs are the anisotropic diffusion equation and the equation that describes the bending of an anisotropic thin plate. In the first approach, the diffusion tensor is introduced and iteratively adapted to the variations and anisotropy of the data. In the second, the rigidity tensor is iteratively adapted to the variations and anisotropy in the data. We demonstrate the effectiveness of the proposed methods in $2D$, specifically on cross-sections of geological models with complex fault networks and thickness variations in the layers.

Key words: Implicit modeling - Structural modeling - High thickness variations - Splines - anisotropic PDE - Interpolation.

Acknowledgements

I would like to express my deep appreciation to the thesis reviewers, Professor Guillaume Caumon and Professor Geraldine Morin, for their active participation in evaluating my work and providing invaluable comments and corrections. A special acknowledgment goes to the members of the jury, Professor Boniface Nkonga and Doctor Colin Daly, for their commitment to being part of my Ph.D. defense.

This work is a result of aligning various efforts, not only my own. First gratitude for this work goes to Azeddine and Bernard, whose guidance and contributions were crucial to bring this thesis to completion.

Being a member of the vibrant research and development team of structural modeling at SLB has been enriching, with passionate modelers with whom discussions were inspiration for my work. I extend special thanks to Thomas Laverne for generously sharing insightful papers and discussions. Emmanuel's critical views and comments, along with Thomas Viard and Arnaud's feedback, were invaluable. I deeply appreciate this team for their culture of knowledge sharing and sense of humor. Moreover, being part of the Aromath team at INRIA, alongside brilliant and passionate researchers, has been a privilege that has further enriched my work.

I also want to express my gratitude to my incredible girlfriend for the limitless love, support and inspiration during my thesis. Her belief in me have been driving me forward even in the face of challenges. I am truly grateful for her presence in my life.

I deeply thank my parents for their unwavering support and love, and the sacrifices they made throughout my life. Their encouragement has been a constant source of strength throughout this journey. Additionally, I want to express my gratitude to my brother and sister for their support and love. I want to acknowledge the significant sacrifices made by my grandmother, who devoted her life to ensure that our family prioritize higher education.

Contents

Abbreviations and notations

$1D$	One-Dimensional space	PDE	Partial Differential Equation
$2D$	Two-Dimensional space	VBM	Volume Based Modeling
$3D$	Three-Dimensional space	DSI	Discrete Smooth Interpolation
RBF	Radial Basis functions	TPS	Thin Plate Splines
PS-splines	Powell-Sabin splines	PS-refinement	Powell-Sabin refinement
FEM	Finite Element Method		

Symbols	Meaning
x	Scalar
$\mathbf{x}$	Vector
$\mathbf{x}^T$	Horizontal vector
^{T}	Transpose of a vector or a matrix
H	Horizon
S_h	Set of all horizons
u	Implicit function
v	Test function
B_i	Basis function associated to the vertex i
$\mathbf{U}$	A vector of unknown coefficients
∇	Gradient operator
∂_i	Derivative in i axis
Δ	Laplacian operator
Δ^2	Bilaplacian operator
λ	Regularization weight
$\nabla^2 u / \mathbf{H}_u$	Symmetric matrix of second-order partial derivatives
Ω	Domain of study

Introduction

Geology is a major scientific discipline that describes the structure of the earth on and beneath its surface and the processes that have shaped that structure. A better comprehension of the subsurface is vital for various tasks such as resource estimation, numerical simulations, and risk management. Numerical models known as geomodels are commonly used to describe subsurface structures, providing a mathematical and computational framework for expressing geological concepts. Often, these structures can be very complex, with several geological faults and many stratigraphic layers. An additional challenge arises from the lack of available data. Nevertheless, the geomodel must faithfully represent the complexity observed in the data.

To build these models, several approaches have been proposed in the past (Mallet 1997, Sprague and Dekemp 2005, Caumon et al. 2009). The foundational approach in structural modeling, known as explicit structural modeling, consists of modeling the contact surfaces between geological units typically with parametric and/or polygonal surfaces (Mallet 1992, Sprague and Dekemp 2005). An alternative approach, referred to as implicit structural modeling, consists of representing the stratigraphic layers by an implicit stratigraphic function. More specifically, the data points are along interfaces delimiting stratigraphic layers, represented as a set of equipotential surfaces called horizons. Implicit structural modeling has been widely used to build geomodels from stratigraphic data (Lajaunie et al. 1997, Frank et al. 2007, Caumon et al. 2013, Hillier et al. 2014). Among the implicit methods, we can distinguish two main classes of interpolation methods. The first class includes methods based on dual kriging or radial basis functions, where the interpolation is based on the data points locations (Lajaunie et al. 1997, Chilès et al. 2007). The second class includes mesh-based methods, which rely on the discretization of the domain of study using a mesh and then the function is approximated using piecewise continuous polynomial basis functions supported around the nodes of the mesh. For example the Discrete Smooth Interpolation methods (DSI) (Mallet 1997, Frank et al. 2007, Irakarama et al. 2022), where the stratigraphic function is discretized on a volumetric/surfacic mesh using finite element basis functions.

Over the two last decades, these methods have reached a significant maturity and led to the development of several modeling softwares in the oil and gas industry, for example volume based modeling (VBM) by Souche et al. (2014). However, these methods present common limitations, especially when dealing with models presenting high thickness variations (Renaudeau 2019, Pizzella 2020). Geological models with strong thickness variations are models that represent geological structures with high variations in the shape and thickness of the layers. These variations are often anisotropic, meaning they vary differently along different directions. These strong variations have long been a concern and a challenge for different implicit modeling methods (Laurent 2016, Renaudeau 2019, Irakarama et al. 2021).

The stratigraphic data can be sparse and irregularly distributed over the domain. To address this, the modeling problem is usually posed as sum of two components: fitting and regularization (Renaudeau 2019, Mallet 1992). The fitting term constrains the implicit function to honor data. On the other hand, the regularization term is introduced to enforce

a good behaviour of the implicit function. The term "good" is subjective and its meaning changes depending on the assumptions made in the modeling problem. The definition of the regularization depends on the problem to be solved. For example in neural networks, regularization is defined as any method that enhances the generalization capability of a network (Santosh et al. 2022). While for inverse ill-posed problems, it is used to introduce prior knowledge and make the approximation of ill-posed (pseudo-) inverses feasible (Benning and Burger 2018). In structural modeling, the regularization term is typically chosen as a measure of smoothness of the implicit function (Renaudeau 2019, Mallet 1992, Irakarama et al. 2022).

In this thesis, we propose a new method to construct the implicit function that represents the stratigraphic data. This function interpolates the data using a piecewise quadratic C^1 Powell-Sabin (PS) splines, and can be regularized via many regularization energies. For the discretization, we use PS-splines on triangular meshes. First, we will provide a brief review of structural modeling and existing techniques in order to contextualize our method as an implicit mesh-based method. Then, we will suggest a new regularity criteria, which are a set of mathematical properties that the implicit function should respect in order to be coherent geologically.

In the context of mesh-based methods, the main component of the implicit modeling approach is the regularization. Therefore, we will examine a wide range of regularization techniques that are widely used in the field of implicit structural modeling using the new regularity criteria we introduced and not only smoothness. We will explore new regularization energies that are linked to two fundamental PDEs, in their general form with spatially varying coefficients, the anisotropic diffusion equation and the equation describing the bending of an anisotropic thin plate. This class of PDEs provides a rich mathematical framework within which the longstanding implicit structural modeling challenges can be addressed such as thickness variations and the behavior of the implicit function in the presence of faults.

The contributions of the thesis are:

- The use of a structural modeling method based on splines. We represent the implicit function using PS-splines, which are C^1 quadratic piecewise polynomials, that can be defined on arbitrary triangulations. In our case, the triangular mesh discretizing the domain is generated conforming to the geological faults.

- We present a new regularization method based on the diffusion energy. To better handle the models presenting high thickness variations, we introduce a diffusion term in the diffusion equation that is iteratively adapted to the shape and the variations in the data. Our method is based on the essential idea that the diffusion equation provides solutions respecting the mean value property and the maximum principle at the boundaries. In this set of solutions, we seek the smoothest solutions, minimizing the Hessian energy. Furthermore, we propose a simple way to allow natural behaviour near domain boundaries and faults. For the discretization, we use Powell-Sabin splines, as an alternative to the standard linear finite elements. They are quadratic splines with global C^1 continuity, defined on triangulation and their use for the discretization of second-order smoothness energies (e.g. Hessian energy) is straightforward. Our method unlike the standard diffusion equation produces solutions with higher regularity and smoothness, free from local extrema and boundary artifacts.

- We present a new regularization method based on the bending energy of an anisotropic

thin plate. The minimizers of this energy are solutions of a fourth order PDE, and obeys on the boundaries to high order boundary conditions, which ensures a minimal bias near the boundaries. We also introduce a rigidity term in the anisotropic thin plate energy that is iteratively adapted to encode the thickness variations and the anisotropy in data. Furthermore, we propose a parameterization for this term that guarantees it remains positive semidefinite. This condition is essential as it ensures the convexity of the regularization energy. The resulting implicit functions exhibit remarkable smoothness, but unlike the solutions of the standard bending energy, they respect the regularity criteria when dealing with models exhibiting strong thickness variations. It is worth noting that the formulation of the energy is independent of the discretization. We used Powell-Sabin splines for the discretization to illustrate the results.

The thesis comprises a total of six chapters. In chapter 1, we give a brief review of structural modeling, and present existing techniques for constructing structural models. We also compare it to other implicit modeling approaches and we identify its limitations. This contextualizes the proposed method within the mesh-based methods framework, where the regularization is the main component. Then, we present a set of regularity criteria that will be considered to evaluate the regularity of the implicit functions throughout the rest of the thesis. In chapter 2, we introduce PS-splines basis functions that we will be used to discretize various regularization energies discussed in this thesis. In chapter 3, we will explore the main regularization techniques within the mesh-based methods framework. Once again, we analyze these methods and identify its common limitations, and elucidate the need for new formulations of the regularization that are able to support the anisotropic behavior, an essential property when dealing with structural models presenting high thickness variations. In chapter 4, we will explore new regularization energies that are linked to two fundamental PDEs, in their general form with spatially varying coefficients, the anisotropic diffusion equation and the equation describing the bending of an anisotropic thin plate. Lastly, in chapter 5, we present an application of our method to geological models, that involve thickness variations and complex faults network.

Publications

- Ayoub Belhachmi, Azeddine Benabbou and Bernard Mourrain. A spline-based regularized method for the reconstruction of complex geological models. Implicit structural modeling. Mathematical Geosciences. Article submitted for publication.

Conferences

- Ayoub Belhachmi, Azeddine Benabbou and Bernard Mourrain. A spline-based regularized method for the reconstruction of complex geological models. Presentation at IAMG2022 Annual conference, August 29-September 3, 2022, Nancy, France.
- Ayoub Belhachmi, Azeddine Benabbou and Bernard Mourrain. A spline-based regularized method for the reconstruction of complex geological models. Presentation at GIMC-SIMAI young 2022 workshop, Septembre 29-30, 2022, Pavia, Italy.
- Ayoub Belhachmi, Azeddine Benabbou and Bernard Mourrain. A spline-based regularized method for the reconstruction of complex geological models. Poster at EDSFA-UCA 2nd year Phd Workshop 2022, 25 Mai, 2022, Nice, France.

Implementations

A MATLAB library has been developed, containing the following features:

- The construction of the PS-splines on arbitrary triangulations and the fitting of a set data points.
- All the various regularization techniques explored in the rest of the thesis.
- The iterative scheme based on the anisotropic diffusion discretized using PS-splines.
- The iterative scheme based on the anisotropic bending energy using PS-splines.

Chapter 1
Structural modeling

This chapter provides a brief review of structural modeling and existing techniques to contextualize the implicit mesh-based methods. This class of methods is presented in the second half of this chapter. Additionally, we compare it to other implicit modeling approaches and we identify its limitations. Subsequently, we outline the assumption we made and the research framework we selected.

1.1 Structural modeling

Structural geology modeling simply refers to the set of numerical methods aiming to construct geological models or geomodels, which are numerical representations of subsurface formations (such as faults, horizons and intrusions) and their associated features on a scale of meters or kilometers in the domain of interest (Thornton et al. 2018). These representations help to understand how these structures form, their orientation, and the history of rock deformation and tectonic processes. Additionally, structural modeling is used to obtain an estimate of the true physical property value or class at any location in a region of the subsurface. These techniques rely on integrating all existing measurements, observations, and knowledge to obtain a well-informed estimate. Often, many simplification using conceptual models based on geological rules are considered, because of the incapacity to accurately describe the properties of the model.

1.1.1 Stratigraphic representation

The stratigraphic approach in structural geology involves applying principles of stratigraphy to represent the geological structures, which can be related to two main types of geological units: stratigraphic layers and intrusive geobodies. The subsurface is represented as a sequence of different stratigraphic layers, also called strata, which are horizontal or sub-horizontal rock layers that have accumulated over time through various geological processes (Cross and Homewood 1997), see Fig. 1.1. These layers are typically composed of rocks with common features. These original deposits, can undergo various deformations over time, caused by many geological processes, such us tectonic events, sedimentation and erosion. These deformations play a role in shaping stratigraphic structures with complex geometries. For example, the tectonic events can lead to the folding and/or shearing of stratigraphic layers, inducing strong thickness variations in the stratigraphic layers, as well as the faulting that creates zones of discontinuities in the stratigraphic sequence. Furthermore, the erosion and sedimentation can expose the stratigraphic layers to disparities between different strata and intrusive bodies. The stratigraphic modeling step is the process of building the intermediate reservoir horizons

based on the interpreted depth horizons and thickness data. A fault network can also be included in order to construct a consistent faulted structural model, see Fig. 1.1.

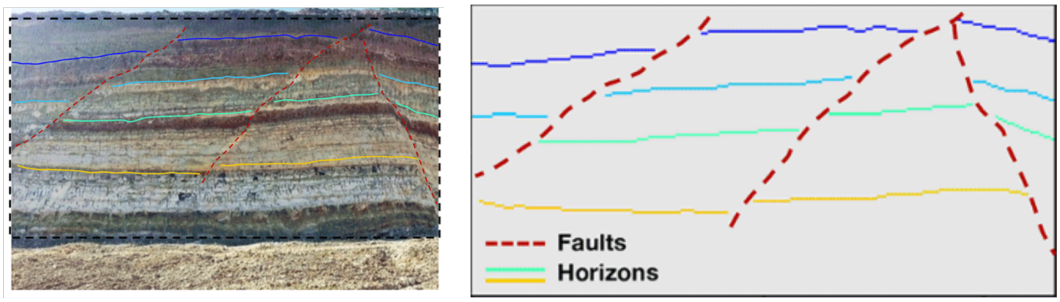

Figure 1.1: An interpreted outcrop, where geological structures are represented as uniform units known as layers or strata, which are separated by interfaces referred to as horizons. These horizons are represented as lines and faults as dashed red lines. Pictures taken from Bi et al. (2022).

1.1.2 The need for accurate models of the geological structures

We model stratigraphic structures to gain a deeper understanding of geological formations, their properties, and their spatial distribution. These models help us interpret subsurface data, make predictions about geological features, and assist in various applications such as resource exploration, environmental assessment, and hazard mitigation. Additionally, it holds significant importance for the oil and gas industry as it is essential in evaluating the geometry of potential layers like source rock, reservoir rock, and cap rock (Yang and Escalona 2011, Legentil et al. 2023). This evaluation is necessary for estimating the volumes of oil and gas reserves, and simulating fluid flow during extraction to optimize production. Fig. 1.2 illustrates the steps involved in a typical workflow for estimating oil and gas reserves. The process starts with the processing and interpretation of data acquired from the field. Subsequently, a structural model is developed, which typically contains fault modeling, horizon modeling, and the creation of a mesh that conforms to the fault network. This structural model is used to construct a stratigraphic model that computes a stratigraphic function which represents the relative geological age of the layers. Following this, a grid is generated, properties are allocated, and the estimation of oil and gas volumes is carried out. This thesis is situated within the structural modeling framework. To be more specific, our approach require as input stratigraphic data, which are a set of points distributed along geological horizons, in addition to a mesh generated conformal to the fault network. Then, the expected output is to produce a stratigraphic model, which is achieved by computing the stratigraphic function honoring the data and should be consistent geologically (Caumon et al. 2013, Irakarama et al. 2022).

Beyond physical properties, modeling stratigraphic structures can also facilitate the assessment of mineral concentrations, which is vital in the mining industry. In mining, the search for high concentrations of specific minerals, such as precious metals like gold, silver, and copper, beneath the earth's surface is essential for economic purposes (Pizzella 2020).

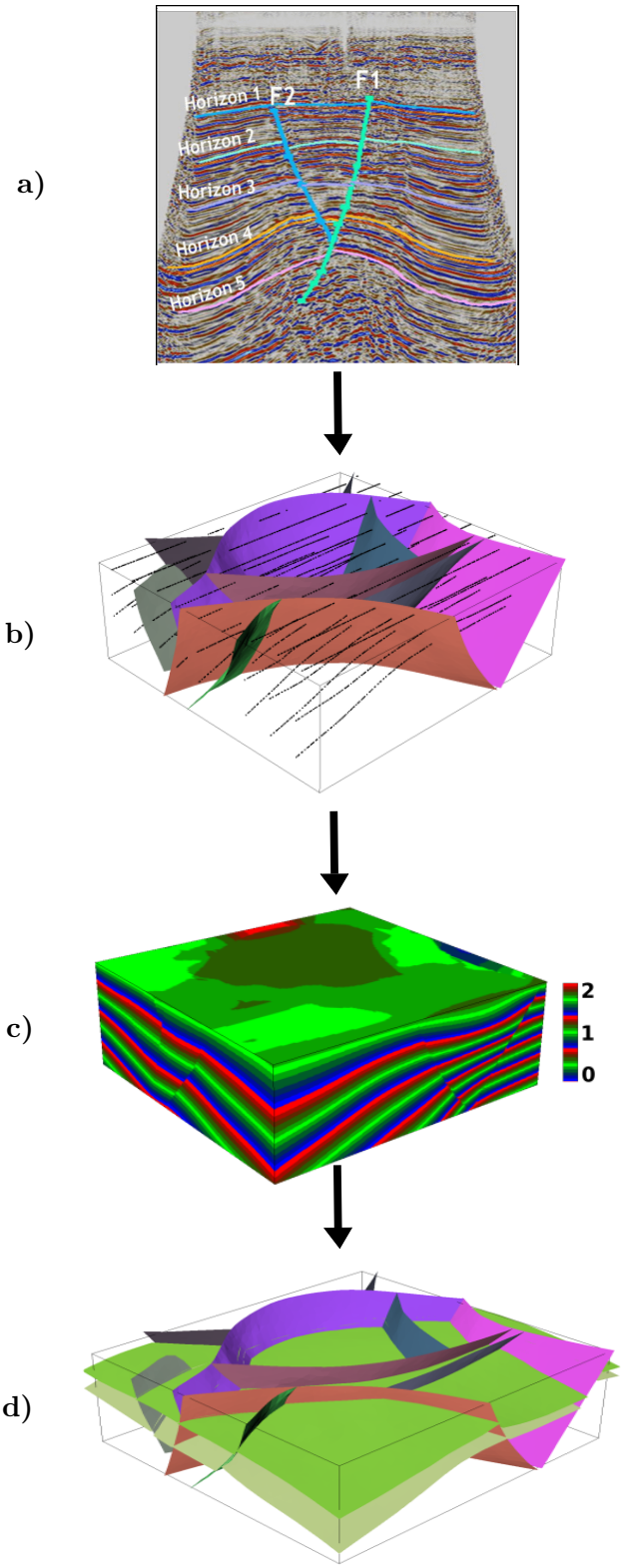

Figure 1.2: A structural modeling workflow begins with data acquisition and interpretation, ending with the extraction of implicit horizons from the isovalues of the stratigraphic function. a) Seismic data interpretation to determine horizons and identify fault network. b) Input data including fault network and data points distributed along horizons. c) Stratigraphic function interpolating data points. d) Extraction of implicit horizons from the isovalues of the stratigraphic function. Picture of the structural model taken from Irakarama et al. (2021), and the picture of the seismic data from Abdul Latiff et al. (2016).

1.1.3 Geological data

The construction of a geomodel is based on integrating all existing measurements (Fig. 1.3), observations, and knowledge to obtain a well-informed estimate (Wellmann and Caumon 2018, Renaudeau 2019). In structural modeling, we generally use points, vectors, and parametric or polygonal lines and surfaces. Given our current limitations in directly measuring these properties over the entire domain of interest. The available data of the field are often sparse and irregularly distributed (Frank et al. 2007).

Seismic data

Seismic data are a valuable source of information in the structural modeling workflow. Seismic data processing involves evaluating the arrival time and amplitude of seismic profiles covering entirely or partially the domain of study, and are produced giving a map of impedance contrasts that can interpreted as contrasts between rock units. Seismic data is particularly effective in detecting faults (Irakarama et al. 2021, Renaudeau (2019)), which are fractures in the stratigraphic layers where rocks have moved relative to each other. Faults are critical in structural modeling since they can influence the movement of fluids (such as oil and water) and can generate earthquakes (Snell et al. 2020).

Wellbore data

Wellbore data include both well cores and geophysical well logs. They are typically images or result from a local geophysical measurement, which inform about the geological properties in the neighborhood of the well. Their interpretation is more difficult, since they do not allow lateral expansion away from the borehole. In addition, they are sparse and might be complicated to honor. Overall, they provide valuable structural information for identifying layer dips and fractures (Wellmann and Caumon 2018), as well as evidences of horizons and faults (Renaudeau 2019).

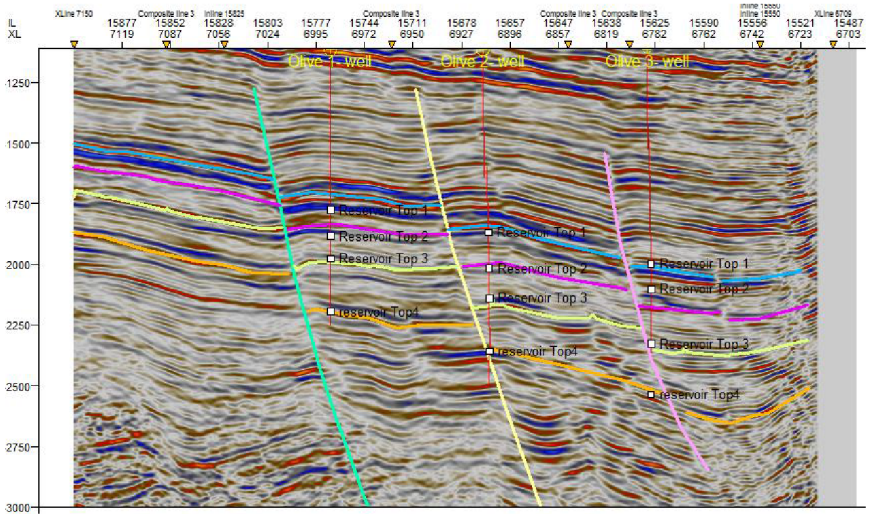

Figure 1.3: Geological data that includes well trace, picked horizon tops and some faults. Picture taken from R and Obiadi (2016).

1.1.4 Geological knowledge and realism

Beyond geological data, there exists geological knowledge that is challenging to quantify but has a strong impact on the modeling process (Madsen et al. 2022). For example, the geological contextual knowledge of the studied zone, or geological concepts like the stratigraphic representation, or assumptions based on the similarities with previously studied geological sites (Renaudeau 2019).

A geologically realistic structural model is a representation of the subsurface as a set of surfaces that define the boundaries of the geological units. It is usually guided by rules of geological realism . In the context of geological modeling, realism refers to the degree to which a model honors the numerical data and obeys to some geological rules (Wellmann and Caumon 2018, Renaudeau 2019). These rules can be based on comparisons with similar geological structure or acceptable simplifications. For instance, Renaudeau (2019) made the general assumption that geological structures should not exhibit in the stratigraphic layers excessively high curvatures. This rule was considered also by Mallet (1992) and Lajaunie et al. (1997). Nevertheless, creating models that describes a structural model in details is not feasible. Therefore, other simplifications can be considered according to the objectives of a particular study (Thornton et al. 2018).

Caumon et al. (2004) and Caumon et al. (2009), established a set of specific criteria for a boundary representation to be a geologically consistent, introducing the concept of sealed model. These criteria figure out how horizons and faults interact with each other. Horizons should not intersect, except if one has been cut by the other (Caumon et al. 2009). However the faults can intersect any type of surface. These concepts were used in structural modeling, see Sprague and Dekemp (2005) (Fig. 1.4). These validity conditions guarantee the creation of a sealed (watertight) model, which is a fundamental concept for the validity of a boundary representation. In the following, we focus on mesh-based methods and we consider that these rules should be respected by the horizons and the fault network.

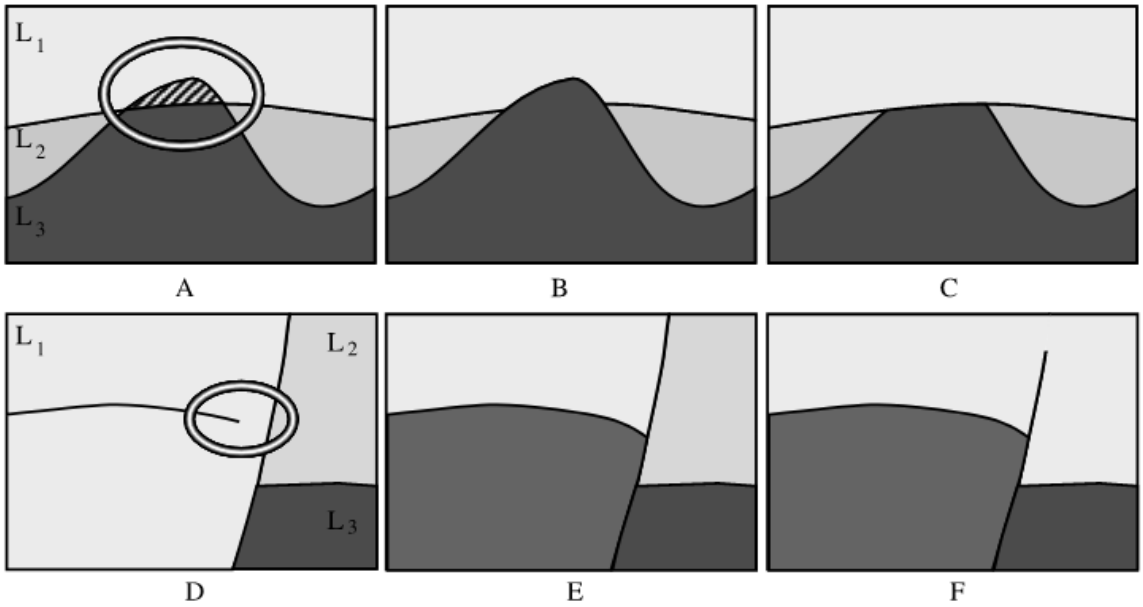

Figure 1.4: Basic surface intersection rules: Overlapping layers (A, hatched area) and leaking layers (D) are invalid; whereas (B), (C), (E), (F) are consistent models. Picture taken from Caumon et al. (2009).

1.2 Explicit structural modeling

The foundational approach in structural modeling, known as explicit structural modeling, consists of modeling the contact surfaces between geological units typically with parametric and/or polygonal surfaces (Mallet 1992, Sprague and Dekemp 2005).

1.2.1 Parametric surfaces

In parametric modeling, surfaces are defined using mathematical equations. These equations are often polynomials and describe the shape of the surface in terms of local parameters. Beziers curves, B-splines and NURBS (Non-Uniform Rational B-splines) are typically used to represent the parametric functions (Rogers 2011). In structural modeling, parametric surfaces were used to model fault blocks (GJØYSTDAL et al. 1985).

1.2.2 Polygonal surfaces

In this method, surfaces are approximated using a set of linked polygons, defining a graph composed of a set of vertices, that are lined using edges or faces. These polygons are often homogeneous (of the same type), but can be also heterogeneous (of different types), for example triangles, quad and arbitrary polygons. In structural modeling, this approach was used to represent complex structures in the pioneering work of Mallet (1989), who introduced the DSI (Discrete smooth interpolation). In this approach, a fitting energy is introduced to fit the numerical data, and a regularization energy called also roughness or fairness is added to ensure the smoothness and the regularity of the surfaces. These techniques require

heavy post-processing to generate a valid model. Often, additional truncations, projections and remeshing are performed to ensure a sealed model with a proper horizon-fault contact. Additionally, there exist some techniques that can automatically repair and ensure validity of geologically inconsistent models (Anquez et al. 2017, Anquez et al. 2019).

1.3 Implicit structural modeling (implicit function, Horizons, Faults, extraction of horizons)

The second approach in structural modeling, known as implicit modeling, offers an alternative perspective that overcomes the limitations of explicit methods. Implicit modeling takes into account all available data at once, including all horizons and discontinuities. Moreover, it enables to express the validity conditions as mathematical constraints that should be respected.

Implicit modeling was used in various fields, including computer graphics (Alliez et al. 2007, Calakli and Taubin 2011) to reconstruct surfaces, and in structural modeling (Renaudeau 2019, Lajaunie et al. 1997, Irakarama et al. 2021, Frank et al. 2007).

1.3.1 Implicit function and iso-surfaces

We define a scalar field u, also called implicit function or stratigraphic function, defined over the entire domain of interest as

$$\begin{aligned} u\colon \mathbb{R}^3 &\to \mathbb{R} \\ \mathbf{x} &\to u(\mathbf{x}). \end{aligned} \tag{1.1}$$

We define an isovalue, also called iso-surface, of this function h_α associated to a constant value α as

$$h_\alpha = \{\mathbf{x} \in \mathbb{R}^3, \quad u(\mathbf{x}) = \alpha\} \tag{1.2}$$

with α a real constant. In $3D$, an isovalue defines a surface, in $2D$ a curve, while in $1D$ a point. The geological surfaces (Horizons) are represented as isovalues of the implicit function u. The implicit function u is constructed in such a way that all data points sampling a geological surface have the same isovalue. The implicit function can represent many geological surfaces, since the function u has an infinity of isovalues (Pizzella 2020, Renaudeau 2019). It is also possible to define different implicit functions, which enables to describe even more complex sequences of geological surfaces with unconformities (Renaudeau 2019).

1.3.2 Unconformities in implicit structural modeling

In geological structural modeling, discontinuities such as faults are often encountered. They represent a surface of contact between several stratigraphic sequences. They need to be implicitly or explicitly determined before being integrated in the construction of the implicit function. In their presence, the domain is split into several conformable sequences, and boolean operations are introduced to create a valid model (Wellmann and Caumon 2018, Renaudeau (2019), Calcagno et al. (2008), Caumon et al. (2013)). Alternatively, the computational mesh to discretize the volumetric domain is generated conformal to the fault network, and the faults are treated as internal boundaries.

1.4 The meshless formulation

In implicit structural modeling, there are two main classes of numerical methods that have been introduced for the construction of the implicit function that interpolates the data points: mesh-based and meshless methods (Wellmann and Caumon 2018, Irakarama 2019). In the context of meshless formulation, the implicit function is expressed as

$$u(\mathbf{x}) = \sum_{p=1}^{Np} u_p \Phi_p(\mathbf{x}) + \sum_{m=1}^{M} a_m p_m(\mathbf{x}) \tag{1.3}$$

where $\Phi_p(\mathbf{x})$ are the basis functions, $p_m(\mathbf{x})$ are monomials, a_m are the corresponding drift coefficients, M is the total number of polynomial terms. The implicit function is expressed as linear combination of the basis function Φ_p and monomials p_m. There exist a wide range of choices of basis functions. Two main categories of basis functions are typically used for the interpolation of data. One is the potential field method introduced by Lajaunie et al. (1997), and based on dual kriging (Chilès et al. 2007, Calcagno et al. 2008, Autin et al. 2015), which has its origins in geostatistics. The second is based on the use of radial basis functions (RBF) (Renaudeau 2019, Pizzella 2020). They are widely used in various fields, including computer graphics, and machine learning, due their ability to handle irregularly distributed data and produce smooth interpolations. In general, the basis functions are defined as

$$\Phi_p(\mathbf{x}) = \phi(\|\mathbf{x} - \mathbf{x_p}\|) \tag{1.4}$$

where ϕ is the generalized covariance and $\|\mathbf{x} - \mathbf{x_p}\|$ is the isotropic distance between the position to evaluate and the data point $\mathbf{x_p}$.

1.4.1 Interpolation of numerical data

Field measurements used for interpolation can be categorized into two distinct types: purely localized information at a specific point or directional information represented by a vector at a particular point. These measurements effectively inform on the construction of the implicit function, through the interpolation of the value of the implicit function, or of its directional derivatives (Pizzella 2020, Renaudeau 2019, Hillier et al. 2014, Chilès et al. 2007).

Data points

- **Reference data points.** At a reference point $\mathbf{p}_0$, an arbitrary value α_0 is assigned to the implicit function. The constraint is written as

$$u(\mathbf{p}_0) = \alpha_0 \tag{1.5}$$

- **Increment data points.** Often, the field measurements enable to assert that a set of data points belongs to the same horizon. The value of the implicit function on these points are unknowns but are equal. Thus, for each pair of points $\mathbf{p}_i, \mathbf{p}_j$ of each horizon H, we can write the constraints as

$$u(\mathbf{p}_i) - u(\mathbf{p}_j) = 0 \quad , \quad \forall (\mathbf{p}_i, \mathbf{p}_j) \in H, \quad \forall H \in S_h, \tag{1.6}$$

  where $\mathbf{p}_i, \mathbf{p}_j$ are two points of the horizon H, S_h corresponds to the set of all horizons..

- **Directional data.** Field measurements can provide information about the orientation of the geological surfaces, i.e the gradient of the implicit function. This information can determine a tangential direction τ to the geological surfaces at a point $\mathbf{p}$. The tangential data can be written as

$$u_\tau(\mathbf{p}) = \tau \cdot \nabla u(\mathbf{p}) = 0 \tag{1.7}$$

  Additionally, it can determine the gradient of the implicit function at a point $\mathbf{p}$, which can be written as

$$\nabla u(\mathbf{p}) = \mathbf{G} \tag{1.8}$$

where $\mathbf{G}$ is a vector that corresponds to the gradient of the implicit function.

1.4.2 Structural discontinuities in meshless methods

In meshless methods, the faults are introduced, via adding a polynomial drifts, see Eq. (1.3), ensuring the discontinuity of the implicit function along the faults (Renaudeau 2019, Wellmann and Caumon 2018, Calcagno et al. 2008). For each fault, we introduce a polynomial drift. This polynomial drift, in turn, is associated to a specific jump function associated with that particular fault. These jump functions are centered around the fault's center, reaching their maximum value at it. Away from the fault's center towards the fault tip, these functions gradually decrease and become zero at the fault tip. Additionally, these functions vanish in a direction perpendicular to the fault's orientation away from the fault. Crucially, these jump functions are active only on one side of the fault, while they are completely deactivated (set to zero) on the opposite side.

1.5 Mesh-based formulation

Mesh-based methods, are numerical techniques that rely on expressing the implicit function using basis functions, which are constructed on a discretized mesh covering the domain Ω. On the mesh, we define basis functions in the space F of regular functions. The implicit function u is defined as

$$u(\mathbf{x}) = \sum_{i=1}^{N_s} B_i(\mathbf{x}) u_i = \mathbf{B}(\mathbf{x})\mathbf{U} \quad \forall \mathbf{x} \in \Omega \tag{1.9}$$

where $\mathbf{B}(\mathbf{x}) = (B_i(\mathbf{x}))_{i=1}^{N_s}$ is a basis of F, $\mathbf{U} = (u_i)_{i=1}^{N_s}$ is a vector of unknowns and N_s is the dimension of F. The basis functions B_i used to represent the implicit function, can be defined using any type of mesh. The mesh discretization is usually performed on simplices. In the context of structural modeling, we commonly use the term Discrete Smooth Interpolation (DSI) method to describe the class of methods based on domain discretization. These methods were originally introduced by Mallet (1989). In DSI, triangular meshes are used. It is also worth noting that DSI was first used in explicit modeling (Mallet 1989, Mallet (1997), Lévy and Mallet 1999), and based on triangular meshes. In the implicit version, they are used in $2D$, and tetrahedra are generally used in 3D (Frank et al. 2007, Souche et al. 2014).

1.5.1 Structural discontinuities

Achieving a discontinuous jump in the implicit function u can be obtained by either modifying the basis functions to break their continuity or by the topology in a way that naturally leads

to discontinuities in u (Renaudeau (2019)). Often in the mesh-based methods, the mesh is created conformal to the faults, ensuring that no mesh element cross them (Fig. 1.5, Fig. 1.6). To achieve the former condition, all the nodes that are in contact with a fault are duplicated on both sides of the fault. As a result, the nodes along the faults are not connected to each other, which also implies that the basis functions associated to these nodes along the faults are not continuous. The former condition allows to create discontinuities and jumps in the implicit function u. In $2D$, the faults are curves, represented using a set of edges, while in $3D$ they are represented using a set of triangles.

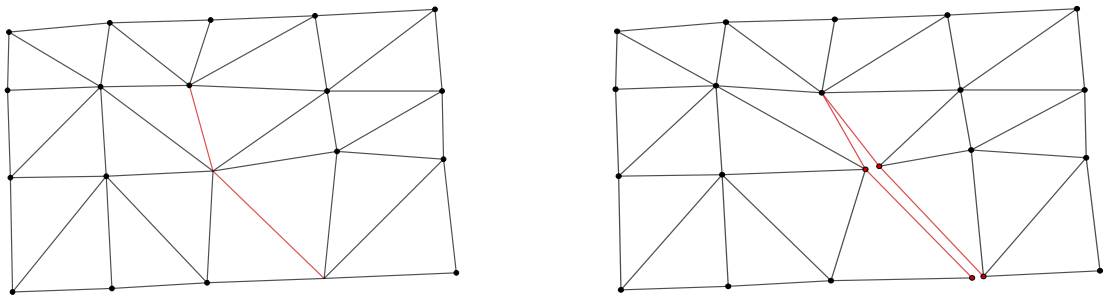

(a) (b)

Figure 1.5: Introduction of structural faults. (a) fault introduced in the mesh. (b) Nodes duplicated on the two sides of the faults. Lines correspond to edges, with red lines signifying the edges of the fault. Dots represent nodes of the mesh, and those marked in red are duplicated nodes.

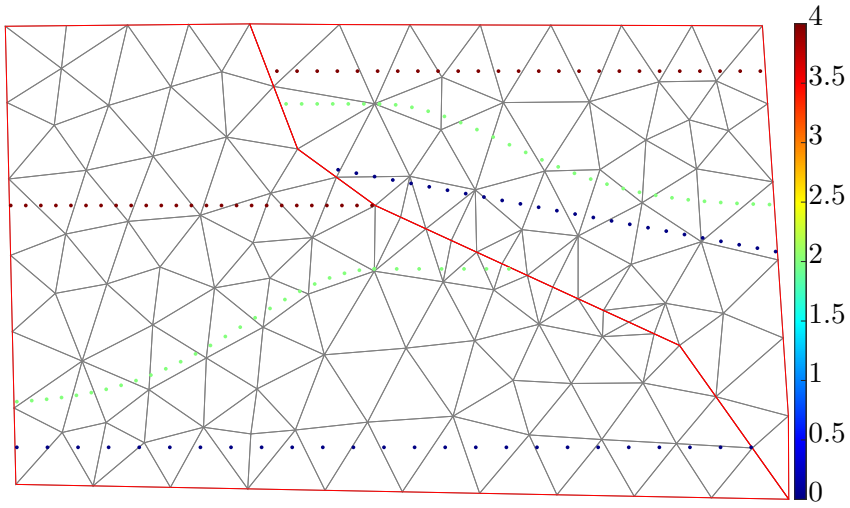

Figure 1.6: The faulted mesh is generated conformal to the faults. Lines in the mesh represent edges, and those highlighted in red represent boundary edges.

1.5.2 Interpolation of data points

In mesh-based methods, a wide range of numerical data can be taken into account. For instance, in DSI, data points are required, and the integration of various types of additional

numerical data, such as gradient information, is possible if these data are available. Data points are distributed along horizons. Each horizon, is associated with a specific isovalue. The constraints related to the data points can be expressed as

$$u(\mathbf{p}) = \alpha_H, \quad \forall \mathbf{p} \in H, \quad \forall H \in S_h \tag{1.10}$$

here, $\mathbf{p}$ is a point belonging to the horizon H, and S_h corresponds to the set of all horizons. Other types of numerical data, like the directional derivatives, are expressed in the same way as in the meshless formulations, see Sect. 1.4.1.

The data points can be sparse and noisy, while the basis functions are locally supported. This leads to an underdetermined system with an infinity of possible solutions. The implicit modeling problem is typically posed as a minimization of a sum of energies (Mallet 1992, Renaudeau 2019)

$$\min_u E_{fit}(u) + \lambda E_{reg}(u) \tag{1.11}$$

where $E_{fit}(u)$ is the fitting energy associated to the data constraints, $E_{reg}(u)$ is the regularization energy associated to the regularity constraints, λ is the regularization weight controlling the tradeoff between the fitting and regularization constraints. In the regularization formulations, the fundamental assumption is that geological surfaces need to be as smooth as possible (Mallet 1989, Renaudeau 2019).

Smoothing techniques, based on the minimization of second-order derivatives, are extensively used as a regularization in the implicit modeling problem, see Irakarama et al. (2022). The DSI methods consider many smoothing operators according to the choice of the basis functions used for interpolation. This includes the Hessian operator (Irakarama et al. 2022), smooth gradient (Souche et al. 2014), constant gradient (Frank et al. 2007) and Laplacian operator (Lévy and Mallet 1999). In his pioneering work, Mallet (1989) introduced as a global roughness, a functional expressed using finite differences scheme, involving the minimization of the first order partial derivatives as well as the second partial derivatives. The Hessian smoothing energy is used by Renaudeau (2019) as a regularization energy. Their approach involves constructing the implicit function using locally defined moving least square interpolants and explicitly minimizing the Hessian energy. In the next chapter, we will discuss in details, the various regularization formulations in structural modeling, we will also discuss the link between the the implicit modeling problem formulation Eq. 1.11 and the DSI least square system.

1.6 Limitations of the meshless methods

The main limit of meshless methods lies in their ability to handle faults. When dealing with a complex fault network, incorporating these faults can be quite challenging. The process of addressing faults requires the definition of fault zones, which is a challenging task to automate especially in $3D$ (Renaudeau 2019, Pizzella 2020).

In the context of meshless methods, the nature of the resulting linear system to be solved is mainly depending on the number of data points to interpolate. Additionally, this system is characterized by its density, since nearly all coefficients are non-zero. Consequently, this density poses a challenge when it comes to solving this system for a large number of data points (Wellmann and Caumon 2018, Renaudeau 2019).

1.7 Limitations of implicit methods

1.7.1 Thickness variations

Geological models with strong thickness variations are models that represent geological structures with high variations in the shape and thickness of the layers. These variations are often anisotropic, meaning they vary differently along different directions, which makes it difficult to obtain a geologically coherent solution that fits the data. Implicit modeling methods on these models, as shown in Fig. 1.7, produce geologically inconsistent solutions, where the mean value property and the maximum principle are violated with the presence of bubbles that are oscillations around local extrema in the resulting implicit function. It is an undesired artifact, because it is geologically incoherent. Bubbles occur in the regions where the variation of thickness in the data is the strongest. In Fig. 1.7,b bubbles are present on the boundaries and around the middle curved horizon, therefore the extraction in red of the isovalue corresponding to this horizon is geologically inconsistent.

To illustrate common limitations of the implicit modeling methods in two dimensions, we use synthetic models with high thickness variation introduced in the data. We refer to these models as bell, extracted layers and faulted synthetic, respectively, as shown in Fig. 1.7, Fig. 1.8, Fig. 1.9d. The thickness variations are present mainly in the y-direction in the extracted layers model, while, the bell and faulted synthetic models are along x and y. The bell model has horizons with values of -1, 0, 1, 2, and 3 from bottom to top and is a benchmark model of Renaudeau (2019). The faulted synthetic model has three horizons with values of 0, 1, and 2 from bottom to top, while the extracted layers model in Fig. 1.8b has horizons with values of 6, 7, 8, and 9 from bottom to top, the value of the youngest is modified and set equal to 11 in Fig .1.8b.

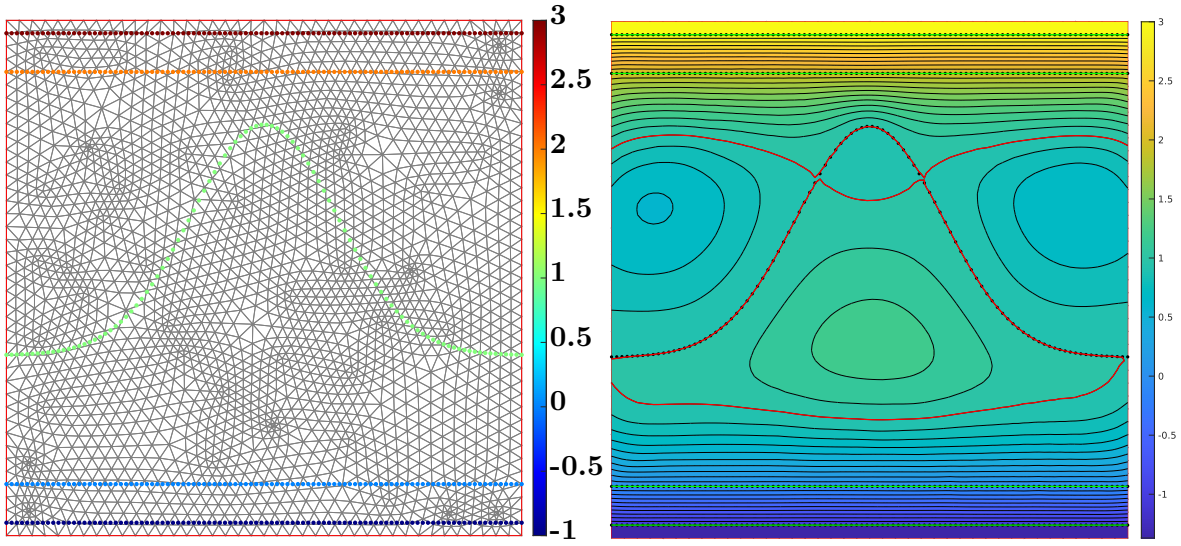

(a) (b)

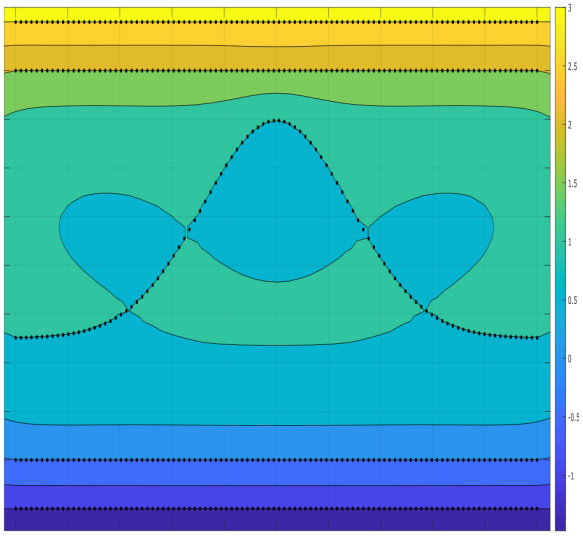

(c)

Figure 1.7: Resulting implicit functions using mesh-based and meshless implicit modeling methods, both regularized with Hessian smoothing energy. (a) Data points, with colors corresponding to the values of each horizon. (b) DSI, a mesh-based method. (c) Example of a meshless method, using thin-plate splines for interpolation with a smoothing constraint as regularization.

In the context of implicit meshless methods, particularly those based on radial basis functions ones, two notable approaches addressed the integration of the anisotropy. Hillier et al. (2014) introduced an implicit approach that uses the orientation data to estimate the directions of anisotropy. Also, Martin and Boisvert (2017) presented a method that is particularly adapted for cases with abundant data, enabling the extraction of local anisotropic properties. The technique uses domain decomposition to capture the anisotropic properties, and adjust the radial basis functions locally. Renaudeau (2019) imposed a direction of anisotropy in the minimization of the Hessian energy, and used the Moving Least Squares basis functions for the discretization. Pizzella (2020) addressed the thickness variations problem by enhancing the implicit modeling problem with anisotropy data that can be available and not used in the interpolation problem. They introduced additional data such as the integration of tangency/second derivative data and/or the inclusion of an anisotropy field.

In mesh-based methods, the existing regularization techniques can also fail to produce geologically coherent solution in models presenting high thickness variations, as it will be shown in the following of the thesis and also discussed in other works (Laurent 2016, Irakarama et al. 2021). These strong variations have long been a concern and a challenge for different implicit modeling methods (Laurent 2016, Renaudeau 2019, Irakarama et al. 2021). Additionally, the values assigned to geological horizons have a strong impact on the resulting implicit functions that describe the geological surfaces. Fig 1.8 shows two different resulting implicit functions for two situations, where the value associated to the youngest horizon is changed, it is equal to 9 in Fig. 1.8a and 11 in Fig. 1.8b. The previous experiment demonstrates that finding optimal values associated to the horizons can potentially address this problem. In

this case, it is easy to find optimal values, since the thickness variations are mainly along one direction. Conversely, it becomes challenging for the bell model, where the thickness of the layers vary strongly in magnitude and directions all over the domain. In Fig. 1.8a, when we adjust the value associated to the youngest horizon, we almost align these horizons within the same plan. This distribution of the horizons is aligned with the smoothing constraints. These constraints aim to minimize second derivatives and seek to produce solutions that are as linear as possible. Therefore, adjusting the values attributed to the horizons, can optimize their distribution in space. In our context, we think that an optimal distribution should be aligned with the regularization objectives. It is worth noting that in the rest of the thesis, we do not address this problem, we rather focus on formulating regularization energies that are able to handle geological data with arbitrary assigned values.

To tackle this issue, heuristic methods based on thickness considerations have been suggested (Caumon et al. 2013). This is feasible, in the case where enough data are available to estimate the scalar field increment by computing the differences relative to a reference value (Lajaunie et al. 1997, Chilès et al. 2007).

In contrast, in meshless formulations like the one described in Lajaunie et al. (1997), there are no predetermined values assigned to the horizons. Instead, an equality constraint is formulated for points that belong to the same horizon. This constraint ensures that points within the same horizon are on the same isovalue. Additionally, only one value is required to define the implicit function. However, it is important to note that meshless methods typically require additional orientation data. In places where the orientation of geological structures is known, the exact value of the gradient's norm (magnitude) remains unknown, since it is not always available. These information are normed vectors to interpolate. For models presenting high thickness variations, the variations of the gradient can be extremely strong and using a normed vector can be not well adapted (Pizzella 2020). The problem of determining the optimal values of data gradient remains challenging and hard to estimate, see Pizzella (2020).

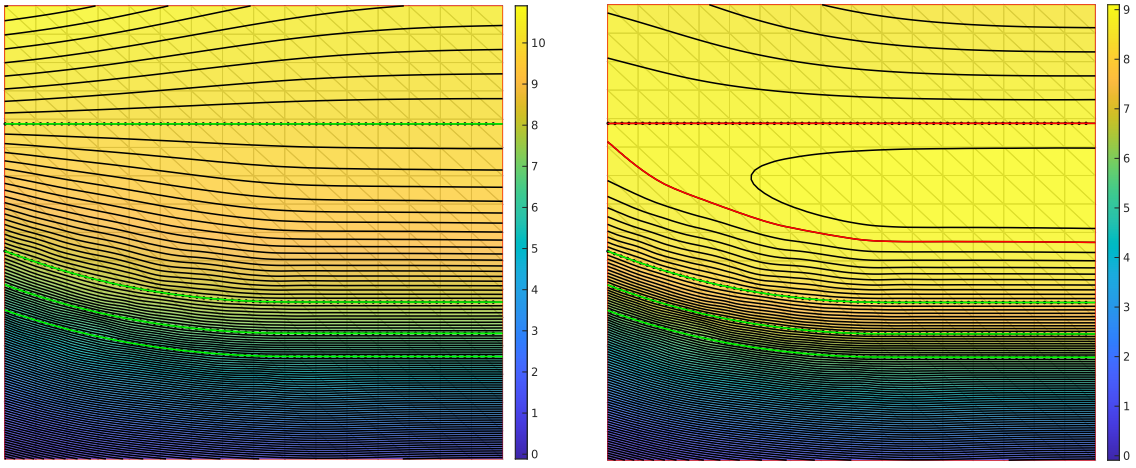

(a) (b)

Figure 1.8: When different values are assigned to a single horizon in the same structural model, it can lead to different resulting implicit functions. (a) geologically coherent. (b) geologically incoherent.

1.8 Expected numerical geomodel

In our context, we assume that we start from a stratigraphic representation of the domain of interest that is a sealed (Waterthight) model (Caumon et al. 2004). As mentioned before (Sect. 1.4), this representation is validating the two fundamental conditions of validity. Only faults may have free borders. We also suppose that based on the available geological data, a fault network and data points along horizons are determined, as well as a bounding box. Then a mesh, specifically a triangular mesh, in the rest of the thesis, is generated conformal to the faults. We generate meshes using constrained Delauney algorithm, in order to obtain elements of good quality (Shewchuk 2002, George and Borouchaki 1998). This condition is important for constructing regular basis functions, which, in turn, are used to represent the implicit function over the entire domain. Additionally, we choose to assign arbitrary values, in the ascending order following the stratigraphic order of the geological sequences. Then, the goal is to compute a stratigraphic function that interpolates data points and is well-defined all over the domain. This function is required to fit the horizons and extrapolate between horizons and far beyond them.

1.8.1 Regularity criteria

The stratigraphic data can be sparse and irregularly distributed over the domain. The regularization term Eq. (1.11) is introduced to enforce a regular behaviour of the implicit function all over the domain. In our specific context, we define a regular function as a function satisfying the following regularity properties:

(i) Mean value property and extrema at the boundaries principle. A regular function must only contain extrema at the boundaries (e.g. interfaces of the geological layers), whilst mean values elsewhere, ensuring no local extrema.

(ii) Function must be smooth, through minimizing a conventional smoothness energy.

(iii) Function should adhere to input data particularly in the proximity of faults or boundary data, with only minimal regularization influence driving the function in these areas.

(iv) Consistent shape of the function far from data.

In order to illustrate the expected properties of a regular function, we present in Fig. 1.9 a set of resulting implicit functions on two different models. Fig. 1.7b shows a smooth function that is presenting many local extrema (strong oscillations). While in Fig. 1.9b, the function is smooth, does not present local extrema, and extrapolate between horizons without violating the mean value property and maximum at the boundaries. It reaches the maximum on the horizons and not in-between, which is more geologically plausible, since these inconsistencies cannot be generated by stratigraphic processes (Wellmann and Caumon 2018).

Smooth surfaces are preferred when representing the geological surfaces. This assumption is fundamental in implicit modeling approaches (Renaudeau 2019, Mallet 1997, Souche et al. 2014). Hence, the function in Fig. 1.9b is preferred over the one in Fig. 1.9a.

The implicit function is required to present minimal bias near the boundaries. In our context, the boundaries are either part of the bounding box or parts of the fault network. For instance, the bounding box has no physical or geological meaning, it is just a virtual box that encloses the data points and the domain of interest. While for the fault, the stratigraphic

properties are defined by the sedimentation which occurred before the faulting of the layers. For example, the presence of faults in Fig. 1.9c implies strong artifacts in the implicit function. While, the function in Fig. 1.9d evolves along the faults in a natural way without artifacts. Furthermore, the implicit function far from the data must keep the same trend of data as much as possible. In Fig. 1.9d, the implicit function keeps the same trend of data.

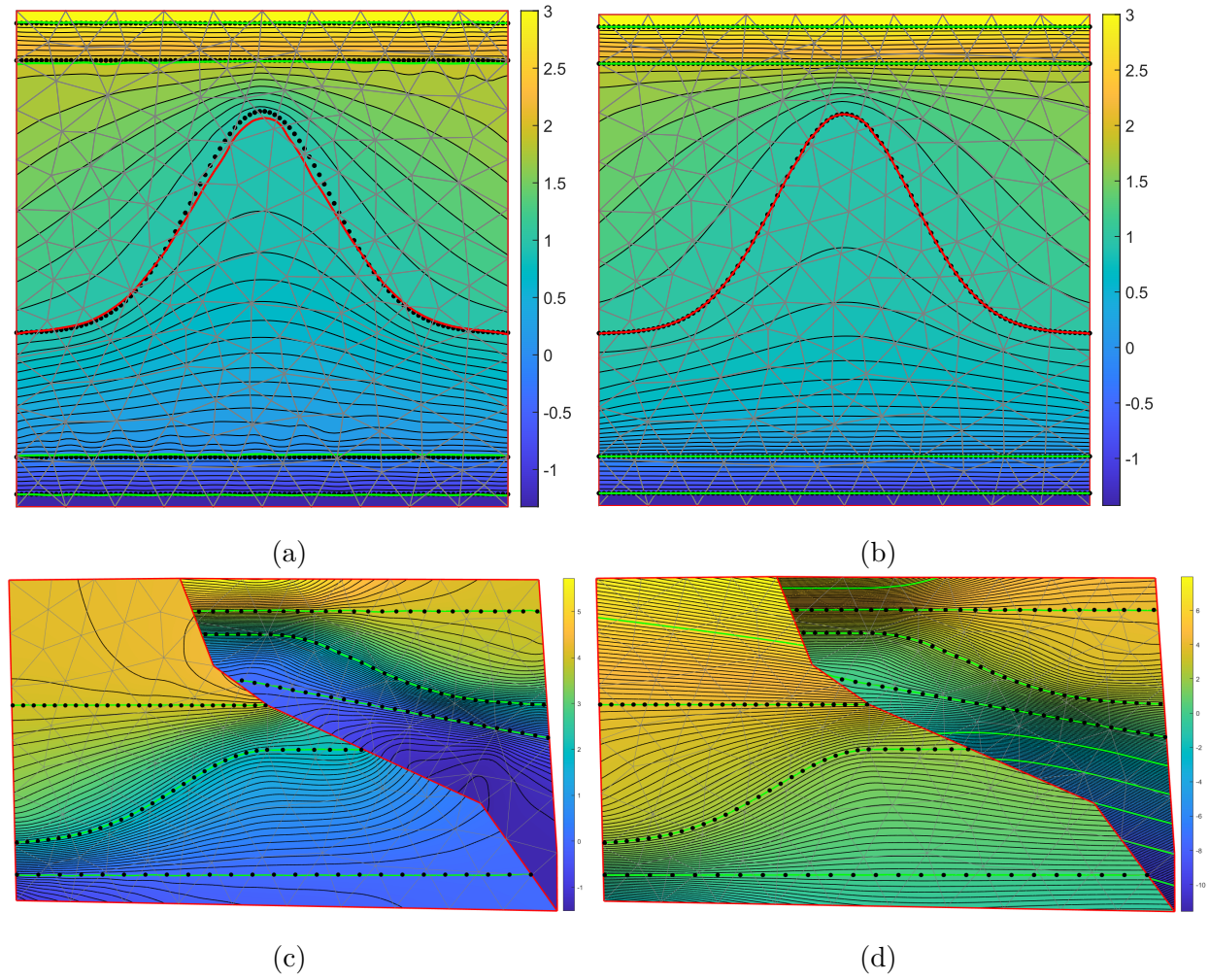

Figure 1.9: Implicit functions computed on two structural models using Eq. (4.17). (b-d) Regular solutions.(a-c) Irregular solutions.

1.9 Objectives

In the rest of the thesis, the regularity criteria introduced beforehand, will be the set of criteria considered to evaluate the regularity of the resulting implicit functions using various techniques. We will focus on mesh-based methods, which means, that we choose to introduce unconformities in the model, by generating a mesh conformal to the discontinuities. We will investigate the use of spline functions to represent the implicit function. We consider only, data points along horizons without directional data.

In the context of mesh-based methods, the main component of the implicit modeling approach is the regularization. We will explore various regularization techniques used in implicit modeling techniques, see Chap. 3. Then, we will focus on formulating regularization energies, that are adapted to our specific interpolation problem. In Chap. 4, a primary attention will be on regularization energies that can be connected to well-known PDEs, which are fundamental mathematical tools for describing a wide range of phenomena in science. PDEs require boundary conditions, where the function is well-defined along the boundary of a regularly shaped domain, to ensure that the solution to the problem is unique. In our context, the implicit function is known only on data points, and it is unknown along the domain boundaries. Nonetheless, we break the norms, by regularizing the implicit function via a PDE, that constructs the implicit function over the entire domain, based only on these given conditions. The focus, will be to enrich the regularization formulation with extra degrees of freedom that allow encoding thickness variations and the anisotropy present in the data, and produce solutions validating all the regularity criteria defined beforehand.

Chapter 2

Powell-Sabin splines

In this chapter, we recall briefly the concepts of Bezier-curves and B-splines representations. These tools are fundamental mathematical descriptions of both curves and surfaces, when extended using tensor product. Then, we present Powell-Sabin splines, which are C^1 quadratic piecewise polynomials defined on arbitrary triangulations. PS-splines are the basis functions that are used for the discretization of the implicit modeling problem in the rest of the thesis.

2.1 B-spline surface

2.1.1 Bezier curves

A Bezier curve (Fig. 2.1) is defined by the linear combination of basis functions and control points

$$\mathcal{C}(\xi) = \sum_{i=0}^{p} B_{i,p}\mathbf{P}_i \tag{2.1}$$

there are a total of $p+1$ control points $\mathbf{P}_i$, and the polygon they form is called the control polygon of $\mathcal{C}$. The functions $B_{i,p}(\xi)$ are the Bernstein polynomials of degree p. The Bernstein polynomials are defined as

$$B_{i,p}(\xi) = \frac{p!}{i!(p-i)!}\xi^i(1-\xi)^{p-i} \tag{2.2}$$

with $\xi \in [0,1]$. Interpolating complex curves using Bezier curves can be challenging, due to the need to add more control points, since using additional control points leads to an increase in the degree. Unfortunately, as the degree increases, the algorithms to manipulate these curves become numerically unstable (Kiendl 2011). These challenges when interpolating complex curves can be overcome by an alternative curve representation called B-Splines, that enables independence of degree and number of control points (See Fig. 2.1 and Fig. 2.2).

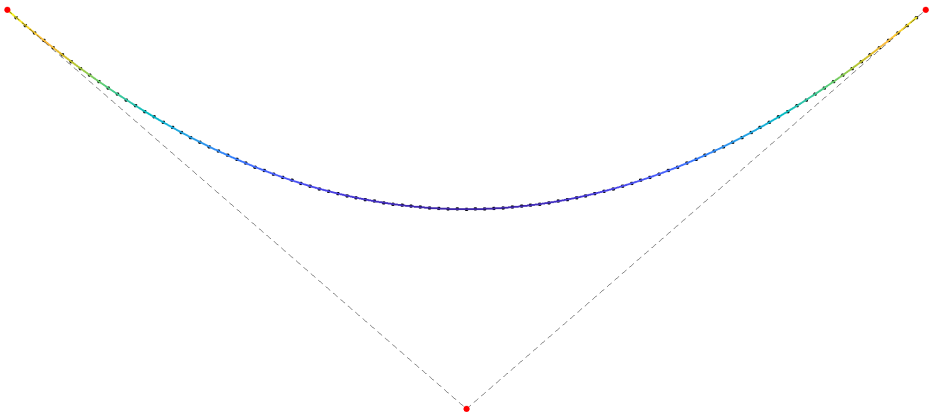

Figure 2.1: Interpolation of data points using a Bezier curve. Red dots represent control points, and black dots represent data points, while dashed lines define the control polygon.

2.1.2 B-splines curves

B-Spline curves, are defined as a linear combination of control points and basis functions. These basis functions, known as B-Splines (Basis-Splines), of a given order p are defined with a recursive relation starting with piecewise constant basis functions (for $p = 0$),

$$B_{i,0}(\xi) = \begin{cases} 1 & \xi_i \leq \xi < \xi_{i+1} \\ 0 & \text{otherwise} \end{cases} \tag{2.3}$$

For $p \geq 1$

$$B_{i,p}(\xi) = \frac{\xi - \xi_i}{\xi_{i+p} - \xi_i} B_{i,p-1}(\xi) + \frac{\xi_{i+p+1} - \xi}{\xi_{i+p+1} - \xi_{i+1}} B_{i+1,p-1}(\xi) \tag{2.4}$$

where the points ξ_i are the knots of the spline, $i = 1, 2, ..., n + p + 1$, and n is the number of basis functions.

- Local support. B-Spline basis functions have a local support, meaning they are non-zero only within the specific interval $[\xi_i, \xi_{i+p+1}]$. This property is crucial for the piecewise definition of B-spline curves or surfaces. Each basis function is responsible for controlling the shape of the spline within its local interval.
- Partition of unity. The sum of all B-spline basis functions should sum to one, $\sum_{i=1}^{n} B_{i,p}(\xi) = 1$. This property ensures that any point of the surface can be expressed as a combination of these basis functions.
- Non-negativity. B-Spline basis functions are always non-negative, $B_{i,p}(\xi) \geq 0$.

- Linear independence. The basis functions are linearly independent. This means that no linear combination of basis function can equal zero unless all the coefficients of the combination are zero.

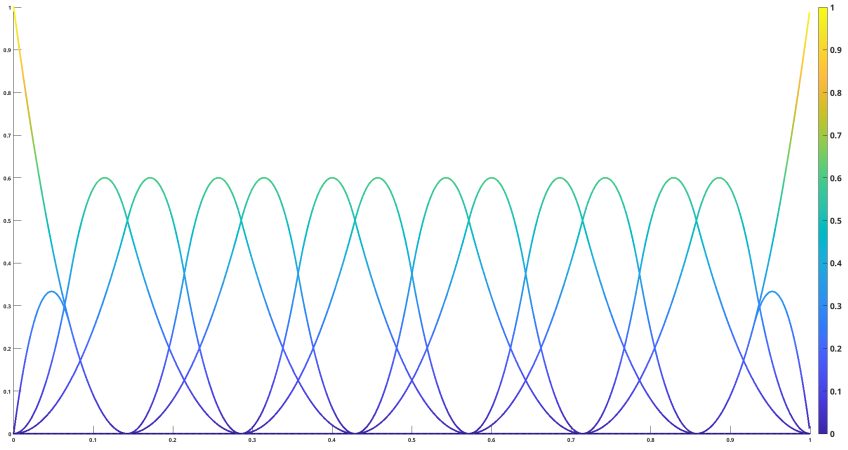

(a)

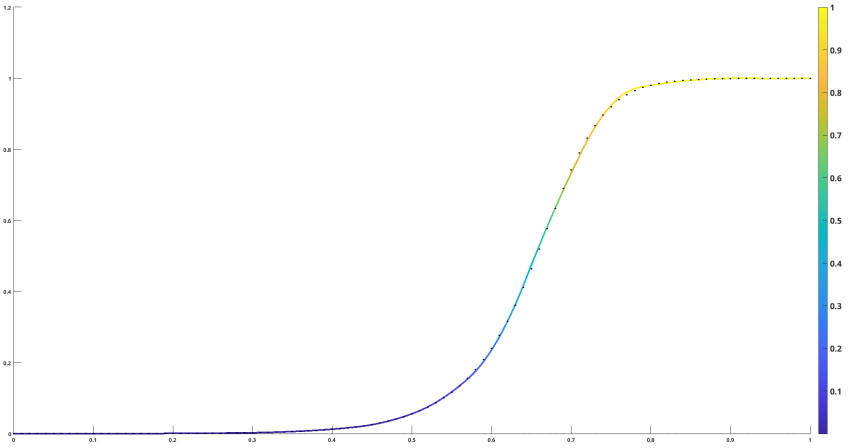

(b)

Figure 2.2: Interpolation of one dimensional data points using quadratic B-splines. Black dots represent data points. (a) Quadratic B-spline basis functions over a particular sequences of knots. (b) B-spline curve fitting the data points represented using the B-splines shown in Fig. 2.2a.

Similar to Bezier curves, a B-Spline curve of degree p is defined by the linear combination of control points and the respective basis functions as

$$\mathcal{C}(\xi) = \sum_{i=1}^{n} B_{i,p}\mathbf{P}_i \tag{2.5}$$

2.1.3 B-Spline surfaces

Starting from the one-dimensional representation Eq. (2.5), B-splines can be extended to higher dimensions by using a tensor product representation. A B-spline surface is defined using the tensor product of B-Spline basis functions. Given a net of control points $n \times m$, two knot vectors $\mathbf{\Xi} = \xi_1, ..., \xi_{n+p+1}$ and $\mathbf{\Theta} = \eta_1, ..., \eta_{m+q+1}$, two polynomial degrees p and q, a tensor product B-Spline surface is defined as

$$\mathbf{S}(\xi, \eta) = \sum_{i=1}^{n} \sum_{j=1}^{m} N_{i,p}(\xi) M_{j,q}(\eta) \mathbf{P}_{ij} \tag{2.6}$$

Tensor product splines have been widely recognized as very powerfull tools for surface fitting and CAGD (Dierckx 1997). However, they come with many limitations. They are restricted to structured rectangular meshes, which does not allow local refinement (Giorgiani et al. 2018). Powell-Splines splines represent an alternative to tensor product splines, which are piecewise quadratic polynomials that are defined on arbitrary triangulations. In the following, we will focus only on these splines.

2.2 Powell-Sabin splines

To obtain an interpolant with C^1 continuity. We first introduce some basic concepts of Bezier triangles and the C^1 quadratic Powell-Sabin 6-split.

2.2.1 Bezier triangles

Consider a non-degenerate triangle T given by three vertices $\mathbf{V}_1, \mathbf{V}_2$, and $\mathbf{V}_3$ in a plane (Fig. 2.3b), having vertices $\mathbf{V}_i$ with Cartesian coordinates (x_i, y_i), $i = 1, 2, 3$. Any arbitrary point $\mathbf{P}$ in T with coordinate $(x, y) \in \mathbb{R}^2$ can be uniquely expressed in terms of its barycentric coordinates $\tau = (\tau_0, \tau_1, \tau_2)$ as

$$\mathbf{P} = \sum_{i=0}^{2} \tau_i \mathbf{V}_i, \quad \sum_{i=0}^{2} \tau_i = 1, \ 0 \leq \tau_i \leq 1 \tag{2.7}$$

They can be determined as the unique solution of the system

$$\begin{bmatrix} x_1 & x_2 & x_3 \\ y_1 & y_2 & y_3 \\ 1 & 1 & 1 \end{bmatrix} \begin{bmatrix} \tau_1 \\ \tau_2 \\ \tau_3 \end{bmatrix} = \begin{bmatrix} x \\ y \\ 1 \end{bmatrix}. \tag{2.8}$$

Let Π_d denote the linear space of bivariate polynomials of total degree of at most d. Then any polynomial $p(x, y)$ in Π_d can be expressed in the Bernstein-Bezier form

$$p(x, y) := p(\tau) = \sum_{i+j+k=d} b_{i,j,k} B^d_{i,j,k}(\tau) \ \text{ with } i, j, k \geq 0 \tag{2.9}$$

$B^d_{i,j,k}(\tau)$ the so-called Bernstein polynomials of degree d, which form a partition of unity on T, such that

$$B^d_{i,j,k}(\tau) = \frac{d!}{i!j!k!}\tau_1^i\tau_2^j\tau_3^k \tag{2.10}$$

$$B^d_{i,j,k}(\tau) \geq 0 \quad \forall (x,y) \in T \tag{2.11}$$

$$\sum_{i+j+k=d} B^d_{i,j,k}(\tau) = 1 \quad \forall (x,y) \in T \tag{2.12}$$

The coefficients $b_{i,j,k}$ are called the Bezier ordinates of the polynomial $p(x,y)$ in the triangle T. The Bezier ordinates $b_{i,j,k}$, associated to the points $(X_{i,j,k}, Y_{i,j,k})$ having barycentric coordinates $(i,j,k)/d$ with respect to the triangle T. The points $(X_{i,j,k}, Y_{i,j,k}, b_{i,j,k})$ are called the control points of the quadratic polynomial on T. They constitute the vertices of four triangles, which is called the Bezier net of the polynomial. The Bezier net has the property that it is tangent to the polynomial surface at the three vertices (Fig. 2.3b).

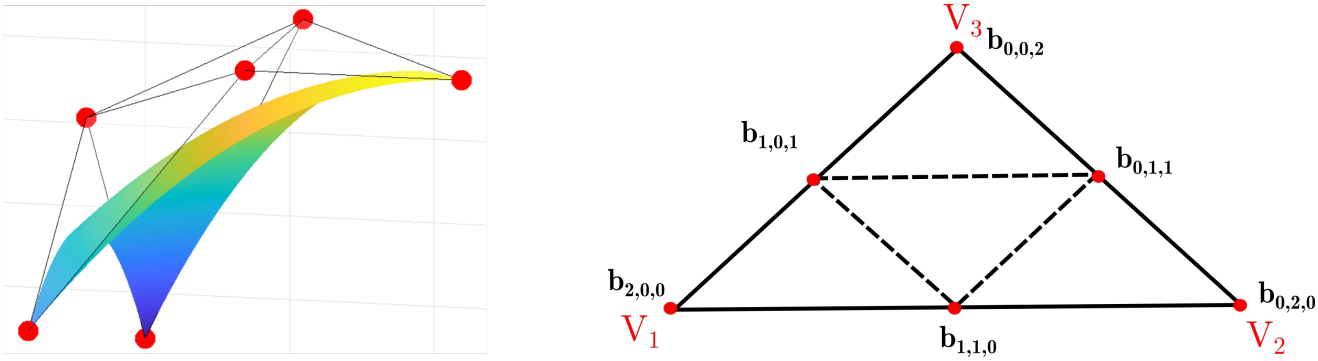

(a) (b)

Figure 2.3: Bezier ordinates of a quadratic polynomial. (a) control point and control net. (b) Bezier ordinates.

Complex surfaces in structural modeling, computer graphics or physical modeling, often require the use of a large number of Bézier triangles for their representation. However, maintaining a desired degree of continuity across these patches introduces a large set of complex conditions between the Bezier ordinates (Speleers 2008). This motivated the use of piecewise polynomials with inherent global continuity. In this section, we introduce the C^1 continuous Powell-Sabin splines.

2.2.2 Powell-Sabin subdivision and continuity conditions

The Powell-Sabin split was introduced to solve the problem of bivariate Hermite interpolation over triangular meshes Eq. (2.14). Let $\Omega \subset \mathbb{R}^2$ be a domain of interest with a boundary $\partial\Omega$ and $\mathcal{T}$ a triangulation of Ω. Let $N_\mathcal{T}$ be the number of elements, and N_v the number of vertices of the mesh $\mathcal{T}$. Each triangle T of the original mesh $\mathcal{T}$ is provided with an inner split-point $\mathbf{C} \in T$ and three edge split-points $(\mathbf{M}_{12}, \mathbf{M}_{23}, \mathbf{M}_{31})$, one on each edge of T, that introduces a segmentation of T into six micro-triangles t_i, $i = 1, .., 6$, see Fig. 2.4.

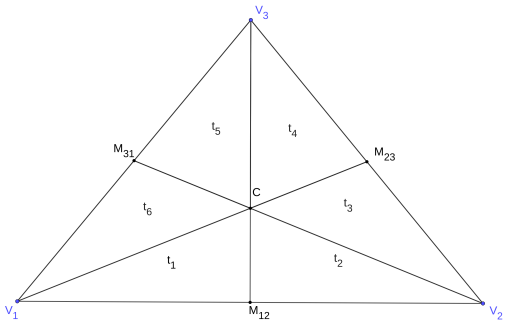

Figure 2.4: The Powell-Sabin 6-split of a triangle $T(\mathbf{V}_1, \mathbf{V}_2, \mathbf{V}_3)$.

The Powell-Sabin refinement (PS-refinement) $\mathcal{T}^*$ of $\mathcal{T}$ partitions each triangle into six smaller triangles in the following way (Fig. 2.5):

- Choose an interior point $\mathbf{C}_i$ inside each triangle T_i.
- Connect the point $\mathbf{C}_i$ to the three vertices of T_i.
- For each edge of T_i
  - that is shared with a triangle T_j, join $\mathbf{C}_i$ to the intersection point $\mathbf{M}_{ij}$ of that edge and the line $(\mathbf{C}_i\mathbf{C}_j)$.
  - that belongs to the boundary $\partial\Omega$, join $\mathbf{C}_i$ to the middle point of that edge.

The resulting PS-refined mesh $\mathcal{T}^*$ contains $6 \times N_{\mathcal{T}}$ elements. Each subtriangle of $\mathcal{T}^*$ is denoted as t_j for $j = 1, ..., 6 \times N_{\mathcal{T}}$. Many possibilities exist for the choice of the interior point $\mathbf{C}_i$ of the triangle T_i. Typically this point is chosen as centroid (called also barycenter) of T_i (Bartoň and Kosinka 2019).A discussion concerning the choice of this point can be found in Dierckx (1997), Kosinka and Cashman 2015, Schumaker and Speleers 2010. We also opted for the centroid option for practical considerations.

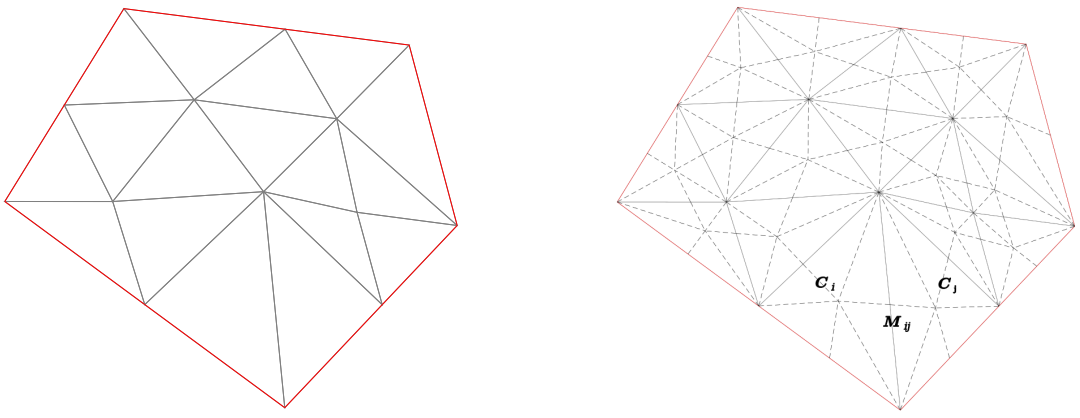

(a) (b)

Figure 2.5: PS-refinement of a triangular mesh. (a) Original mesh. (b) refined mesh.

The space of piecewise quadratic polynomials on $\mathcal{T}^*$ with global C^1-continuity is called the Powell-Sabin spline space:

$$S_2^1(\mathcal{T}^*) := \left\{ u \in C^1(\Omega) : u|_t \in \Pi_2, t \in \mathcal{T}^* \right\}. \tag{2.13}$$

Each $u \in S_2^1(\mathcal{T}^*)$ consists of $6 * N_{\mathcal{T}}$ quadratic Bezier triangles (one on each subtriangle in Fig. 2.4 or Fig. 2.5). Powell and Sabin (1977) proved that the following interpolation problem

$$u(\mathbf{V}_k) = f_k, \quad \frac{\partial u}{\partial x}(\mathbf{V}_k) = f_{x,k}, \quad \frac{\partial u}{\partial y}(\mathbf{V}_k) = f_{y,k}, \quad k = 1, ..., N_v \tag{2.14}$$

has a unique solution $u(x, y) \in S_2^1(\mathcal{T}^*)$ for any given set of N_v $(f_k, f_{x,k}, f_{y,k})$-triplets. Hence, the dimension of the Powell-Sabin spline space $S_2^1(\mathcal{T}^*)$ equals $3N_v$.

In other words, a spline function in the space $S_2^1(\mathcal{T}^*)$ is fully determined, only if we know the value of this function and its gradients on all the vertices of the mesh $\mathcal{T}$. In contrary of classical linear interpolants, where only the values of the function are needed. Also given our context, where the gradient of the implicit function is usually not available and the data points do not cover all the mesh vertices, a legitimate question that can arise at this point is why we are seeking an interpolant that asks for more conditions to fully determine the solution. In the rest of the thesis, we will show that the behaviour of the solution all over the domain is mainly determined by the choice of the regularization considered and that an appropriate choice of the regularization is the way to overcome the undetermined nature of our problem. Furthermore, we will also illustrate that using PS-splines, we are able to produce surfaces of higher smoothness and regularity using meshes with reduced number of vertices.

2.2.3 A B-spline representation

Dierckx (1997) presented a geometric method to construct a normalized basis for the spline space $S_2^1(\mathcal{T}^*)$. Every spline function in this space can be represented as

$$u(x, y) = \sum_{i=1}^{N_v} \sum_{j=1}^{3} u_{i,j} B_i^j(x, y) \tag{2.15}$$

The functions $B_i^j(x, y)$ are called Powell-Sabin B-splines. To construct these PS B-splines $B_i^j(x, y),\ j = 1, 2, 3$, with support on the molecule M_i of vertex $\mathbf{V}_i$. This molecule is defined as the union of all triangles of the original triangulation that contains $\mathbf{V}_i$. The basis functions $B_i^j(x, y)$ are uniquely defined by specifying their values and gradients at each vertex of $\mathcal{T}$. The structure of the support M_i implies that

$$B_i^j(\mathbf{V}_k) = 0, \quad \frac{\partial B_i^j}{\partial x}(\mathbf{V}_k) = 0, \quad \frac{\partial B_i^j}{\partial y}(\mathbf{V}_k) = 0, \tag{2.16}$$

for any vertex $\mathbf{V}_k \neq \mathbf{V}_i$, and we set

$$B_i^j(\mathbf{V}_i) = \alpha_{ij}, \quad \frac{\partial B_i^j}{\partial x}(\mathbf{V}_i) = \beta_{ij}, \quad \frac{\partial B_i^j}{\partial y}(\mathbf{V}_i) = \gamma_{ij}. \tag{2.17}$$

The values $(\alpha_{i,j}, \beta_{i,j}, \gamma_{i,j}),\ j = 1, 2, 3$, should be carefully chosen so that the corresponding basis functions, constructed by Eq. (2.14) and Eq. (2.17)-Eq. (2.16), form a convex partition

of unity. For each vertex $\mathbf{V}_i$, we associate three points $\mathbf{Q}_{i,j} = (X_{i,j}, Y_{i,j})$, $j = 1, 2, 3$, such that, for $i = 1, ..., N_v$

$$\begin{bmatrix} \alpha_{i,1} & \alpha_{i,2} & \alpha_{i,3} \\ \beta_{i,1} & \beta_{i,2} & \beta_{i,3} \\ \gamma_{i,1} & \gamma_{i,2} & \gamma_{i,3} \end{bmatrix} \begin{bmatrix} X_{i,1} & Y_{i,1} & 1 \\ X_{i,2} & Y_{i,2} & 1 \\ X_{i,3} & Y_{i,3} & 1 \end{bmatrix} = \begin{bmatrix} x_i & y_i & 1 \\ 1 & 0 & 0 \\ 0 & 1 & 0 \end{bmatrix} \tag{2.18}$$

It follows that the corresponding basis function B_i^j sum up to one. Moreover, for every point $\mathbf{P}$ of coordinates (x, y) we have

$$\mathbf{P} = \sum_{i=1}^{N_v} \sum_{j=1}^{3} \mathbf{Q}_{i,j} B_i^j(\mathbf{P}) \tag{2.19}$$

The points $\mathbf{Q}_{i,j}$ are Greville points or domain points of the functions B_i^j, see for more details Buffa and Sangalli (2016). The triangle $t_i^c = (\mathbf{Q}_{i,1}, \mathbf{Q}_{i,2}, \mathbf{Q}_{i,3})$ is referred to as the PS triangle associated with the vertex $\mathbf{V}_i$. Eq. (2.18) it implies that for each vertex $\mathbf{V}_i$ three functions B_i^j are uniquely determined by the points $\mathbf{Q}_{i,j}$, $j = 1, 2, 3$ (Fig. 2.10). Furthermore,

- $\alpha_i = (\alpha_{i,1}, \alpha_{i,2}, \alpha_{i,3})$ are the barycentric coordinates of $\mathbf{V}_i$ with respect to t_i^c.
- $\beta_i = (\beta_{i,1}, \beta_{i,2}, \beta_{i,3})$ and $\gamma_i = (\gamma_{i,1}, \gamma_{i,2}, \gamma_{i,3})$ are the barycentric directional coordinates with respect to t_i^c, respectively, in the $x-$ and $y-$direction.
- at the vertex $\mathbf{V}_i$, the basis functions B_i^j has a directional derivative equal to zero in the direction of the edge of t_i^c opposite to $\mathbf{Q}_{i,j}$.

Then, for each vertex $\mathbf{V}_i$ we define its PS points as the vertex itself and the midpoints of all the edges of the PS refinement $\mathcal{T}^*$ containing $\mathbf{V}_i$. Moreover, Dierckx (1997) showed that basis functions B_i^j, $j = 1, 2, 3$, are positive if and only if the PS triangle t_i^c contains all the PS points associated with the vertex $\mathbf{V}_i$.

Finally, the PS B-splines associated with each vertex $\mathbf{V}_i$ are uniquely determined using the triple of points $\mathbf{Q}_{i,j}, j = 1, 2, 3$, that constitutes the PS triangle. Therefore, the PS triangles are used to geometrically describe the PS B-splines and their properties instead of α_i, β_i, γ_i (See Fig. 2.6 and Fig. 2.7). Fig. 2.7 shows three linearly independent PS B-splines around the same vertex.

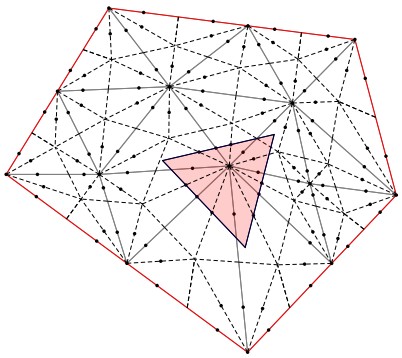

Figure 2.6: PS refinement and PS triangle around a vertex of a given triangulation.

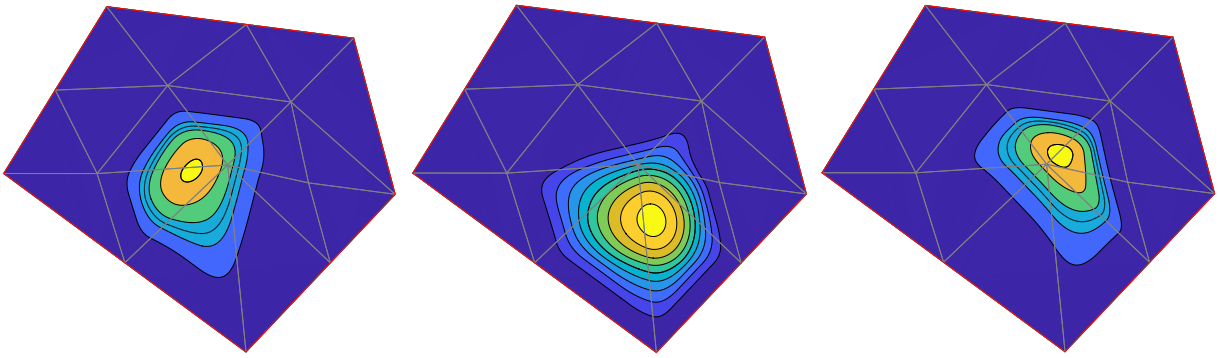

(a) (b) (c)

Figure 2.7: Three Basis functions around the vertex in Fig. 2.6.

PS triangles are not uniquely defined since the only condition is that it contains all the PS points (Maes and Bultheel 2006, Speleers et al. 2012). Giorgiani et al. (2018) showed that as the area of the PS triangles increases the three basis functions become more alike. An optimal PS triangle is a triangle of minimal area that contains all the PS points (Dierckx 1997, Maes and Bultheel 2006, Speleers et al. 2012, Giorgiani et al. 2018). This results in finding the minimal area triangle that encloses a convex polygon. For this problem an optimal algorithm exits, with a computational cost $O(n)$, with n the number of PS points, proposed by O'Rourke et al. (1986). Giorgiani et al. (2018) considered this algorithm for the construction of optimal PS triangles. In this thesis, we also used this algorithm for the construction of minimal area PS triangles (Fig. 2.8). Giorgiani et al. (2018) considered specific conditions on PS triangle for the vertices along the boundaries to simplify the imposition of boundary conditions. Also, Chen et al. (2021) used a special choice PS triangle for the vertices along the boundaries for the imposition of Dirichlet boundary conditions. More discussion on the construction of optimal PS triangles can be found in (Speleers 2008, Speleers et al. 2012.

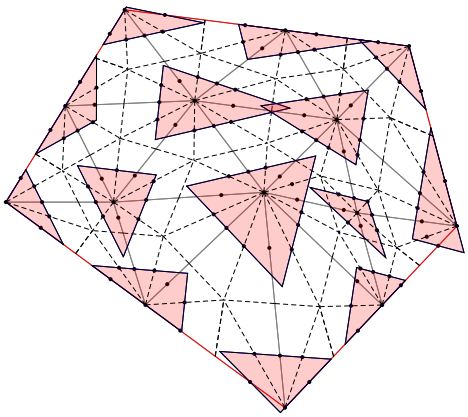

Figure 2.8: PS triangles of minimal area and PS points. PS points that are Bezier domain points, are depicted using black dots. The PS triangles that are highlighted in red, are triangles of minimal area. Each is associated to a vertex and contains the set of PS points around it.

2.2.4 PS control triangles

Referring to the representation Eq. (2.15), control points are defined as

$$\mathbf{c}_{i,j} = (\mathbf{Q}_{i,j}, u_{i,j}) \tag{2.20}$$

These points define the PS control triangles $T_i^c = (\mathbf{c}_{i,1}, \mathbf{c}_{i,2}, \mathbf{c}_{i,3})$, which are tangent to the spline surface $z = u(x, y)$ at the vertices $\mathbf{V}_i$. The projection of the control triangles T_i^c in the $(x, y)-$plane are simply the PS triangles t_i^c.

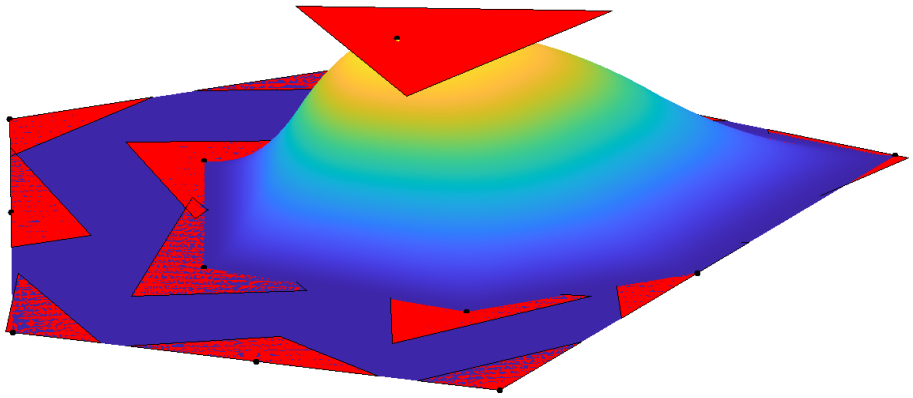

Figure 2.9: PS-spline surface and its control triangles.

Fig. 2.9 shows a PS spline and its tangent control triangles. Using these control triangles, the PS spline surface can be edited locally. This property is very usefull in structural modeling, since often the constructed model need to updated after new data become available.

2.2.5 The Bezier ordinates of a PS-spline

We consider the triangle $T(\mathbf{V}_1, \mathbf{V}_2, \mathbf{V}_3)$ in the triangulation $\mathcal{T}$. We assume that the points in Fig. 2.4 have the following barycentric coordinates

$$\begin{array}{llll} \mathbf{V}_1(1,0,0), & \mathbf{V}_2(0,1,0), & \mathbf{V}_3(0,0,1), & \mathbf{C}(c_1,c_2,c_3) \\ \mathbf{M}_{12}(\lambda_{12},\lambda_{21},0), & \mathbf{M}_{23}(0,\lambda_{23},\lambda_{32}), & \mathbf{M}_{31}(\lambda_{13},0,\lambda_{31}) & \end{array}$$

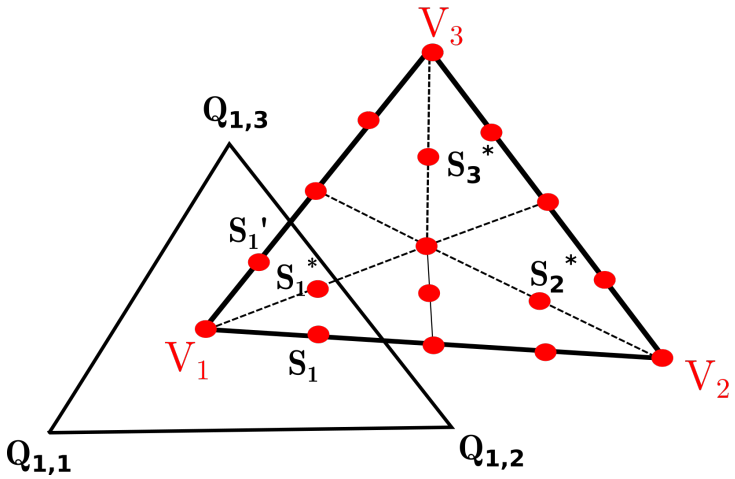

Figure 2.10: PS refinement of a triangle $T(\mathbf{V}_1, \mathbf{V}_2, \mathbf{V}_3)$, with the PS triangle $t_1^c = (\mathbf{Q}_{1,1}, \mathbf{Q}_{1,2}, \mathbf{Q}_{1,3})$ around the vertex $\mathbf{V}_1$.

On each of the six triangles $\mathcal{T}^*$ the Powell-Sabin spline is a quadratic polynomial, that can be represented in the Bezier representation.

$$s_1 = \alpha_{1,1}u_{1,1} + \alpha_{1,2}c_{1,2} + \alpha_{1,3}u_{1,3} \tag{2.21}$$
$$b_1 = L_{1,1}u_{1,1} + L_{1,2}u_{1,2} + L_{1,3}u_{1,3} \tag{2.22}$$
$$d_1 = L^*_{1,1}u_{1,1} + L^*_{1,2}u_{1,2} + L^*_{1,3}u_{1,3} \tag{2.23}$$
$$c_1 = L'_{1,1}u_{1,1} + L'_{1,2}u_{1,2} + L'_{1,3}u_{1,3} \tag{2.24}$$

where $(\alpha_{1,1}, \alpha_{1,2}, \alpha_{1,3})$ are the barycentric coordinates of vertex $\mathbf{V}_1$ with respect to the PS triangle t_1^c, while the triplets $(L_{1,1}, L_{1,2}, L_{1,3})$, $(L^*_{1,1}, L^*_{1,2}, L^*_{1,3})$ and $(L'_{1,1}, L'_{1,2}, L'_{1,3})$ are the barycentric coordinates of the PS points around the vertex $\mathbf{V}_1$, $\mathbf{S}_1$, $\mathbf{S}_1^*$, $\mathbf{S}_1'$, respectively, with respect to the PS triangle t_1^c (Fig. 2.10). Similarly, we can compute (s_2, b_2, d_2, c_2) and (s_3, b_3, d_3, c_k) (Fig . 2.11). The rest of the Bezier ordinates are derived from the inherent continuity conditions, for example

$$m_1 = \lambda_{12}b_1 + \lambda_{21}b_2 \tag{2.25}$$
$$e_1 = \lambda_{12}d_1 + \lambda_{21}d_2 \tag{2.26}$$
$$\omega = c_1d_1 + c_2d_2 + c_3d_3 \tag{2.27}$$

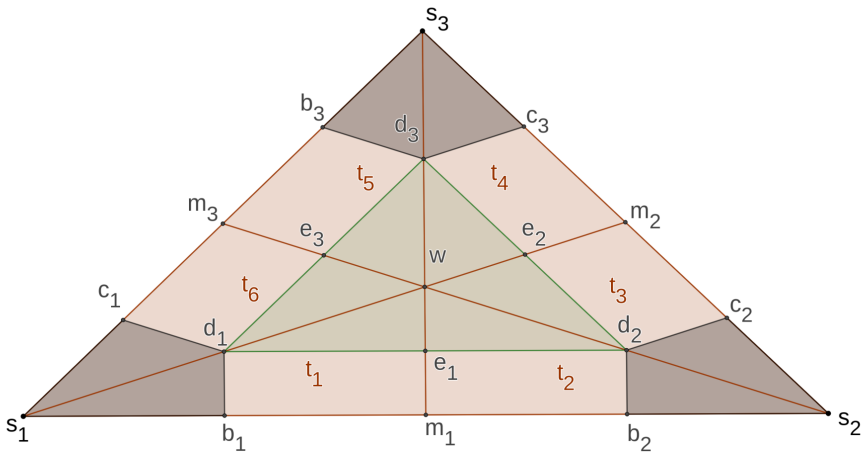

Figure 2.11: The Bezier ordinates of a PS spline on the triangle $T(\mathbf{V}_1, \mathbf{V}_2, \mathbf{V}_3)$.

2.3 PS-splines for finite element analysis

The Finite Element Method (FEM) is an effective technique for solving partial differential equations (PDEs). It achieves this, by approximating the PDE solution within a chosen subspace of the solution space through a suitable projection. Typically, this involves selecting a basis for the approximation space and then solving a resulting linear system of equations to determine the coefficients associated with this basis. Consequently, the selection of an appropriate approximation space is crucial, since it directly affects the quality of the solution and the computational efficiency (Speleers 2008).

Using splines as basis functions in FEM methods has many advantages. For example, the additional global smoothness of the spline interpolant introduces stability to the numerical solution (Hughes et al. 2005, Speleers et al. 2012, Bazilevs et al. 2007). Concerning the use of PS-splines in Finite element, the foundational work of Speleers (2008) explains how to generate the basis functions and to treat boundary conditions for the resolution of second order elliptic problems. Speleers et al. (2012) also used the PS splines for solving the advection-diffusion-reaction problems. Later in Veiga et al. (2015) and May et al. (2015), it was used for solving the equation of bending of thin plate, where C^1 continuity of the basis is needed to deal with second derivatives of the displacement that arise in the strain energy expression. Giorgiani et al. (2016) analyzed the finite element methods based on PS-splines, for PDEs in two dimensions. Later, Giorgiani et al. (2018) presented a finite element scheme based on PS-splines for the $2D$ Euler equations in supersonic regime and introduced a stabilization to reduce oscillations. Chen et al. (2021) used PS-Splines to discretize high-order phase-field models for brittle fracture in anisotropic materials, which results in a fourth order PDE for the damage evolution and necessitates C^1 continuity of the basis functions.

Tensor product splines are typically defined on rectangular meshes and do not allow local refinement of the mesh. In contrast, PS-splines are defined on arbitrary triangulations, which allow adaptive refinement. This property is essential when discretizing anisotropic equation (Giorgiani et al. 2018). PS-splines allow straightforward adaptive refinement of the mesh.

2.4 A spline-based method for implicit structural modeling

In the context of mesh-based methods, the optimization problem for the construction of the implicit functions is expressed as a sum of two energies, see Eq. (1.11). First, the fitting energy that constrains the implicit function to honor the data as much as possible. In this context, splines emerge as powerfull tool for accurately fitting the data point (Speleers 2008, Dierckx 1997). Second, the regularization energy that imposes a regular behaviour of the implicit function across the entire domain. It can be chosen as Hessian or Laplacian energies, and discretized using a finite element scheme (Irakarama et al. 2022). In this case, the discretization of second order derivatives used in the Hessian energy minimization with splines is straightforward compared to the classic linear discretization. Furthermore, the smoothness assumption of the stratigraphic layers is usually considered (Renaudeau 2019, Mallet 1997, Souche et al. 2014). Thus, the inherent C^1 continuity of the PS-splines aligns with this assumption.

Over the decades, mesh generation techniques using triangulations has become mature, with the development of many robust and efficient meshing algorithms and softwares (Druyor 2011, George et al. 2007). Several modeling softwares have been developed in the oil and gas industry based on implicit mesh-based methods based on simplices, for example volume based modeling (VBM) by Souche et al. (2014). In this context, PS-splines are a good choice since they can be constructed on arbitrary meshes. Furthermore, in $2D$ for example, the PS-refinement of the mesh involves dividing each triangle to six sub-triangles, where each sub-triangle is a quadratic Bezier-surface. Remarkably, this expansion increases the degrees of freedom by a factor of only three, due to the inherent C^1 continuity. This condition enhances the smoothness and the regularity of the solutions, and reduces the dimensions of the PS-space compared to working with the full space of quadratic polynomials (Speleers 2008).

2.5 Extension of Powell-Sabin splines to $3D$

Speleers (2013) presented a method for constructing a normalized basis for the multivariate quadratic spline space defined over a generalized Powell-Sabin refinement of a triangulation in $\mathbb{R}^S$, $s \geq 1$. This method provides a generalization of the normalized B-spline representation of Dierckx (1997) for $s = 2$ and Sbibih et al. (2012) for $s = 3$, and the basis functions share the same properties, nonnegativity, local support and partition of unity. Geometrically, the construction is equivalent to determining a set of small simplices that must contain a specific set of points (Fig. 2.12). Furthermore, the univariate PS-splines using the multivariate representation in Speleers (2013) corresponds to the classical quadratic normalized B-splines. In the rest of the thesis, we will use these univariate PS-splines, for fitting one dimensional data points.

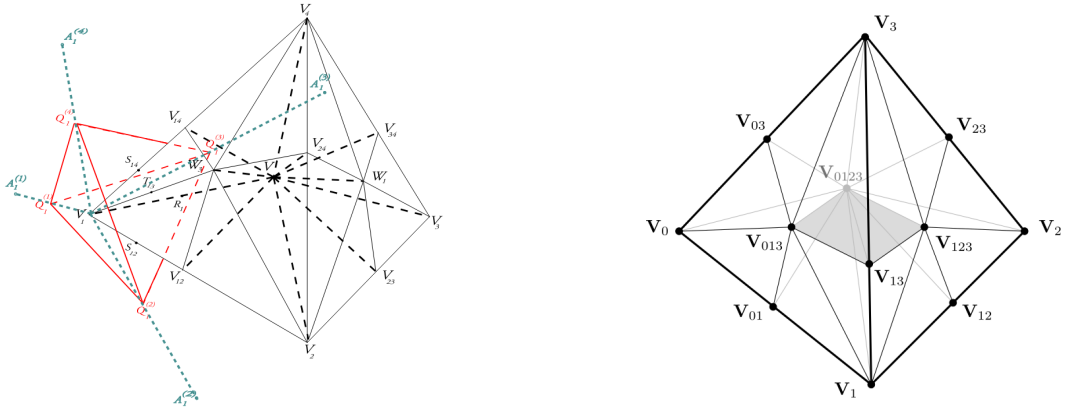

(a) (b)

Figure 2.12: PS-split and PS triangle in three dimensions. (a) PS-tetrahedral containing the set of PS-points (Picture of Sbibih et al. 2012). (b) PS-split of a tetrahedral in three dimensions (Picture of Speleers 2013).

While it appears to be a feasible option, it is worth noting that we did not conduct experiments on the construction of Speleers 2013 in $3D$. In the rest of the thesis, the formulations of the implicit modeling problem Eq. (1.11) will be presented using generic notations for basis function.

Chapter 3

Regularization

The regularization of the implicit function is the main ingredient of any implicit modeling approach. Regularization techniques are used for selecting a specific set of functions, in the solution space, which satisfy the regularity criteria desired in the resulting function. In this chapter, we introduce a wide range of regularization techniques that are widely used in the field of implicit structural modeling. We start by posing the implicit structural modeling as a regularized data fitting problem. Then, we recall the Discrete Smooth Interpolation (DSI) generic framework for the interpolation of geological models, and we discuss the classical regularization techniques considered in DSI using linear interpolation basis functions. Additionally, we recall classical regularization energies and we demonstrate the results on some models presenting thickness variations. We conclude by discussing common challenges such as strong oscillations in the presence of high thickness variations.

3.1 Implicit modeling problem as a minimization of a sum of quadratic energies

We consider a domain $\Omega \subset \mathbb{R}^2$ with N_p stratigraphic data points (x_p, y_p, z_p) for $p = 1 : N_p$, and an implicit function u interpolating the data: $u(x_p, y_p) = z_p$. Each subset of points with equal value z_p represents a horizon. The domain Ω is discretized with a mesh conformal to the discontinuities (geological faults). On the mesh, we define N_s basis functions in the space F of regular functions. The implicit function u is defined as

$$u(\mathbf{x}) = \sum_{i=1}^{N_s} B_i(\mathbf{x}) u_i = \mathbf{B}(x)\mathbf{U} \quad \forall \mathbf{x} \in \Omega \tag{3.1}$$

where $\mathbf{B}(\mathbf{x}) = (B_i(\mathbf{x}))_{i=1}^{N_s}$ is a basis of F, $\mathbf{U} = (u_i)_{i=1}^{N_s}$ is a vector of unknowns and N_s is the dimension of F. To obtain a solution of the interpolation problem of the geological data points over the domain Ω, we minimize the fitting energy E_{fit}, with η_p fitting weights associated to

each of the data points.

$$E_{fit}(u) = \sum_{p=1}^{Np} \eta_p^2 (u(x_p, y_p) - z_p)^2 \tag{3.2}$$

$$= \sum_{p=1}^{Np} \eta_p^2 (\mathbf{B}(x_p, y_p)\mathbf{U} - z_p)^T (\mathbf{B}(x_p, y_p)\mathbf{U} - z_p) \tag{3.3}$$

$$= \sum_{p=1}^{Np} \eta_p^2 (\mathbf{U}^T \mathbf{B}(x_p, y_p)^T \mathbf{B}(x_p, y_p)\mathbf{U} - 2\mathbf{U}^T \mathbf{B}(x_p, y_p)^T z_p + z_p^2) \tag{3.4}$$

To obtain a minimizer of the fitting energy, we set the gradient with respect to $\mathbf{U}$ to zero, and the equivalent linear system to solve is

$$\sum_{p=1}^{Np} \eta_p^2 \mathbf{B}(x_p, y_p)^T \mathbf{B}(x_p, y_p)\mathbf{U} = \sum_{p=1}^{Np} \eta_p^2 \mathbf{B}(x_p, y_p)^T z_p \tag{3.5}$$

which can be written as a linear system

$$\mathbf{A_{fit}}^T \mathbf{A_{fit}} \mathbf{U} = \mathbf{A_{fit}}^T \mathbf{Z} \tag{3.6}$$

where $\mathbf{A_{fit}}$ is a matrix of size (N_p, N_s) and $\mathbf{Z}$ a column vector of size N_p. Each row p in $\mathbf{A_{fit}}$ corresponds to a constraint associated with a data point that has coordinates (x_p, y_p) and a corresponding value z_p. The matrix $\mathbf{A_{fit}}$ and the vector $\mathbf{Z}$ are expressed as

$$(\mathbf{A_{fit}})_{p,j} = \eta_p B_j(x_p, y_p), \qquad \mathbf{Z}(p) = \eta_p z_p \quad \text{for } 1 \leq p \leq N_p, 1 \leq j \leq N_s \tag{3.7}$$

Solving the linear system Eq. (3.6) is equivalent to minimizing

$$\min_{\mathbf{U}} \|\mathbf{A_{fit}}\mathbf{U} - \mathbf{Z}\|^2 \tag{3.8}$$

In our context, the data can be sparse and noisy, and basis functions are locally supported. This leads to an underdetermined system with an infinity of possible solutions. To restrict the space of solutions a regularization term is introduced. The implicit modeling problem is posed as a minimization of a sum of energies

$$\min_u E_{fit}(u) + \lambda E_{reg}(u) \tag{3.9}$$

where $E_{fit}(u)$ is the fitting energy associated to the data constraints, $E_{reg}(u)$ is the regularization energy associated to the regularity constraints, λ is the regularization weight controlling the tradeoff between the fitting and regularization constraints.

3.1.1 Resulting linear systems to solve for the minimization of a regularization energy

Let $E_{reg}(u)$ be a regularization energy on u, that we assume quadratic and convex in u. We can then represent it using a symmetric semi-definite positive matrix $\mathbf{D}$ as

$$E_{reg}(u) = \mathbf{U}^T \mathbf{D} \mathbf{U} - 2\mathbf{U}^T \mathbf{B} + c \tag{3.10}$$

where $\mathbf{D} \in \mathbb{R}^{N_s \times N_s}$, $\mathbf{B} \in \mathbb{R}^{N_s \times 1}$, $c \in \mathbb{R}$. The fitting energy is discretized as

$$E_{fit}(u) = \mathbf{U}^T {\mathbf{A_{fit}}}^T \mathbf{A_{fit}} \mathbf{U} - 2\mathbf{U}^T {\mathbf{A_{fit}}}^T \mathbf{Z} + \mathbf{Z}^T \mathbf{Z} \tag{3.11}$$

The regularized fitting problem 3.9 is then minimized by setting the gradient vector to zero, and the equivalent linear system to solve is

$${\mathbf{A_{fit}}}^T \mathbf{A_{fit}} \mathbf{U} + \lambda \mathbf{D} \mathbf{U} = {\mathbf{A_{fit}}}^T \mathbf{Z} + \lambda \mathbf{B} \tag{3.12}$$

An alternative way to formulate problem 3.9 is to pose the system as least square minimization of

$$\begin{bmatrix} \mathbf{A_{fit}} \\ \sqrt{\lambda}\mathbf{R} \end{bmatrix} U = \begin{bmatrix} \mathbf{Z} \\ \mathbf{0} \end{bmatrix} \tag{3.13}$$

where $\mathbf{R}$ is a matrix of the set of the linear constraints related to a given regularization operator. Then, the equivalent minimized quadratic energy problem on $\mathbf{U}$ is

$$\min_{\mathbf{U}} \|\mathbf{A_{fit}} \mathbf{U} - \mathbf{Z}\|^2 + \lambda \mathbf{U}^T \mathbf{R}^T \mathbf{R} \mathbf{U} \tag{3.14}$$

Minimizing the fitting linear constraints $\|\mathbf{A_{fit}} \mathbf{U} - \mathbf{Z}\|^2$ with respect to $\mathbf{U}$, is equivalent to minimizing the fitting energy E_{fit}. However, to ensure equivalence for the regularization parts the equality $\mathbf{R}^T \mathbf{R} = \mathbf{D}$ must be guaranteed. Understanding the equivalent quadratic energy formulation enables to link the set of regularization constraints to a specific quadratic regularization energy in order to better interpret the effect of these constraints on the resulting solutions of the minimization problem 3.13.

3.2 Discrete Smooth Interpolation methods

Discrete Smooth Interpolation (DSI) is a class of methods widely used in structural modeling, that provides a generic framework for the interpolation of geological data. These methods are based on the discretization of the domain of interest Ω using a mesh. In $2D$ problems, triangular elements, while in $3D$, tetrahedral elements are commonly employed (Irakarama et al. (2022), Lévy and Mallet (1999)). Alternatively, grids can also be utilized for discretization (Mallet (1989), Irakarama et al. (2021)). The implicit function is then expressed using a set of basis functions constructed on the mesh. The basis functions choice is customary the classical piecewise linear finite elements on simplices (Frank et al. (2007), Souche et al. (2014)). The degrees of freedom are the values of the function at the vertices of the mesh.

$$\forall \mathbf{x} \in \Omega, \quad u(\mathbf{x}) = \sum_{i \in N_v} \phi^{v_i}(\mathbf{x}) u_i = \mathbf{\Phi}(\mathbf{x}) \mathbf{U} \tag{3.15}$$

with N_v number of meh nodes, the vector $\mathbf{\Phi}(\mathbf{x}) = (\phi^{\mathbf{v}_i})_{i=1,N_v}$ and $\phi^{\mathbf{v}_i}$ is the piecewise linear Lagrange basis function associated to the node $\mathbf{v}_i$, such that $\phi^{\mathbf{v}_i}(\mathbf{v}_j) = \delta_{ij}$ for vertices $\mathbf{v}_i, \mathbf{v}_j$ and u_i is the corresponding coefficient. Each data constraint $u(x_p, y_p) = z_p$ is discretized as

$$u(x_p, z_p) = \sum_{i \in N_v} \phi^{v_i}(x_p, y_p) u_i = \mathbf{\Phi}(x_p, y_p) \mathbf{U} = z_p \tag{3.16}$$

in the vector $\mathbf{\Phi}(x_p, y_p)$ at maximum only 3 basis functions are not null, the three basis functions related to the mesh nodes where the point is located. To obtain a solution which best interpolates data, we solve in a least square sense the system 3.4 by minimizing

$$\min_{\mathbf{U}} \|\mathbf{A_{fit}}\mathbf{U} - \mathbf{Z}\|^2 \tag{3.17}$$

The discretization of the geological data constraints in DSI methods is equivalent to the minimization of the fitting energy in addition to regularization energies, that we are going to describe.

3.2.1 DSI regularizations

The geological data are often sparse and irregularly distributed on the domain. Since the interpolation is mesh-based, roughness factors (Mallet (1989)) are added to select a specific set of solutions in the space of all functions. These roughness terms are discretized as well, and assembled into a linear system that is added to the geological data constraints. The DSI system is then expressed as

$$E_{fit}(u) = \|\mathbf{A_{fit}}\mathbf{U} - \mathbf{Z}\|^2 + R(\mathbf{U}) \tag{3.18}$$

where R corresponds to the discretized roughness constraints, which is a quadratic term with respect to $\mathbf{U}$ of the form $\mathbf{R}(\mathbf{U}) = \mathbf{U}^T\mathbf{W}\mathbf{U}$, with $\mathbf{W}$ a positive semidefinite matrix. The previous energy is then minimized to find a solution satisfying the data fitting constraints, as well as the roughness constraints. The DSI system is equivalent to the minimization problem we considered in Eq. (3.9). The choice of roughness/regularization criteria in the DSI methods does not follow a general rule. It is determined by the properties desired in the resulting implicit function. Various roughness penalizations were considered in DSI methods. For example in his pioneering work, Mallet (1989) considered a global roughness term R expressed as a sum of a set criterions $(R_i)_{i=1:5}$ involving, respectively, the minimization of first order derivatives of the implicit functions with respect to x and y, as well as, the second order derivatives with respect to xx, xy and yy over all the domain, respectively denoted, R_i, for $i = 1:5$. The roughness criterions are positive semidefinite quadratic energies with respect to the vector of unknowns $\mathbf{U}$. The roughness criteria discretized over all the nodes as

$$R(u) = \sum_{i=1:5} c_i R_i(u) = \gamma(R_1(u) + R_2(u)) + (1-\gamma)(R_3(u) + R_4(u) + R_5(u)) \tag{3.19}$$

where

$$R_i(u) = \sum_{k \in K_i} \mu_i(k) R_i(u \mid k) \tag{3.20}$$

with c_i are weights associated to each roughness criteria R_i and $\mu_i(k)$ are weights associated to each node. The terms

$$R_i(u \mid k) = (\sum_{\alpha \in N_i(k)} v_i^\alpha(k) u_\alpha)^2 \tag{3.21}$$

can be written as

$$R_i(u \mid k) = u_\alpha^T [W_i(k)] u_\alpha \tag{3.22}$$

$v_i^\alpha(k)$ here are the coefficients associated to the unknowns related to the set $N_i(k)$ of nodes connected to the node k and N the total number of the nodes.

As an example, we develop the matrix $\mathbf{W}_3(k)$ associated to the roughness criteria $R_3(u \mid k)$ for nodes on a grid. The operator ρ here, approximates the partial second derivative with respect to xx at the node k using the difference finite scheme as

$$\rho_{xx}(u)(k) = \begin{bmatrix} 1 & -2 & 1 \end{bmatrix} \begin{bmatrix} u_{k-1} \\ u_k \\ u_{k+1} \end{bmatrix} \tag{3.23}$$

$$(\rho_{xx}(u)(k))^2 = \begin{bmatrix} u_{k-1} & u_k & u_{k+1} \end{bmatrix} \begin{bmatrix} 1 \\ -2 \\ 1 \end{bmatrix} \begin{bmatrix} 1 & -2 & 1 \end{bmatrix} \begin{bmatrix} u_{k-1} \\ u_k \\ u_{k+1} \end{bmatrix} \tag{3.24}$$

$$= \begin{bmatrix} u_{k-1} & u_k & u_{k+1} \end{bmatrix} \mathbf{W} \begin{bmatrix} u_{k-1} \\ u_k \\ u_{k+1} \end{bmatrix} \tag{3.25}$$

$\mathbf{W}_3(k)$ is a sparse squared symmetric matrix of size (N, N), the entries $[k-1 : k+1, k-1 : k+1]$ of this matrix, are simply the elements of the matrix $\mathbf{W}$ of size $(3, 3)$. Then the regularization criterion is globally defined as

$$R_3(u) = \sum_{k \in K_i} \mu_i(k) \mathbf{U}^T \mathbf{W}_3(k) \mathbf{U} \tag{3.26}$$

Mallet (1989) neglected the cross partial derivative to decrease the number of nonnull elements in the resulting global linear system to solve, since it has little influence.

$$R(u) = \gamma(R_1(u) + R_2(u)) + (1 - \gamma)(R_3(u) + R_4(u)) \tag{3.27}$$

Lévy and Mallet (1999) considered a discrete squared Laplacian functional as fairness energy for smoothing arbitrary meshes based on the DSI formulation, namely

$$F_{\Delta^2}(u) = \int_\Omega \mu(x)(\Delta u(x))^2 dx \tag{3.28}$$

They proposed a simple discretization for this energy, based on the following insight

$$\Delta u(v_k) \simeq \frac{1}{\mid D(k) \mid} \int_{D(k)} div(\nabla u) dx \tag{3.29}$$

$$\simeq \frac{1}{\mid D(k) \mid} \int_{\partial D(k)} \nabla u(s) \cdot \mathbf{N}(s) ds \tag{3.30}$$

where $D(k)$ is the domain of vertex of index k and $\mid D(k) \mid$ denotes the area of $D(k)$, see Fig. 3.1. The vector $\mathbf{N}$ denotes the normal to the border $\partial D(k)$ of $D(k)$. By choosing the linear piecewise finite elements for interpolation, the gradient is constant over each triangle $T(k, \alpha_1, \alpha_2)$. The length of the edge $E(\alpha_1, \alpha_2)$ is denoted by $\mid E(\alpha_1, \alpha_2) \mid$. Then the integral is transformed to the following sum

$$\simeq \frac{1}{\mid D(k) \mid} \sum_{T(k,\alpha_1,\alpha_2) \subset D(k)} \mid E(\alpha_1, \alpha_2) \mid \nabla u(T) \cdot \mathbf{N}(T) \tag{3.31}$$

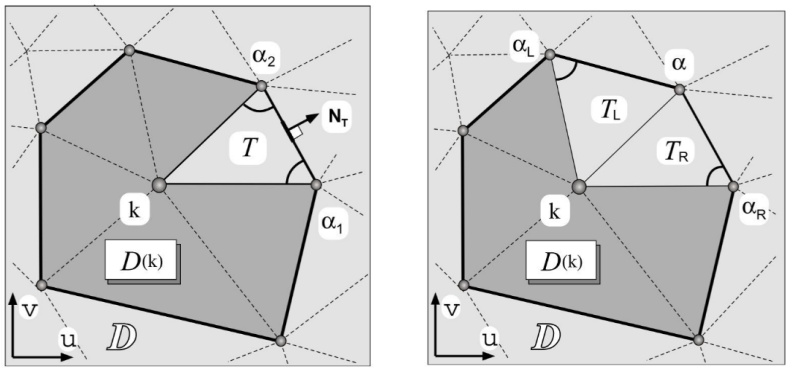

(a) (b)

Figure 3.1: Approximating the Laplacian on a triangulated surface, figures from Lévy and Mallet (1999).

Let $\tau(\hat{\alpha} \mid T)$ denote the absolute value of the contangent of the angle at the vertex α in the triangle T (see Fig. 3.1):

$$\tau(\hat{\alpha} \mid T) = \mid cotg(\hat{\alpha}) \mid \tag{3.32}$$

Then, the expression $\mid E(\alpha_1, \alpha_2) \mid \nabla u(T) \cdot \mathbf{N}(T)$ can be rewritten as

$$\mid E(\alpha_1, \alpha_2) \mid \nabla u(T) \cdot \mathbf{N}(T) = u(\alpha_1)\tau(\hat{\alpha_2} \mid T) + u(\alpha_2)\tau(\hat{\alpha_1} \mid T) + u(v_k)(-\tau(\hat{\alpha_2} \mid T) + \tau(\hat{\alpha_1} \mid T)$$

The discrete Laplacian is then computed as

$$Du(v_k) = \frac{3}{\sqrt{\mid D(k) \mid}} \sum_{\alpha \in N(k)} v^{\alpha}(k) u(\alpha) \tag{3.33}$$

where, $\forall \alpha \in N(k) - k$

$$\begin{cases} v^{\alpha}(v_k) = \frac{1}{3}\tau(\hat{\alpha_R} \mid T_R) + \tau(\hat{\alpha_L} \mid T_L) + B^{\alpha}(v_k) \\ v^{k}(v_k) = -\sum_{\alpha \in N(k)-k} v^{\alpha}(v_k) \end{cases} \tag{3.34}$$

$B^{\alpha}(v_k)$ is a coefficient for the vertices on the boundaries of the domain, see Lévy and Mallet (1999) for more details. The functional Eq. (3.28), is then approximated using the discrete Laplacian Eq. (3.33) as

$$F_{D^2}(u) = \sum_{k \in \Omega} \mu(k)(Du(k))^2 \frac{1}{3} \mid D(k) \mid \tag{3.35}$$

Irakarama et al. (2021) introduced a regularization operator based on the minimization of the second derivatives forming the Hessian matrix, defined as

$$\mathbf{h}(u)(x) = \begin{cases} \chi_{xx}(u)(x) \\ \sqrt{2}\chi_{xy}(u)(x) \\ \chi_{yy}(u)(x) \end{cases} \tag{3.36}$$

The operators χ_{ij} approximates the partial second derivative $\frac{\partial^2}{\partial ij}$, using linear finite elements on a tetrahedral mesh. The minimization problem to solve in a least square sense is

$$\begin{bmatrix} \mathbf{A_{fit}} \\ \mathbf{H} \end{bmatrix} \mathbf{U} = \begin{bmatrix} \mathbf{Z} \\ \mathbf{0} \end{bmatrix} \tag{3.37}$$

where $\mathbf{H}$ corresponds to the discretized set of constraints related to the regularization operator $\mathbf{h}$.

$$\mathbf{H} = \begin{bmatrix} \mathbf{D}_{xx} \\ \sqrt{2}\mathbf{D}_{xy} \\ \mathbf{D}_{yy} \end{bmatrix} \tag{3.38}$$

$\mathbf{D}_{ij}$ are the discretized constraints corresponding to the operator $\chi_{ij}(u)(x)$. Then, solving Eq. (3.36) is equivalent to solving the following linear system

$$(\mathbf{A_{fit}}^T \mathbf{A_{fit}} + \mathbf{H}^T \mathbf{H})\mathbf{U} = \mathbf{A_{fit}}^T \mathbf{Z} \tag{3.39}$$

$$(\mathbf{A_{fit}}^T \mathbf{A_{fit}} + \begin{bmatrix} \mathbf{D}_{xx}^T & \sqrt{2}\mathbf{D}_{xy}^T & \mathbf{D}_{yy}^T \end{bmatrix} \begin{bmatrix} \mathbf{D}_{xx} \\ \sqrt{2}\mathbf{D}_{xy} \\ \mathbf{D}_{yy} \end{bmatrix} \mathbf{U} = \mathbf{A_{fit}}^T \mathbf{Z} \tag{3.40}$$

$$(\mathbf{A_{fit}}^T \mathbf{A_{fit}} + \mathbf{D}_{xx}^T \mathbf{D}_{xx} + 2\mathbf{D}_{xy}^T \mathbf{D}_{xy} + \mathbf{D}_{yy}^T \mathbf{D}_{yy})\mathbf{U} = \mathbf{A_{fit}}^T \mathbf{Z} \tag{3.41}$$

This discretization considered here can be seen as equivalent to the discretization of the Hessian energy on a uniform Cartesian grids. The partial second derivatives are approximated using the finite difference operators and the integral is discretized simply by multiplying by the cell surface/volume, see Renaudeau (2019).

3.2.2 Gradient based regularization

Several software and algorithms in geomodeling developed by and for the oil and gas industry heavily rely on DSI methods. For example, Volume Based Modeling algorithm for the software Petrel by Souche et al. (2014). In Volume Based Modeling (VBM) the domain is discretized using a triangular mesh and the basis functions to represent the implicit function are the classical linear finite elements. The choice of the regularization technique is based on the assumption that the smoothest possible solutions are preferred. Two regularization operators were used to obtain smooth resulting implicit functions: the constant gradient constraint Frank et al. (2007) and the smooth gradient Souche et al. (2014).

Constant gradient constraints

The constant gradient constraint can be described as

$$\mathbf{n}_i \cdot \nabla u(t) - \mathbf{n}_i \cdot \nabla u(t') = 0 \quad \forall t \in T(\Omega),\ \forall t' \in N(t) \tag{3.42}$$

$T(\Omega)$ is the set of mesh elements and $N(t)$ is the set of adjacent elements to t, while $\mathbf{n}_i$ is the unit normal vector of the edge e_i shared between t and t'. This constraint applied for each triangle of the mesh, aims to minimize the discontinuities of the gradients on a triangle and its neighbours. These discretized set of constraints are related to the discretization of the Laplacian operator. Another advantage of the previous discretization is that enables to get rid of the integration term on the boundaries, leading to a boundary free interpolation using the Laplacian operator, see Irakarama et al. (2022) for more details.

Smooth gradient regularizations

The smooth gradient constraint is expressed as

$$\nabla u_t - \frac{1}{n_b} \sum_{t' \in N(t)} \nabla u_{t'} = 0 \tag{3.43}$$

where $N(t)$ is the set of adjacent elements to the element t, n_b is the number of the elements in $N(t)$. The basis functions are piecewise linear, the gradients are piecewise constant on each triangle. The smooth gradient regularization constrains the gradient to be the average of the neighbouring gradients in the two directions x and y, leading to smoother solutions.

For comparison between the resulting implicit functions using different regularization techniques, we create models with different level of thickness variations. In Fig. 3.2 d, the thickness variations are introduced in the data along the radial direction. The data points along the rings have the same isovalue, and the three rings have $1, 2, 10$ as values. In Fig. 3.2c, the data points are along five horizons, four of which are flat, while the middle has curved shape resembling a bell. The horizons have as values $-1, 0, 1, 2, 3$, respectively, from the bottom to the top. We consider in Fig. 3.2b only two rings and three horizons in Fig. 3.2a, for two reasons. First, the data points are positioned far from the boundaries which encourages the natural boundary conditions to appear. Secondly, the thickness variations are weaker than the cases in Fig. 3.2c,d. We refer to the models represented in Figs. 3.2a, b, c, d, respectively, as Bell, Rings, Bell Hv and Rings Hv.

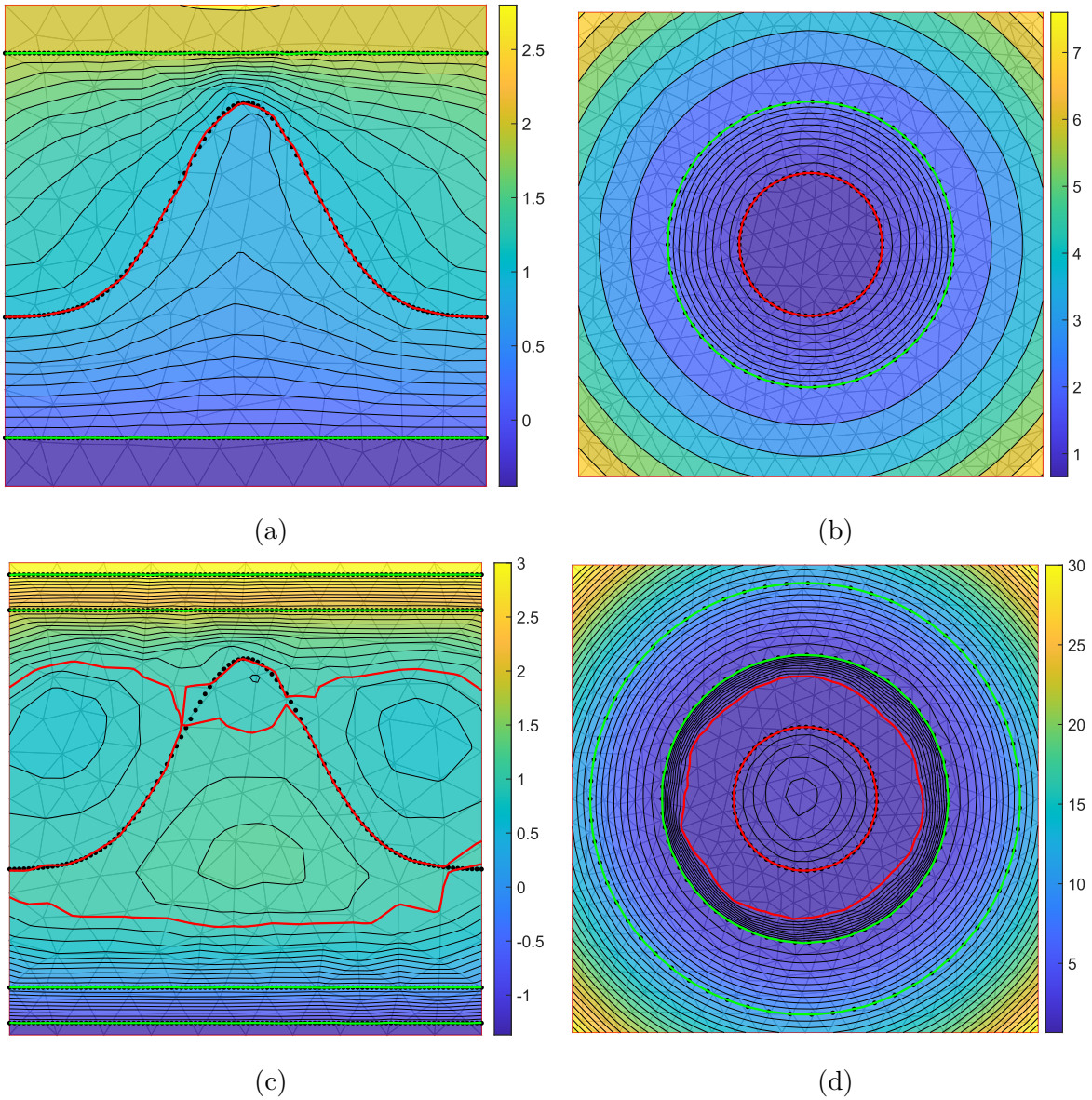

Figure 3.2: Resulting implicit functions using the smooth gradient regularization. (a) Bell ($\lambda = 1$). (b) Rings ($\lambda = 1$). (c) Bell Hv ($\lambda = 1$). (d) Rings Hv ($\lambda = 1$).

Figs.3.2 shows the resulting implicit functions obtained using the smooth gradient regularization on models with varying levels of thickness variations. Figs.3.2a, b, represent models with moderate thickness variations, while Figs.3.2c, d, represents models with high thickness variations. The resulting implicit function in Fig. 3.2b appears smooth and regular. This smoothness is maintained until the boundaries, and the same trend of the data is preserved. While, in Fig. 3.2a, the solution is regular but lacks smoothness due to the low refinement level of the mesh used and the linearity of the interpolation basis functions. However the solutions in Fig. 3.2c, d, exhibit oscillations and violates the regularity criteria. These oscillations arise as a consequence of the high thickness variations present in the data.

3.2.3 Mean value coordinates

Mean value coordinates Floater (2003) are a generalization of barycentric coordinates which are used to express a value of a vertex in a planar triangulation as a convex combination of values at neighbouring vertices. In barycentric coordinates, any point inside a triangle can be expressed as a linear combination of the triangle vertices, where the weights are proportional to the areas of the respective sub-triangles formed by the point and the triangle vertices. Mean value coordinates extend this concept to k-sided polygons, and any vertex of the triangulation can be expressed as convex combination of its neighbouring vertices. Mean value coordinates and barycentric coordinates have applications in various fields, including computer graphics, mesh parametrization, see Nieto and Susin (2013) for a survey. They provide a discrete analog to the Laplacian differential operator within a triangulated domain based on the local properties of the mesh. As example in Fig. 3.3 the vertex $\mathbf{v}_0$ inside the polygon formed by the set of its k neighbouring vertices.

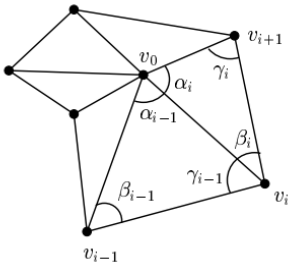

Figure 3.3: Star-shaped polygon (figure from Floater 2003)

Floater (2003) presented a set of positive coordinates λ_i verifying

$$\begin{cases} \sum_{i=1}^{k} \lambda_i \mathbf{v}_i = & \mathbf{v}_0 \\ \sum_{i=1}^{k} \lambda_i = & 1 \end{cases} \tag{3.44}$$

$$\lambda_i = \frac{\omega_i}{\sum_{j=1}^{k} \omega_j}, \qquad \omega_i = \frac{\tan(\alpha_{i-1}/2) + \tan(\alpha_i/2)}{\|v_i - v_0\|} \tag{3.45}$$

These weights were motivated by the approximation of solutions of the harmonic equation by piecewise linear elements. A linear function $u \in S_1^0(T)$ verifying $u(\mathbf{v}) = \sum_{i=1}^{k} \lambda_i u(\mathbf{v}_i)$ for all the interior vertices of the triangulation, is approximating a harmonic function in Ω, which means respecting the mean value property and the maximum principle at the boundaries, see Floater (2003) for more details.

The mean value coordinates can be used to construct a regularization operator R_{Mv} ensuring the mean value property of the implicit function (i.e. free from local extrema), that is expressed as

$$R_{M_v}(u)(\mathbf{v}) = u(\mathbf{v}) - \sum_{i=1}^{k} \lambda_i u(\mathbf{v}_i) \quad \forall \mathbf{v} \in T \tag{3.46}$$

expressing these constraints using the linear classical finite elements is straightforward, since the degrees of freedom are the values of the implicit function on the nodes of the mesh. Let $\mathbf{M_v}$ be a squared matrix of size (N_v, N_v), be the resulting linear system of R_{M_v}, with N_v the

number of mesh vertices. Each row of $\mathbf{M_v}$ corresponds to the constraint 3.46, for a given vertex $\mathbf{v}$. However, for the vertices on the boundaries, we can not have a closed polygon. A different linear constraint is added on all the vertices of the boundary, constraining the function to be the average of the two neighbouring vertices on the boundary, weighted by the length of their adjacent edges. For instance, the constraint on the vertex $\mathbf{v}_7$ in Fig. 3.4 is expressed as

$$u(\mathbf{v}_7) = \frac{\|\mathbf{v}_6 - \mathbf{v}_7\|}{\|\mathbf{v}_6 - \mathbf{v}_1\|} u(\mathbf{v}_1) + \frac{\|\mathbf{v}_1 - \mathbf{v}_7\|}{\|\mathbf{v}_6 - \mathbf{v}_1\|} u(\mathbf{v}_6) \tag{3.47}$$

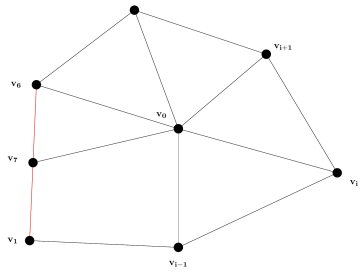

Figure 3.4: Star-shaped polygon with vertices on the boundary of the domain. Red lines for the edges on the boundary.

Then, the equivalent linear system to solve is

$$(\mathbf{A_{fit}}^T \mathbf{A_{fit}} + \mathbf{M_v})\mathbf{U} = \mathbf{A_{fit}}^T \mathbf{Z} \tag{3.48}$$

In Fig. 3.5a, the solution is well defined on the boundaries, due to the presence of the two horizons near the boundaries, at the bottom and the top. While, in Fig. 3.5b and c, the function is exhibiting wild oscillations on the boundaries, because of the lack of data near the boundaries. To uniquely determine the weights associated to each vertex of the interior, we need to fix the values of the function on the boundaries. Then, the linear system solved is

$$(\mathbf{A_{fit}}^T \mathbf{A_{fit}} + \mathbf{M_v})\mathbf{U} = \mathbf{A_{fit}}^T \mathbf{Z} + \mathbf{B} \tag{3.49}$$

The right-hand vector $\mathbf{B}$ of size N_v is added to include the contributions of fixing the values of the function on the boundaries as Dirichlet boundary conditions. However, in our context the implicit function is not known on the boundaries. Instead, we suggest to fix the values of the function on the boundaries, by setting it equal to a given regular function on the boundaries, that is not necessarily fitting well the data. Then, we use the mean value coordinates, to construct a regular solution fitting better data based on the fixed values on the boundaries. Iteratively, we fix the last solution on the boundaries, and we solve the same system again to improve the data fitting while ensuring the regularity of the function by using the mean value coordinates.

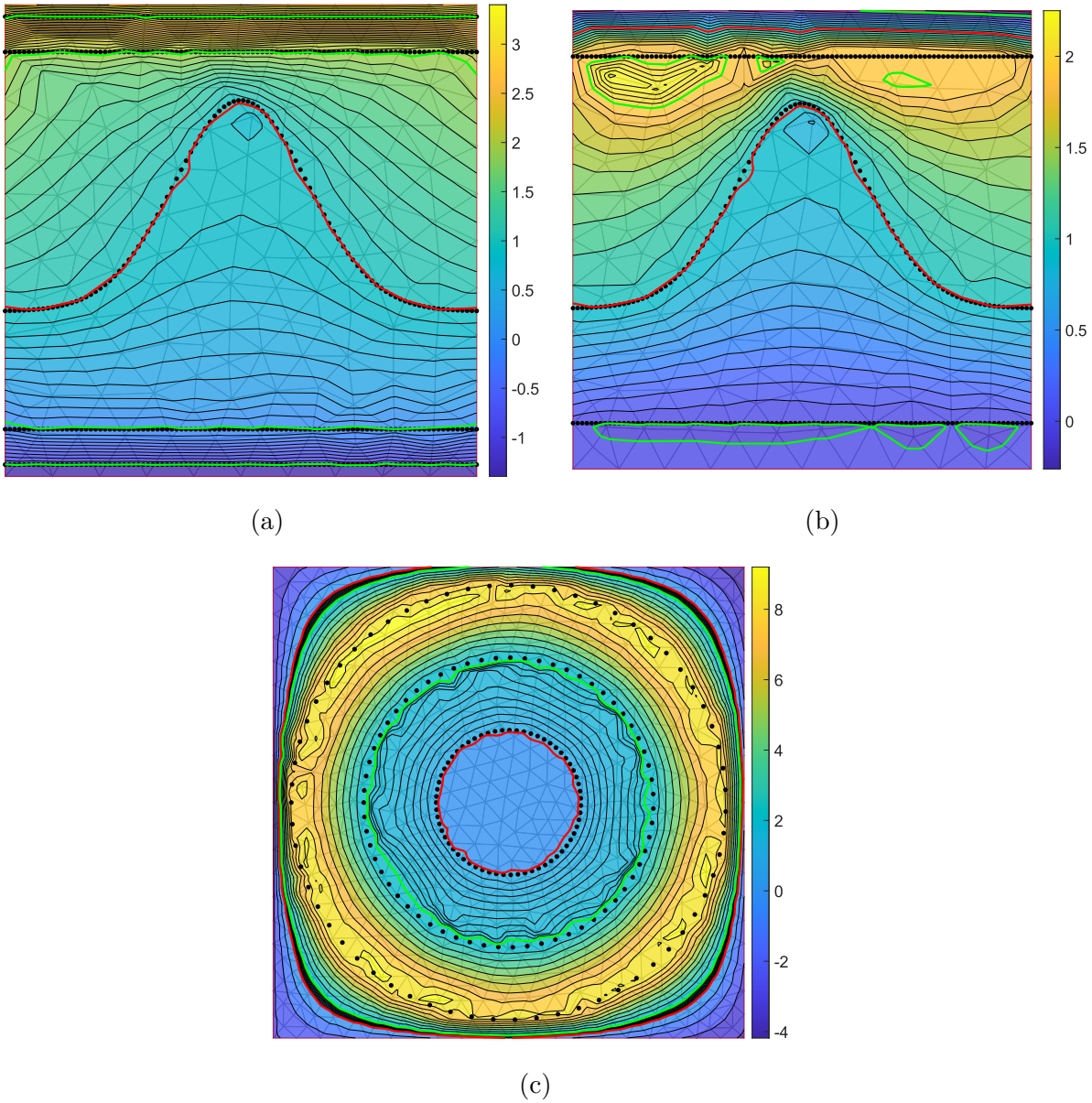

(a) (b)

(c)

Figure 3.5: Mean value coordinates for interpolation (Eq. 3.46). (a) Bell Hv. (b) Bell. (c) Rings Hv.

The idea behind this method is to start with an initial guess that is regular and not necessarily fitting well the data, as shown in Fig. 3.6a and Fig. 3.7a. Then, through an iterative process, we update the values on the boundaries, based on the previous solutions. Usually in few iterations we converge to a fixed point solution, that is fitting better data, while maintaining the mean value property, see Figs. 3.6b and 3.7b.

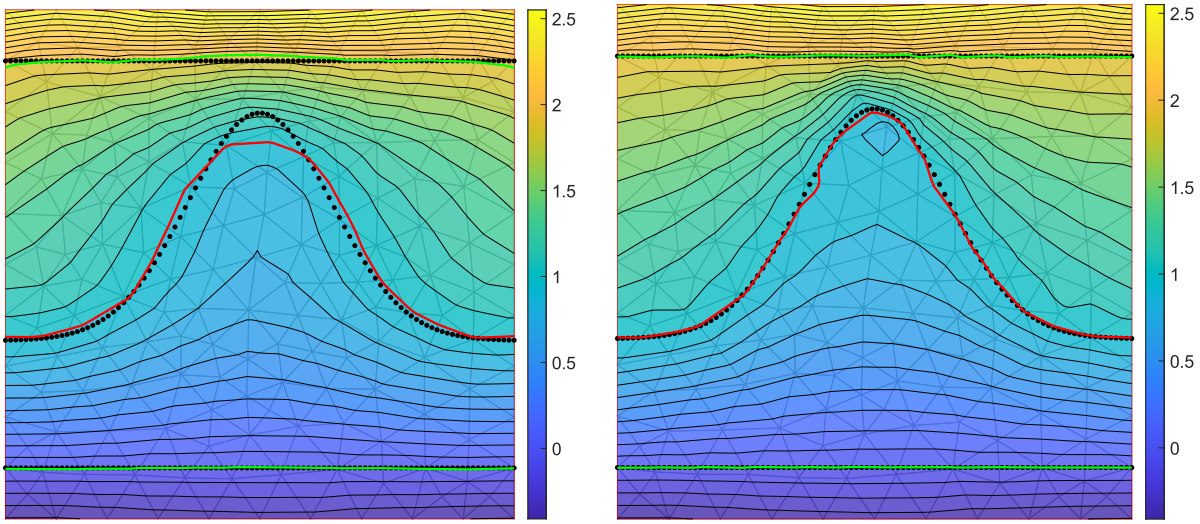

(a) (b)

Figure 3.6: Resulting implicit functions using the iterative process (Sect. 3.2.3). (a) Initial solution . (b) Final solution.

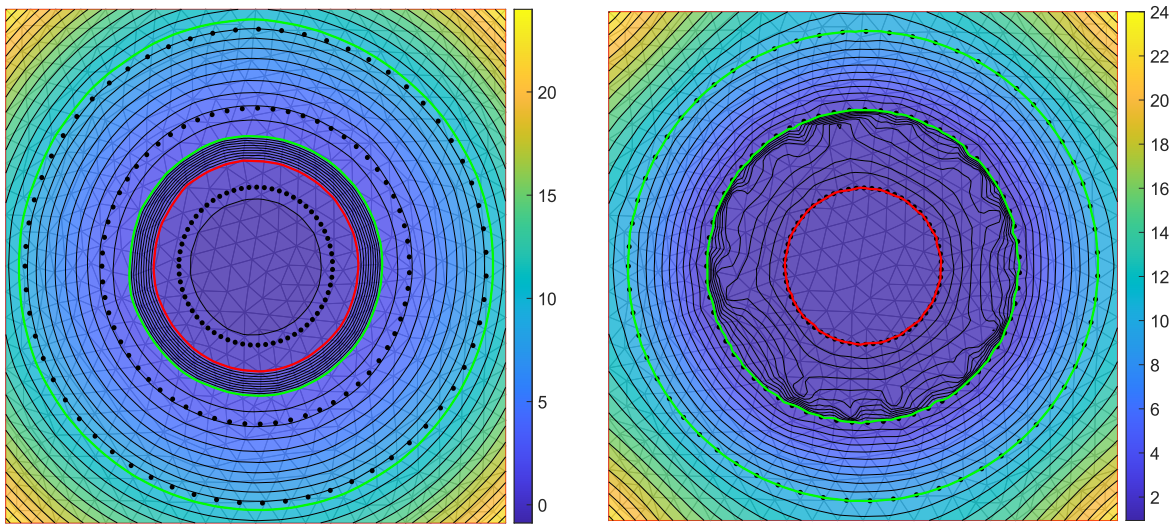

(a) (b)

Figure 3.7: Resulting implicit functions using the iterative process (Sect. 3.2.3). (a) Initial solution . (b) Final solution.

3.3 PS splines based regularization operators

Powell Sabin splines are piecewise quadratic basis functions, that are locally supported. When used for interpolating sparse and irregularly distributed data, the problem to solve is under-determined. A smoothness term is then introduced as regularization to select smooth

solutions, in the solution space. In this section, we introduce a set of regularization operators that are based on the PS-splines representation.

3.3.1 C^2 continuity

DIERCKX et al. (1992) introduced the C^2 continuity constraints for the PS-splines inspired from the continuity constraints for tensor product splines. The idea is to obtain of a smooth spline that respects the compromise between fitting data and presents minimal discontinuities in its second derivatives. We consider two triangles $T_b = T(\mathbf{P}_1\mathbf{R}_{12}\mathbf{Z})$ and T_c =T($\mathbf{P}_2\mathbf{Z}\mathbf{R}_{12}$) sharing the edge $\mathbf{Z}\mathbf{R}_{12}$, with $(\lambda_1, \lambda_2, 0)$ the barycentric coordinates of the point Z in the triangle $T(\mathbf{P}_1\mathbf{P}_2\mathbf{Z})$. In Fig. 3.8, b_{ijk} and $c_{i,j,k}$ are the coefficients of the implicit function in the Bézier basis of degree 2, respectively on, T_b and T_c. Then, the continuity constraints on the implicit function across the edge $\mathbf{Z}\mathbf{R}_{12}$, see Fig. 3.8, can be written as:

$$C^0 \text{ continuity: } c_{002} = b_{002}, \quad c_{011} = b_{011}, \quad c_{022} = b_{020} \tag{3.50}$$

$$C^1 \text{ continuity: } \lambda_1(b_{101} - b_{011}) + \lambda_2(c_{101} - c_{011}) = 0 \tag{3.51}$$

$$\lambda_1(b_{110} - b_{020}) + \lambda_2(c_{110} - c_{020}) = 0 \tag{3.52}$$

$$C^2 \text{ continuity: } \lambda_1^2(b_{200} - 2b_{110} + b_{020}) - \lambda_2^2(c_{200} - 2c_{110} + c_{020}) = 0 \tag{3.53}$$

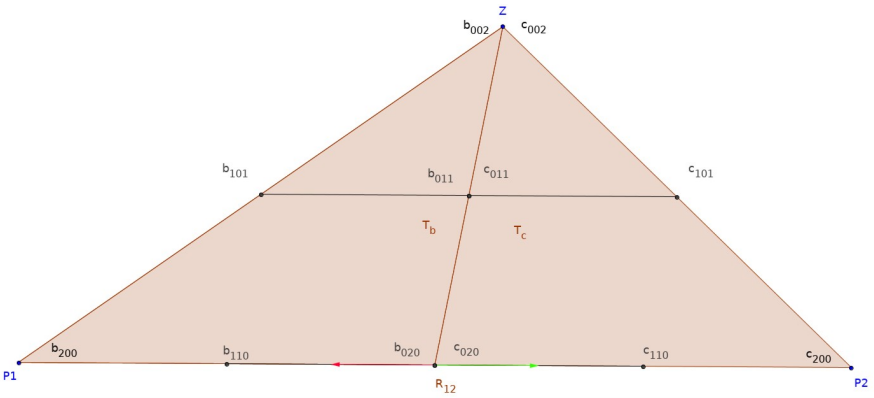

Figure 3.8: Bézier coefficients on two Bézier triangles (T_b, T_c) sharing the edge (ZR_{12}).

The conditions Eq. (3.50), Eq. (3.51) and Eq. (3.52) are verified by construction for the implicit function defined using the PS-splines. The C^2 continuity condition Eq. (3.53) is not necessarily verified since PS-splines are only C^1. Adding this constraint will ensure C^2 continuity across the edge $\mathbf{Z}\mathbf{R}_{12}$. For the triangles of the original mesh sharing an intern edge, the C^2 continuity condition is written using the Bézier coefficients located on the line joining the centers of the two triangles $T(\mathbf{P}_1\mathbf{P}_2\mathbf{P}_3)$ and $T(\mathbf{P}_2\mathbf{P}_4\mathbf{P}_3)$. In Fig. 3.9, the two triangles T($\mathbf{P}_4\mathbf{P}_3\mathbf{P}_2$) and $T(\mathbf{P}_1\mathbf{P}_2\mathbf{P}_3)$ share the edge $(\mathbf{P}_3\mathbf{P}_2)$. $\mathbf{R}_{32}$ is the intersection point of the edge $\mathbf{P}_3\mathbf{P}_2$ and the line joining the centers of the triangles. The Bézier coefficients located at the centers are w_1 and w_2, m at R_{32}, θ_1 and θ_2 at the middle points of $\mathbf{R}_{32}$ and the triangles centers, while $(\lambda_1^{'}, \lambda_2^{'}, 0)$ are the barycentric coordinates with respect to the triangle T(w_1, w_2, P_3). Then the C^2 continuity condition across the edge $(\mathbf{P}_3\mathbf{P}_2)$ can be written as:

$$\lambda_1^{'2}(w_1 - 2\theta_1 + m) - \lambda_2^{'2}(w_2 - 2\theta_2 + m) = 0 \tag{3.54}$$

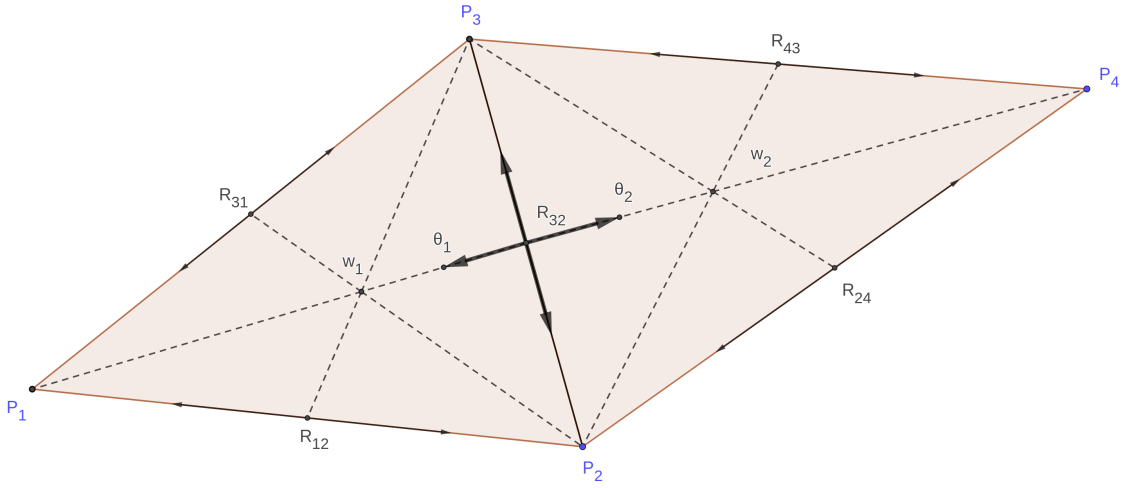

Figure 3.9: Bézier coefficients on two macro triangles sharing the edge ($\mathbf{P}_2\mathbf{P}_3$).

To ensure C^2 continuity, we write Eq. (3.53) across all the edges of the triangulation and Eq. (3.54) across intern edges of the triangulation which are shared by two triangles. These equations are assembled in a matrix $\mathbf{R}_2$ of the size (n,N_s), where N_s is the dimension of the Powell-Sabin splines space and $n = e_{bd} + 2e_i$, such that e_{bd} is the number of edges on the boundaries of the domain and e_i is the number of the interior edges. Likewise DSI methods where the fitting constraints are discretized on a discrete domain, and assembled into a least-squares system of linear equations supplemented with a smoothing regularization, $\mathbf{R}_2$ smoothing operator can be added to the fitting constraints and to solve a linear least-square system to find a smooth solution fitting data. Let ω be a coefficient controlling the tradeoff between the fitting constraints and the smoothing effect of the C^2 continuity regularization.

The C^2 smoothing regularization depends on the PS-splines basis functions representation unlike the Hessian or the Dirichlet energy that can be expressed independently of the choice of the basis functions. It tends to constrain the spline function to be C^2 while it is only C^1 by construction.

The C^2 continuity regularization produces smooth and regular solution in Fig. 3.10b. While, in Fig. 3.10a, the solution appears flat because it minimizes the curvature, but fails to be regular near the boundaries. However the solutions in Fig. 3.10c, d, are smooth but exhibit oscillations and violates the regularity criteria.

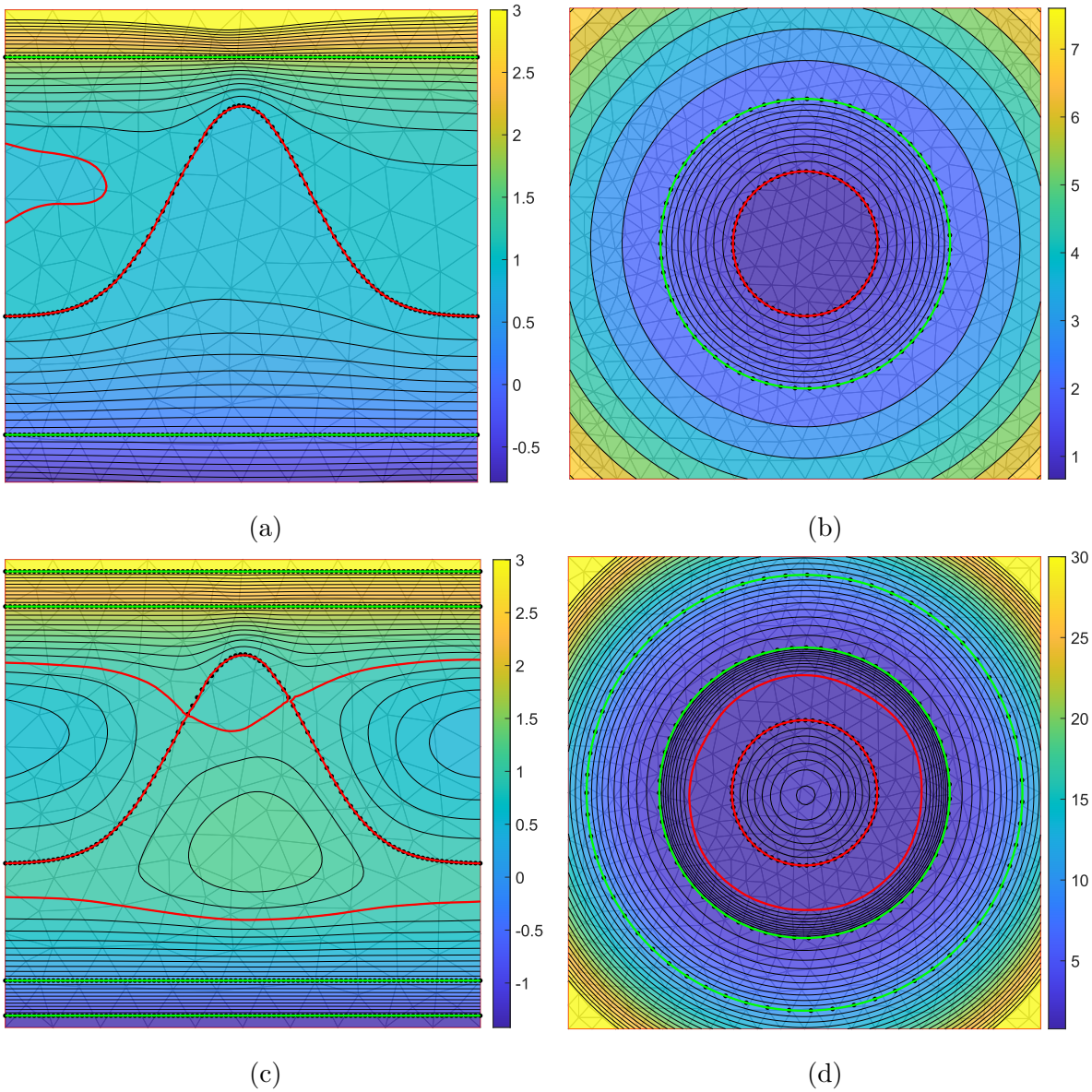

Figure 3.10: Resulting implicit functions using the C^2 continuity regularization. (a) Bell ($\lambda = 1$). (b) Rings ($\lambda = 1$). (c) Bell Hv ($\lambda = 1$). (d) Rings Hv ($\lambda = 1$).

3.3.2 Null second derivatives

PS-splines are piecewise quadratic splines with C^1 continuity. Therefore, the second partial derivatives are piecewise constant and non continuous per subtriangle of the PS refinement. We introduce a regularization operator similar to the regularization operator of Irakarama et al. (2022) based on the minimization of the components of the Hessian matrix independently.

$$\mathbf{R}(u)(x) = \begin{cases} u_{xx} = 0 \\ \sqrt{2}u_{xy} = 0 \\ u_{yy} = 0 \end{cases} \tag{3.55}$$

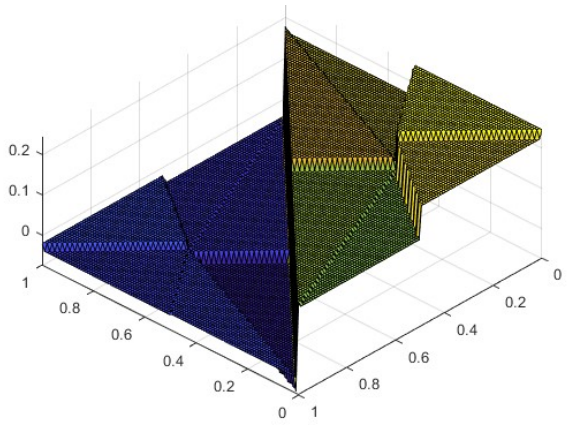

Figure 3.11: Piecewise constant second derivatives of PS-splines

A major advantage of the use of the PS-splines is the straightforward discretization of second order partial derivatives. To discretize Eq. 3.55, we constrain each subtriangle to have null second partial derivatives in the three directions xx, xy and yy. The same constraints are applied on all the subtriangles of the PS refinement, giving a linear system $\mathbf{D}$ of the size $3 \times n_t \times 6$, with n_t the number of the mesh elements.

$$\begin{bmatrix} \mathbf{A_{fit}} \\ \lambda \mathbf{D} \end{bmatrix} \mathbf{U} = \begin{bmatrix} \mathbf{Z} \\ \mathbf{0} \end{bmatrix} \tag{3.56}$$

By searching for a solution in a least square sense of the fitting constraints supplemented with the discretized regularization operator $\mathbf{D}$, we look for a solution fitting data while having minimal second derivatives. The coefficient λ controls the tradeoff between the two constraints.

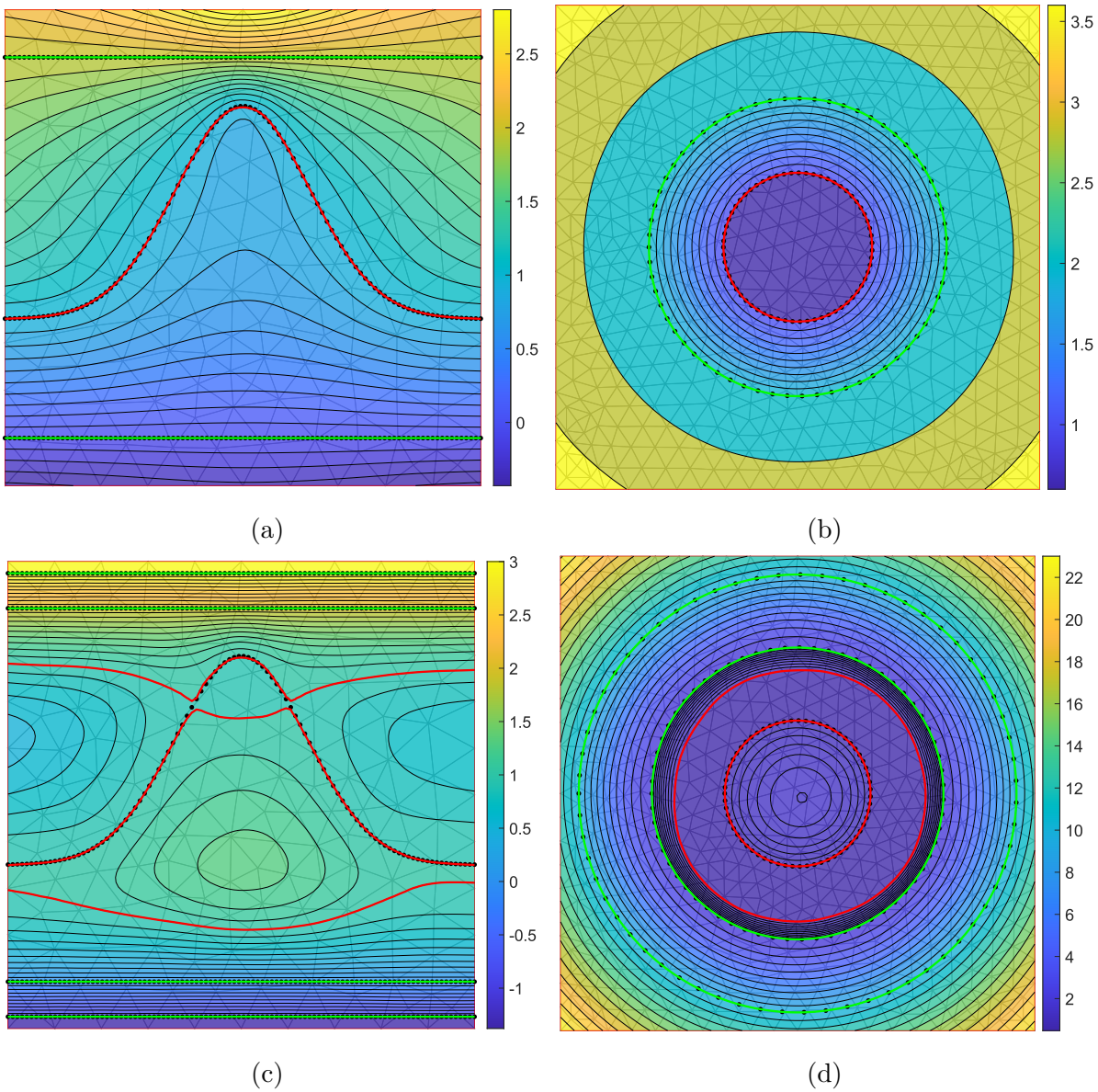

Figure 3.12: Resulting implicit functions using the null second derivative regularization. (a) Bell ($\lambda = 1$). (b) Rings ($\lambda = 1$). (c) Bell Hv ($\lambda = 1$). (d) Rings Hv ($\lambda = 1$).

The null second derivatives regularization successfully produces smooth and regular solutions in Fig. 3.12a, b. While in Fig. 3.12c, d, the solutions are indeed smooth, but they exhibit oscillations and do not respect the regularity criteria.

3.3.3 Mean value constraint on second derivatives

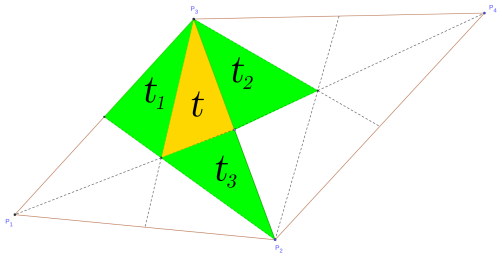

Figure 3.13: Set of subtriangles $N(t) = (t_1, t_2, t_3)$ sharing an edge with the subtriangle t

$$\mathbf{R}(u)(x) = \begin{cases} u_{xx,t} - \frac{1}{n_b} \sum_{t' \in N(t)} u_{xx,t'} = 0 \\ u_{xy,t} - \frac{1}{n_b} \sum_{t' \in N(t)} u_{xy,t'} = 0 \\ u_{yy,t} - \frac{1}{n_b} \sum_{t' \in N(t)} u_{yy,t'} = 0 \end{cases} \tag{3.57}$$

The partial second derivatives of the implicit function u on each subtriangle t is constrained to be the average of the second derivatives of the neighbouring subtriangles in all directions. These constraints attempts to minimize the discontinuities in the second derivatives, pushing the second derivatives to vary smoothly across subtriangles. To discretize 3.57, we constrain the second order partial derivatives in the three directions xx, xy and yy, on each subtriangle to be the average of the second order partial derivatives of the neighbouring subtriangles. The same constraints are applied on all the subtriangles of the PS refinement, giving a linear system $\mathbf{M_v}$ of the size $3 \times n_t \times 6$, with n_t the number of the mesh elements.

$$\begin{bmatrix} \mathbf{A_{fit}} \\ \lambda \mathbf{M_v} \end{bmatrix} \mathbf{U} = \begin{bmatrix} \mathbf{Z} \\ \mathbf{0} \end{bmatrix} \tag{3.58}$$

By searching for a solution in a least square sense of the fitting constraints supplemented with the discretized regularization operator $\mathbf{M_v}$, we look for a solution fitting data while having smooth second derivatives. The coefficient λ controls the tradeoff between the two constraints.

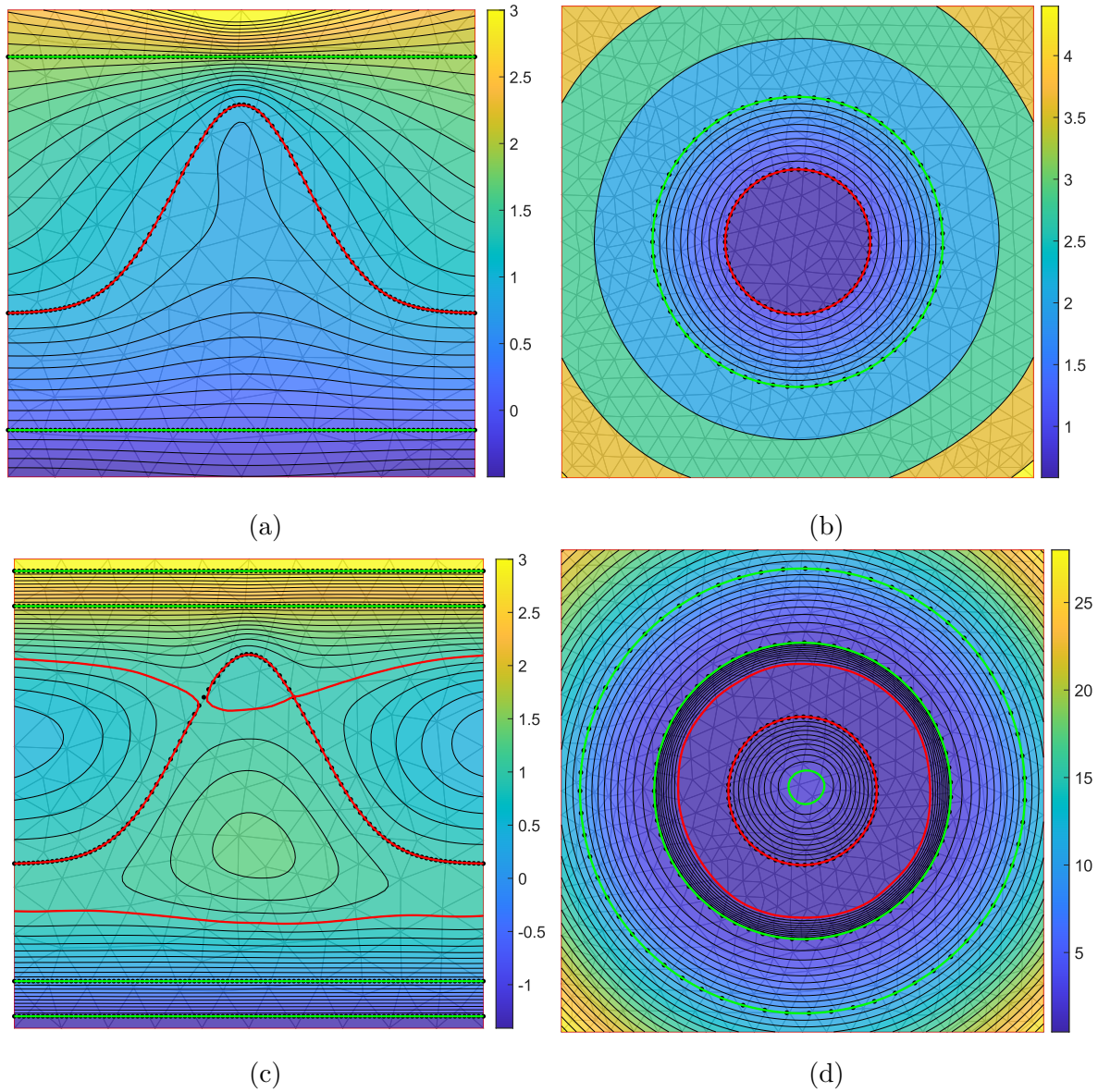

(a) (b)

(c) (d)

Figure 3.14: Resulting implicit functions using the mean value constraint on the second derivatives. (a) Bell ($\lambda = 1$). (b) Rings ($\lambda = 1$). (c) Bell Hv ($\lambda = 1$). (d) Rings Hv ($\lambda = 1$).

The regularization method imposing mean value constraints on the second derivatives, generates smooth and regular solutions in Fig. 3.14b. However, in Fig. 3.12a, the solution is failing to be maintain regularity in the region under the dome. Meanwhile, in Fig. 3.14c, d, the solutions are smooth but present wild oscillations. For instance, in the center of the rings, the value of the function is greater than two, while it should be inferior to one.

3.3.4 Mean value coordinates on PS-splines gradients

The mean value coordinates are based on approximating the Laplace operator by piecewise linear functions. Whereas, for other discretizations, such as PS-splines, which are piecewise quadratic polynomials, constraining a quadratic basis functions using discrete constraints derived for linear piecewise finite elements might fail to produce smooth solutions and do not allow to take advantage of the smoothness properties of these splines. On the other hand, the first order derivatives of PS-splines are linear and piecewise continuous. Therefore, we can apply the mean value coordinates constraints on the first order derivatives with respect to x and y. Then, the fitting constraints discretized using the PS-splines and supplemented with the regularization operator on the first order derivatives with respect to x and y, are solved in a least square sense to find a solution fitting the data points, while ensuring smoothness via the minimization of the first order derivatives.

3.4 Harmonic functions and Dirichlet energy

Harmonic functions are solutions of the standard Laplace equation

$$\Delta u = 0 \tag{3.59}$$

which describes the stationary state of the heat diffusion phenomenon. They benefit from interesting properties, including maximum principle and mean value, which are desirable in our problem. A harmonic function interpolating geological data, will vary between consecutive horizons without any local extrema. The maximum principle at the boundaries guarantees that the maximum of the implicit function is at the boundaries, data points along horizons can be seen as Dirichlet boundary conditions. For example, between two horizons the maximum are reached on the horizons. While the mean value ensures that between consecutive horizons, the function is free from local extrema. The weak form of Laplace equation, using integration by parts is

$$\int_\Omega \Delta u v \; ds = 0 \Leftrightarrow \int_\Omega \nabla u \cdot \nabla v \; ds - \int_{\partial\Omega} (\nabla u \cdot \mathbf{n}) v \; dx = 0 \qquad \forall v \in H^1(\Omega) \tag{3.60}$$

where n is the unit normal vector to the boundaries $\partial\Omega$. The Neumann boundary condition, $\nabla u \cdot \mathbf{n} = g(x)$, specifies the normal derivative of u on the boundaries. It is also called a natural boundary condition. The Dirichlet energy of a function $u \in H^1(\Omega)$ is defined as

$$E_{\nabla^2}(u) = \frac{1}{2} \int_\Omega \|\nabla u\|^2 \; d\Omega - \int_{\partial\Omega} g(x) u dx \tag{3.61}$$

We define the set

$$H^1_n(\Omega) = \{u \in H^1(\Omega) \mid \nabla u \cdot \mathbf{n} = g(x) \;\; on \;\; \partial\Omega\} \tag{3.62}$$

Proposition 3.4.1. *A function u minimizing the Dirichlet energy over $H^1(\Omega)$ Eq. (3.61), is a solution of the Laplace equation subject to $\nabla u \cdot \mathbf{n} = g(x)$.*

Proof. Consider u a minimizer of Eq. (3.61) over $H^1(\Omega)$, we choose $v \in H^1(\Omega)$, we write $i(h) = E_{\nabla^2}(u + hv)$ with $h \in \mathbb{R}$, thus

$$\begin{aligned} i(h) &= \frac{1}{2}\int_\Omega \|\nabla u + h\nabla v\|^2 \; d\Omega - \int_{\partial\Omega} g(x)(u + hv)dx \\ &= \int_\Omega \frac{1}{2}\|\nabla u\|^2 + h\nabla u \cdot \nabla v + \frac{h^2}{2}\|\nabla v\|^2) \; d\Omega - \int_{\partial\Omega} g(x)(u + hv)dx \end{aligned}$$

Since u minimizes E_{∇^2} over $H^1(\Omega)$, and $u + hv \in H^1(\Omega)$

$$0 = i'(0) = \int_\Omega \nabla u \cdot \nabla v \; d\Omega - \int_{\partial\Omega} g(x)v dx \tag{3.63}$$

This is exactly the weak formulation Eq. (3.60), with $\nabla u \cdot \mathbf{n} = g(x)$. □

The Dirichlet energy is commonly used as smoothness energy in geometry processing. For examples, Alliez et al. (2007) introduced an anisotropic discrete Dirichlet energy for surface reconstruction. Pinkall and Polthier (1993) used the Dirichlet energy to compute discrete minimal surfaces. In our case, the Dirichlet energy is introduced as regularization energy in the Implicit modeling problem as

$$\min_u E_{fit}(u) + \lambda E_{\nabla^2}(u) \tag{3.64}$$

The resulting solutions of the minimization problem Eq. (3.64) are fitting the data and benefiting of the regularity properties of the Dirichlet energy. The penalization of the gradient via the minimization of the L_2 norm of the gradient of the function all over the domain, filters solutions presenting wild variations. Additionally, the Dirichlet energy is also related to the minimization of the area, producing a minimal surface interpolating the data, see Courant (1977).

In Figs. 3.15, we consider the Dirichlet energy as regularization, specifying as Neumann boundary condition $g(x) = 0$. The resulting implicit functions are maintaining the regularity criteria between the horizons, even in the cases with high thickness variations in Fig. 3.15. It can be attributed to the properties of the harmonic functions, such as mean value property and the strong maximum principle. However, they lack smoothness, and along the boundaries strong artifacts are observed. When minimizing the Dirichlet energy Eq. (3.61) over all the space $H^1(\Omega)$, the natural boundary condition that emerges is the vanishing Neumann boundary condition, . It implicitly imposes that the normal component on the boundaries of the gradient of the implicit function vanishes, which leads to contours of the function terminating perpendicular to the boundary. These conditions introduce a strong bias in the solutions near the boundaries. In the model Fig. 3.15b, the solution is constant on the boundaries, while a solution keeping the same circular trend of the data is preferred. This undesired effect makes the use of Dirichlet energy with vanishing Neumann boundary condition unsuitable for our application.

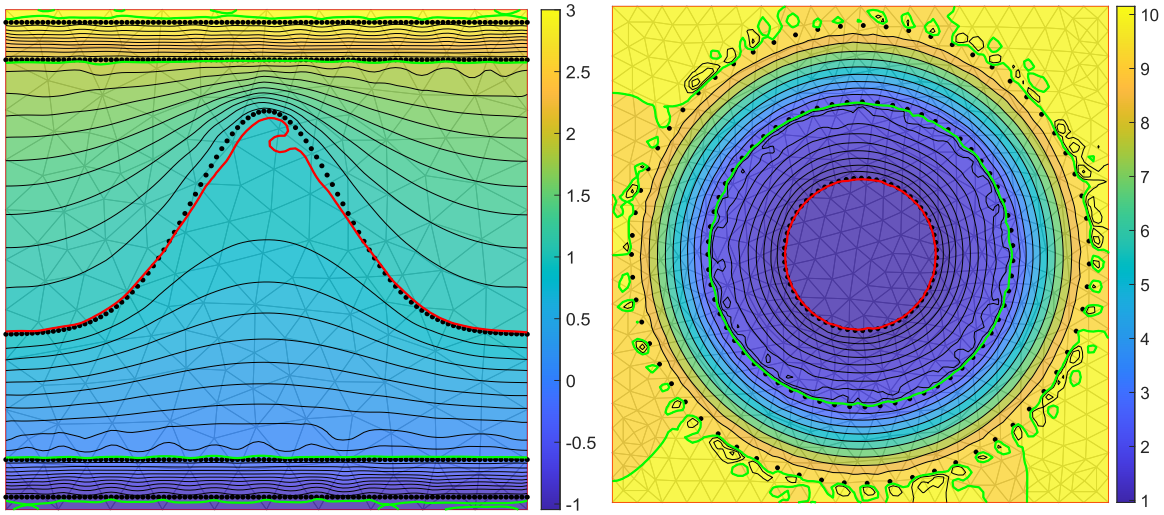

(a) (b)

Figure 3.15: Resulting implicit functions using the Dirichlet energy as a regularization. (a) Bell Hv ($\lambda = 1$). (b) Rings Hv ($\lambda = 1$).

Optimizing the Dirichlet energy over $H^1(\Omega)$ in $1D$ is simply $\int_\Omega (u')^2 dx$. The resulting function in Fig. 3.16, tends to be linear between the data points to fit, since the functional is based on minimizing the first order derivative. Far from the data points and near the boundaries, the function is constant, which means that the first derivative is null, thus the function is constant. This condition is aligned with the minimization objectives. The behaviour that exhibits the $1D$ solution is repeated in the $2D$ example in Fig. 3.15a, which can be seen simply as translation of this solution on the points in $2D$ along the horizons.

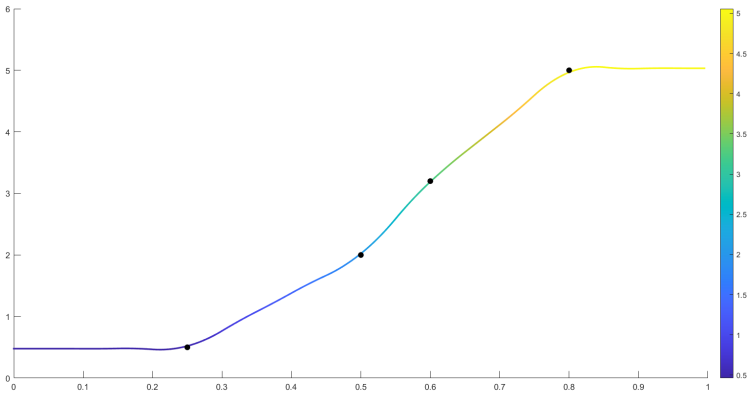

(a)

Figure 3.16: $1D$ interpolation using Dirichlet energy.

3.5 Natural boundary conditions

Natural boundary conditions, also known as implicit boundary conditions, are the conditions that emerge when minimizing a regularization energy over the space of all functions (i.e without specifying boundary conditions). These implicit boundary conditions arise from the properties of the regularization term considered and the functional space in which the minimization problem is solved. For example, regularization terms based on differential equations, might encourage smoothness or impose constraints on the derivatives of the function. This can lead to natural boundary conditions that enforce smoothness or other properties at the boundaries of the domain. In some cases, these properties might align with the desired properties along the boundaries, leading to an appropriate behaviour, and sometimes might not, leading to undesired artifacts. Therefore, it is crucial to be aware of the potential effects and ensure that the implicit boundary conditions enforced by the regularization align with the regularity criteria introduced beforehand.

3.6 Laplacian energy

The Laplacian is a well-known smoothness energy, that is related to the Biharmonic equation. It involves high order partial derivatives. The Laplacian energy is widely used in geometry processing, data interpolation and mesh fairing. For examples, Jacobson et al. (2011) computes weights for interpolating geometric data using the Laplacian energy subject to bounds constraints. Alliez et al. (2007) uses it for surface construction from a set of data points, by optimizing the anisotropic Dirichlet energy subject to the minimization of the Bilaplacian operator. The Laplacian energy is defined as

$$E_{\Delta^2}(u) = \frac{1}{2}\int_\Omega (\Delta u)^2 \; d\Omega = \frac{1}{2}\int_\Omega (u_{xx} + u_{yy})^2 \; d\Omega \tag{3.65}$$

The Biharmonic equation is

$$\Delta^2 u = 0 \tag{3.66}$$

Proposition 3.6.1. *Minimizers of the Laplacian energy over $H^2(\Omega)$ are solutions of the Biharmonic equation.*

Proof. To deduce the weak form of the biharmonic equation, we integrate by parts

$$\int_\Omega \Delta^2 u v \;\; d\Omega = \int_\Omega div(\nabla(\Delta u)) v \;\; d\Omega \qquad \forall v \in H^2(\Omega) \tag{3.67}$$

$$= \int_\Omega \nabla(\Delta u) \cdot \nabla v \;\; d\Omega - \int_{\partial\Omega} (\nabla(\Delta u) \cdot \mathbf{n}) v dx \;\; \forall v \in H^2(\Omega) \tag{3.68}$$

Using integration by parts

$$\int_\Omega \Delta u \Delta v \;\; d\Omega = \int_\Omega \Delta v \Delta u \;\; d\Omega = \int_\Omega \nabla v \cdot \nabla(\Delta u) \;\; d\Omega - \int_{\partial\Omega} (\nabla v \cdot \mathbf{n}) \; \Delta u \; dx \tag{3.69}$$

we deduce that

$$\int_\Omega \nabla v \cdot \nabla(\Delta u) \;\; d\Omega = \int_\Omega \Delta u \Delta v \;\; d\Omega + \int_{\partial\Omega} (\nabla v \cdot \mathbf{n}) \; \Delta u \; dx \tag{3.70}$$

We substitute the previous term in Eq. (3.68) to obtain the weak form

$$\int_\Omega \Delta^2 uv \;\; d\Omega = \int_\Omega \Delta u \Delta v \;\; d\Omega + \int_{\partial\Omega} \Delta u \; (\nabla v \cdot \mathbf{n}) - (\nabla(\Delta u) \cdot \mathbf{n}) v \; dx \qquad \forall v \in H^2(\Omega) \quad (3.71)$$

Now, consider u a minimizer of Eq. (3.65) over $H^2(\Omega)$, we choose $v \in H^2(\Omega)$, we write $i(h) = E_{\Delta^2}(u + hv)$ with $h \in \mathbb{R}$, thus

$$\begin{aligned} i(h) &= \frac{1}{2} \int_\Omega (\Delta u + h\Delta v)^2 \; d\Omega \\ &= \int_\Omega \frac{1}{2}(\Delta u)^2 + h\Delta u \Delta v + \frac{h^2}{2}(\Delta v)^2 \; d\Omega \end{aligned}$$

Since u minimizes E_{Δ^2} over $H^2(\Omega)$, and $u + hv \in H^2(\Omega)$

$$0 = i'(0) = \int_\Omega \Delta u \Delta v \; d\Omega \quad (3.72)$$

This becomes

$$\int_\Omega \nabla v \cdot \nabla(\Delta u) \;\; d\Omega - \int_{\partial\Omega} (\nabla v \cdot \mathbf{n}) \; \Delta u \; dx = 0 \qquad \forall v \in H^2(\Omega) \quad (3.73)$$

This equality is holding for any choice of v. Thus, $\Delta^2 u = 0$ in Ω, which ends the proof of the proposition. □

Furthermore, the natural boundary conditions emerging when minimizing the Laplacian energy are (Stein (2020), Courant (1977))

$$\begin{cases} \nabla(\Delta u) \cdot \mathbf{n} &= 0 \\ \Delta u &= 0 \end{cases} \quad (3.74)$$

In Fig. 3.17a, b, a boundary artifact appears along the boundaries, which is due to the natural boundary conditions of the Laplacian energy. Solutions of the Laplacian energy satisfy on the boundaries the condition $\Delta u = 0$, which is not enough restrictive and introduce a lot of noise, since many noisy harmonic functions satisfy $\Delta u = 0$ on the boundary. On the other hand, the solutions of the Laplacian energy, are smooth since they are solutions of the Biharmonic equation in the interior of the domain. However, in the cases of high thickness variations in Fig. 3.17c, d, these solutions present oscillations and do not respect the regularity criteria.

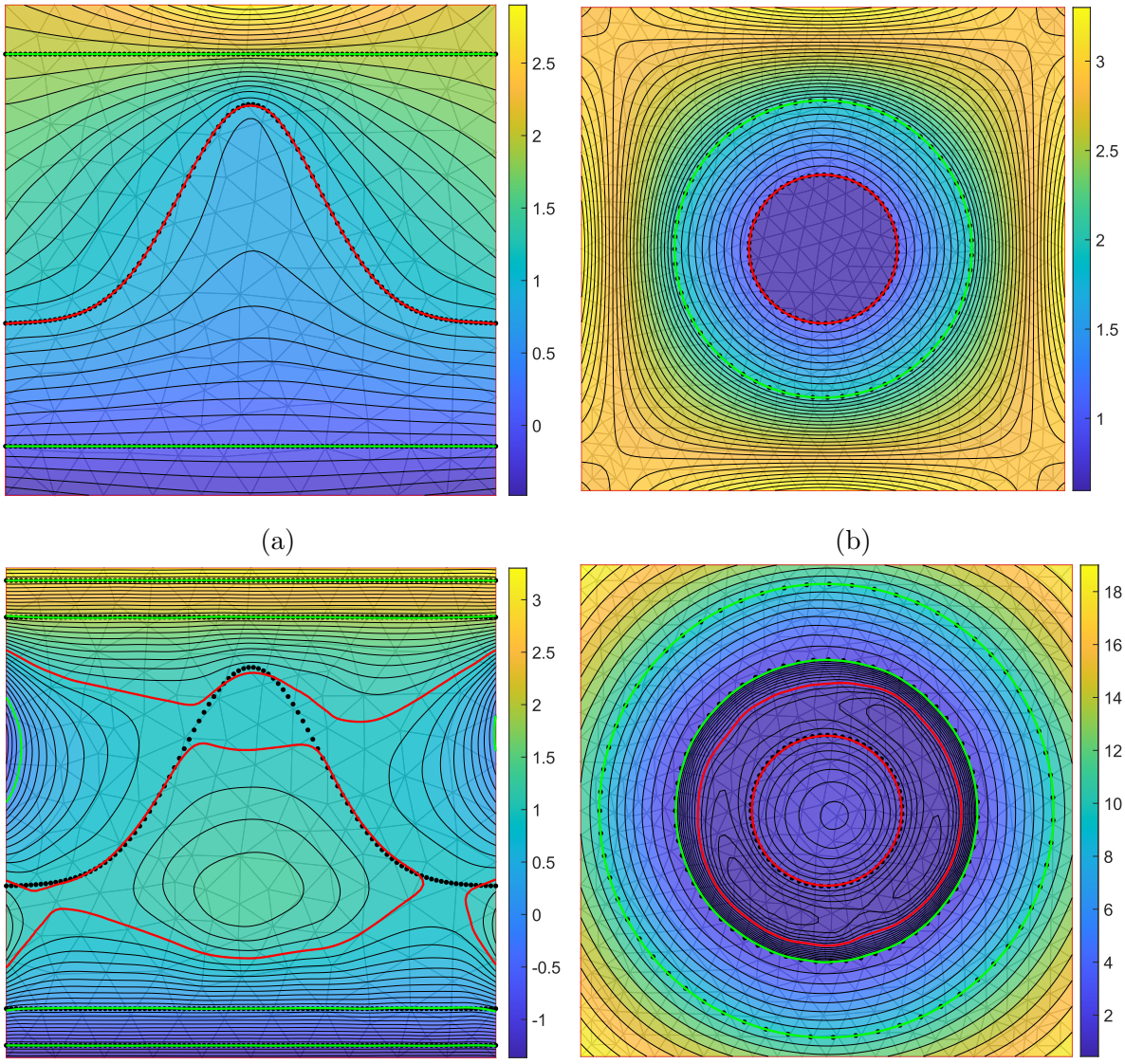

Figure 3.17: Resulting implicit function using Laplacian energy as regularization energy. (a) Bell. (b) Rings. (c) Bell Hv. (d) Rings Hv.

3.7 Hessian energy

The Hessian energy also called squared Hessian (Stein et al. 2018), roughness, bending or thin-plate energy, depending on the field of application, is a well-known regularization technique in data smoothing, image processing and many other engineering fields. Renaudeau (2019) considered the Hessian energy as regularization energy for the implicit modeling problem Eq. (3.9). The assumption made is that the regularity criteria is smoothness. It is a smoothing energy based on the minimization over all the domain Ω of the squared partial second derivatives entries of the Hessian matrix, $\mathbf{H}_u \in \mathbb{R}^{d\times d}$. Moreover, we have the following

result for minimizers of the Hessian energy, see Stein et al. (2018).

$$E_{H^2}(u) = \int_\Omega \|\mathbf{H}_u\|_F^2 = \int_\Omega (u_{xx}^2 + 2u_{xy}^2 + u_{yy}^2)\ d\Omega \tag{3.75}$$

Proposition 3.7.1. *Minimizers of the Hessian energy are solutions of the biharmonic equation.*

Proof. Let u be a minimizer

$$E_{H^2}(u) = \frac{1}{2}\int_\Omega \mathbf{H}_u : \mathbf{H}_u \quad d\Omega \tag{3.76}$$

where $X : Y = tr(X^T Y)$ is the Frobenius inner product which generates the Frobenius norm $X : X = \|X\|_F$. Then, for every smooth variation $u + hv$ with $h > 0$, one takes the derivative with respect to h and evaluates at $h = 0$. This gives

$$E_{H^2}(u + hv) = \frac{1}{2}\int_\Omega \mathbf{H}_{u+hv} : \mathbf{H}_{u+hv} \quad d\Omega \tag{3.77}$$

$$= \frac{1}{2}\int_\Omega (\mathbf{H}_u + h\mathbf{H}_v) : (\mathbf{H}_u + h\mathbf{H}_v) \quad d\Omega \tag{3.78}$$

$$\frac{\partial}{\partial h}(\frac{1}{2}\int_\Omega (\mathbf{H}_u + h\mathbf{H}_v) : (\mathbf{H}_u + h\mathbf{H}_v)\ d\Omega) = \frac{1}{2}\int_\Omega 2(\mathbf{H}_u : \mathbf{H}_v) + 2h(\mathbf{H}_v : \mathbf{H}_v)\ d\Omega \tag{3.79}$$

By setting $h = 0$, we get

$$\int_\Omega \mathbf{H}_u : \mathbf{H}_v\ d\Omega = 0 \tag{3.80}$$

Now, we show that the minimizer u verify the weak form of the biharmonic equation for every v. Starting from

$$\int_\Omega (\Delta u)v \quad d\Omega = -\int_\Omega \nabla u \cdot \nabla v \quad d\Omega + \int_{\partial\Omega} (\nabla u \cdot \mathbf{n})v\ dx \tag{3.81}$$

Then, by replacing u and v by ∇u^T and ∇v^T in Eq. (3.81):

$$\int_\Omega \nabla\Delta u \cdot \nabla v \quad d\Omega = -\int_\Omega \mathbf{H}_u : \mathbf{H}_v \quad d\Omega + \int_{\partial\Omega} (\mathbf{H}_u \cdot \mathbf{n}) \cdot \nabla v\ dx \tag{3.82}$$

Replacing u by Δu in Eq. (3.81):

$$\int_\Omega (\Delta^2 u)v \quad d\Omega = -\int_\Omega \nabla\Delta u \cdot \nabla v \quad d\Omega + \int_{\partial\Omega} (\nabla\Delta u \cdot \mathbf{n})v\ dx \tag{3.83}$$

From Eq. (3.82) and Eq. (3.83) we get

$$\int_\Omega (\Delta^2 u)v \quad d\Omega = \int_\Omega \mathbf{H}_u : \mathbf{H}_v \quad d\Omega - \int_{\partial\Omega} (\mathbf{H}_u \cdot \mathbf{n}) \cdot \nabla v\ dx + \int_{\partial\Omega} (\nabla\Delta u \cdot \mathbf{n})v\ dx \tag{3.84}$$

$$\int_\Omega (\Delta^2 u)v \quad d\Omega + \int_{\partial\Omega} (\mathbf{H}_u \cdot \mathbf{n}) \cdot \nabla v\ dx - \int_{\partial\Omega} (\nabla\Delta u \cdot \mathbf{n})v\ dx = \int_\Omega \mathbf{H}_u : \mathbf{H}_v \quad d\Omega \tag{3.85}$$

Now, using Eq. (3.80), we have that u is a solution of the biharmonic equation regardless of the boundary conditions

$$\Delta^2 u = 0 \text{ in } \Omega \tag{3.86}$$

□

Furthermore, Stein et al. (2018) showed that the natural boundary conditions are

$$\begin{cases} \mathbf{n}^T \mathbf{H}_u \mathbf{n} = 0 & on \quad \partial\Omega \\ \nabla \Delta u \cdot \mathbf{n} + \nabla(\mathbf{t}^T \mathbf{H}_u \mathbf{n}) = 0 & on \quad \partial\Omega \end{cases} \tag{3.87}$$

They present higher smoothness and satisfy on the boundaries, a specific natural boundary condition, studied and analyzed by Stein et al. (2018), forcing the function to be only linear in the normal direction to the boundaries. This behaviour is interesting in our application, since no explicit boundary condition is available.
Solutions of the Hessian energy minimization are solutions of the Biharmonic equation in the interior and satisfy a specific natural boundary conditions that encourages the function to be linear in the normal direction. Fig. 3.18b illustrates the natural behaviour of the function near boundaries, keeping the same trend of the data and free from boundary artifact. In the cases of high thickness variations in Figs. 3.18c, d, the solutions are smooth, but present oscillations.

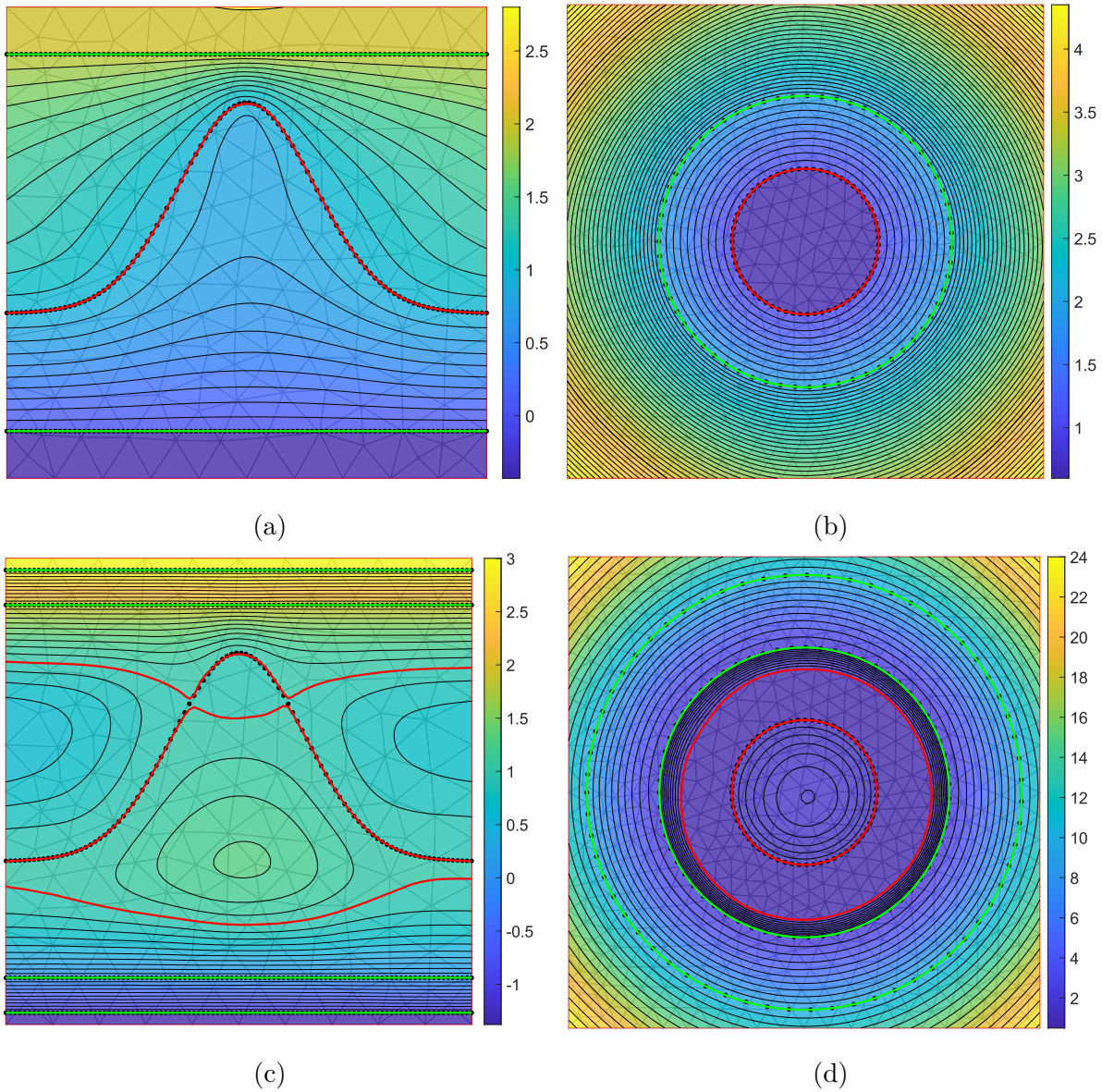

(a) (b)

(c) (d)

Figure 3.18: Resulting implicit functions using the Hessian energy. (a) Bell ($\lambda = 1$). (b) Rings ($\lambda = 1$). (c) Bell Hv ($\lambda = 1$). (d) Rings Hv ($\lambda = 1$).

To solve the Bilaplacian in $1D$, let us first derive the weak formulation

$$\int_\Omega u''''(x)v dx = 0 \tag{3.88}$$

$$\int_\Omega u'''(x)v'dx - [u'''(x)v(x)] = 0 \tag{3.89}$$

$$\int_\Omega u''(x)v''dx - [u''v'(x)] + [u'''(x)v(x)] = 0 \tag{3.90}$$

Then, the natural boundary conditions in $1D$ are on the two extremities of the domain:

$$u''(e) = u'''(e) = 0 \tag{3.91}$$

On the other hand, in $1D$ the Hessian energy and the Laplacian energy are identical, and expressed as

$$\min_u \int_\Omega (u'')^2 \, d\Omega \tag{3.92}$$

if u is a minimizer then is a minimizer for all smooth variation $u + hv$ with $h > 0$. Then one takes the derivative with respect to h and evaluates at $h = 0$. This gives

$$\frac{\partial}{\partial h}(\frac{1}{2}\int_\Omega (u'' + hv'')^2 \, d\Omega) = \frac{\partial}{\partial h}\int_\Omega (u'' + hv'')v'' \, d\Omega \tag{3.93}$$

By setting $h = 0$ in Eq. (3.93), we obtain

$$\int_\Omega u''v'' \, d\Omega \tag{3.94}$$

which means that u is a solution of $u''''(x) = 0$. The resulting function (Fig. 3.19) tends to be linear between the data points to fit, since the functional is based on minimizing the second order derivatives. Far from the data points and near from the boundaries, the function is linear, which means that the second derivative is null. The behaviour that exhibits the $1D$ solution far from the boundaries, is aligned with the natural boundary conditions of the Hessian energy, that implicitly implies that second order derivative is null.

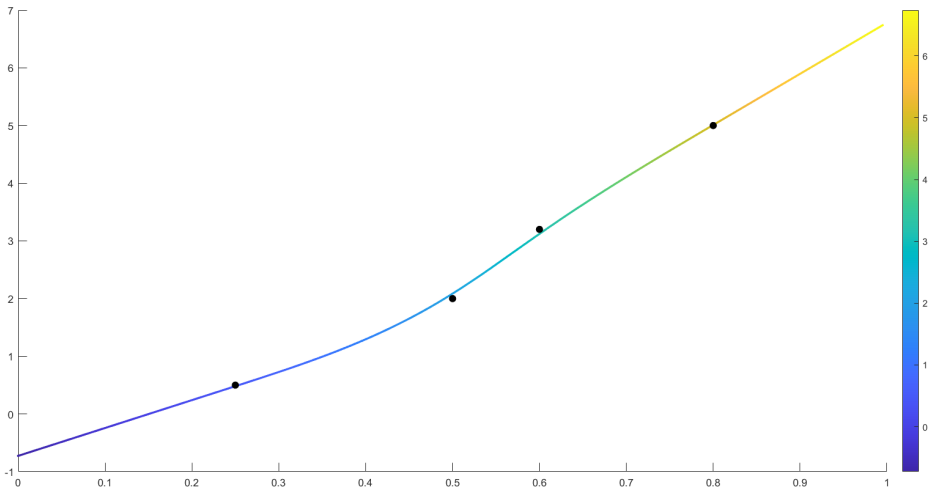

(a)

Figure 3.19: $1D$ interpolation using the Hessian energy

3.7.1 Adapted Hessian smoothing

In the pioneering works of (Mallet 1989, Lévy and Mallet 1999), the roughness criterions are associated with a weight that is expressed as a function varying over the domain, to control the importance of smoothing of certain zones. However, the use of a uniform weighting was suggested, by setting setting the value of the weighting function equal to 1 throughout the

domain. Another choice, is to consider a positive weight, expressed as the squares of the discrepancies between the value of the function on each node and the mean value of the neighbors, see Mallet (1992) for more details. Renaudeau (2019) introduced the Weighted Curvature Minimization (WCM), that locally adaptes the minimization of the Hessian energy, by weighting the smoothing differently in space using a function $\lambda(r)$, with r the distance of data points.

$$\frac{1}{2}\int_{\Omega} \lambda(r)\, \|\mathbf{H}_u\|_F^2 \; d\Omega \tag{3.95}$$

The idea behind this method is to heavily penalize the curvature of the function far from data, and allow high curvature near the data points. A more general form of this energy can be obtained by setting the weighting function λ as a piecewise smooth function, that can be expressed using the same basis functions space, where the function u is represented, see Merchel et al. (2023). The concept is to apply different curvature penalization in the domain, to preserve some sharp features present in the data. Lenz et al. (2022) introduced a positive weight function, to smooth out only the control points that are poorly constrained. However, the formulation Eq. (3.95) is only isotropic since only the intensity of smoothing is modulated (i.e. the same smoothing intensity applied to all directions). Renaudeau (2019) also introduced a minimization of the Hessian energy in a certain anisotropy direction $\mathbf{d}$, expressed as

$$\frac{1}{2}\int_{\Omega} \lambda_d(\mathbf{d}^T\mathbf{H}_u\mathbf{d})^2 \; d\Omega \tag{3.96}$$

The aim of minimizing this term is to adapt the penalization of the curvature in the anisotropy direction. This vector can change direction, which enables to locally adapt the direction of the penalization to address the problem of thickness variations.

The previous methods add several extra parameters to the modeling problem. These parameters includes an additional weight function that determines how the smoothing weight varies, and the range of its influence around data points, se Renaudeau (2019). Additionally, it necessitates a refined discretization to ensure the weighting function produces the desired effect on the resulting implicit function. On the other hand, despite the benefits and improvements that the additional parameters might offer, there is a challenge in determining the weighting function. Currently, there is no automated or standardized approach to compute these weighting functions. For more details, see Renaudeau (2019) and Martin and Boisvert (2017).

To illustrate the opportunities that promises the adaptative smoothing, we introduce an extra term minimizing the Hessian energy in the main direction of anisotropy in this model, in the y-diretion.

$$E_{Reg}(u) = \int_{\Omega} (\|\mathbf{H}_u\|_F^2 + 10(\mathbf{e}_y^T\mathbf{H}_u\mathbf{e}_y)^2) \; d\Omega \tag{3.97}$$

In Fig. 3.20a, the penalization of the curvature in the y-direction, produces a solution that presents a different behaviour compared to the isotropic Hessian energy 3.18a. The implicit function presents more regularity in the distances between consecutives isovalues, along the y-direction. This example illustrates the opportunities to produce smoother solutions with higher regularity, that are adapted to the geometry of the data, while maintaining the regularity criteria.

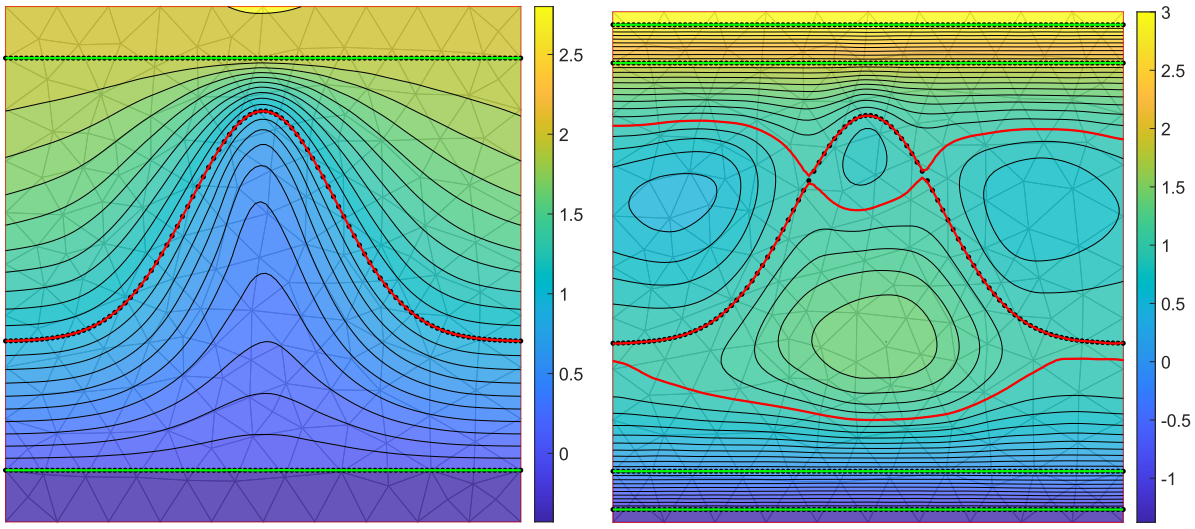

(a) (b)

Figure 3.20: Resulting implicit functions using the adapted Hessian energy (Eq .3.97) as regularization. (a) Bell ($\lambda = 1$). (b) Bell Hv ($\lambda = 1$).

3.8 Weak formulation associated to the implicit structural modeling problem

To find the weak form associated to the energy minimzation problem we presented beforehand, see Eq. 3.9. We derive the weak form associated to the fitting energy and the regularization energy.

$$\phi(h) = E_{fit}(u + hv) = \sum_{p=1}^{Np} \eta_p^2((u + hv)(x_p, y_p) - z_p)^2 \tag{3.98}$$

If u is a minimizer, the function ϕ must have a minimum at 0. Then

$$\phi'(0) = \frac{\partial E_{fit}(u + hv)}{\partial h} \mid_{h=0} = \sum_{p=1}^{Np} \eta_p^2 v(x_p, y_p)(u(x_p, y_p) - z_p) \tag{3.99}$$

Let consider the case where the regularization term is the Dirichlet energy

$$E_{Reg}(u) = \frac{1}{2} \int_\Omega \|\nabla u\|^2 \ d\Omega \tag{3.100}$$

Similarly to Eq. (3.99), the weak form of the Dirichlet energy is

$$\frac{\partial E_{Reg}(u + hv)}{\partial h} \mid_{h=0} = \int_\Omega \nabla u \cdot \nabla v \ d\Omega \tag{3.101}$$

Thus the weak form of the minimization problem Eq. (3.9) is

$$\lambda \int_\Omega \nabla u \cdot \nabla v \ d\Omega + \sum_{p=1}^{Np} \eta_p^2 u(x_p, y_p) v(x_p, y_p) = \sum_{p=1}^{Np} \eta_p^2 z_p v(x_p, y_p) \qquad \forall v \in H^1(\Omega) \tag{3.102}$$

The obtained weak form is a sum of discrete and continuous operator. If we consider that we have high density of data points to interpolate, likewise image smoothing where the input is a noisy image known all over the domain, we can replace the sums with integrals. Thus, we can rewrite Eq. (3.102) as

$$\lambda \int_{\Omega} \nabla u \cdot \nabla v \; d\Omega + \int_{\Omega} \eta_p^2 u(x_p, y_p) v(x_p, y_p) = \int_{\Omega} \eta_p^2 z_p v(x_p, y_p) \tag{3.103}$$

This weak formulation can be linked to the following Diffusion-reaction equation

$$\lambda \Delta u + \alpha u = f \tag{3.104}$$

subject to $\nabla u \cdot \mathbf{n} = 0$ on $\partial\Omega$, and α is positive coefficient. The solution of this minimization problem depends on the weight of the regularization considered. When the regularization weight is high, the solutions tends to be solutions of the Diffusion equation. Conversely, when the regularization weight is weak, the solutions are determined mainly by the fitting energy.

3.9 Different discretizations of the Hessian energy

The solutions of the minimization problem 3.9 are mainly determined by the choice of the regularization, rather than the discretization method used. As shown in Fig. 3.21a, a solution using Thin-plate splines subject to the minimization of the Hessian energy, exhibits oscillations similar to the solutions of the minimization of the Hessian energy, using different discretizations. In Fig. 3.21b, linear piecewise $P1$ finite elements on a triangular mesh, are used to represent the implicit function, and to discretize the Hessian energy using a mixed finite element method (Stein et al. (2022)). We observe that using different discretizations, solutions of the Hessian energy are exhibiting similar oscillatory behaviour, especially on the models presenting high thickness variations.

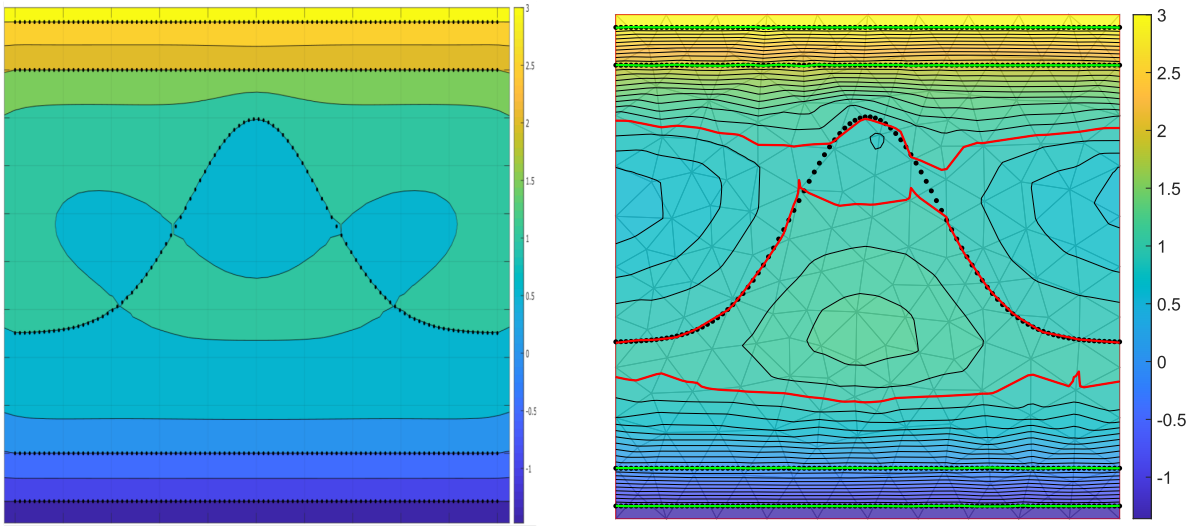

(a) (b)

Figure 3.21: Resulting implicit functions using the Hessian energy as regularization with different discretizations. (a) Thin-plate splines. (b) $P1$ piecewise linear elements.

3.10 Conclusions

We presented in this chapter a set of regularization techniques that are widely used in the field of implicit structural modeling specifically, and in the fields of computer graphics, shape modeling and surface reconstruction, where obtaining smooth solutions is important. We can distinguish two main classes in these regularization techniques. First, techniques based on expressing the set of regularization constraints as linear constraints on the degrees of freedom associated to the basis functions where the implicit function is represented. For instance, the smooth gradient constraint or the mean value constraint on second derivatives. In the case of the smooth gradient constraint, the basis functions are linear, and the gradients are constant piecewise. Then we apply a mean value constraint on the gradient to obtain smoother solutions. Similarly, the second derivatives of the PS-splines are piecewise constant, and a mean value on the second derivatives is applied to obtain solutions with higher smoothness. These techniques are specific to these representations and might not be adapted to other discretizations.

The second class of regularization methods, includes methods that are independent of the basis functions used to represent the implicit function. For instance, regularization energies such as Dirichlet energy, Laplacian energy or Hessian energy. These methods involve the minimization of a functional expressed as an integral of the partial order derivatives of the implicit function over the domain.

The formulation of the regularization constraints as a regularization energy of the second class presents many advantages. First, it is easier to link it with known PDE. Finding the PDE related to the energy minimization, will enable to characterize the behaviour of its solutions, in the interior, to describe the order of smoothness of the resulting solutions, as well as the behaviour near the boundaries, by determining the type of natural boundary conditions implicitly assumed. When we consider a technique based on the basis representation in which the implicit function is expressed, it is not obvious, to analyze the equivalent energy minimization problem, and which PDE it relates to. For instance, using the mean value on the second derivatives on PS-splines, enables to obtain smooth solutions, but it is not clear which conventional smoothing energy it is equivalent to and what implicit boundary conditions are implicitly applied.

The existing regularization techniques can fail to reproduce geologically coherent solution in models presenting high thickness variations. In the models Fig. 3.18c, d, strong oscillations were observed in the resulting implicit functions, often called bubble effect. High order smoothing techniques produces solutions presenting stronger oscillations. The assumption of smoothness and isotropy is not adapted to the anisotropy present in data. Therefore, the formulation of a new regularization technique is necessary in order to achieve solutions that respects all the regularity criteria desired, see Sect.1.8.1.

Chapter 4

New formulations of the regularization

PDEs with spatially varying coefficients are powerful mathematical tools used to describe a wide range of phenomena in various fields of science and engineering. For instance, in heat conduction problems involving heterogeneous composite materials, the thermal conductivity may vary spatially. This variation influences how heat is conducted within the material, and it is essential to accurately model these variations to design energy-efficient systems. In aerospace engineering, anisotropic composite materials are extensively used in various components, including aircraft wings, spacecraft components, and satellite structures. The continuous advancement of composite materials and manufacturing processes continues to push the boundaries of aerospace design and performance, leading to more efficient, lighter, and stronger aerospace vehicles. In all these applications, the use of spatially varying coefficients in PDEs allows for a more accurate and realistic representation of the underlying physical processes. This, in turn, motivated our interest for this class of PDEs. In this chapter we present two novel formulations of the regularization energy. First, we present our formulation of the regularization based on the nonlinear anisotropic diffusion with an iterative scheme in which the diffusion tensor is iteratively adapted to the variations and the anisotropy of data. Second, we introduce a new regularization energy based on the bending energy of anisotropic thin plates.

4.1 Diffusion equation

A PDE is a matheamtical equation that involves partial derivatives of an unknown function with respect to multiple independent variables. It describes how the function and its derivatives are related. In this section, we study the steady diffusion equation, that refers to a state in which the diffusion process remains constant with respect to time. In other words, the derivative with respect of time is null. It is a 2nd order linear elliptic equation of the form

$$\begin{cases} div(\mathbf{C}\nabla u) = f(\mathbf{x}) & in \quad \Omega \\ u = d & on \quad \partial\Omega \\ \mathbf{C}\nabla u \cdot \mathbf{n} = g & on \quad \partial\Omega \end{cases} \tag{4.1}$$

here $\mathbf{C}(\mathbf{x}) : \Omega \to \mathbb{R}^{d\times d}$ is a symmetric diffusion tensor field, and d is the dimension of Ω. While $f(\mathbf{x}) : \Omega \to \mathbb{R}$ is the source term. The Dirichlet and Neumann boundary conditions, are respectively, $d(\mathbf{x}) : \partial\Omega \to \mathbb{R}$ and $g(\mathbf{x}) : \partial\Omega \to \mathbb{R}$. The boundary condition $d(\mathbf{x})$ specifies the values of the function, and $g(\mathbf{x})$ instead specify derivatives (e.g. heat flow through the

boundary). The Dirichlet boundary condition is often called essential boundary conditions, while Neumann boundary condition is called a natural boundary condition (Cheng and Cheng 2005). The source term $f(\mathbf{x})$ can represent various physical phenomena depending on the specific application. In electrostatics, for instance, it represents the charge density distribution. In heat diffusion, it represents the heat source. For $\mathbf{C}(\mathbf{x}) = \mathbf{I}_d$, Eq. (4.1) reduces to the Poisson equation that has the form

$$\Delta u = f \tag{4.2}$$

subject to Dirichlet or Neumann boundary conditions.

4.1.1 Smoothing the solutions of the Diffusion equation

In his pioneering work, Mallet (1989) introduced as regularization, a functional expressed using finite differences scheme, involving the minimization of the first order partial derivatives as well as the second partial derivatives. This choice of regularization, was motivated by the fact that the layers are generally horizontal (i.e. flat), which corresponds to minimal first order partial derivatives. The minimal second derivatives can be linked to the hypothesis that the layers were deformed under the action of geological stresses, and that the shearing stresses are related to second order derivatives. We will establish a clear link between the Hessian smoothing energy and the potential energy of a bended thin plate in Sect. 4.5

In surface reconstruction from point cloud, which are not oriented. Alliez et al. (2007), considered the biharmonic energy as smoothness term in this fitting problem. By incorporating this term, the aim is to add extra regularity to the solutions. It can be seen as measure of the smoothness of the gradients. Thus, it enhances the regularity of the gradients, leading to smoother solutions. Calakli and Taubin (2011) instead added the Hessian energy as smoothness term, to obtain a smooth distance function, that is interpolating the values and the gradients of a function on a set of data points.

Barrera et al. (2008) presented a method to construct a surface approximating a set of Lagrangian data (i.e known values of the function only or with known derivatives), and formulated this problem as minimization of a fitting energy supplemented with the Dirichlet and the Hessian energy. They considered the Dirichlet energy as a measure of the surface area. While the Hessian energy is added to ensure the minimal energy condition of the functions in the minimization space. They considered the space of C^1 quadratic polynomials, constructed on a triangulation via the Powell-Sabin refinement.

Smith and Wessel (1990) introduced as regularization a partial differential equation combining the Laplacian and bilaplacian operators. For seismic data regularization, Fomel and Claerbout (2001) suggested the use of a diffusion tensor allowing for an anisotropic smoothing in some predefined directions. Wang and Solomon (2021), considered the Bilaplacian energy as smoothness energy, to obtain smoother solutions of the anisotropic diffusion equation.

Harmonic functions that are obtained by solving the Laplace equation, Eq. (3.59), or minimizing the Dirichlet energy Eq. (3.61), produces solutions respecting the mean value property and the maximum principle at the boundaries, ensuring no local extrema (Fig. 4.3a). However, these solutions lack smoothness, and present some oscillations in the region of high thickness variations as illustrated in Fig. 4.3a. Smoother Harmonic solutions can be obtained by adding a smoothness term to the minimization problem using the Dirichlet energy. Many conventional high order smoothness energies can be added to obtain smoother harmonic solutions. For example, the Bilaplacian energy or the Hessian energy. Smoothness energies,

that are dependent on the basis functions of the discretization space can be considered as well, as long as they tend to minimize second or higher derivatives. To obtain the smoothest harmonic solutions honoring the fitting constraints, we consider the following minimization problem

$$\min_u E_{fit}(u) + \lambda E_{\nabla^2}(u) + \mu E_{H^2}(u) \tag{4.3}$$

which can be expanded as

$$\min_u E_{fit}(u) + \frac{\lambda}{2}\int_\Omega \|\nabla u\|_1^2 \; d\Omega + \frac{\mu}{2}\int_\Omega \left\|\nabla^2 u\right\|_F^2 \; d\Omega \tag{4.4}$$

Fig. 4.1a shows the solution of the Dirichlet energy regularization discretized using PS-splines, while Fig. 4.1b shows the solution of the minimization problem Eq. (4.3), discretized using the PS-splines. This solution is smoother, while maintaining the mean value property and maximum principle at the boundaries, which are properties of the harmonic functions.

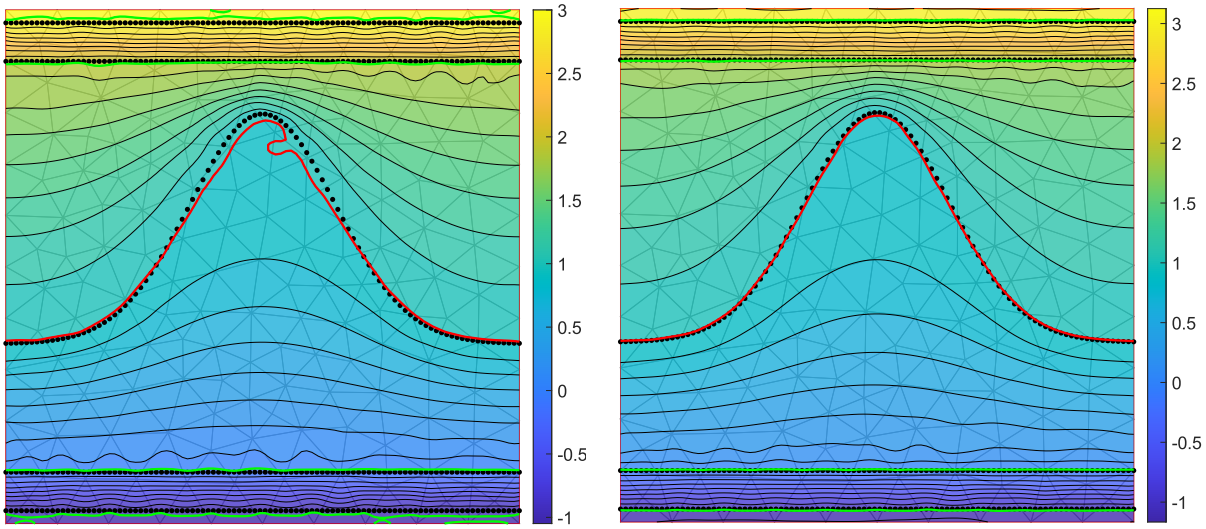

(a) (b)

Figure 4.1: Smoother harmonic solution obtained by adding the Hessian energy term, and discretized using the PS-splines. (a) Harmonic solution of Eq. (3.61) ($\lambda = 1$). (b) Smooth harmonic solution of Eq. (4.3) ($\lambda = 1, \mu = 1$).

In Figs. 4.2, we conduct the same experiment, using a the $P1$ linear finite elements. In this case, the proposed formulation in Eq. (4.3) enables to obtain smoother solutions of the harmonic equation.

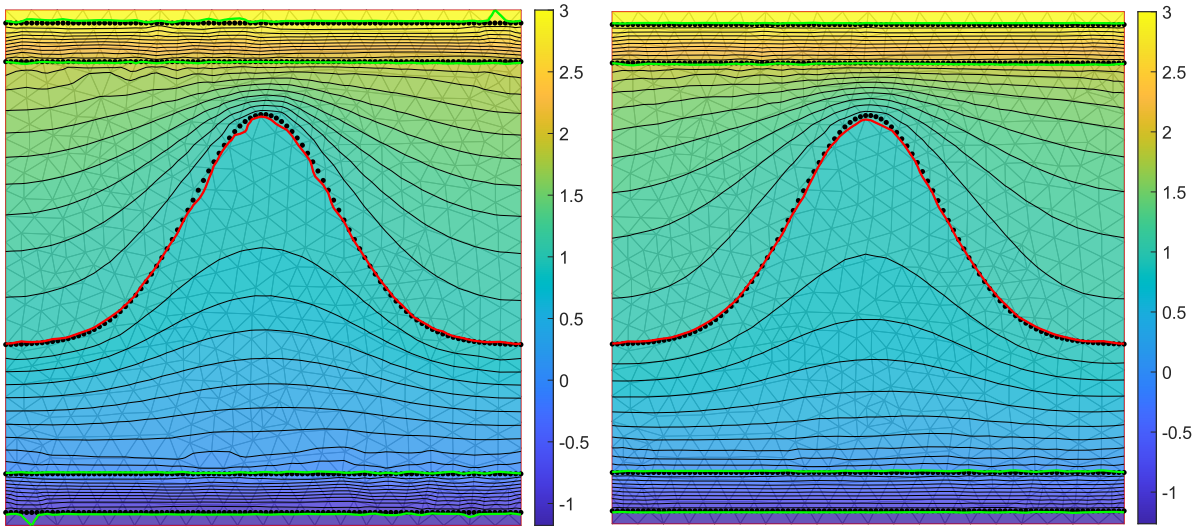

(a) (b)

Figure 4.2: Smoother harmonic solution obtained with the additional Hessian energy term discretized using the $P1$ linear elements. (a) Harmonic ($\lambda = 1$). (b) Smooth harmonic ($\lambda = 1, \mu = 1$).

The weak oscillations, that are still present in the smooth solutions, are due to the isotropic nature of the Laplace equation. In the next sections, we investigate the use of the parameters of the anisotropic diffusion equation to obtain solutions that present higher smoothness, while respecting the regularity criteria.

4.1.2 Handling the boundaries

When minimizing the Dirichlet energy or solving the standard Laplace equation Eq. (3.59), the natural boundary condition that emerges is the vanishing Neumann condition. It implicitly imposes that the normal derivative on the domain boundaries of the implicit function vanishes, which results in contours of the implicit function ending perpendicular to the domain boundaries to fulfill this condition. This is an undesired effect that makes the use of the diffusion equation unsuitable for our application.
Irakarama et al. (2022) proposed a free boundary discretization for the Laplacian avoiding this bias at the boundary. They use linear Lagrange elements as basis functions, and Crouzeix-Raviart nonconforming linear elements as test functions. Their method is based on a specific choice of basis functions and test functions spaces. In our work we avoid restricting ourselves to a specific choice of discretization. We propose a simpler technique to avoid the implicit vanishing Neumann boundary condition by constructing an approximation of Neumann boundary condition instead of neglecting the integral of the normal derivative on the boundaries. The normal derivative on the boundaries, is the rate of change of the implicit function along the normal direction to the boundaries. It describes how the implicit function contours finish on the boundaries. To obtain an estimation of Neumann boundary condition, we propose to construct a first approximation u_0 using the Hessian smoothing energy as regularization with a high regularization weight λ, in order to obtain a regular solution on the boundaries. Then, we use the normal derivative on the boundaries of the solution u_0 as a

Neumann condition such that

$$\int_{\Omega} \nabla u \cdot \nabla v \; ds = \int_{\partial\Omega} (\nabla u_0 \cdot \mathbf{n}) v \; dx \qquad \forall v \in H^1(\Omega) \tag{4.5}$$

Solving Eq. (4.5) is equivalent to minimizing the following diffusion energy (Evans 2010)

$$E_{Dif}(u) = \frac{1}{2} \int_{\Omega} \|\nabla u\|_1^2 \; d\Omega - \int_{\partial\Omega} g u \; dx \quad with \quad g = \nabla u_0 \cdot \mathbf{n} \quad on \quad \partial\Omega \tag{4.6}$$

A solution of the problem Eq. (4.6) with the diffusion energy as regularization, inherits good behaviour near the domain boundaries and presents the regularity properties of the diffusion equation.

The use of the diffusion equation implies implicitly a vanishing Neumann boundary condition, leading to contours finishing perpendicular to the boundaries, as shown in Fig. 4.3a. This strong artifact is undesired for our application due to the presence of discontinuities inside the domain in Fig. 4.3a. To overcome this limitation, we first construct a function obtained using the Hessian smoothing with a high weight in Fig. 4.3b, giving a regular function inside the domain and naturally finishing on the boundaries. We use its normal component of the gradient on the boundaries as Neumann initial boundary condition and to compute the first solution in both the iterative schemes that we will introduce in the next sections, Eq. (4.18)-Eq. (4.12). For the next iterations in both schemes, we use the normal component of the gradient of the previous solution to update the Neumann boundary condition. Our solution finally respects all the regularity criteria and fitting constraints with a natural behaviour near boundaries, free from the artifact shown in Fig. 4.3c.

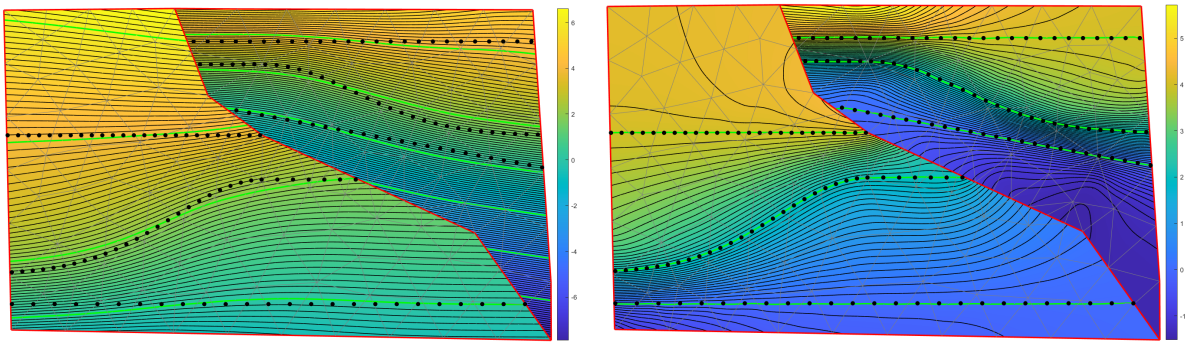

(a) (b)

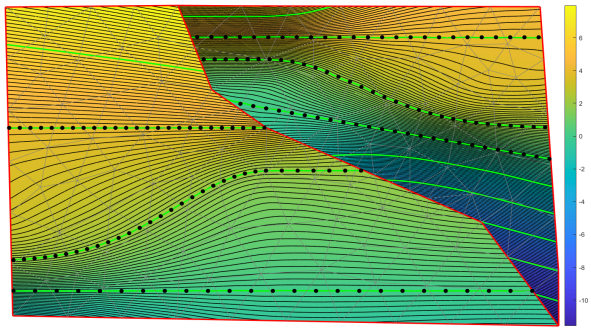

(c)

Figure 4.3: (a) Resulting implicit function with implicit vanishing Neumann condition on the boundaries (Eq. 4.17) ($\lambda = 1, \mu = 1$). (b) Resulting implicit function with a high smoothing weight using the Hessian energy ($\lambda = 1$). (c) Resulting implicit function free from boundary artifact using our method (Eq. 4.17) ($\lambda = 1, \mu = 1$).

The Diffusion PDE Eq. (4.1) provides a rich framework to describe various physical phenomenon. It includes various boundary conditions, and various degrees of freedom, such as the source term and the diffusion tensor. We will investigate its use as regularization for the implicit modeling problem. First, a method based on Poisson equation, where the source term is involved in an optimization problem (Sect. 4.1.3). Second, a formulation that is based on optimization with respect to the diffusion tensor (Sect. 4.2).

4.1.3 Source term/Poisson method

Laplace equation corresponds to Eq. (4.2) with a vanishing source term $f(\mathbf{x})$. In the context of implicit structural modeling the source term is unknown. This term can be rewritten as

$$f(\mathbf{x}) = div(\mathbf{N}(\mathbf{x})) \tag{4.7}$$

where $\mathbf{N}(\mathbf{x})$ is a determined vector field describing the implicit function to reconstruct, we call it guiding field. We propose to approximate this field using the numerical data. Then, the Poisson approach can be adapted to our problem to construct the unknown implicit function. Furthermore, solving the following Poisson equation

$$\Delta u = div(\mathbf{N}) \tag{4.8}$$

subject to $\nabla u \cdot \mathbf{n} = g(\mathbf{x})$, gives the equivalent weak formulation

$$\int_\Omega \nabla u \cdot \nabla v \; d\Omega - \int_{\partial\Omega} g(\mathbf{x}) v dx = \int_\Omega \mathbf{N} \cdot \nabla v \; d\Omega \tag{4.9}$$

which is equivalent to minimizing the following energy

$$E_{\nabla^2}(u, g, \mathbf{N}) = \frac{1}{2} \int_\Omega \|\nabla u - \mathbf{N}\|^2 \; d\Omega - \int_{\partial\Omega} g(\mathbf{x}) u dx \tag{4.10}$$

Crane et al. (2013), introduced a novel method for distance computation. using the heat flow, instead of solving the eikonal equation, which is of the form

$$| \nabla \phi(\mathbf{x}) | = 1, \quad \forall \mathbf{x} \in \Omega \tag{4.11}$$

subject to a Dirichlet boundary condition $\phi_{|\gamma} = 0$ on a subset γ of the domain. This equation is non linear and hyperbolic, hence difficult to discretize and to solve. Instead, Crane et al. (2013) converted this equation to a quadratic convex minimization problem on the gradient of u. The problem of finding the function with the closest gradient to the vector field X, which is a unit vector obtained by normalizing the opposite heat flow vector. The heat flow vector is obtained simply by diffusing heat along the subset γ for some amount of time. Inspired by this method, we construct a vector field all over the domain that approximates the gradient of the implicit function. Then, to regularize the implicit function, we solve the Poisson equation Eq. (4.2) with the divergence of this vector field as source term. We propose the following non linear problem with respect to u and $\mathbf{N}$

$$\min_{u,\mathbf{N}} E_{fit}(u) + \lambda E_{\nabla^2}(u, g, \mathbf{N}) + \mu E_{H^2}(u) \tag{4.12}$$

In words, we seek for the smoothest solution, that is guided by the vector field $\mathbf{N}(\mathbf{x})$. Near the boundaries, its behavior is determined by $g(\mathbf{x})$. To solve this non linear problem, we propose the iterative scheme Algorithm. 1. We suggest to start from a regular solution u_0, that can be obtained using a high smoothing weight associated to the Hessian energy. For initial values, we set $\mathbf{N}_0(\mathbf{x}) = \nabla u_0$ and $g_0(\mathbf{x}) = \nabla u_0 \cdot \mathbf{n}$. Iteratively, we solve the following algorithm

Algorithm 1 Iterative algorithm for nonlinear anisotropic diffusion energy minimization.

Require: Initial solution $u_0 \leftarrow \min_u E_{fit}(u) + \lambda_0 E_{H^2}(u)$ for a high regularization weight λ_0.
  while dif $\geq \varepsilon$ **do**
    $g = \nabla u_{k-1} \cdot \mathbf{n}$, $\mathbf{N}_{k-1} = \nabla u_{k-1}$;
    $u_k = \min_u E_{fit}(u) + \lambda E_{\nabla^2}(u, g_{k-1}, \mathbf{N}_{k-1}) + \mu E_{H^2}(u)$;
    $dif = E_{fit}(u_{k-1}) - E_{fit}(u_k)$;
  end while

Figs. 4.4 show the results of the iterative scheme we introduced in Algorithm. 1. The figures on the left, show the initial solution u_0, that we construct using a heavy smoothing weight associated to the Hessian energy. These initial solutions, present high regularity, due to the high smoothing weight. Also, they give the right directions along which the gradient of the implicit function should be aligned, eventhough they are not fitting the data. In the regularization formulation Eq. (4.12), only the gradient of the function is constrained. It is done in a weak sense via the source term. The final solution in Fig. 4.4c, is regular and fitting data, and presents a natural behaviour near the domain boundaries. In this model, the thickness variations, are mainly along the y-direction. In the two other models, Figs. 4.4f, i, the solutions are not regular, particularly in regions where the thickness variations are strong. In the first iterations Fig. 4.4b, d, h, the solutions successfully, fit the data, and are regular.

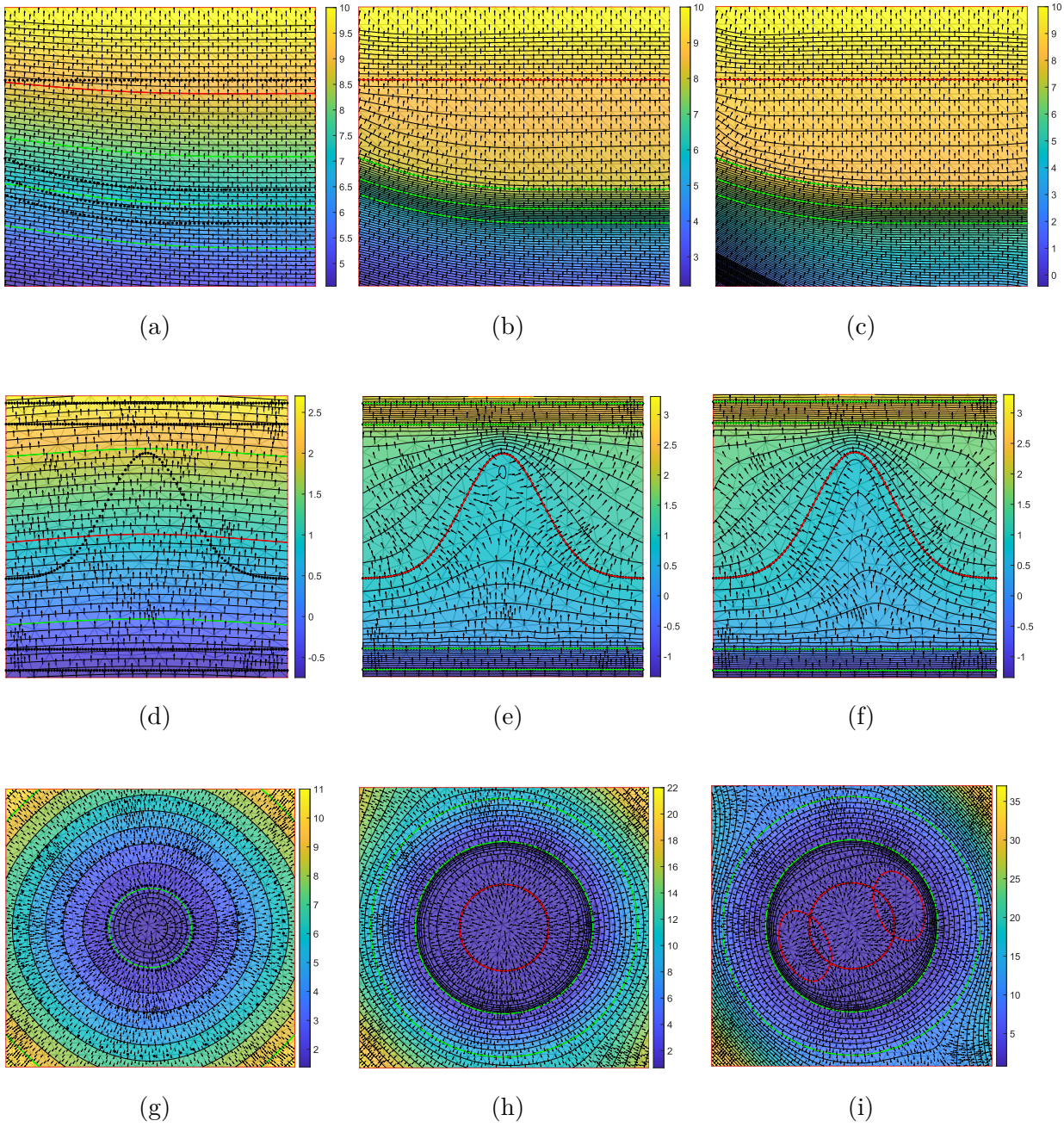

Figure 4.4: Resulting implicit functions using the iterative scheme Algorithm. 1. (a)-(d)-(g) regular solution. (b)-(e)-(h) first iteration ($\lambda = 1, \mu = 1$). (c)-(f)-(i) final solution ($\lambda = 1, \mu = 1$).

Figs. 4.5 show the resulting solution using the iterative scheme without the Hessian energy term in the Eq. (4.12). In this case, the first solutions contains some small oscillations. In the next iterations, these small oscillations are amplified and introduce strong artifacts in the final solutions.

These experiments, illustrate that the solutions, of the iterative scheme Eq. (4.12), can produce regular solutions in models where the thickness variations are strong. However, it is

very sensitive to the oscillations of the vector field $\mathbf{N}$. To overcome this issue, other constraints can be added on the guiding vector field to ensure on each iteration it is presenting minimal oscillations. For instance, Knöppel et al. (2013) presented a method to obtain the smoothest direction field on surfaces based on solving the Poisson equation. Although this option seems interesting, we did not explore it.

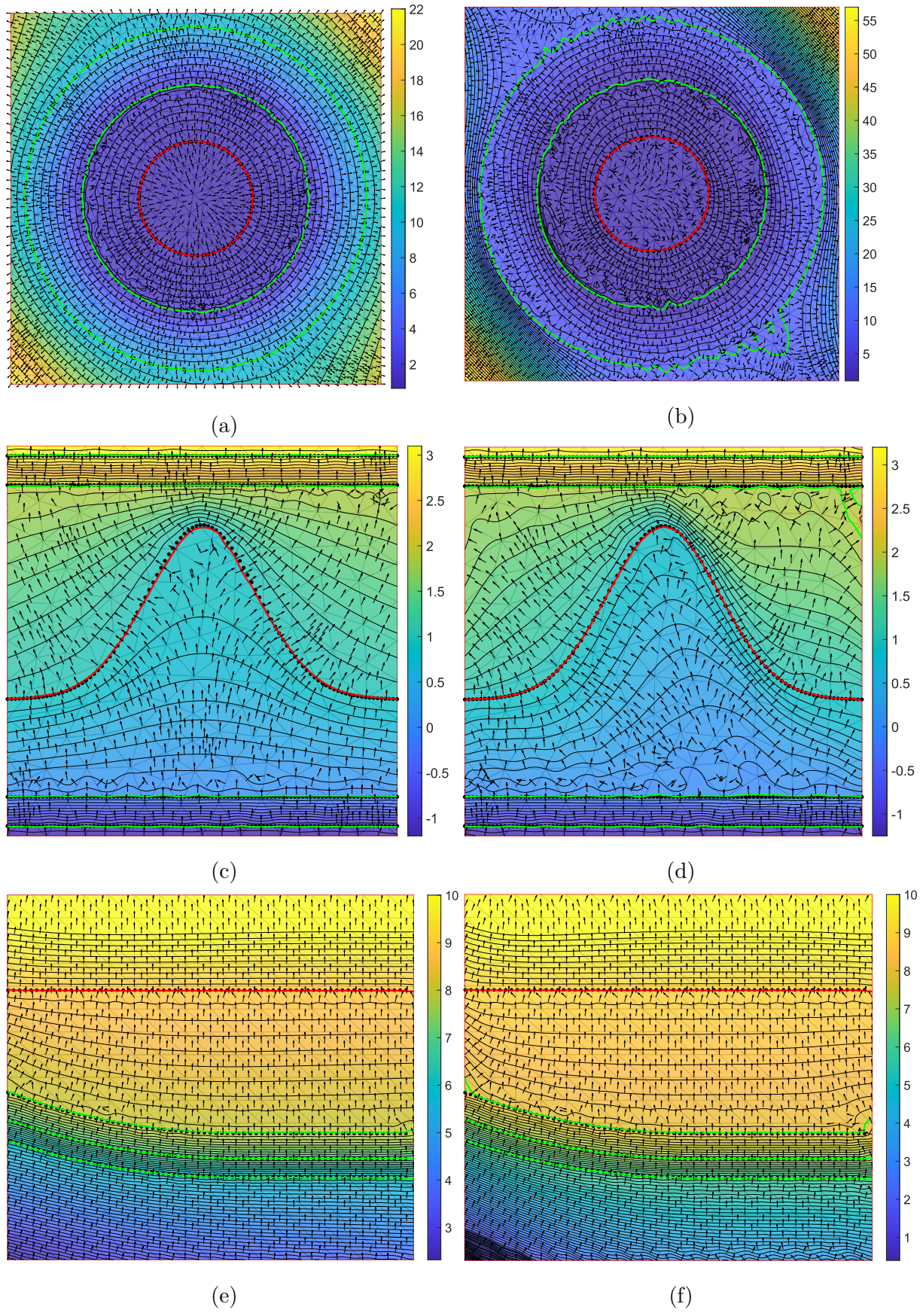

Figure 4.5: Resulting implicit functions using the iterative scheme Algorithm. 1 without the Hessian smoothing term. (a)-(c)-(e) first iteration ($\lambda = 1, \mu = 1$). (b)-(d)-(f) final solution ($\lambda = 1, \mu = 1$).

4.1.4 Isotropic and anisotropic diffusion

Anisotropic nonlinear diffusion is a powerful technique in image and geometry processing. It was introduced by Perona and Malik (1990) to smooth and denoise images while preserving sharp edges, based on the equation $div(c\nabla u) = 0$, with diffusion coefficient $c = g(\nabla u)$ such as $g(\nabla u) = \frac{1}{1+\|\nabla u\|^2}$ or other functions inverting the norm of the gradient. This method is only isotropic, since it uses a scalar diffusion coefficient, and may not be sufficient to accurately describe models presenting anisotropic thickness variations.

The anisotropic diffusion process can be described using a variant of the heat diffusion partial differential equation (PDE)

$$\Delta^C = div(\mathbf{C}\nabla u) = 0. \tag{4.13}$$

The anisotropic Laplacian $\Delta^C = div(\mathbf{C}\nabla u)$ has spatially varying coefficients that weight the derivatives along different directions, specified by a diffusion tensor field $\mathbf{C}$, such that $\mathbf{C} = (c_{ij})$ with $c_{ji} = c_{ij}$ for $i, j = 1 : d$.

Andreux et al. (2015) introduced an anisotropic Laplace-Beltrami operator, for shape analysis, using a diagonal tensor encoding some geometrical extrinsic quantities. Expressed in the orthonormal basis of principal curvature directions, the diagonal entries of their tensor chosen as function of the principal curvatures, privileging diffusion in one of the principal curvature directions. The diffusion tensor $\mathbf{C}$ can be also defined

$$\mathbf{C} = c_{\|}\mathbf{b} \otimes \mathbf{b} + c_{\perp}(\mathbf{I}_d - \mathbf{b} \otimes \mathbf{b}), \tag{4.14}$$

where the vector $\mathbf{b} \in \mathbb{R}^d$ represents the anisotropy direction, $c_{\|}$ and $c_{\perp}$ are the parallel and perpendicular diffusion coefficients, respectively, and $\mathbf{I}_d$ is the identity matrix. This representation is used in the context of magnetized plasmas in Tokamak (Giorgiani et al. 2020), where the parallel diffusion $c_{\|}$ is chosen several orders of magnitude higher (up to 10^9) than the perpendicular diffusion coefficient $k_{\perp}$, favoring the diffusion in the anisotropy direction. Wang and Solomon (2021) proposed optimization on the diffusion tensor to construct an optimal weights for geometric data interpolation, based on a positive semidefinite tensor representation where the coefficients of this tensor are unknowns of the problem.

In our context, models can exhibit a high anisotropy, where data present thickness variations along different directions. The anisotropy directions are unknowns unlike the other fields of applications of the anisotropic diffusion equation. There exist techniques for estimating global directions; however obtaining information about local anisotropy in data remains a very challenging task. Inspired by the success of the anisotropic diffusion in all these application fields, we propose an iterative scheme in which the diffusion tensor is iteratively adapted to the anisotropy present in data. We consider the anisotropic Laplacian Δ^C defined by the symmetric diffusion tensor field $\mathbf{C}(\mathbf{x}) : \Omega \to \mathbb{R}^{d\times d}$, where d is the dimension of Ω. For $d = 2$, we use c_1, c_2, c_3 scalar functions to denote the diffusion coefficients, respectively, in the directions: xx, xy, yy.

$$\Delta^C = div(\mathbf{C}\nabla u) \qquad \text{with} \qquad \mathbf{C} = \begin{pmatrix} c_1 & c_2 \\ c_2 & c_3 \end{pmatrix}. \tag{4.15}$$

The tensor representation of the diffusion generalizes the standard Laplacian for $\mathbf{C} = \mathbf{I}_d$ and the isotropic nonhomogeneous diffusion for $\mathbf{C} = c(\mathbf{x})\mathbf{I}_d$, with $c(\mathbf{x})$ a scalar-value diffusion

function. Solving the anistropic diffusion equation is equivalent to minimizing the following energy (Evans 2010)

$$E_{Dif(\mathbf{C})}(u,g) = \frac{1}{2}\int_{\Omega} \nabla u^T(\mathbf{x})\mathbf{C}(\mathbf{x})\nabla u(\mathbf{x}) \;\; d\Omega - \int_{\partial\Omega} g(\mathbf{x})u(\mathbf{x})dx, \tag{4.16}$$

where $g(\mathbf{x})$ corresponds to the Neumann condition $g(\mathbf{x}) = \nabla u_0(\mathbf{x})^T\mathbf{C}\mathbf{n}$ for $x \in \partial\Omega$ and $\mathbf{n}$ is the interior normal to $\partial\Omega$ with u_0 a regular solution on the domain boundaries constructed using the technique described in Sect. 4.1.2.

4.2 A fitting method with diffusion regularization

In this section, we investigate the use of the anisotropic diffusion PDEs as regularization. Then we propose a new formulation based on the nonlinear anisotropic diffusion with an iterative scheme in which the diffusion tensor is iteratively adapted to the variations and the anisotropy in data.

4.2.1 New formulation of regularization based on diffusion PDE

We consider the following nonlinear minimization problem with respect to the unknowns u and $\mathbf{C}$

$$\min_{u,\mathbf{C}} E_{fit}(u) + \lambda E_{H^2}(u) + \mu E_{Dif(\mathbf{C})}(u,g). \tag{4.17}$$

The regularization term in our new formulation is a sum of two energies, weighted by two scalars μ and λ, controlling respectively the tradeoff between the diffusion and the smoothing. The diffusion energy is based on the anisotropic diffusion PDE, providing anisotropic solutions that respect the mean value property and the maximum principle, ensuring no local extrema. The Hessian energy term is added to ensure smoothness of the solution. In the set of solutions of the anisotropic diffusion equation with the diffusion tensor $\mathbf{C}$, the smoothest solutions are selected by minimizing the Hessian energy. The diffusion energy defined with the anisotropic diffusion tensor $\mathbf{C}$, generates solutions that are adapted to the anisotropy present in data, providing extra degrees of freedom for the modeling problem. Thus, the formulation of our problem is nonlinear regarding the two variables: the implicit function u and the diffusion tensor $\mathbf{C}$.

To solve this nonlinear minimization problem, we propose an iterative scheme that involves the two problem unknowns u and $\mathbf{C}$. In our scheme we solve first for u, then for $\mathbf{C}$ and we repeat until the difference between the fitting energies of consecutive iterations is less than a chosen threshold ε. The diffusion energy is quadratic in u and is convex if the tensor $\mathbf{C}$ is positive semi-definite. In this case, the solution is unique. However, the diffusion energy with respect to the coefficients of the diffusion tensor $\mathbf{C}$ is linear and can be either positive or negative. Thus, minimizing this energy with respect to $\mathbf{C}$ can be challenging as the solution is not well-defined. To address this issue, we introduce a proxy problem that replaces the original diffusion energy when optimizing for $\mathbf{C}$. We propose to minimize instead a quadratic convex energy with respect to $\mathbf{C}$. To do so, we first optimize the following objective function with respect to $\mathbf{C}$ for a given u

$$\min_{C}\Big(\int_{\Omega} \|\mathbf{C}\nabla u\|^2 \quad d\Omega + \omega_1 E_{H^2}(\mathbf{C}) + \omega_2 \int_{\Omega} \|\mathbf{C} - \mathbf{I}_d\|_F^2 \;\; d\Omega\Big). \tag{4.18}$$

We then inject $\mathbf{C}$ solution of Eq. (4.18) and we optimize with respect to u

$$\min_u (E_{fit}(u) + \lambda E_{H^2}(u) + \mu E_{Dif(\mathbf{C})}(u, g)). \tag{4.19}$$

Minimizers of the quadratic energy $\int_\Omega \|\mathbf{C}\nabla u^*\|^2 \, d\Omega$ with respect to the components of the diffusion tensor $\mathbf{C}$ for a given u^*, give minimal quantity $\mathbf{C}\nabla u^*$. Thus, the diffusion tensor $\mathbf{C}$ is adapted based on the intensity and the direction of the gradient ∇u^*. In regions where the gradient ∇u^* is strong, we minimize strongly the tensor $\mathbf{C}$ in the direction of the gradient ∇u^*, allowing less diffusion regularization to permit strong variations of the implicit function. Conversely, where ∇u^* is small, we minimize less the tensor $\mathbf{C}$ and therefore regularize more reducing the variations of the implicit function in the direction of ∇u^*. The Hessian smoothing term $\omega_1 E_{H^2}(\mathbf{C})$ on the components of the diffusion tensors is added to obtain smooth diffusion coefficients with minimal oscillations. A third term $\omega_2 \int_\Omega \|\mathbf{C} - \mathbf{I}_d\|_F^2 \, d\Omega$ of a distance penalization from the standard diffusion where the diffusion tensor is the identity matrix $\mathbf{I}_d$, to avoid the trivial null tensor as solution for this problem.

To construct an initial solution u_0, we only use the Hessian energy as regularization associated with a high regularization weight λ_0, favoring regularity over a good fitting of data. $\mathbf{C}$ is then obtained via optimizing Eq. (4.18) with $u = u_0$. Using $\mathbf{C}$ and $g(\mathbf{x}) = \nabla u_0(\mathbf{x})^T \mathbf{C}\mathbf{n}$ as Neumann boundary condition we obtain the next u. At step (i), $\mathbf{C}_i$ is obtained via minimizing the Eq. (4.18) based on u_{i-1}. In the same way u_i is obtained via minimizing Eq. (4.19) based on $\mathbf{C}_{i-1}$ and $g(\mathbf{x}) = \nabla u_{i-1}(\mathbf{x})^T \mathbf{C}_i \mathbf{n}$ on the boundaries as Neumann boundary condition. We keep iterating until the difference between the fitting energies of the current and the previous iteration is less than a chosen threshold ε.

Algorithm 2 Iterative algorithm for nonlinear anisotropic diffusion energy minimization.

Require: Initial solution $u_0 \leftarrow \min_u E_{fit}(u) + \lambda_0 E_{H^2}(u)$ for a high regularization weight λ_0.
  while dif $\geq \varepsilon$ **do**
    $\mathbf{C}_i \leftarrow \min_{\mathbf{C}} E_{Dif}(\mathbf{C}, u_{i-1}) + \omega_1 E_{H^2}(\mathbf{C}) + \omega_2 \int_\Omega \|\mathbf{C} - \mathbf{I}_d\|_F^2 \, d\Omega$;
    $g = \nabla u_{i-1}^T \mathbf{C}_i \mathbf{n}$;
    $u_i \leftarrow \min_u E_{fit}(u) + \lambda E_{H^2}(u) + \mu E_{Dif(\mathbf{C}_i)}(u, g)$;
    $dif = E_{fit}(u_{i-1}) - E_{fit}(u_i)$;
  end while

4.2.2 Tangential diffusion along faults

Discontinuities such as faults are often encountered in geological structural modeling. The generated mesh is conformal to the faults in discrete implicit approaches. The nodes on the faults are duplicated from either sides allowing a jump in the implicit function. Faults are considered as inner boundaries of the domain Ω. We note $\partial\Omega_{in} \subset \partial\Omega$ the set of faults. Each fault is composed of a set of edges. In cases where the stratigraphic layers exhibit a large thickness variation along the faults, solutions of our method might not respect the mean value property and no local extrema along the faults. For this reason, we add an extra constraint to our regularization formulation Eq. (4.16) only on faults. Along the faults $\partial\Omega_{in}$, in the tangential direction to the edges composing the faults, we apply the anisotropic diffusion PDE

$$(c_t u_t)_t = 0, \tag{4.20}$$

where $c_t = \mathbf{t}^T\mathbf{C}\mathbf{t}$ and u_t is the derivative of the implicit function u in the direction $\mathbf{t}$. The weak formulation is derived by multiplying Eq. (4.20) by a test function v and integrating over $\partial\Omega_{in}$

$$\int_{\partial\Omega_{in}} c_t u_t v_t \; ds = [c_t(\mathbf{x})u_t(\mathbf{x})v(\mathbf{x})]_{\mathbf{x}\in E}, \qquad \forall v \in H^1(\Omega), \tag{4.21}$$

E is the set of nodes on the extremities of the faults. As illustrated in Fig. 4.6, we integrate Eq. (4.21) over the fault first from e_1 towards e_2 and then in the opposite direction from the other side.

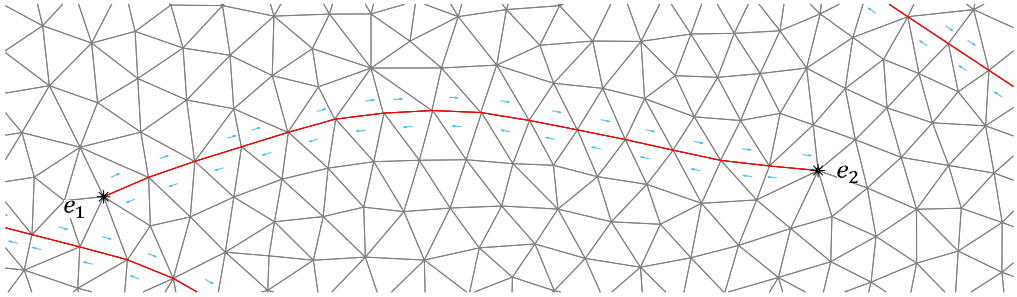

Figure 4.6: Fault inside the mesh with extremities e_1, e_2. Red line represents the fault, blue arrows represent the direction of the fault edges in both sides.

The resulting implicit boundary condition is a vanishing derivative in the direction t at the extremities of the faults. In order to avoid $u_t(\mathbf{x}) = 0$ for $\mathbf{x} \in E$, we set $u(\mathbf{x}) = u_{i-1}(\mathbf{x})$ and $\nabla u(\mathbf{x}) = \nabla u_{i-1}(\mathbf{x})$ for $\mathbf{x} \in E$ as Dirichlet and Neumann boundary condition, leading to solving over all Ω the following PDE system

$$\begin{cases} div(\mathbf{C}\nabla u) = 0 & in \;\; \Omega, \\ \nabla u^T\mathbf{C}\mathbf{n} = g & on \;\; \partial\Omega, \\ (c_t u_t)_t = 0 & on \;\; \partial\Omega_{in}, \\ u(\mathbf{x}) = u_{i-1}(\mathbf{x}) \;,\; \nabla u(\mathbf{x}) = \nabla u_{i-1}(\mathbf{x}) & for \; \mathbf{x} \in E. \end{cases} \tag{4.22}$$

Equivalently we minimize the following modified diffusion energy

$$E_{Dif(\mathbf{C})}(u,g) = \frac{1}{2}\int_\Omega \nabla u^T(\mathbf{x})\mathbf{C}(\mathbf{x})\nabla u(\mathbf{x}) \;\; d\Omega - \int_{\partial\Omega} g(\mathbf{x})u(\mathbf{x})dx + \frac{1}{2}\int_{\partial\Omega_{in}} c_t(u_t(\mathbf{x}))^2 dx \tag{4.23}$$

$$s.t \;\; u(\mathbf{x}) = u_{i-1}(\mathbf{x}), \;\; \nabla u(\mathbf{x}) = \nabla u_{i-1}(\mathbf{x}) \;\; for \; \mathbf{x} \in E.$$

4.2.3 Discretization

In this section, we discretize the energies used in the iterative scheme Eqs. (4.18)-(4.19) as well as the fitting energy Eq. (3.4). Our formulation is generic (i.e. it works for any choice of basis functions $(B_i)_{i=1:N_s}$ of F where one is able to discretize the diffusion and squared Hessian energy). The implicit function u is defined as $\forall \mathbf{x} \in \Omega, \; u(\mathbf{x}) = \sum_{i=1}^{N_s} B_i(\mathbf{x})u_i = \mathbf{B}(\mathbf{x})\mathbf{U}$, where $\mathbf{B}(\mathbf{x}) = (B_1(\mathbf{x}), ..., B_{N_s}(\mathbf{x}))$ is a basis of F and $\mathbf{U} = (u_1, ..., u_{N_s})^T$ is the vector of unknowns. Minimizing the fitting energy Eq. (3.4) is equivalent to solving the following linear system

$$\sum_{p=1}^{Np} \eta_p \mathbf{B}(x_p, y_p)^T\mathbf{B}(x_p, y_p)\mathbf{U} = \sum_{p=1}^{Np} \eta_p \mathbf{B}(x_p, y_p)^T z_p. \tag{4.24}$$

We write this system as

$$\mathbf{A_{fit}U} = \mathbf{Z} \tag{4.25}$$

In order to discretize $E_{H^2}(u)$ over the domain Ω, we consider the bilinear form h over F

$$h(u,v) = \int_\Omega (u_{xx}v_{xx} + 2u_{xy}v_{xy} + u_{yy}v_{yy})\ d\Omega. \tag{4.26}$$

We define a sparse matrix $\mathbf{H} \in \mathbb{R}^{(N_s \times N_s)}$

$$E_{H^2}(u) = \int_\Omega \|H_u\|_F^2 = \mathbf{U}^T\mathbf{H}\mathbf{U} \ \text{ s.t } \ \mathbf{H}_{ij} = h(B_i, B_j) \qquad \text{for} \quad i,j = 1:N_s. \tag{4.27}$$

Minimizing $E_{H^2}(u)$ gives the linear system $\mathbf{HU} = \mathbf{0}$. We also express the diffusion energy using the basis functions as

$$\begin{aligned} E_{Dif(\mathbf{C})}(u,g) = \frac{1}{2}\int_\Omega \mathbf{U}^T\nabla\mathbf{B}(\mathbf{x})^T\mathbf{C}(\mathbf{x})\nabla\mathbf{B}(\mathbf{x})\mathbf{U}\ \ d\Omega - \int_{\partial\Omega} g(\mathbf{x})\mathbf{B}(\mathbf{x})\mathbf{U}dx \\ + \frac{1}{2}\int_{\partial\Omega_{in}} \mathbf{U}^T(\mathbf{t}^T\mathbf{C}\mathbf{t})(B_t(\mathbf{x})^T B_t(\mathbf{x}))\mathbf{U}dx, \end{aligned} \tag{4.28}$$

where $B_t(\mathbf{x}) = (\partial_t(B_i))$ is the derivative of the basis functions in the tangential direction to the faults. Therefore, minimizing Eq. (4.28) with respect to u, gives a linear system of the form $\mathbf{\Delta}^C\mathbf{U} = \mathbf{N}^C$, where

$$\mathbf{\Delta}^C_{ji} = \int_\Omega \mathbf{C}(\mathbf{x})\nabla B_i \cdot \nabla B_j\ \ d\Omega + \int_{\partial\Omega_{in}} (\mathbf{t}^T\mathbf{C}(\mathbf{x})\mathbf{t})\partial_t(B_i)\partial_t(B_j)\ dx, \quad i,j = 1:N_s, \tag{4.29}$$

$$\mathbf{N}^C_j = \int_{\partial\Omega} g(\mathbf{x})B_j\ dx. \tag{4.30}$$

To discretize the anisotropy symmetric tensor $\mathbf{C} = \begin{pmatrix} c_1 & c_2 \\ c_2 & c_3 \end{pmatrix}$, each diffusion coefficient c_1, c_2, c_3 is discretized using the basis functions $(B_i(\mathbf{x}))_{i=1}^{N_s}$ in F such that

$$\forall \mathbf{x} \in \Omega \qquad c_j(\mathbf{x}) = \sum_{i=1}^{N_s} B_i(\mathbf{x})c_{j,i} = \mathbf{B}(\mathbf{x})\mathbf{C}_j,\ \ j = 1:3. \tag{4.31}$$

We use the flat vector $\mathbf{C} = \begin{bmatrix} \mathbf{C}_1 \\ \mathbf{C}_2 \\ \mathbf{C}_3 \end{bmatrix}$ to store the degrees of freedom of the three diffusion coefficients. The terms of the minimization problem (ii) are discretized as follows

$$\|\mathbf{C}\nabla u\|^2 = (\mathbf{C}\nabla u)^T(\mathbf{C}\nabla u) \qquad \text{for a given } \ u. \tag{4.32}$$

$$\mathbf{C}\nabla u = \begin{bmatrix} c_1u_x + c_2u_y \\ c_2u_x + c_3u_y \end{bmatrix} = \begin{bmatrix} u_x & u_y & 0 \\ 0 & u_x & u_y \end{bmatrix} \begin{bmatrix} c_1 \\ c_2 \\ c_3 \end{bmatrix} = \left[\begin{bmatrix} u_x & u_y & 0 \\ 0 & u_x & u_y \end{bmatrix} \otimes \mathbf{B}(\mathbf{x}) \right] \mathbf{C}. \tag{4.33}$$

Using the formulation above, we get

$$\int_\Omega \|\mathbf{C}\nabla u\|^2\ d\Omega = \int_\Omega \mathbf{C}^T \left[\begin{bmatrix} u_x^2 & u_xu_y & 0 \\ u_xu_y & u_x^2 + u_y^2 & u_xu_y \\ 0 & u_xu_y & u_y^2 \end{bmatrix} \otimes [\mathbf{B}(\mathbf{x})^T\mathbf{B}(\mathbf{x})] \right] \mathbf{C}\ \ d\Omega. \tag{4.34}$$

The Hessian energy for the diffusion coefficients is simply

$$E_{H^2}(\mathbf{C}) = E_{H^2}(c_1) + E_{H^2}(c_2) + E_{H^2}(c_3) = \int_\Omega \mathbf{C}^T(\mathbf{I}_3 \otimes \mathbf{H})\mathbf{C} \quad d\Omega. \tag{4.35}$$

The distance from the identity matrix explained in Sect. 4.2.1 can be expressed as

$$\int_\Omega \|\mathbf{C} - Id\|_F^2 \; d\Omega = \int_\Omega (c_1 - 1)^2 + (c_3 - 1)^2 + 2c_2^2 \; d\Omega. \tag{4.36}$$

Then we minimize it by solving the following linear system

$$\left[\begin{bmatrix} 1 & 0 & 0 \\ 0 & 2 & 0 \\ 0 & 0 & 1 \end{bmatrix} \otimes \mathbf{M}\right] \mathbf{C} = \begin{bmatrix} 1 \\ 0 \\ 1 \end{bmatrix} \otimes \int_\Omega \mathbf{B}(\mathbf{x})^T \; d\Omega, \text{ with } \; \mathbf{M} = \int_\Omega \mathbf{B}(\mathbf{x})^T\mathbf{B}(\mathbf{x}) \; d\Omega. \tag{4.37}$$

4.2.4 Linear system weighting

The minimization problem Eq. (4.19) gives rise to a linear system of the form

$$\mathbf{AU} = \mathbf{B}, \tag{4.38}$$

where the matrix $\mathbf{A}$ and the column vector $\mathbf{B}$ are expressed as

$$\mathbf{A} = \mathbf{A_{fit}} + \lambda\mathbf{H} + \mu\boldsymbol{\Delta}^C \qquad \text{and} \qquad \mathbf{B} = \mathbf{Z} + \mu\mathbf{N}^C. \tag{4.39}$$

The weights λ and μ associated, respectively, with the diffusion and Hessian energy, control the tradeoff between fitting the data and regularizing the solution, as well as the tradeoff between the diffusion properties and smoothness.

We use the weighting function m that gives the average of the absolute values of the matrix elements, defined from $\mathbb{R}^{N_s \times N_s} \to \mathbb{R}$ as

$$m(\mathbf{M}) = \frac{1}{N_s^2} \sum_{i,j=1}^{N_s} |\mathbf{M}_{ij}|. \tag{4.40}$$

We apply this function to the matrices $\mathbf{A_{fit}}$, $\mathbf{H}$, $\boldsymbol{\Delta}^C$ resulting, respectively, from the fitting, Hessian and diffusion energies. The quantities $\frac{m(\mathbf{A_{fit}})}{m(\mathbf{H})}$ and $\frac{m(\mathbf{A_{fit}})}{m(\boldsymbol{\Delta}^C)}$ estimate, respectively, the average relative weight of $\mathbf{A_{fit}}$ to $\mathbf{H}$ and to $\boldsymbol{\Delta}^C$. We introduce two coefficients $0 \leq \alpha \leq 1$ and $\beta \geq 0$ such that

$$\begin{cases} \lambda &= (1-\alpha)\beta\frac{m(\mathbf{A_{fit}})}{m(\mathbf{H})}, \\ \mu &= \alpha\beta\frac{m(\mathbf{A_{fit}})}{m(\boldsymbol{\Delta}^C)}. \end{cases} \tag{4.41}$$

The values of α and β define the solutions of Eq. (4.18): β is controlling the tradeoff between fitting and regularization, while α the balance between the diffusion and the Hessian smoothing effect. For $\alpha = 0.5$ and $\beta = 2$, the three components have an equal contribution. A small value of β is privileging the fitting but can compromise the regularity of the surface mostly for models with high thickness variations. Taking $0 \leq \alpha \leq 1$ ensures staying in between the two extrema: the regularization is complete smoothing for $\alpha = 0$ and only a diffusion for $\alpha = 1$.

4.3 Comparison of diffusion schemes

In this section, we present a comparison between three diffusion schemes. Standard diffusion with the diffusion tensor set as the identity matrix, isotropic diffusion as introduced in Sect. 4.1.4 and anisotropic diffusion as introduced in Eq. (4.16). We consider the iterative scheme on u and $\mathbf{C}$, respectively, Eqs. (4.19)-(4.18) for the isotropic and the anisotropic diffusion. The final solutions obtained are shown for comparison. For comparison, we create models with thickness variations introduced in the data along one direction (y direction) in Figs. 4.7a, b, c first model and along two directions in the second and third, respectively, in Figs. 4.7d, e, f and Figs. 4.7g, h, i. In Figs. 4.7d, e, f data points along the rings have the same isovalue, and the three rings have $1, 2, 10$ as values. In Figs. 4.7g, h, i the values on the horizons are: $-1, 0, 1, 2, 3$, respectively, from the bottom to the top.
The three diffusion schemes produce regular and globally smooth solutions, respecting the mean value property and the maximum principle at the boundaries. In the first model, where the thickness variation is only along the y-direction, almost no difference is visually observed between the three different solutions. However, significant differences are observed in the regions with anisotropic high thickness variations: the flat region under the curved horizon in the bell model and between the rings with isovalue 1 and 2 in the rings model. In these regions the standard diffusion fails to produce smooth curves and some undesired oscillations are observed. The isotropic diffusion produces fewer oscillations and the curves are smoother than the standard diffusion. The anisotropic diffusion using the diffusion tensor is visually producing solutions with higher smoothness and respecting the regularity criteria, with a perfect fitting as well of the curved horizon in the middle highlighted in red; see Fig. 4.7i. Decreasing the regularization weight improves the fitting of this horizon in the standard and isotropic case, as shown in Figs. 4.7g, h, respectively; however, it introduces more oscillations.

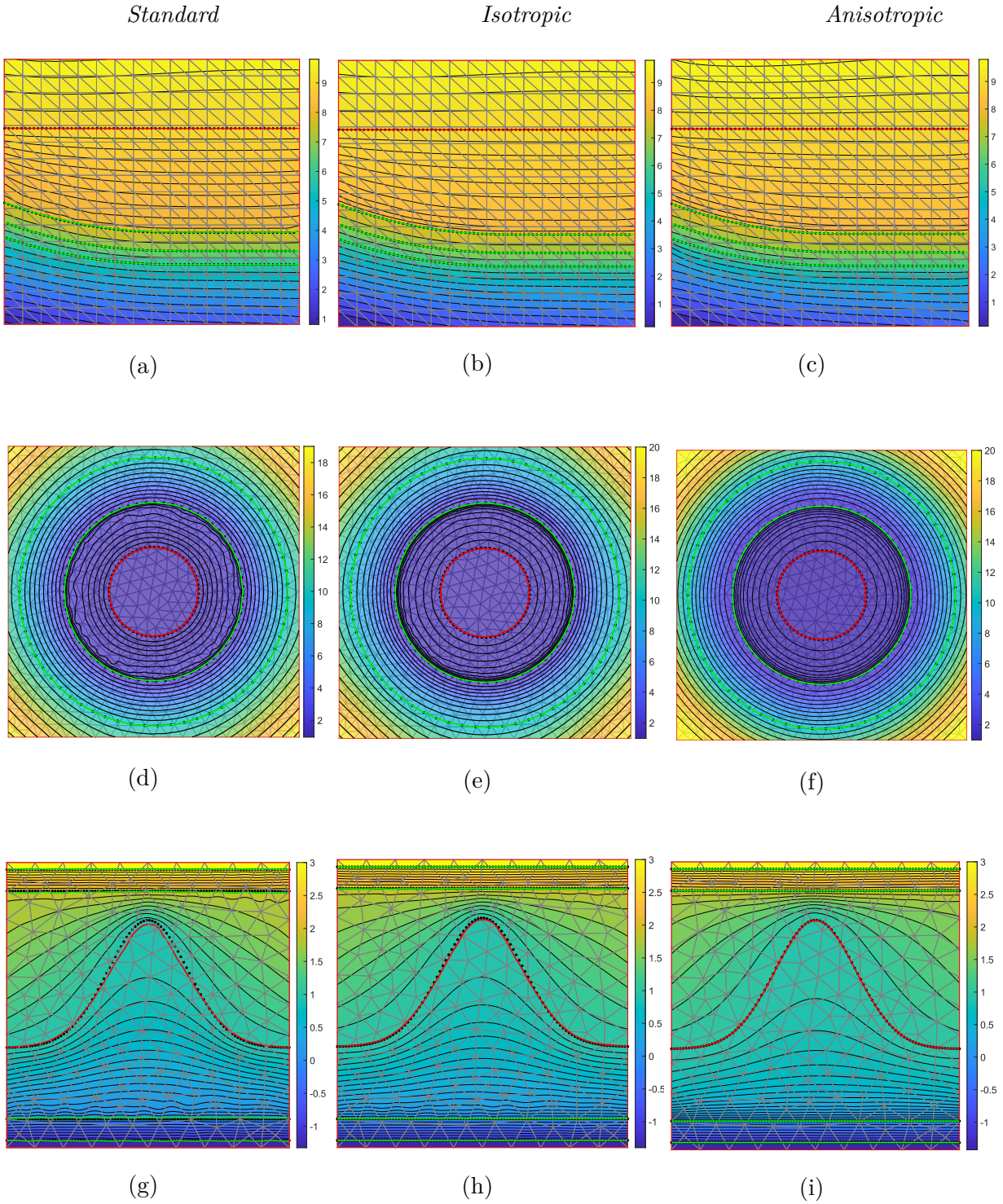

Figure 4.7: Resulting implicit functions using diffusion schemes in a high thickness variations models

Mesh refinement effect

The level of refinement of the mesh highly determines the quality of fitting and the regularity of the solutions of the minimization problem Eq. (4.17). Our method, shown in Fig. 4.8c, produces successfully smooth solution respecting all the regularity constraints and fitting data, on meshes with a coarse level of refinement as shown in the previous comparison section. On the three examples shown in Fig. 4.8, the mesh refinement increases the quality of data fitting. For the standard diffusion (Fig. 4.8a) and isotropic diffusion (Fig. 4.8b), the refinement improved the fitting but some oscillations in the flat region under the top of the curved horizon are introduced. Meanwhile, the anisotropic diffusion provides higher smoothness and regularity and the nonlocal extrema property is holding. The main difference is in the smoothness of the curves in the flat region, where the thickness variation is strong and the implicit function varies weakly. In the case of interest in this region, a high refinement is necessary to maintain the good properties of the solutions of our method. Advanced refinement techniques, such as adaptative mesh, can be an effective way to improve the quality of solutions. Adaptive refinement techniques allow the mesh to be more refined in areas where the high thickness variations are present and in the anisotropy directions. We refer to the model in Fig. 4.8 as bell refined.

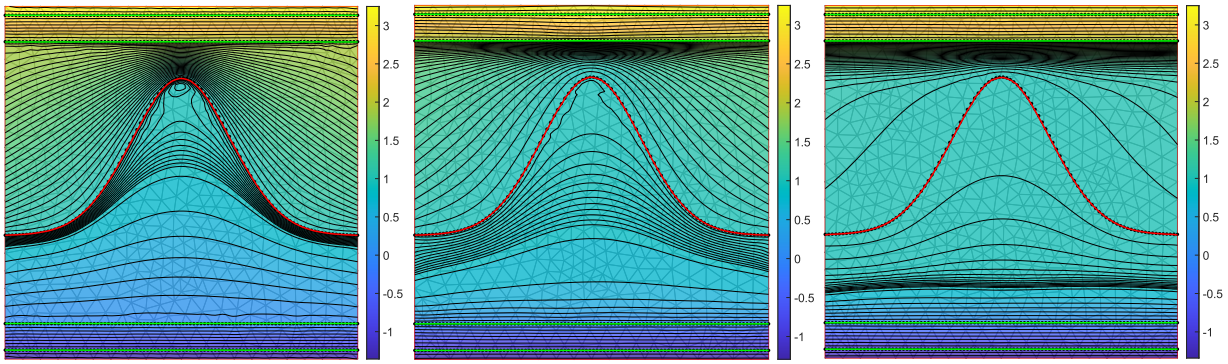

(a) (b) (c)

Figure 4.8: Resulting implicit function on a refined mesh of (a) standard diffusion, (b) isotropic diffusion, (c) anisotropic diffusion

4.4 Diffusion tensor parameterization

The minimization of Eq. (4.18) on tensor $\mathbf{C}$ aims to minimize the diffusion coefficients $(c_i)_{i=1:3}$, while keeping c_1 and c_3 within the range of 0 to 1. However, this approach does not guarantee that the resulting tensor $\mathbf{C}$ will be positive semidefinite. We also considered a proxy problem that replaces the diffusion energy when optimizing with respect to $\mathbf{C}$. We aim here to introduce a parameterization of the diffusion tensor in order minimize the same convex quadratic energy with respect to u and $\mathbf{C}$.

Wang and Solomon (2021) introduced a parameterization of the diffusion tensor using the Cholesky factorization, which guarantees that tensors are p.s.d. We apply the same parametrization in our method to ensure that tensors stay positive semidefinite. We decompose

the diffusion tensor $\mathbf{C}$ using the Cholesky factorization as

$$\begin{bmatrix} c_1 & c_2 \\ c_2 & c_3 \end{bmatrix} = \begin{bmatrix} a & 0 \\ b & c \end{bmatrix} \begin{bmatrix} a & b \\ 0 & c \end{bmatrix} = \begin{bmatrix} a^2 & ab \\ ab & b^2 + c^2 \end{bmatrix} \tag{4.42}$$

We use the parameters (a, b, c) instead of the initial parameters of the tensor $\mathbf{C}$

$$\int_\Omega \begin{bmatrix} u_x & u_y \end{bmatrix} \begin{bmatrix} a & 0 \\ b & c \end{bmatrix} \begin{bmatrix} a & b \\ 0 & c \end{bmatrix} \begin{bmatrix} u_x \\ u_y \end{bmatrix} \tag{4.43}$$

To define the energy functional to optimize with respect to the functions a, b and c, we rewrite the system as

$$\int_\Omega \begin{bmatrix} a & b & c \end{bmatrix} \begin{bmatrix} u_x & 0 \\ u_y & 0 \\ 0 & u_y \end{bmatrix} \begin{bmatrix} u_x & u_y & 0 \\ 0 & 0 & u_y \end{bmatrix} \begin{bmatrix} a \\ b \\ c \end{bmatrix} \tag{4.44}$$

which can expanded as

$$\int_\Omega \begin{bmatrix} a & b & c \end{bmatrix} \begin{bmatrix} u_x^2 & u_x u_y & 0 \\ u_x u_y & u_y^2 & 0 \\ 0 & 0 & u_y^2 \end{bmatrix} \begin{bmatrix} a \\ b \\ c \end{bmatrix} \tag{4.45}$$

We define the functional energy to minimize with respect to $\mathbf{C}$ using the parameters (a, b, c) as

$$\begin{aligned} \int_\Omega \begin{bmatrix} a & b & c \end{bmatrix} \begin{bmatrix} u_x^2 & u_x u_y & 0 \\ u_x u_y & u_y^2 & 0 \\ 0 & 0 & u_y^2 \end{bmatrix} \begin{bmatrix} a \\ b \\ c \end{bmatrix} + \omega_a E_{H^2}(a) + \omega_b E_{H^2}(b) + \omega_c E_{H^2}(c) \\ + \int_\Omega \lambda_a (a-1)^2 + \lambda_c (c-1)^2 + \lambda_b b^2 \; d\Omega \end{aligned} \tag{4.46}$$

Similarly to the Eq. (4.19), the Hessian smoothing terms $\omega_i E_{H^2}(i)$ for $i = a, b, c$ on each of the parameters are added to obtain smooth diffusion coefficients with minimal oscillations. The term $\int_\Omega \lambda_a (a-1)^2 + \lambda_c (c-1)^2 + \lambda_b b^2 \; d\Omega$ penalizes the deviation from the standard diffusion condition, for which the $\mathbf{C} = \mathbf{I}_d$. The previous condition enables to avoid the trivial null tensor as solution for this problem. We associated different weights (ω_i, λ_i) for $i = a, b, c$ to each parameter of the optimization, in order to provide better control of the tradeoff between the penalization on deviation from the standard case and the smoothness of each parameter.

Using the new parameterization explained above, we finally expressed the problem of finding the smoothest solution of the anisotropic diffusion energy as an iterative resolution of a single convex quadratic problem with respect to the implicit function u, and the parameters a, b and c, forming the tensor diffusion $\mathbf{C}$. Fig. 4.9 shows the resulting implicit using the diffusion energy with the parameterization Eq. (4.43). The solution of the Diffusion equation with the new parameterization present higher regularity and smoothness. Based on experimentations, the main observation is that on most of the models we obtained visually similar results to the non parameterized energy, however on some models where the data presents high curvature, they exhibit a different behaviour. For instance the solution in Fig. 4.9, where the distances between the iso-contours are more regular than the solution in Fig. 4.8c. The both solutions are respecting the regularity criteria, but presents two different profiles, which is due to the effect of the new parameterization.

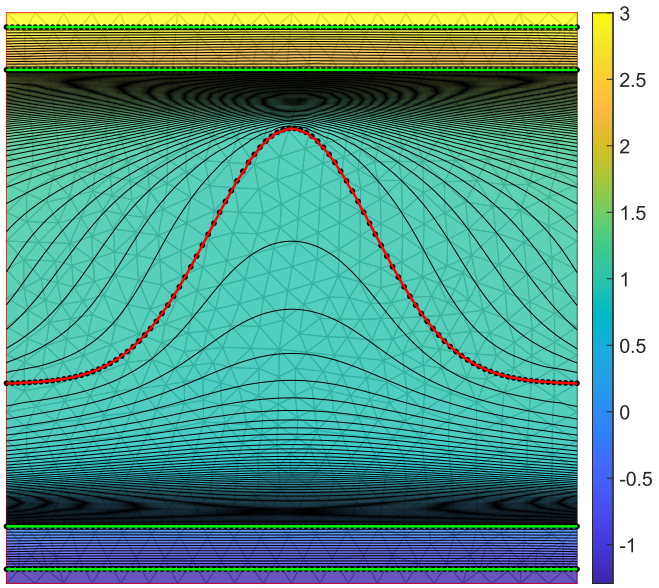

Figure 4.9: Resulting implicit using the diffusion energy with the parameterization Eq. (4.43).

Figs. 4.10c, d, show the resulting implicit functions and the black vectors are the gradients of the implicit function. Figs. 4.10a, e, show the principal directions of the parameterized diffusion tensor, the green vector corresponds to the smallest eigenvalue and the black vector is associated to the largest eigenvalue. Figs. 4.10b, f, exhibit the ratio of the largest eigenvalue by the smallest, which measures ratio of anisotropy and the condition number of the diffusion tensor as well. The main observation is that the principal direction associated to the weakest eigenvalue is aligned with the vector gradient of the implicit function, which means that the diffusion energy highly penalizes the perpendicular part of the gradient and allows variations only along the gradient direction. The diffusion tensor can be physically assimilated to a resistance or a filter, that allows variations mainly along the gradient direction. A correction criteria on the diffusion tensors to ensure that they are aligned with the gradient vector, can be added as criteria to ensure that the tensors are faithfully representing the variations and the anisotropy of the implicit function. The ratio of the largest eigenvalue to the smallest eigenvalue, present a measure of the anisotropy in the model. It is varying over the domain, taking the highest values in the regions of high thickness variations and takes the value 1 in the isotropic regions. It is also the condition number of the diffusion tensor. The implicit function is represented using basis functions, which are constructed on arbitrary meshes. Wang and Solomon (2021) used adapted meshes to solve anisotropic Laplacian since it enhances the quality of the solutions. In our experiments, the meshes used do not encode the alignment with the anisotropy directions. Our solutions will more likely not benefit of a an anisotropy tensor with a high ratio between the smallest and largest eigenvalues. A large condition number indicates that the tensor is ill-conditioned, which can lead to numerical instability. We suggest to bound the condition number of the tensor. Assuming that the optimized tensors encode the right directions of anisotropy, this can be achieved simply by keeping the directions and bounding only the ratio of anisotropy $k(\mathbf{C})$ by a reasonable value.

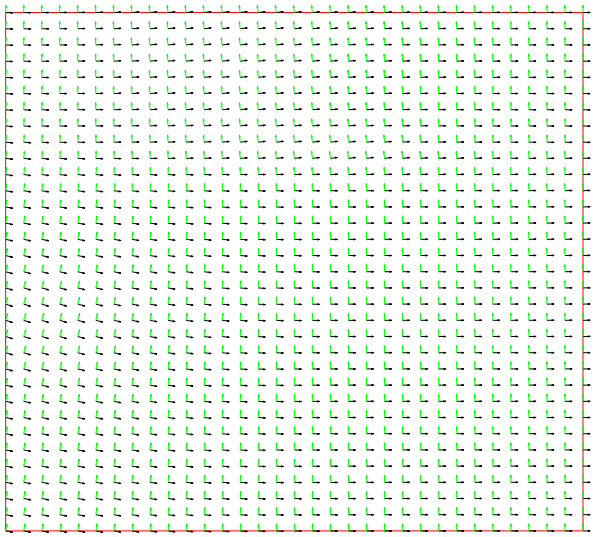

(a)

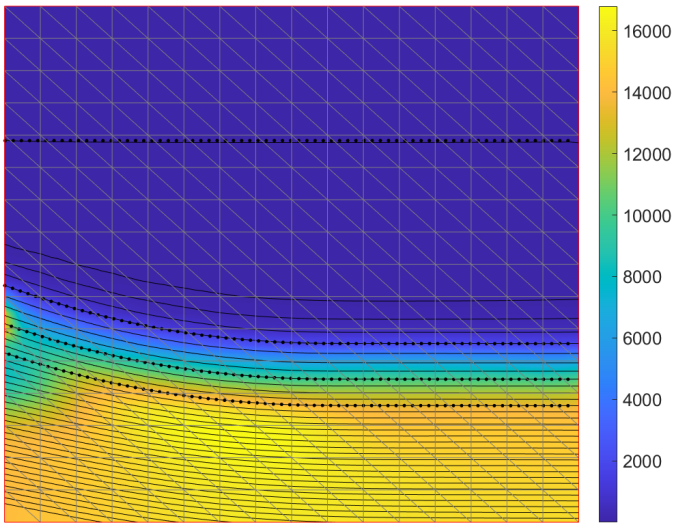

(b)

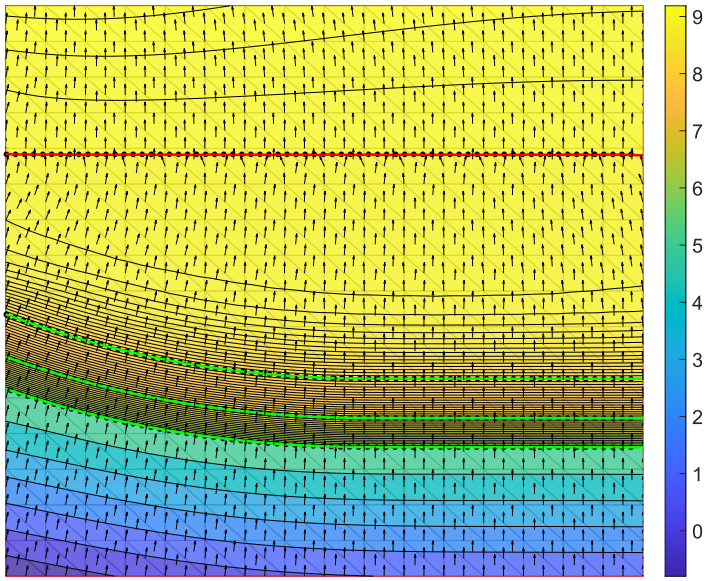

(c)

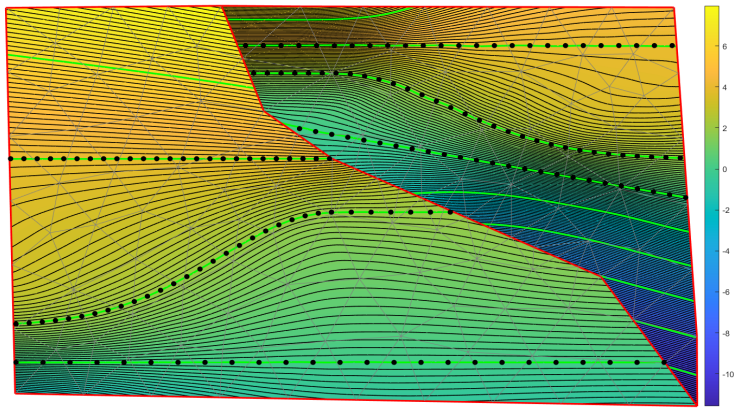

(d)

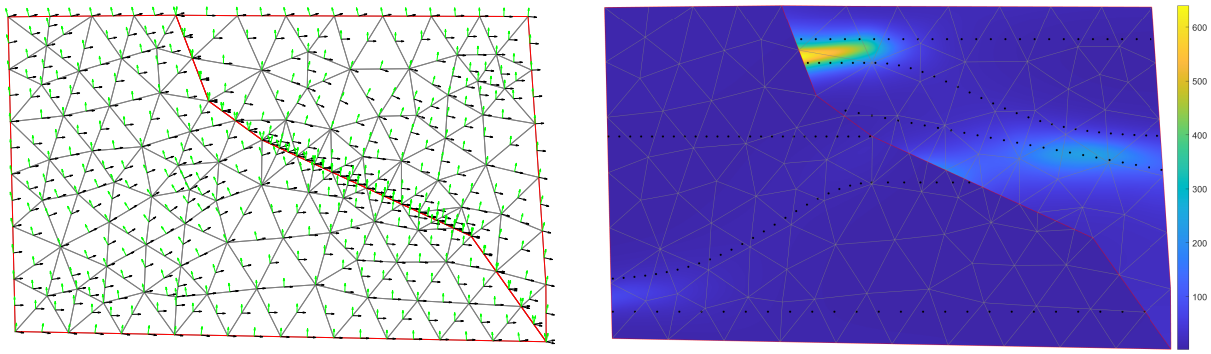

(e) (f)

Figure 4.10: (c)-(d) Resulting implicit functions using the ansiotropic diffusion energy. (a)-(e) Principal directions of diffusion over all the domain, green the direction associated to the smallest eigenvalue and in black the direction of the largest eigenvalue. (b)-(f) Condition number of the diffusion tensor $\kappa(\mathbf{C})$ over all the domain.

4.4.1 Discussion

Our method depends on the initial solution u_0 obtained using the Hessian smoothing energy. We use this solution to compute the initial diffusion tensor. For some models where curvature is important, starting from a very penalized solution u_0 (i.e. with high smoothing weight) can result in a final solution where some regions of the model are flat. In this case a less penalized solution u_0 should be privileged.

Our approach is based on approximating the Neumann boundary condition to prevent the issue of vanishing implicit Neumann boundary condition. We first consider as an approximation the normal on the boundaries component of the gradient of the initial solution u_0. During the iterative process, we use the normal component of the gradient of the previous solution as Neumann boundary condition. In regions where there are no data, the final solution will tend to have the same trend of the initial solution. Irakarama et al. (2022) proposed a free boundary discretization for the Laplacian, by using a specific choice of the space of basis functions and test function. A similar approach can be applied to obtain a free boundary

discretization for the anisotropic Laplacian. Our method as well can be adapted to get rid of the integral on the boundary. We suggest to consider a diffusion tensor, with coefficients represented using constant piecewise function associated to the center of each element. For the implicit function, we could use $P1$ elements as basis functions to represent the implicit function and for test function we choose the Crouzeix-Raviart elements. Starting from the weak form of the anisotropic diffusion equation

$$\int_\Omega div(\mathbf{C}\nabla u)v \; d\Omega = \int_\Omega \mathbf{C}\nabla u \cdot \nabla v \; d\Omega - \int_{\partial\Omega} (\mathbf{C}\nabla u) \cdot \mathbf{n} \; v \; dx \tag{4.47}$$

We can reformulate the boundary term as

$$\int_{\partial\Omega} (\mathbf{C}\nabla u) \cdot \mathbf{n} \; v \; dx = \sum_{t_j \in T_B} (\mathbf{C}\nabla \phi_i) \cdot \mathbf{n}_i \int_{t_j} w(\mathbf{x}) \; dx = 0 \tag{4.48}$$

where t_j is a triangle belonging to the set of triangles on the boundaries, denoted as T_B. While, ϕ_i are the linear P_1 basis functions and $w(x)$ are the Crouzeix-Raviart elements as test functions. In this setting, the gradient of the basis functions is constant as well as the diffusion tensor coefficient and we can take them out of the integral on the boundary. The integral along the boundary on the test functions is remaining, which is vanishing for the Crouzeix-Raviart test functions. It is worth noting, we did not discretize the problem, so we did not verify whether this approach effectively eliminates the integral on the boundary.

4.5 The anisotropic bending energy

In this section, we explore the use of the bending energy of anisotropic thin plates as regularization. Then, we propose a new formulation based on the anisotropic bending energy with an iterative scheme in which the anisotropic rigidity tensor is iteratively adapted to encode the thickness variations and the anisotropy in data.

4.5.1 The bending energy of anisotropic plate

The bending energy (or thin plate energy) measures the global curvature of a thin plate being bended to fit spatially distributed data points. In implicit structural modeling, this energy smooths globally the stratigraphic function and its iso-surfaces. In $2D$, the implicit function interpolating data points $(x, y, u(x, y))$ represents a surface in $3D$ and can be considered as a thin plate to bend to fit data points (Renaudeau 2019). The thin plates theory is a two-dimensional mathematical model that is used to determine the stresses and deformations in thin plates subjected to forces and moments (Love 1888, Reddy 2006). The theory assumes that a mid-surface plane can be used to represent a three-dimensional plate in two-dimensional form. A plate is a structural element defined by two flat parallel surfaces, where loads are applied transversely. The distance between these two surfaces defines the thickness of the plate, which is small compared with other dimensions of the plate. Depending on its material properties, a plate can be either anisotropic, with different properties in different directions, or isotropic, with similar properties in all directions. For anisotropic plates, the resistance to mechanical actions is different for different directions. Thus, the formulations intended for isotropic bodies are irrelevant (Lekhnitskii et al. 1968). In implicit structural modeling the data to interpolate, exhibits strong variations and anisotropy. Therefore, it is necessary to encode the anisotropy in the bending energy to minimize. The theory of bending of anisotropic thin plates Lekhnitskii et al. (1968) is based on the following assumptions (Fig. 4.11)

(i) Straight sections which are normal to the middle surface in the undeformed state remain straight and normal to the deformed middle surface after loading.

(ii) The normal stresses σ_z in cross-sections parallel to the middle plane of the plate are small compared with the stresses in the transverse cross-section, σ_x, σ_y, and σ_{xy}.

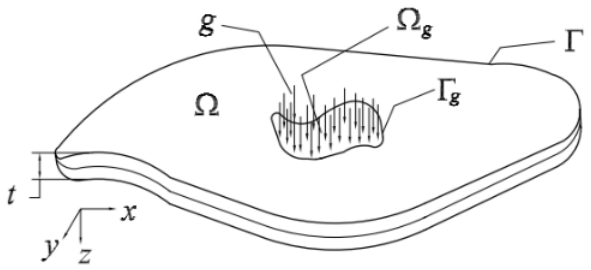

Figure 4.11: Thin plate, figure from Albuquerque et al. (2006) .

Consider a plate following the assumptions defined above. Lekhnitskii et al. (1968) showed

that the lateral mid-surface deflection w satisfies the following differential equation:

$$D_{11}\frac{\partial^4 w}{\partial^4 x} + 4D_{16}\frac{\partial^4 w}{\partial^3 x \partial y} + 2(D_{12}+2D_{66})\frac{\partial^4 w}{\partial^2 x \partial y^2} + 4D_{26}\frac{\partial^4 w}{\partial^x \partial y^3} + D_{22}\frac{\partial^4 w}{\partial^4 y} = 0 \tag{4.49}$$

For an orthotropic plate where the $x-$and $y-$axes are coinciding with the principal axes (Lekhnitskii et al. 1968)

$$\begin{cases} D_{11} = D_1,\ D_{22} = D_2,\ D_{12} + 2D_{66} = D_3 \\ D_{16} = D_{26} = 0 \end{cases} \tag{4.50}$$

then, Eq. (4.49) is reduced as

$$D_1\frac{\partial^4 w}{\partial^4 x} + 2D_3\frac{\partial^4 w}{\partial^2 x \partial y^2} + D_2\frac{\partial^4 w}{\partial^4 y} = 0 \tag{4.51}$$

While for an isotropic plate (Lekhnitskii et al. 1968)

$$D_1 = D_2 = D_3 = \frac{Eh^3}{12(1-v^2)} \tag{4.52}$$

and Eq. (4.49) becomes simply

$$D\Delta^2 u = 0 \tag{4.53}$$

The equivalent expression for the potential energy of bending for the anisotropic plate is (Lekhnitskii et al. 1968)

$$V = \int_\Omega [D_{11}(\frac{\partial^2 w}{\partial^2 x})^2 + 2D_{12}\frac{\partial^2 w}{\partial^2 x} + D_{22}(\frac{\partial^2 w}{\partial^2 y})^2 + 4D_{66}(\frac{\partial^2 w}{\partial x \partial^y})^2 + 4(D_{16}\frac{\partial^2 w}{\partial^2 x} + D_{26}\frac{\partial^2 w}{\partial^2 y})\frac{\partial^2 w}{\partial x \partial y}]\partial x \partial y \tag{4.54}$$

which can be rewritten as

$$\int_\Omega \begin{bmatrix} w_{xx} & w_{xy} & w_{yy} \end{bmatrix} \begin{bmatrix} D_{11} & 2D_{16} & D_{12} \\ 2D_{16} & 4D_{66} & 2D_{26} \\ D_{12} & 2D_{26} & D_{22} \end{bmatrix} \begin{bmatrix} w_{xx} \\ w_{xy} \\ w_{yy} \end{bmatrix} d\Omega \tag{4.55}$$

In the orthotropic case it becomes

$$\int_\Omega \begin{bmatrix} w_{xx} & w_{xy} & w_{yy} \end{bmatrix} \begin{bmatrix} D_1 & 0 & 0 \\ 0 & 2D_3 & 0 \\ 0 & 0 & D_2 \end{bmatrix} \begin{bmatrix} w_{xx} \\ w_{xy} \\ w_{yy} \end{bmatrix} d\Omega \tag{4.56}$$

While in the isotropic case it is simply

$$\int_\Omega \begin{bmatrix} w_{xx} & w_{xy} & w_{yy} \end{bmatrix} \begin{bmatrix} D & 0 & 0 \\ 0 & 2D & 0 \\ 0 & 0 & D \end{bmatrix} \begin{bmatrix} w_{xx} \\ w_{xy} \\ w_{yy} \end{bmatrix} d\Omega \tag{4.57}$$

The deflection w is only along the z direction and is simply the implicit function u that describes the surface considered as a bended thin plate. The thin plate is bent by forces acting at points so that the deflections at these points are the z_p values of the data points to

be fit. On can imagine that the fitting energy corresponds to the deformation energy applied to the plate. In the ideal scenario where all data points lie on a plane, there is no need to bend the plate. The thin plate in its initial state is flat (Fig. 4.12a). However, when the data points to fit define a surface of strong curvatures, the plate must undergo a bending process (Fig. 4.12b). In this context, the promising optimization parameter appears to be the rigidity of the plate. Adjusting the rigidity of the plate means modifying its resistance to the bending. Subsequently, it affects the response of the plate to bending and ultimately the resulting shape of the plate. Thus, the rigidity of the plate must adapted to the data points. For regions where the data presents high curvature, the plate must be softer to allow maximal deflection. Conversely, the regions with weak curvature corresponds to regions with weak deflections, which means the rigidity must be high.

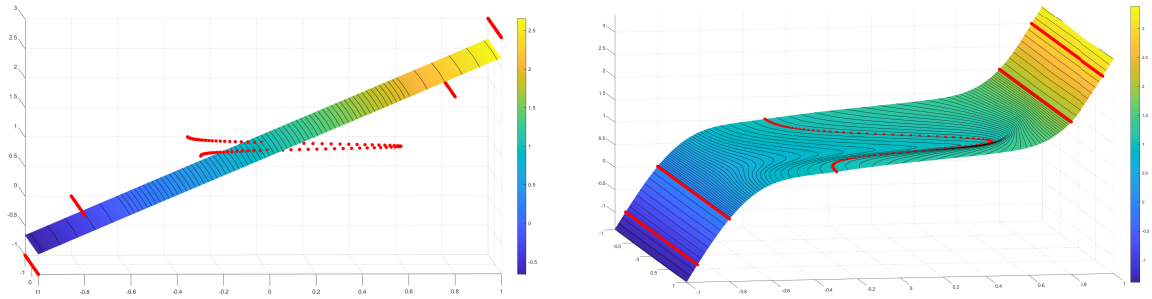

(a) (b)

Figure 4.12: (a) A thin plate is initially flat . (b) A thin plate is bended subject to deformations.

In the following, we will simplify our analysis by neglecting the physical aspect of certain factors associated to the rigidities D_{ij} of the anisotropic plate. For example, in the Eq. (4.54), that describes the anisotropic case, there are factors of 2 and 4 associated to D_{16} and D_{66}, respectively. We will neglect these factors and consider the entries of the rigidity tensor $\mathbf{T}$ as functions to be determined. Therefore, Eq. (4.54) can be reformulated and simplified as

$$\int_{\Omega} \begin{bmatrix} u_{xx} & u_{yy} & u_{xy} \end{bmatrix} \mathbf{T} \begin{bmatrix} u_{xx} \\ u_{yy} \\ u_{xy} \end{bmatrix} \, d\Omega \tag{4.58}$$

We consider the generalized anisotropic bending energy defined by the symmetric rigidity tensor field $\mathbf{T}(\mathbf{x}) : \Omega \to \mathbb{R}^{3\times 3}$, for $d = 2$, is the dimension of Ω. We use $T_{ij}(\mathbf{x})$, $i, j = 1 : 3$, scalar functions to denote the rigidity, respectively, in the directions ij of deformations. The tensor representation of the rigidity term generalizes the bending energy of an isotropic plate for $\mathbf{T} = \begin{bmatrix} 1 & 0 & 0 \\ 0 & 1 & 0 \\ 0 & 0 & 2 \end{bmatrix}$ and the isotropic nonhomogeneous plate for $\mathbf{T} = d(\mathbf{x}) \begin{bmatrix} 1 & 0 & 0 \\ 0 & 1 & 0 \\ 0 & 0 & 2 \end{bmatrix}$, with $d(\mathbf{x})$ a scalar-value rigidity function. In the formalism of Lekhnitskii et al. (1968), the materials are supposed homogeneous and the rigidity coefficients are constant, while in our formulation Eq. (4.58), the rigidity functions are scalar functions varying over the domain. The linear elasticity hypothesis is supposed and the formalism of Lekhnitskii et al. (1968) is holding.

4.5.2 Generalized Hooke's Law and Voigt notation

In the formalism of Lekhnitskii et al. (1968), the material model is supposed elastic, which means that a linear relation between strains and stresses is assumed. In this context, the generalized Hooke's law relates strains $\mathbf{S}$ and stress $\mathbf{E}$ by the elasticity tensor $\mathbf{C}$ as (Kiendl 2011)

$$\mathbf{S} = \mathbf{C} : \mathbf{E} \tag{4.59}$$

$$S_{ij} = C_{ijkl} E_{kl} \tag{4.60}$$

where $\mathbf{S}$ and $\mathbf{E}$ are second order tensors. While $\mathbf{C}$ is a linear map from $\mathbb{R}^{d\times d} \rightarrow \mathbb{R}^{d\times d}$. Thus, it is a tensor of 4^{th} order and contains d^4 coefficients, which means 81 in $3D$ and 16 in $2D$. Using the symmetry properties of the stress and strain tensor and the properties of the material, the number of independent coefficients can be tremendously reduced. As the stress and strain tensors are symmetric $\sigma_{ij} = \sigma_{ji}$ and $\varepsilon_{kl} = \varepsilon_{lk}$, there are only 6 unknown stress and strain components rather than 9. The symmetry of stress tensor induces that $C_{ijkl} = C_{jikl}$. Similarly the symmetry of the strain tensor: $C_{ijkl} = C_{jilk}$. Thus the number of coefficients can be reduced to 36 in $3D$. In addition to the elasticity assumption this number reduces to 21 and to 6 in $2D$. In $2D$, we can develop the stress tensor $\mathbf{S}$ and the strain tensor $\mathbf{E}$ as:

$$\mathbf{S} = \begin{bmatrix} \sigma_{xx} & \sigma_{xy} \\ \sigma_{xy} & \sigma_{yy} \end{bmatrix}, \quad \mathbf{E} = \begin{bmatrix} \varepsilon_{xx} & \varepsilon_{xy} \\ \varepsilon_{xy} & \varepsilon_{yy} \end{bmatrix} \tag{4.61}$$

The strain tensor describes the deflection or deformation of a material body. It characterizes how the shape of the material changes due to applied forces or displacements. The strain tensor can be obtained from the displacements field of the material, which represents how each point in the material has moved from its original position. Under the assumptions of the formalism of Lekhnitskii et al. (1968) introduced beforehand, a simple relationship between deflection of the center plane $w(x, y)$ and the displacements $d_1(x, y, z)$ and $d_2(x, y, z)$:

$$d_1 = -z\frac{\partial w}{\partial x} \tag{4.62}$$

$$d_2 = -z\frac{\partial w}{\partial y} \tag{4.63}$$

Then, strains can be expressed as:

$$\varepsilon_{xx} = -z\frac{\partial^2 w}{\partial x^2} \tag{4.64}$$

$$\varepsilon_{yy} = -z\frac{\partial^2 w}{\partial y^2} \tag{4.65}$$

$$\varepsilon_{xy} = -z\frac{\partial^2 w}{\partial x \partial y} \tag{4.66}$$

The strain ε_{xy} in the formalism of Lekhnitskii et al. (1968) is associated with a factor 2. We choose to include it in the rigidity associated to this strain, in order to show the link with the Hessian of the deflection.

$$\mathbf{E} = -z \begin{bmatrix} w_{xx} & w_{xy} \\ w_{xy} & w_{yy} \end{bmatrix} \tag{4.67}$$

the coordinates z will be eliminated when integrating along the thickness of the plate. The strain tensor is related to the second derivatives of the deflection w and in this case is simply the Hessian matrix of w. Thus, the potential energy due to bending can be expressed as

$$E_P = \frac{1}{2}\int_\Omega \mathbf{E} : \mathbf{C} : \mathbf{E} \tag{4.68}$$

$$= \frac{1}{2}\int_z z^2 dz \int_{x,y} \mathbf{E} : \mathbf{C} : \mathbf{E} \tag{4.69}$$

$$= \frac{1}{2}\frac{t^3}{12}\int_{x,y} \mathbf{H}_w : \mathbf{C} : \mathbf{H}_w \tag{4.70}$$

We derived the strain energy using the constitutive law that links stress strain and integrating over the domain. The integral of the thickness multiplied by the elasticity constants are flexual rigidities of the material and the deflection is simply the implicit function. Then, we can rewrite as

$$E_p = \frac{1}{2}\int_\Omega \mathbf{H}_u : \mathbf{T}^h : \mathbf{H}_u \;\; d\Omega \tag{4.71}$$

where $\mathbf{H}_u$ is the Hessian of u and $\mathbf{T}^h$ is a fourth order tensor. We introduce the Voigt notation, to reduce the dimensions of the quadratic form Eq. (4.70). We suppose that $\mathbf{T}^h$ is the representation of $\mathbf{T}$ as fourth order tensor, and we can reduce the Hessian second order tensor to a vector as

$$\begin{bmatrix} u_{xx} \\ u_{yy} \\ u_{xy} \end{bmatrix} \tag{4.72}$$

This leads to the formulation of the anisotropic bending energy introduced in Eq. (4.58). In the following, we choose to use the form of the anisotropic bending energy in Eq. (4.58), due to the reduced number of indices. This choice simplifies the discretization. Alternatively, the form in Eq. (4.71) can be used. Palmer et al. (2021) introduced an operator that generalizes the fourth-order Bilaplacian operator to support anisotropic behavior. The anisotropy is parameterized by a symmetric frame field, that allows the control of local directions of variations. They defined the following variational problem

$$\Sigma_{T,\varepsilon}(u) = \frac{1}{2}\int_\Omega \nabla^2 u : \mathbf{T}^\varepsilon : \nabla^2 u \;\; d\Omega \tag{4.73}$$

$$\mathbf{T}^\varepsilon := \|\mathbf{T}_p\|\mathbf{I} - (1-\varepsilon)\mathbf{T}_p \tag{4.74}$$

where $\mathbf{I}$ denotes the fourth order identity tensor whose characteristics property is that $\mathbf{I} : S_p = S_p$ for any symmetric second order tensor S_p, $\varepsilon \in [0,1]$ to ensure the ellipticity of the formulation. This functional measures the alignment to the frame field $\mathbf{T}^\varepsilon$. It is an optimization problem on the Hessian of a scalar field, for which the primary directions of curvature occur along the component of the frame field $\mathbf{T}_p$. It is worth noting, that we kept the same notations as Palmer et al. (2021). To facilitate comparisons, we just add an underscored letter p to their notations.

4.5.3 Rigidity tensor parameterization

The anisotropic bending energy, through the rigidity tensor $\mathbf{T}$, can be used to encode the anisotropy present in data. Physically, one can imagine that the data points to fit, apply a

deformation on the thin plate, and that the surface to construct is a thin plate. The shape of the surface to construct is based on the regularization energy considered. If the classical isotropic bending energy is considered, the assumption made is that our material is isotropic, and perhaps the state with oscillations is minimizing the bending energy. Our problem, physically, is the problem of finding a thin plate with a specific anisotropic rigidity, that leads to a regular surface, when it is deformed under the stress applied by the data points. The rigidity is the resistance of a thin plate against bending deformation. Changing the rigidity tensor is changing the resistance of the material, therefore changing the material response to the stress applied.

The anisotropic bending energy defined with the anisotropic rigidity tensor $\mathbf{T}$ provides an extra degree of freedom for the modeling problem. Thus, the formulation of our problem Eq. (4.58) is nonlinear regarding the two variables: the implicit function u and the rigidity tensor $\mathbf{T}$. To solve this nonlinear minimization problem, we propose an iterative scheme that involves the two problem unknowns u and $\mathbf{T}$. In our scheme we solve first for u, then for $\mathbf{T}$ and we repeat while the difference between the fitting energies of consecutive iterations is less than a chosen threshold ε. The bending energy is quadratic in u and is convex if the tensor $\mathbf{T}$ is positive semi-definite. In this case, the solution is unique. However, the diffusion energy with respect to the coefficients of the tensor $\mathbf{T}$ is linear and can be either positive or negative. Thus, minimizing this energy with respect to $\mathbf{T}$ can be challenging as the solution is not well-defined. The anisotropic bending energy Eq. (4.58), is well defined when the tensor $\mathbf{T}$ is psd.

$$\mathbf{T} = \begin{bmatrix} T_{11} & T_{12} & T_{13} \\ T_{12} & T_{22} & T_{23} \\ T_{13} & T_{23} & T_{33} \end{bmatrix} \geq 0 \tag{4.75}$$

Using a Cholesky factorization we can rewrite the tensor $\mathbf{T}$ as

$$\begin{bmatrix} a & 0 & 0 \\ b & c & 0 \\ d & e & f \end{bmatrix} \begin{bmatrix} a & b & d \\ 0 & c & e \\ 0 & 0 & f \end{bmatrix} = \begin{bmatrix} a^2 & ab & ad \\ ab & b^2+c^2 & bd+ce \\ ad & bd+ce & d^2+e^2+f^2 \end{bmatrix} \geq 0 \tag{4.76}$$

To define the energy functional to optimize with respect to the functions a, b and c, d, e, f, we rewrite the system as

$$\begin{bmatrix} a & b & c & d & e & f \end{bmatrix} \begin{bmatrix} u_{xx}^2 & u_{xx}u_{xy} & 0 & u_{xx}u_{yy} & 0 & 0 \\ u_{xx}u_{xy} & u_{xy}^2 & 0 & u_{yy}u_{xy} & 0 & 0 \\ 0 & 0 & u_{xy}^2 & 0 & u_{xy}u_{yy} & 0 \\ u_{xx}u_{yy} & u_{yy}u_{xy} & 0 & u_{yy}^2 & 0 & 0 \\ 0 & 0 & u_{xy}u_{yy} & 0 & u_{yy}^2 & 0 \\ 0 & 0 & 0 & 0 & 0 & u_{yy}^2 \end{bmatrix} \begin{bmatrix} a \\ b \\ c \\ d \\ e \\ f \end{bmatrix} \tag{4.77}$$

We use the Hessian energy for each rigidity scalar functions, and the sum of the constraints is denoted by $E_{H^2}(\mathbf{T})$. The aim is to obtain smooth functions, in order to construct rigidity coefficients that are smoothly varying over the domain

$$E_{H^2}(\mathbf{T}) = \omega_a E_{H^2}(a) + \omega_b E_{H^2}(b) + \omega_c E_{H^2}(c) + \omega_d E_{H^2}(d) + \omega_e E_{H^2}(e) + \omega_f E_{H^2}(f) \tag{4.78}$$

A penalization over the function is applied, by minimizing the distance to the parameters, that corresponds to the isotropic case. The sum of the constraints is denoted by $I_{iso}(\mathbf{T})$.

$$I_{iso}(\mathbf{T}) = \int_\Omega \lambda_a (a-1)^2 + \lambda_c (c-\sqrt{2})^2 + \lambda_f (f-1)^2 + \lambda_b b^2 + \lambda_d d^2 + \lambda_e e^2 \; d\Omega \tag{4.79}$$

Natural boundary conditions

Taking the first variation of $\Sigma_{T,\varepsilon}$ with respect to u gives the following Euler-Lagrange equations:

$$\int_\Omega \sum_{i,j,k,l} \mathbf{T}^\varepsilon_{ijkl}(\partial_i\partial_j u)(\partial_k\partial_l v) = 0 \tag{4.80}$$

for any smooth test function $v \in H^2(\Omega)$. Integrating by parts yields:

$$\int_\Omega \partial_k(\mathbf{T}^\varepsilon_{ijkl}(\partial_i\partial_j u)\partial_l v \; d\Omega - \int_{\partial\Omega} \mathbf{T}^\varepsilon_{ijkl}(\partial_i\partial_j u)\partial_l v n_k \; d\Omega = 0 \tag{4.81}$$

$$\int_\Omega \partial_k\partial_l(\mathbf{T}^\varepsilon_{ijkl}(\partial_i\partial_j u)v \; d\Omega - \int_{\partial\Omega} [\mathbf{T}^\varepsilon_{ijkl}(\partial_i\partial_j u)\partial_l v n_k - \partial_k(\mathbf{T}^\varepsilon_{ijkl}(\partial_i\partial_j u))n_l v] = 0 \tag{4.82}$$

Eliminating the test functions v, we obtain the following PDE with natural boundary conditions:

$$\partial_k\partial_l(\mathbf{T}^\varepsilon_{ijkl}(\partial_i\partial_j u) = 0 \quad in \quad \Omega \tag{4.83}$$

$$\mathbf{T}^\varepsilon_{ijkl}(\partial_i\partial_j u)\partial_l v n_k = 0 \quad on \quad \partial\Omega \tag{4.84}$$

$$\partial_k(\mathbf{T}^\varepsilon_{ijkl}(\partial_i\partial_j u))n_l v = 0 \quad on \quad \partial\Omega \tag{4.85}$$

Solutions of the anisotropic thin plate energy minimization are solutions of a fourth order anisotropic operator in the interior and satisfy a specific natural boundary conditions that involves normal second derivatives on the boundaries to vanish. This encourages the function to be as linear as possible on the boundaries. These solutions presents higher smoothness and faithfully able to represent the anisotropic behaviour that the data exhibit, which is encoded in the anisotropic rigidity tensor. Furthermore, Palmer et al. (2021) showed that if the tensor $\mathbf{T}$ is boundary aligned, the reduced second-order boundary conditions is

$$(\nabla^2 u)\mathbf{n} = 0 \quad on \quad \partial\Omega \tag{4.86}$$

Intuitively, when $\mathbf{T}$ is boundary-aligned, the natural boundary condition says that u is linear along the normal direction at the boundary, similarly to the natural boundary conditions studied by Stein et al. (2018).

We propose to analyse the the anisotropic thin plate energy in $1D$, and derive its natural boundary conditions. The aim is to illustrate its behaviour when fitting one dimensional data points and the effect of the natural boundary conditions. The anisotropic thin plate energy in $1D$ is simply:

$$\min_{u,t} \int_\Omega (t(\mathbf{x})u''(\mathbf{x}))^2 \; d\Omega \tag{4.87}$$

which is equivalent to solving the following partial differential equation

$$(tu'')'' = 0 \tag{4.88}$$

with the following natural boundary conditions on the two extremities of the domain:

$$tu''(e) = (tu'')'(e) = 0 \tag{4.89}$$

It can be deduced from the weak form of Eq. (4.88). For any test function v

$$\int_{\Omega}(tu'')''(\mathbf{x})vdx = 0 \tag{4.90}$$

$$\int_{\Omega}(tu'')'(\mathbf{x})v'dx - [(tu'')'(\mathbf{x})v(\mathbf{x})] = 0 \tag{4.91}$$

$$\int_{\Omega} tu''(\mathbf{x})v''dx - [tu''v'(\mathbf{x})] + [(tu'')'(\mathbf{x})v(\mathbf{x})] = 0 \tag{4.92}$$

Fig. 4.13 shows one dimensional interpolation using the thin plate energy. Fig. 4.13a, is obtained using the standard isotropic form of the thin plate energy, while Fig. 4.13b is obtained using the anisotropic thin plate energy Eq. (4.87). The solution in Fig. 4.13a interpolate well the data points, but violates the mean value property and the maximum at the boundaries. It exhibits strong oscillations, even though measures minimal Hessian energy which is aligned with the minimization constraints. This example, confirms the idea that regular solutions when interpolating data presenting high thickness variations, are unlikely to be obtained through the use of smoothing energies, for which the isotropy assumption is made. Therefore, it justifies the essential need to alternative smoothness measures to better capture the underlying variations in the data, leading to more accurate and effective regularization results. The resulting functions (Fig. 4.13b) tends to be linear between the data points to fit, however present strong curvatures where the data points change trend. Far from the data points and near the boundaries, the function is linear, which means that the second derivative is null. The behaviour that exhibits the $1D$ solution far from the boundaries, is aligned with the natural boundary condition of Eq. (4.87), that implicitly implies that second order derivative is null.

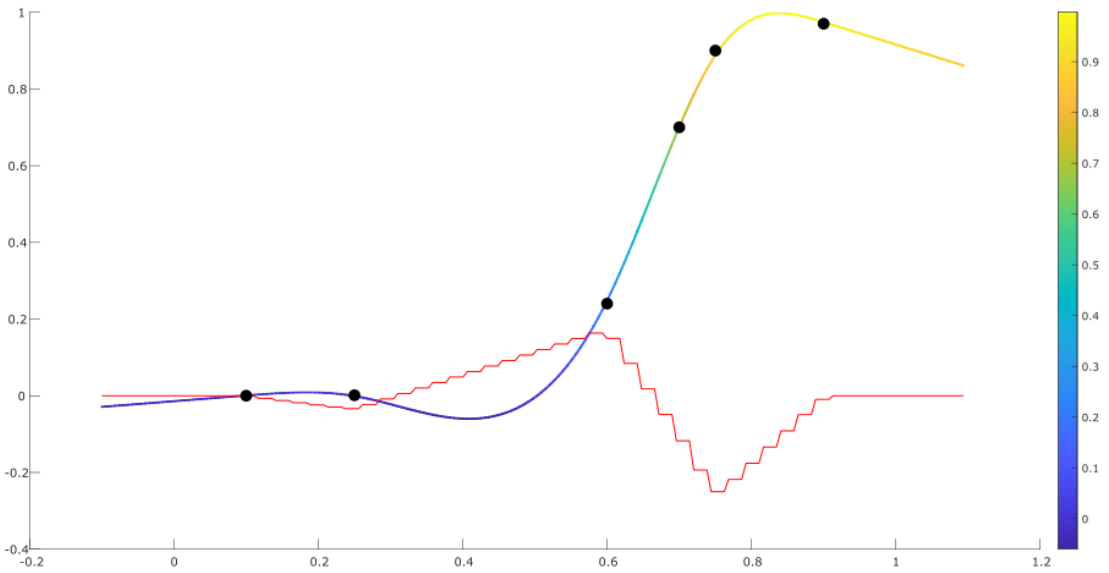

(a) $E_{H^2} = 6.46$

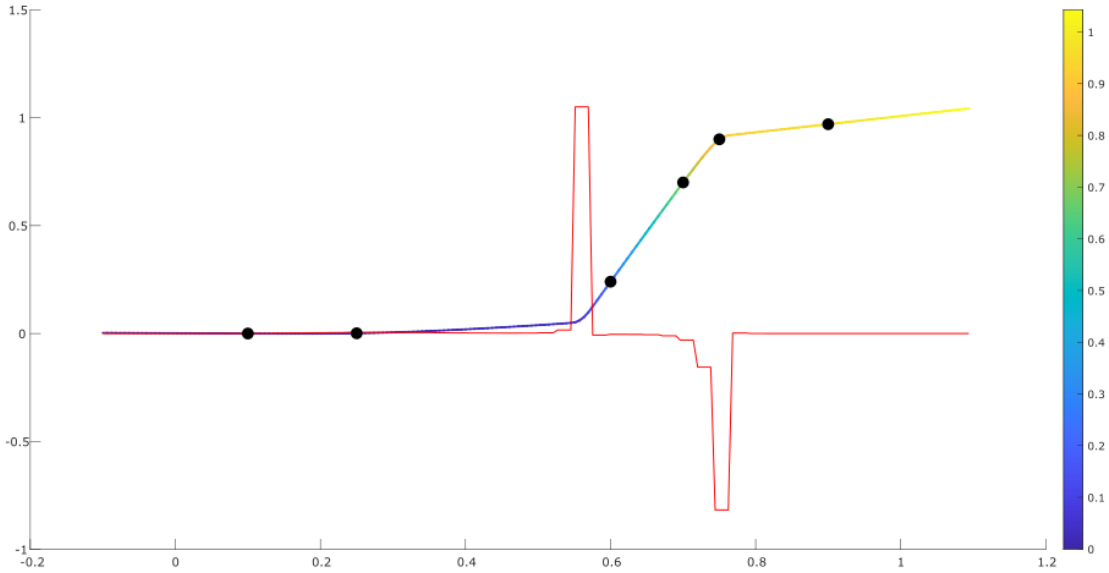

(b) $E_{H^2} = 31.20$

Figure 4.13: One dimensional interpolation using PS-splines in $1D$ with the following regularizations (a) Isotropic homogeneous thin plate energy. (b) Anisotropic non homogeneous thin plate energy. Red lines are second derivatives. E_{H^2} is measuring the Hessian energy of the solutions.

4.5.4 Discretization of the anisotropic bending energy

In this section, we discretize the energies used in the iterative scheme Eqs. (4.58)-(4.77). Our formulation is generic (i.e. it works for any choice of basis functions $(B_i)_{i=1:N_s}$ of F). The implicit function u is defined as $\forall \mathbf{x} \in \Omega,\ u(\mathbf{x}) = \sum_{i=1}^{N_s} B_i(\mathbf{x}) u_i = \mathbf{B}(\mathbf{x})\mathbf{U}$, where $\mathbf{B}(\mathbf{x}) = (B_1(\mathbf{x}), ..., B_{N_s}(\mathbf{x}))$ is a basis of F and $\mathbf{U} = (u_1, ..., u_{N_s})^T$ is the vector of unknowns. We first express the Bending energy using the basis functions as

$$E_B(u, \mathbf{T}) = \frac{1}{2} \int_\Omega \mathbf{U}^T \mathbf{V_B}(\mathbf{x})^T \mathbf{T}(\mathbf{x}) \mathbf{V_B}(\mathbf{x}) \mathbf{U} \ \ d\Omega = \mathbf{U}^T \mathbf{H}^A \mathbf{U} \tag{4.93}$$

We define $\mathbf{V_B}(\mathbf{x})$ based on the Voigt notation as a flat vector containing the second derivatives of the basis functions as

$$\mathbf{V_B}(\mathbf{x}) = \begin{bmatrix} \mathbf{B}_{xx}(\mathbf{x}) \\ \mathbf{B}_{yy}(\mathbf{x}) \\ \mathbf{B}_{xy}(\mathbf{x}) \end{bmatrix} \tag{4.94}$$

where $\mathbf{H}^A \in \mathbb{R}^{(N_s \times N_s)}$ is the resulting matrix. To discretize the anisotropy symmetric rigidity tensor $\mathbf{T} = \begin{bmatrix} T_{11} & T_{12} & T_{13} \\ T_{12} & T_{22} & T_{23} \\ T_{13} & T_{23} & T_{33} \end{bmatrix}$, we consider the auxiliary parameters of the optimization problem Eq. (4.77). Using the Cholesky factorization

$$\begin{bmatrix} a & 0 & 0 \\ b & c & 0 \\ d & e & f \end{bmatrix} \begin{bmatrix} a & b & d \\ 0 & c & e \\ 0 & 0 & f \end{bmatrix} = \begin{bmatrix} a^2 & ab & ad \\ ab & b^2 + c^2 & bd + ce \\ ad & bd + ce & d^2 + e^2 + f^2 \end{bmatrix} \geq 0 \tag{4.95}$$

Each parameter a, b, c, d, e, f is represented using the basis functions $(B_i(\mathbf{x}))_{i=1}^{N_s}$ such that

$$\forall \mathbf{x} \in \Omega \ \ a(\mathbf{x}) = \mathbf{B}(\mathbf{x})\mathbf{A}, b(\mathbf{x}) = \mathbf{B}(\mathbf{x})\mathbf{B}, c(\mathbf{x}) = \mathbf{B}(\mathbf{x})\mathbf{C} \tag{4.96}$$

$$d(\mathbf{x}) = \mathbf{B}(\mathbf{x})\mathbf{D}, e(\mathbf{x}) = \mathbf{B}(\mathbf{x})\mathbf{E}, f(\mathbf{x}) = \mathbf{B}(\mathbf{x})\mathbf{F} \tag{4.97}$$

Then, the Eq. (4.77) can be expressed

$$\begin{bmatrix} u_{xx} & u_{yy} & u_{xy} \end{bmatrix} \begin{bmatrix} a & 0 & 0 \\ b & c & 0 \\ d & e & f \end{bmatrix} \begin{bmatrix} a & b & d \\ 0 & c & e \\ 0 & 0 & f \end{bmatrix} \begin{bmatrix} u_{xx} \\ u_{yy} \\ u_{xy} \end{bmatrix} \tag{4.98}$$

$$\begin{bmatrix} a & b & d \\ 0 & c & e \\ 0 & 0 & f \end{bmatrix} \begin{bmatrix} u_{xx} \\ u_{yy} \\ u_{xy} \end{bmatrix} = \begin{bmatrix} u_{xx} & u_{yy} & 0 & u_{xy} & 0 & 0 \\ 0 & 0 & u_{xx} & 0 & u_{yy} & 0 \\ 0 & 0 & 0 & 0 & 0 & u_{xy} \end{bmatrix} \begin{bmatrix} a \\ b \\ c \\ d \\ e \\ f \end{bmatrix} \tag{4.99}$$

$$\left[\begin{bmatrix} u_{xx} & u_{yy} & 0 & u_{xy} & 0 & 0 \\ 0 & 0 & u_{xx} & 0 & u_{yy} & 0 \\ 0 & 0 & 0 & 0 & 0 & u_{xy} \end{bmatrix} \otimes \mathbf{B}(\mathbf{x}) \right] \mathbf{\Theta} \tag{4.100}$$

We use the flat vector $\mathbf{\Theta} = \begin{bmatrix} \mathbf{A} \\ \mathbf{B} \\ \mathbf{C} \\ \mathbf{D} \\ \mathbf{E} \\ \mathbf{F} \end{bmatrix}$ to store the degrees of freedom of all the auxiliary optimization parameters. Thus, the Eq. (4.77) can be expressed as

$$\int_\Omega \mathbf{\Theta}^T \left[\begin{bmatrix} u_{xx}^2 & u_{xx}u_{yy} & 0 & u_{xx}u_{xy} & 0 & 0 \\ u_{xx}u_{yy} & u_{yy}^2 & 0 & u_{xy}u_{yy} & 0 & 0 \\ 0 & 0 & u_{xx}^2 & 0 & u_{xx}u_{yy} & 0 \\ u_{xx}u_{xy} & u_{xy}u_{yy} & 0 & u_{xy}^2 & 0 & 0 \\ 0 & 0 & u_{xx}u_{yy} & 0 & u_{yy}^2 & 0 \\ 0 & 0 & 0 & 0 & 0 & u_{xy}^2 \end{bmatrix} \otimes \left[\mathbf{B}(\mathbf{x})^T \mathbf{B}(\mathbf{x}) \right] \right] \mathbf{\Theta} \ d\Omega \quad (4.101)$$

We consider that the weights w_i are equal to one in Eq. (4.78). Then, the Hessian energy to smooth the optimization parameters is simply

$$E_{H^2}(\mathbf{T}) = \int_\Omega \mathbf{\Theta}^T (\mathbf{I}_6 \otimes \mathbf{H}) \mathbf{\Theta} \quad d\Omega, \quad (4.102)$$

We also consider that the weights λ_i are equal to one in Eq. (4.79). Thus, the distance from the isotropic homogeneous state can be expressed as

$$I_{iso}(\mathbf{T}) = \int_\Omega (a-1)^2 + (c-1)^2 + (f-\sqrt{2})^2 + b^2 + d^2 + e^2 \ d\Omega \quad (4.103)$$

Then, we minimize it by solving the following linear system

$$\left[\mathbf{I}_6 \otimes \mathbf{M} \right] \mathbf{\Theta} = \begin{bmatrix} 1 \\ 0 \\ 1 \\ 0 \\ 0 \\ \sqrt{2} \end{bmatrix} \otimes \int_\Omega \mathbf{B}(\mathbf{x})^T \ d\Omega \ \text{ , with } \ \mathbf{M} = \int_\Omega \mathbf{B}(\mathbf{x})^T \mathbf{B}(\mathbf{x}) \ d\Omega \quad (4.104)$$

Algorithm 3 Iterative minimization scheme of the anisotropic thin plate energy

Require: Initial solution $u_0 \leftarrow \min_u E_{fit}(u) + \lambda_0 E_{H^2}(u)$ for a high regularization weight λ_0.
  while dif $\geq \varepsilon$ **do**
    $\mathbf{T}_i \leftarrow \min_{\mathbf{T}} E_B(\mathbf{T}, u_{i-1}) + E_{H^2}(\mathbf{T}) + I_{iso}(\mathbf{T})$;
    $u_i \leftarrow \min_u E_{fit}(u) + \lambda E_B(u, \mathbf{T}_i)$;
    $dif = E_{fit}(u_{i-1}) - E_{fit}(u_i)$;
  end while

To determine the regularization weight denoted λ in Algorithm. 3, which is associated to the anisotropic bending energy, we set

$$\lambda = p \frac{m(\mathbf{A_{fit}})}{m(\mathbf{H}^A)} \quad (4.105)$$

with p a positive scalar. When $p = 1$, the influence of fitting and smoothing is equivalent. Similarly, to determine the regularization weight associated to the standard Hessian energy, we use Eq. (4.105) by replacing $\mathbf{H}^A$ with $\mathbf{H}$. In the following, we will specify only the coefficient p, that is used to compute the regularization weight λ for the standard Hessian energy and the anisotropic bending energy.

Fig. 4.14 shows a comparison between two forms of the thin plate energy: the standard form and the anisotropic form. The comparison is performed on models characterized by strong thickness variations. Specifically, in Fig. 4.14c, where the two lower horizons were intentionally tilted to introduce higher levels of anisotropy. Figs. 4.14a, c, show the solutions of the standard thin plate energy (Hessian energy) as regularization. The standard Hessian energy solutions violates the regularity criteria and presents strong oscillations. Figs. 4.14b, d, show solutions of the anisotropic thin plate energy. The effect of the anisotropic rigidity tensor is remarkable, since it iteratively encodes the anisotropy and variations present in the data. Similarly to the previous one dimensional example, the solutions of our anisotropic thin plate energy present visually greater smoothness and regularity. The former is attributed to the ability of the anisotropic rigidity tensor to better adapt to data by effectively aligning the curvature of the implicit function to the directional variations of curvature encoded in the anisotropic rigidity tensor. The former is attributed to the ability of the anisotropic rigidity tensor to better adapt to the strong curvatures that the horizons exhibit. Then, our method is effectively aligning the curvature of the implicit function to the directional variations of curvature encoded in the anisotropic rigidity tensor. Additionally, the solutions of the thin plate energy preserve better the sharp features present in data compared to the solutions of the anisotropic diffusion energy Fig. 4.9, while validating all the regularity criteria. These results demonstrates that the failure of high order smoothness energies such as the standard Hessian energy Eq. (3.75) to produce regular solutions in the context of strong thickness variations, is not due to the smoothness assumption. Instead, we believe it is because of the isotropic assumption that is implicitly made when using the standard form of these energies.

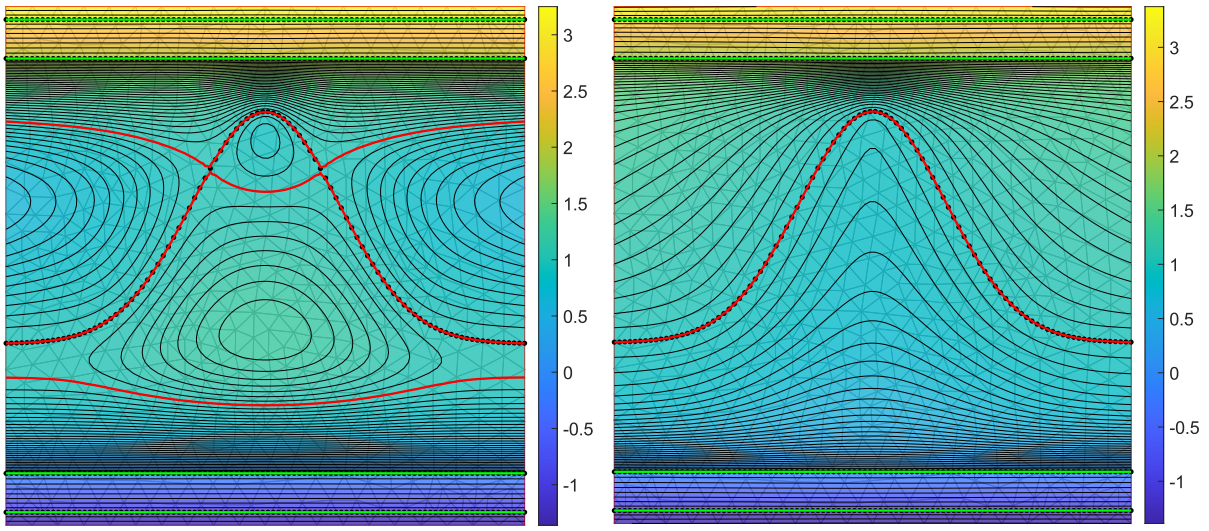

(a) (b)

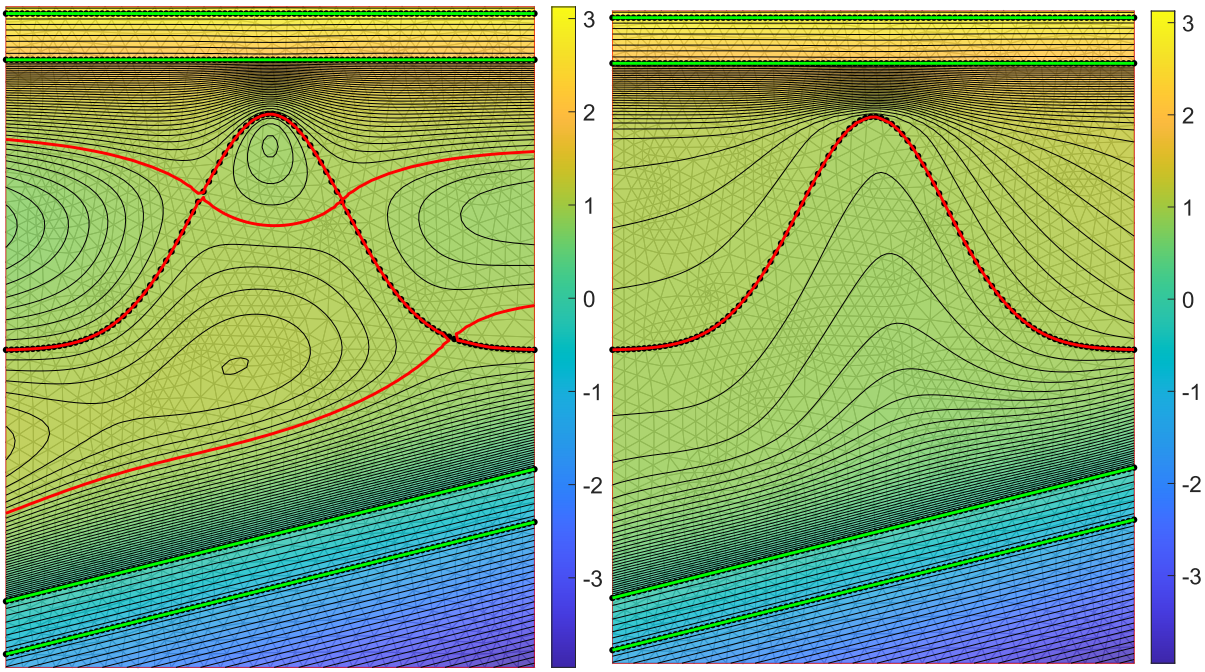

(c) (d)

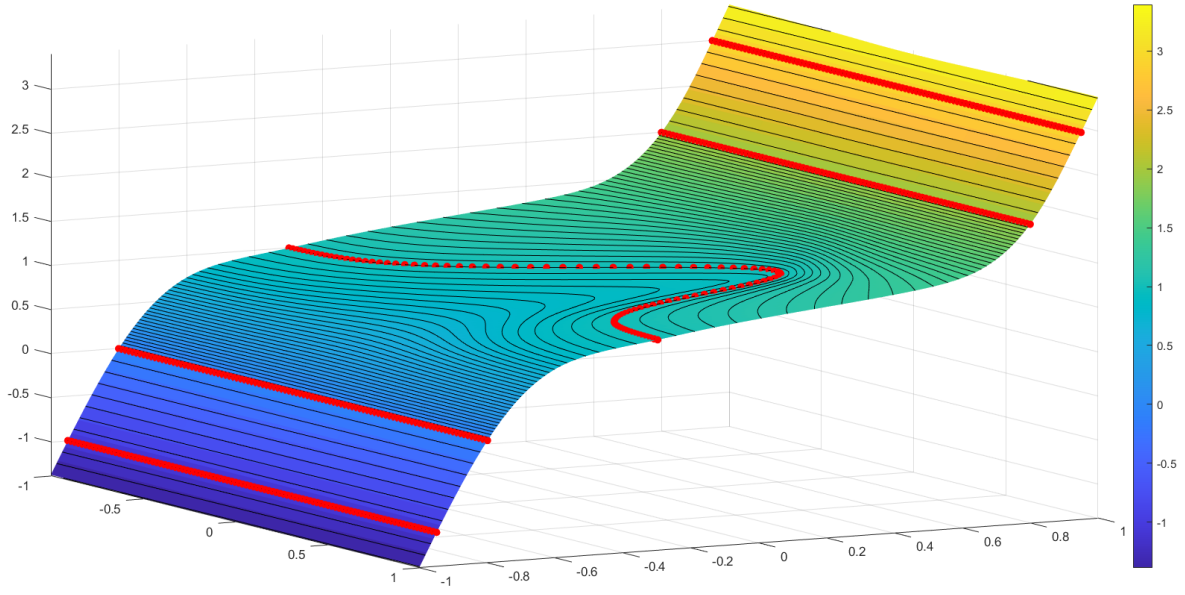

(e)

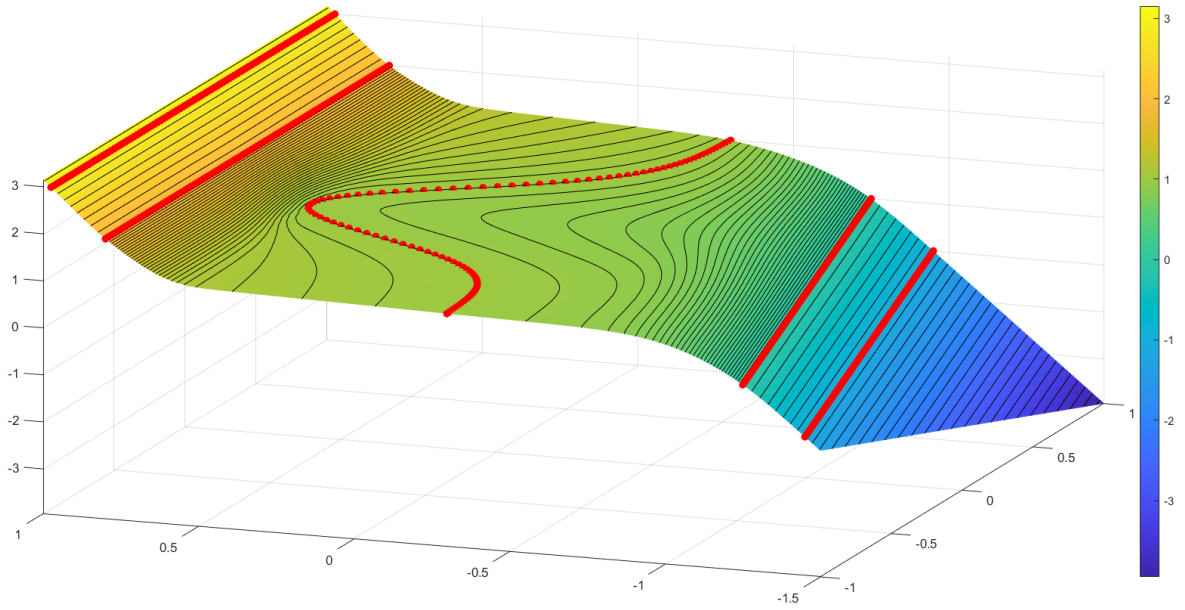

(f)

Figure 4.14: Resulting implicit function using the thin plate energy on models presenting high thickness variations. (a)-(c) Isotropic standard thin plate energy ($\lambda = 1$). (b)-(d) Anisotropic thin plate energy ($\lambda = 1$). (e)-(f) $3D$ surfaces of the solutions plot in $2D$ respectively (b) and (d).

4.6 Extension of the new formulations of the regularization to $3D$

In this section we provide the extension of the regularization formulations to $3D$, for the anisotropic diffusion energy Eq. (4.16) and the anisotropic bending energy Eq. (4.58). The anisotropic diffusion energy is

$$E_{Dif(\mathbf{C})}(u,g) = \frac{1}{2}\int_{\Omega} \nabla u^T(\mathbf{x})\mathbf{C}(\mathbf{x})\nabla u(\mathbf{x}) \;\; d\Omega - \int_{\partial\Omega} g(\mathbf{x})u(\mathbf{x})dx \tag{4.106}$$

In $3D$, we add the variable z

$$\nabla u = \begin{bmatrix} u_x & u_y & u_z \end{bmatrix}, \; C = \begin{bmatrix} c_{xx} & c_{xy} & c_{xz} \\ c_{xy} & c_{yy} & c_{yz} \\ c_{xz} & c_{yz} & c_{zz} \end{bmatrix} = \begin{bmatrix} c_1 & c_4 & c_5 \\ c_4 & c_2 & c_6 \\ c_5 & c_6 & c_3 \end{bmatrix} \tag{4.107}$$

Then, the formulation becomes

$$\int_{\Omega} \begin{bmatrix} u_x & u_y & u_z \end{bmatrix} \begin{bmatrix} c_1 & c_4 & c_5 \\ c_4 & c_2 & c_6 \\ c_5 & c_6 & c_3 \end{bmatrix} \begin{bmatrix} u_x \\ u_y \\ u_z \end{bmatrix} dxdydz - \int_{\partial\Omega} g(\mathbf{s})u(\mathbf{s})ds \tag{4.108}$$

The boundaries of the domain, denoted as $\partial\Omega$, includes both the boundaries of the domain and fault surfaces. Concerning the extension to $3D$ of the tangential diffusion introduced in Eq. (4.23). In $2D$, faults are simply lines and represented as a set of edges. Subsequently, the tangential diffusion along the faults is integrated edge by edge and the boundary conditions are introduced at the extremities of the faults. Similarly in 3D, where the faults become surfaces, we integrate triangle by triangle and the boundary conditions are introduced along the boundaries of the faults.

To extend the formulation of the anisotropic bending energy to $3D$, we first define the operator $\mathbf{L}(u) = \begin{bmatrix} u_{xx} \\ u_{yy} \\ u_{xy} \end{bmatrix}$. Then, the anisotropic bending energy can be expressed as

$$\int_{\Omega} \begin{bmatrix} u_{xx} & u_{yy} & u_{xy} \end{bmatrix} T \begin{bmatrix} u_{xx} \\ u_{yy} \\ u_{xy} \end{bmatrix} \; d\Omega = \int_{\Omega} \mathbf{L}(u)^T \mathbf{T} \mathbf{L}(u) \; d\Omega \tag{4.109}$$

Then, we add the variable z and the operator $\mathbf{L}(u)$ in $3D$ becomes

$$\mathbf{L}(u) = \begin{bmatrix} u_{xx} \\ u_{yy} \\ u_{zz} \\ u_{xy} \\ u_{xz} \\ u_{yz} \end{bmatrix} \tag{4.110}$$

In $3D$, the tensor $\mathbf{T}$ is a symmetric tensor field $\mathbf{T}(\mathbf{x}) : \Omega \to \mathbb{R}^{6\times 6}$. This tensor contains $T_{ij}(\mathbf{x})$, $i,j = 1:6$, 36 scalar functions in total. However, because it is symmetric the number of independent coefficients is given by

$$\sum_{i=1}^{n}\sum_{j=1}^{i-1} j \tag{4.111}$$

which results in 21 independent coefficients. It is worth noting that the Cholesky parameterization, which is applied for both rigidity and diffusion tensors in $2D$, can also be employed in $3D$.

Chapter 5
Applications

In this chapter, we aim to demonstrate the effectiveness of the proposed methods on complex geological models. We will conduct a comparative analysis of the resulting implicit functions using three regularization energies: the standard Hessian energy, the anisotropic diffusion energy, and the anisotropic bending energy.

5.1 Handling high thickness variations in complex geological models

In this section, we show the effectiveness of our methods on complex geological models that contain faults. We first evaluate our methods on a faulted model presenting no significant thickness variation and another presenting strong thickness variation. The faulted model in Fig. 5.1 contains seven horizons. The values assigned to the horizons are in the ascending order from the bottom to the top, ranging from one to seven. The thickness variation in this model is not pronounced, since the thickness of the layers between these horizons is relatively uniform.

Figs. 5.1 show resulting implicit functions using the standard Hessian energy and our anisotropic methods as regularization; Fig. 5.1a illustrates the generated solution using the standard Hessian energy, while Figs. 5.1 b and c illustrate, solutions generated using the anisotropic diffusion and anisotropic bending energy, respectively. Our methods produce a regular solution throughout the entire domain, displaying good behaviour near the boundaries and faults. Similarly, the Hessian smoothing solution respects all the regularity criteria. Visually, the solutions are similar, except near the fault inside the domain due to the use of the tangential diffusion constraint introduced on the faults for the anisotropic diffusion (See Figs. 5.1d, e and f).

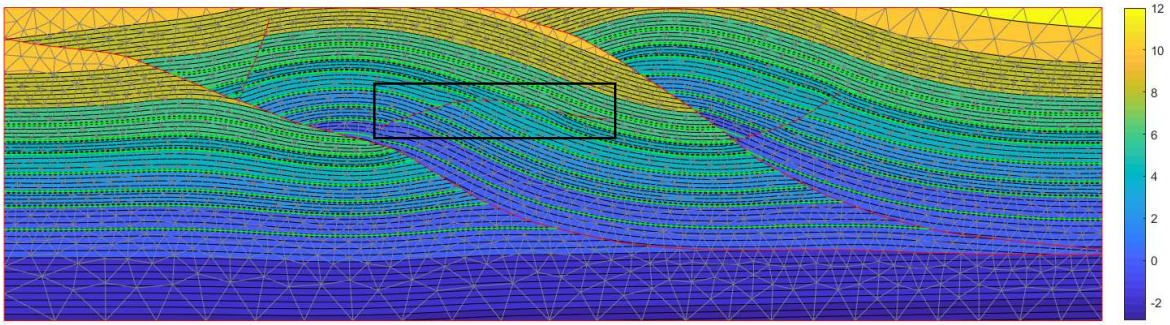

(a)

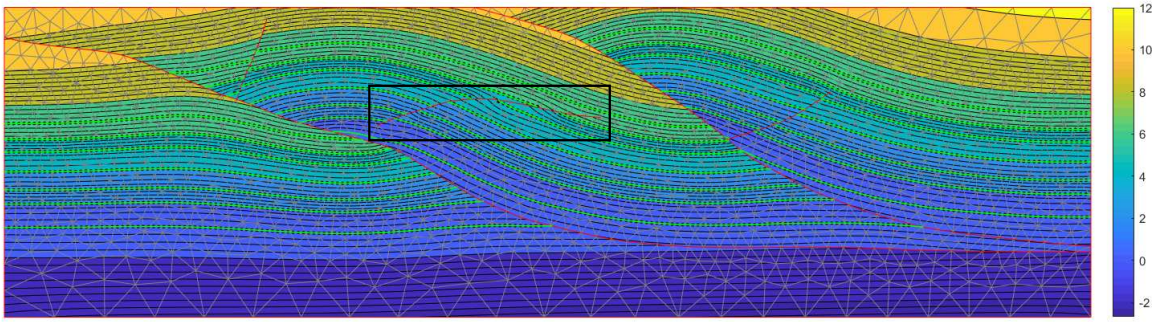

(b)

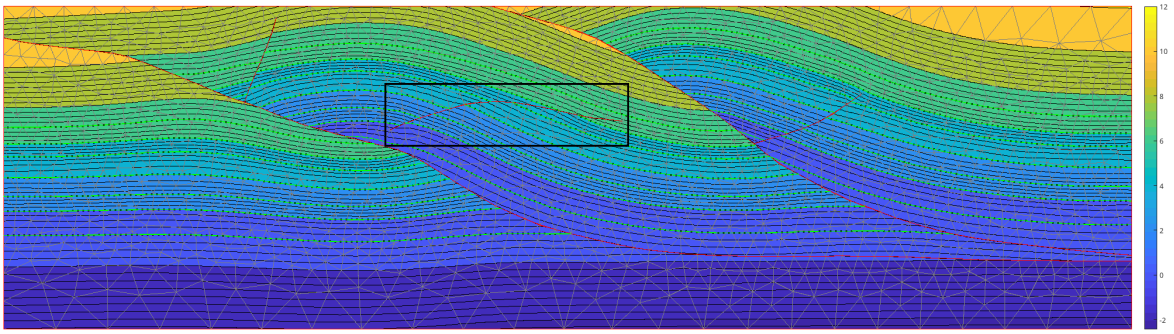

(c)

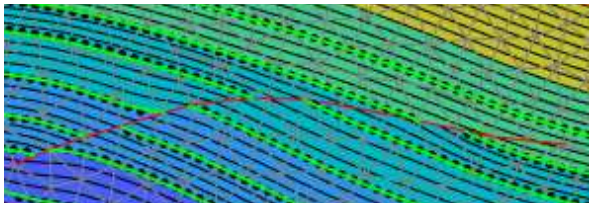

(d)

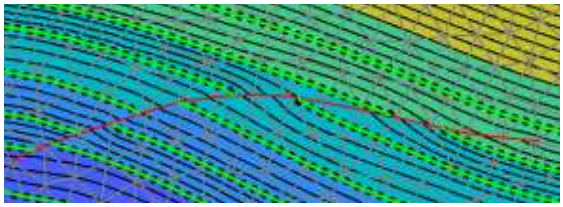

(e)

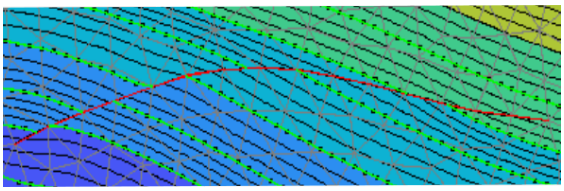

(f)

Figure 5.1: Geological benchmark model of Renaudeau (2019). (a) Resulting implicit function using the Hessian energy, (b) Resulting implicit function using anisotropic diffusion. (c) Resulting implicit function using anisotropic bending energy. (d) A zoomed-in view of the area within the black frame in Figure (a), (e) A zoomed-in view of the area within the black frame in Figure (b). (f) A zoomed-in view of the area within the black frame in Figure (c).

The model in Fig. 5.2 has been obtained by removing horizons $4, 5$ and 7. To further complicate the problem, the value associated with the horizon 6 has been changed to 4. These modifications induce a very strong thickness variations, particularly along the fault inside the domain. We refer to the models Fig. 5.1 and Fig. 5.2 respectively as Geo and Geo refined.

The Hessian smoothing fails to produce a regular solution (Fig. 5.2a). The maximum principle and the mean value property are violated throughout the domain. The resulting implicit function increases until it reaches the value 4, and then decreases, which induces a wrong extraction of the horizon 4, being extracted twice. The method Eq. (4.16) with no tangential diffusion along the faults, generates a regular solution within the domain. However, along the faults it is not maintaining the mean value and the maximum principle, resulting in the formation of bubbles. To overcome this limitation, we introduced the tangential diffusion along the faults in the diffusion energy Eq. (4.23). It ensures the respect of the regularity criteria along the faults, thereby eliminates the bubbles as shown in Fig. 5.2d.

In Fig .5.2c, the anisotropic bending energy produces a regular solution, but violates the regularity criteria along the faults. It is worth noting that we had to refine the mesh to obtain this solution, and the refined mesh contains 3 times the number of vertices as the initial one. We also believe that introducing an additional constraint that controls the bending energy along the faults, similar to the tangential diffusion, might address this limitation.

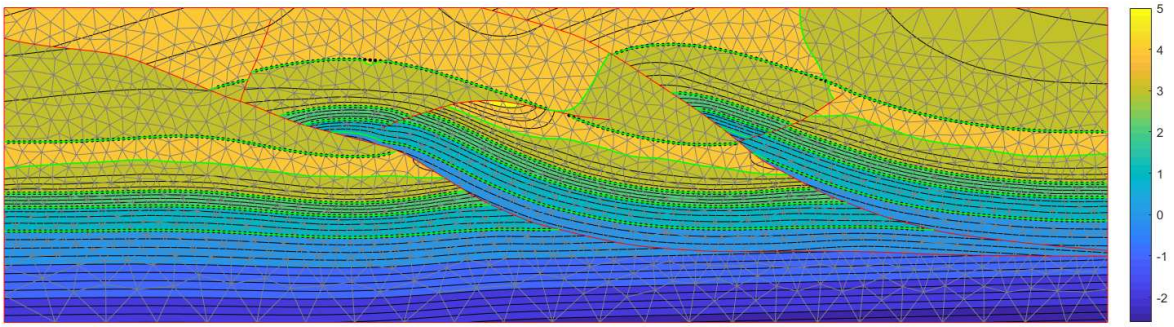

(a)

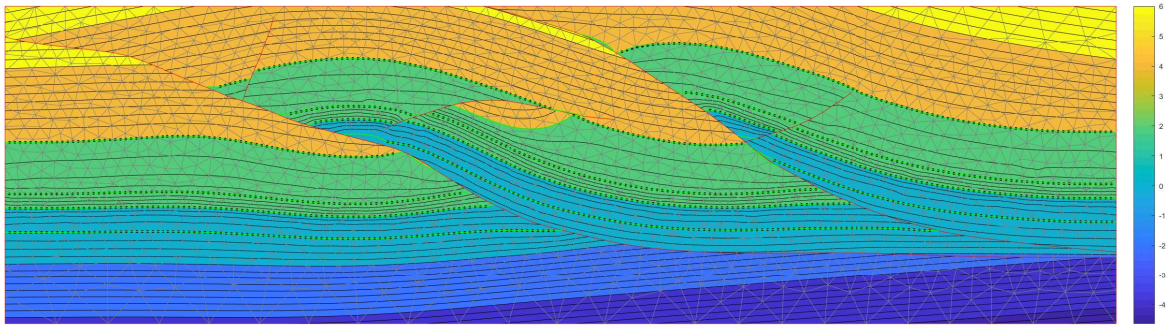

(b)

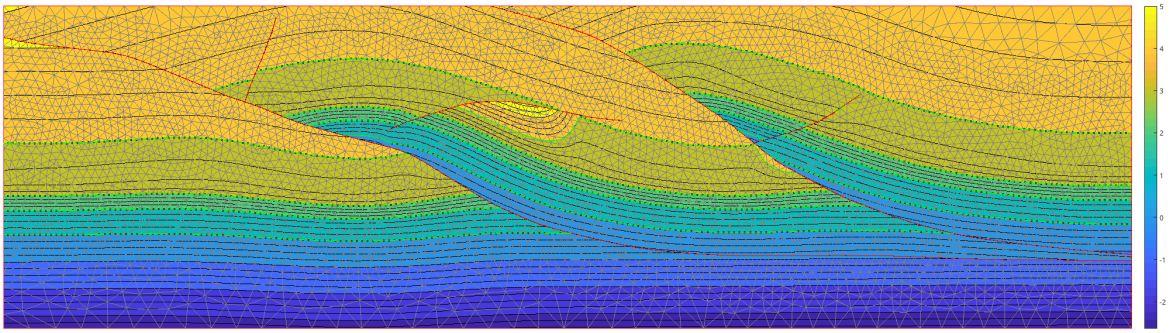

(c)

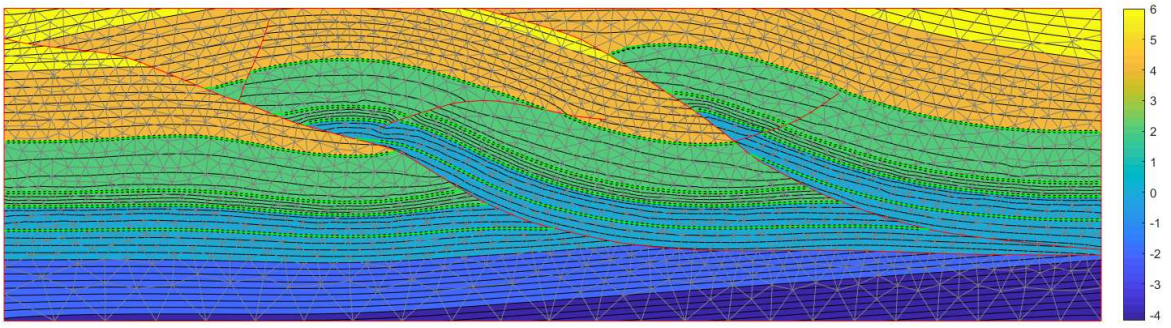

(d)

Figure 5.2: (a) Resulting implicit function using the Hessian energy (Eq .3.76), (b) resulting implicit function using our method without the tangential diffusion constraint (Eq. 4.17), (c) resulting implicit function using our method with the tangential diffusion constraint (Eq. 4.17).

5.2 Handling complex fault network

In the following, we examine two $3D$ geological models. The first one is Gullfaks, an oil and gas field located in the Norwegian sector of the North Sea (structurae (2023)). The second model is the Thrust-Belt model, which is characterized by the presence of folded layers and thrust faults (McClay et al. (2004)). Figs. 5.3a and b show, respectively, the Gullfaks model and the Thrust-Belt model. Given that the proposed methods in this thesis are developed only for $2D$ applications, we will consider selected cross-sections of the $3D$ models shown in Fig. 5.3. This involves initially selecting a specific plane, that we intersect with the fault surfaces, resulting in a set of segments in $2D$ that represent the faults. Then, we generate a mesh that conforms to these lines, we also project the data points onto this plane.

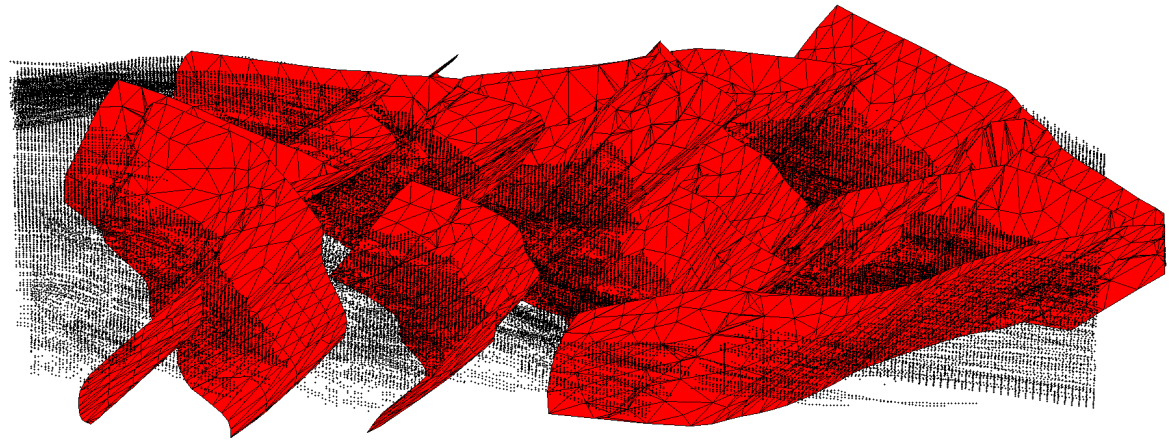

(a)

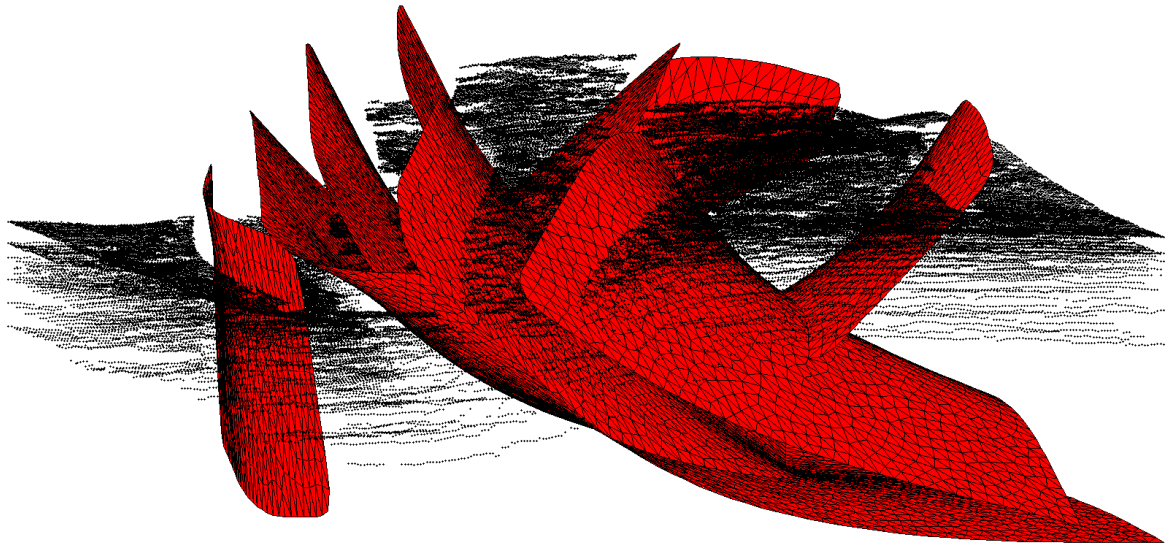

(b)

Figure 5.3: $3D$ geological models. (a) Gullfaks. (b) Thrust-Belt. Black dots are data points and the red surfaces represent faults.

Figs. 5.4 show the resulting implicit functions in a model obtained as a cross section of the 3D Gullfaks model. The values are assigned to the horizons as follows: 1 to the bottom horizon, 2 is assigned to the middle horizon, and 3 is assigned to the top horizon. The aim here is to examine the behaviour of the regularization methods when the fault network includes a set of finite faults (i.e. a fault that ends inside the domain boundary), and the horizons are far from the domain boundaries. The three resulting implicit functions are regular all over the domain, however they present different behaviours near the faults. The anisotropic diffusion along the faults yields a solution that exhibits a better regularity as shown in Fig. 5.4b. This is due to the tangential diffusion term that ensures a better control in that direction. In Fig. 5.5a, we can observe the principal directions of the diffusion tensor associated with this solution. We can also see that the direction associated to the smallest eigenvalue is aligned with the gradient of the solution. The condition number of the diffusion tensor over all the domain is shown in Fig. 5.5b. We remark that the ratio of anisotropy is nearly constant all over the domain. This indicates that this model does not present significant thickness variations.

In Fig. 5.4c, the generated solution using the anisotropic bending energy is shown. This solution presents more curvature and seems to reverse the trend, exhibiting non monotonicity along the faults, especially the finite fault at the bottom of the domain. This experiment confirms the idea that an additional constraint, along the tangential direction for the anisotropic bending energy, can provide a better control along the faults. The solution obtained using the standard Hessian energy shown in Fig. 5.4a also lacks regularity along the faults.

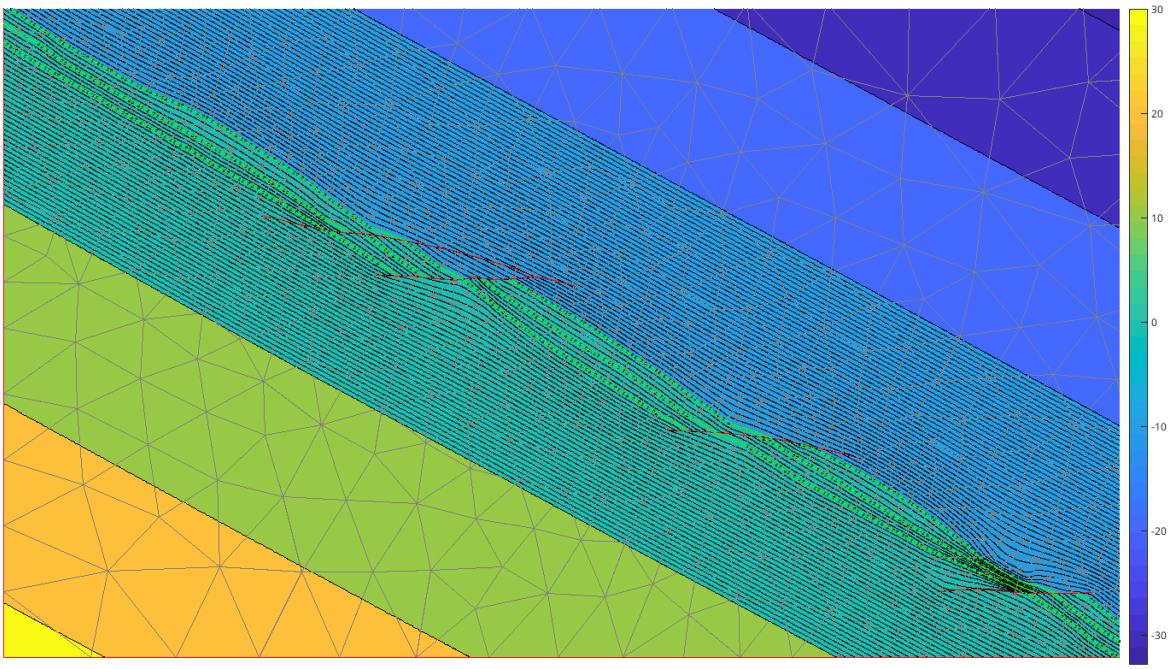

(a)

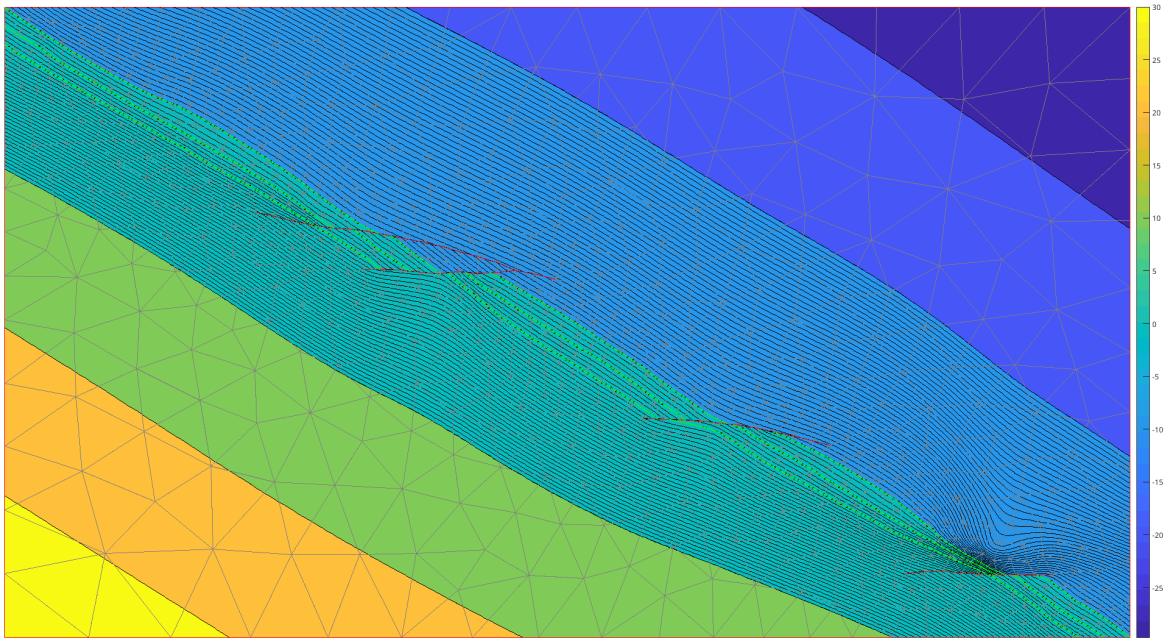

(b)

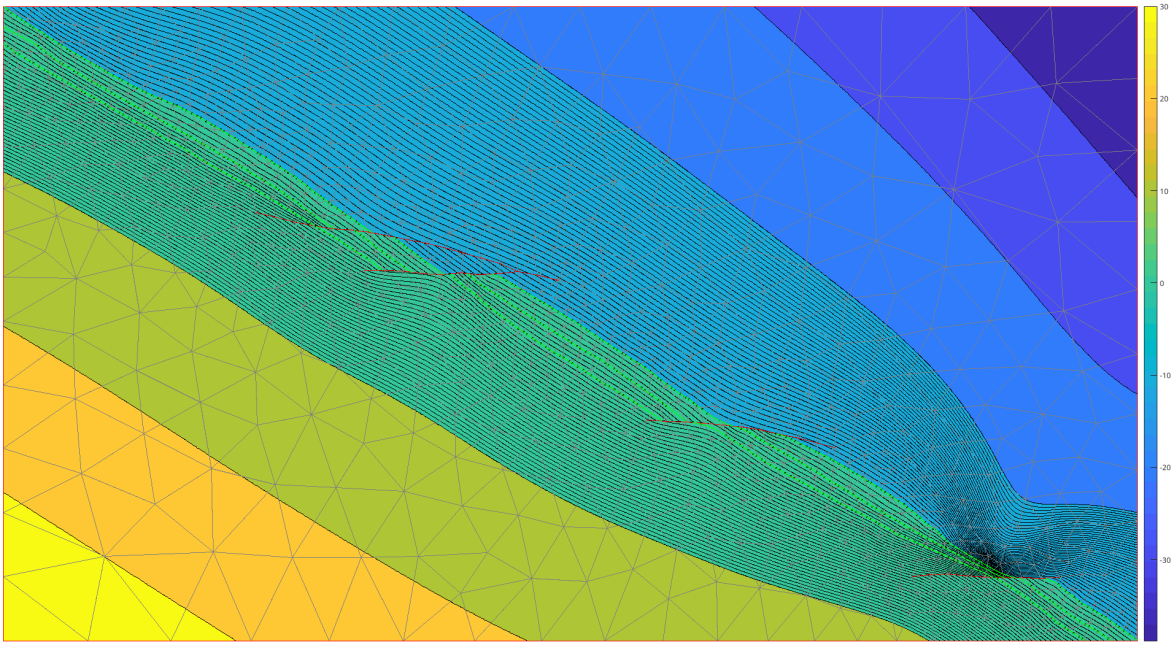

(c)

Figure 5.4: Resulting implicit functions using: (a) Standard Hessian energy (Eq. 3.76). (b) Anisotropic diffusion (Eq. 4.17). (c) Anisotropic bending energy (Eq. 4.58).

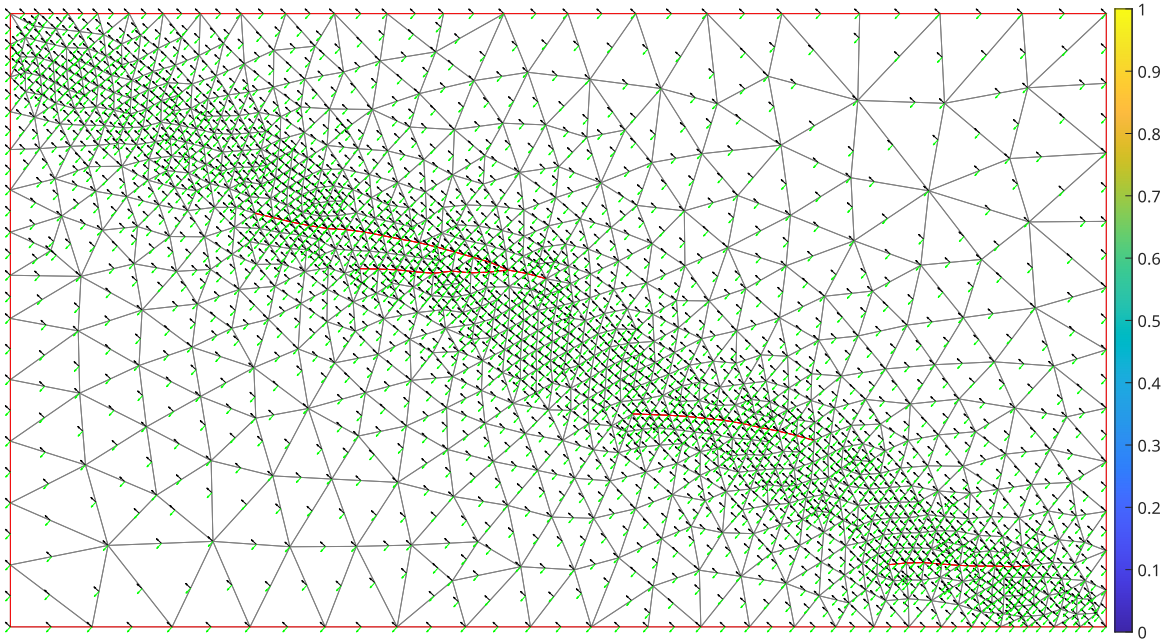

(a)

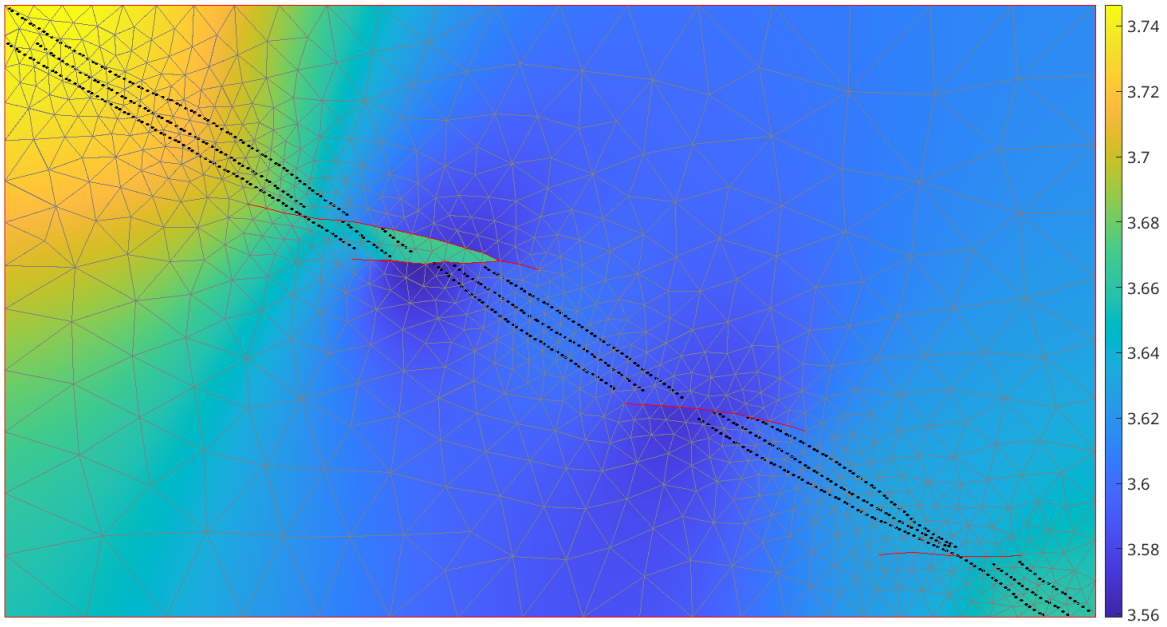

(b)

Figure 5.5: Principal directions and the condition number of the diffusion tensor associated with the solution shown in Fig. 5.4a. (a) Principal directions of diffusion over all the domain, green the direction associated to the smallest eigenvalue and in black the direction of the largest eigenvalue. (b) Condition number of the diffusion tensor over all the domain.

5.3 Handling noisy data

While testing the proposed methods on the Thrust-Belt model, we focused on a specific cross-section shown in Fig. 5.6. However, within this cross-section, the number of data points available was very limited and does not include all the horizons in this model. To address this, we projected a set of points that are at a specific distance from this cross-section plane. As a result, the collected points are very noisy. Furthermore, in some regions, we can observe that the data points are inaccurately distributed within the domain. We seek here to test the sensitivity of the regularization methods to the noise that is present in the data. Figs. 5.6c, d and e, show the resulting implicit functions using the anisotropic diffusion, respectively, for $\beta = 1, 10, 100$, and $\alpha = 0.9$. The solution for $\beta = 1$ is presenting strong oscillations, however it remarkably maintains the mean value property and the maximum principle at the boundaries. The strong oscillations in this case can be attributed to the iterative process of the anisotropic diffusion scheme, which means that if we obtain a solution with poor regularity, subsequent solutions are likely to exacerbate the issue. When we increase the regularization weight, starting from $\beta = 10$, we observe an improvement in the regularity of the solutions. Nevertheless, it comes at the expense of the precision of fitting the data points.

In Fig. 5.6a, we see the generated solution using the standard Hessian energy with $p = 10000$, see Eq. (4.105). This solution is regular, obtained using a strong smoothing weight, which leads to erase the features of the model. While, in Fig. 5.6b, we see the solution obtained using the anisotropic bending energy with $p = 10000$. In both cases, where data points are very noisy, we observe that regular solutions are obtained only when using very high smoothing weight computed using $p = 10000$.

We observe that for a high regularization weight the three regularization methods shown, respectively, in Fig. 5.6a, b and e, are very similar. This is due to the use of a high regularization weight, which effectively filter the noise but also erase features in the data. These experiments show the effectiveness of the proposed methods for noise filtering. When dealing with data that is very noisy and present geologically inconsistent trends, taking a high regularization weight is an effective approach to generate regular solutions. It is worth noting that our proposed methods involves a higher computational cost compared to the standard Hessian energy. We believe that in cases where the data is extremely noisy and the main objective is to obtain a regular solution at the expense of erasing the data features, the standard Hessian energy might be a better solution.

Using the solution obtained with the anisotropic diffusion for a $\beta = 100$, shown in Figure 5.6e, we randomly sample a set of data points along the extracted horizons, which are represented by the green lines. These data points are then used for interpolation. In Figs. 5.7, we present the resulting implicit functions, using the standard Hessian energy, anisotropic diffusion energy, and the anisotropic bending energy as regularization. The generated solutions using our proposed methods are regular and effectively handle a complex fault network.

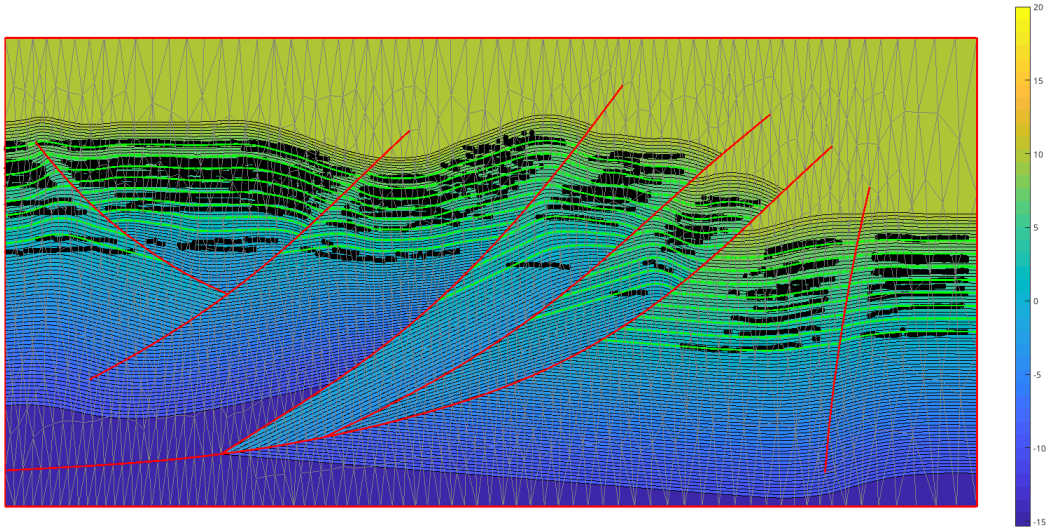

(a)

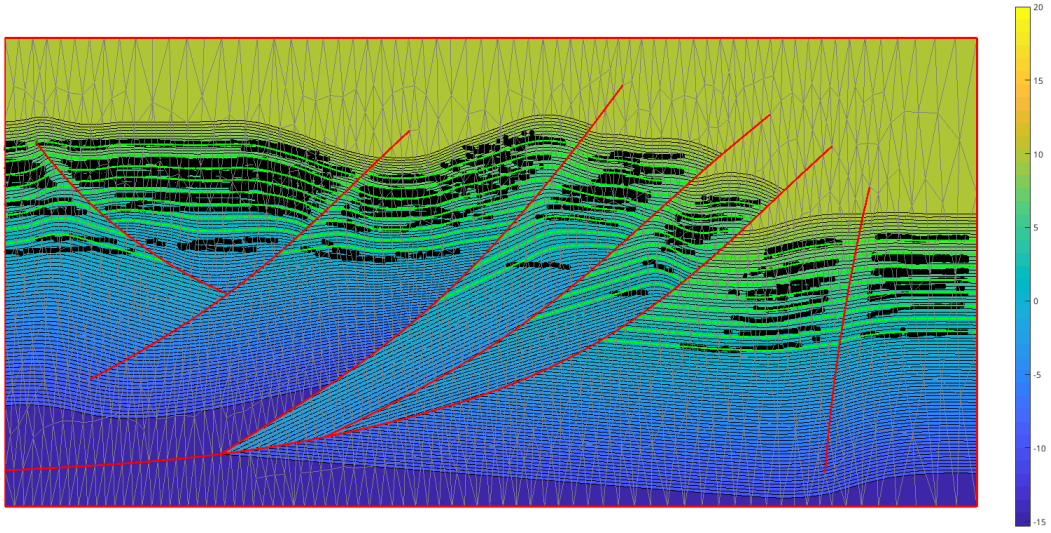

(b)

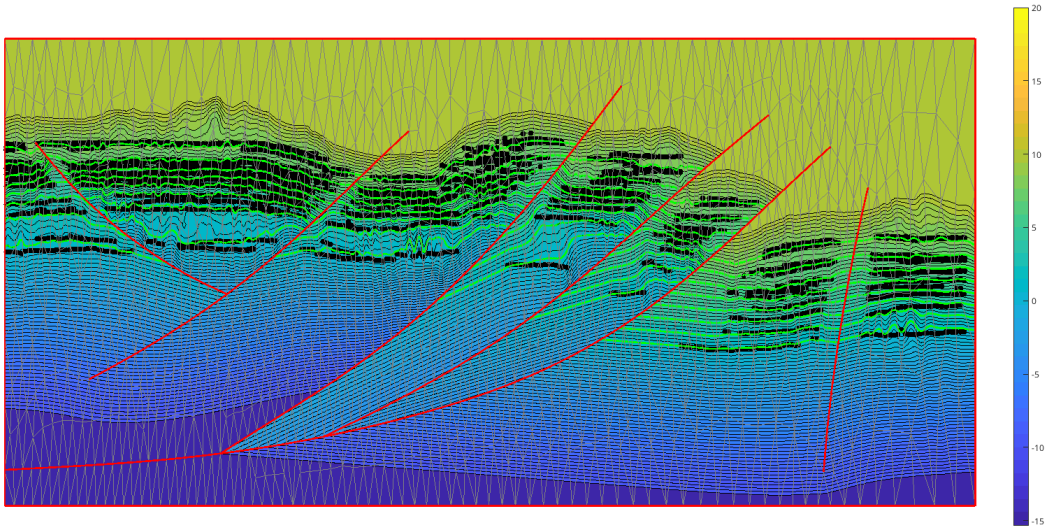

(c)

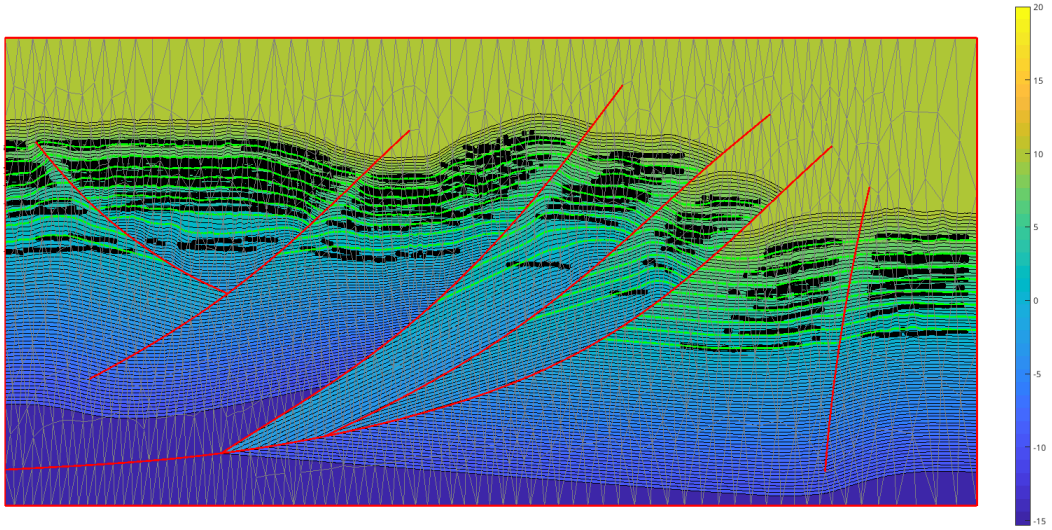

(d)

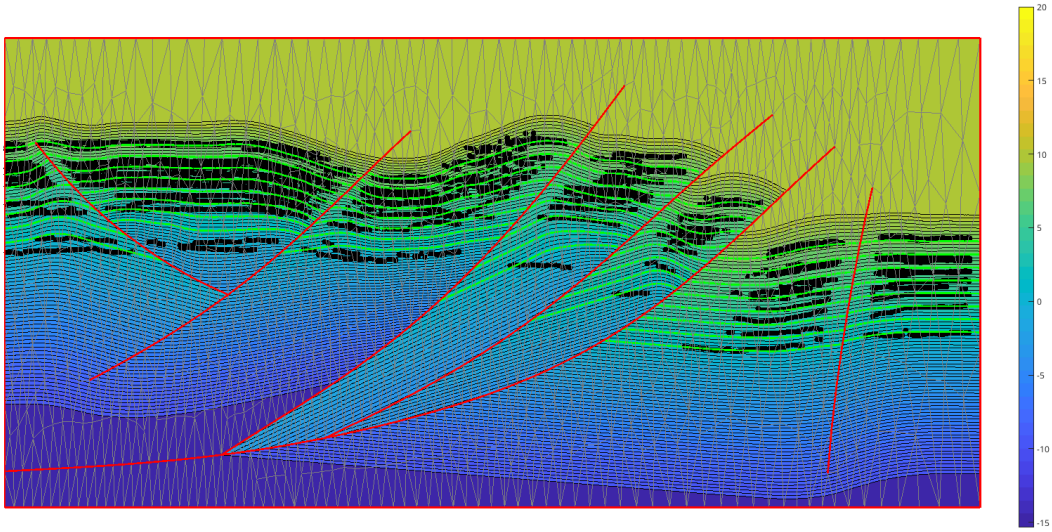

(e)

Figure 5.6: Regularization effect when interpolating a set of highly noisy data points. Resulting implicit functions using various settings: (a) Standard Hessian energy with $p = 10000$ (Eq. 3.76). (b) Anisotropic Hessian energy with $p = 10000$ (Eq. 4.58). (c) Anisotropic diffusion with $\alpha = 0.9$ and $\beta = 1$ (Eq. 4.17). (d) Anisotropic diffusion with $\alpha = 0.9$ and $\beta = 10$ (Eq. 4.17). (e) Anisotropic diffusion with $\alpha = 0.9$ and $\beta = 100$ (Eq. 4.17).

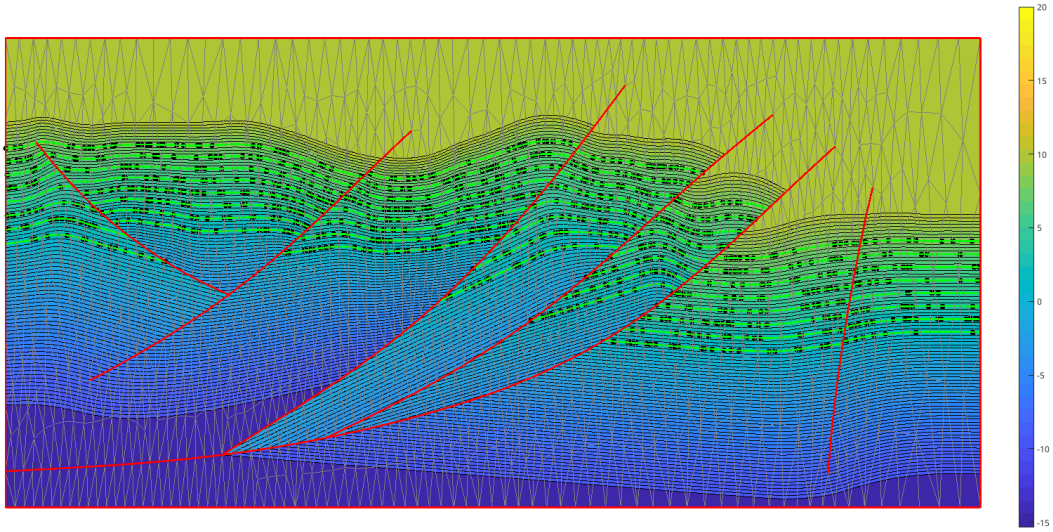

(a)

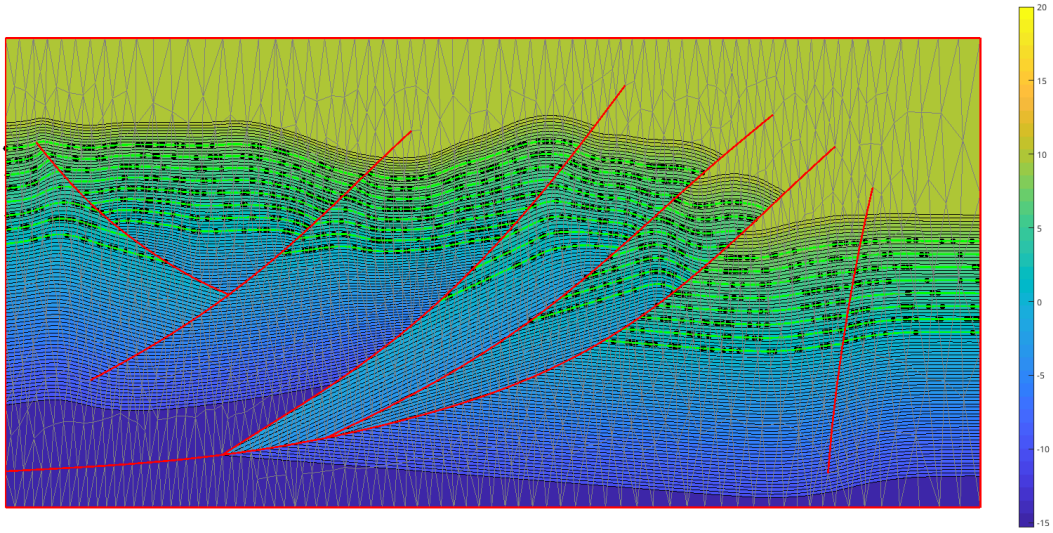

(b)

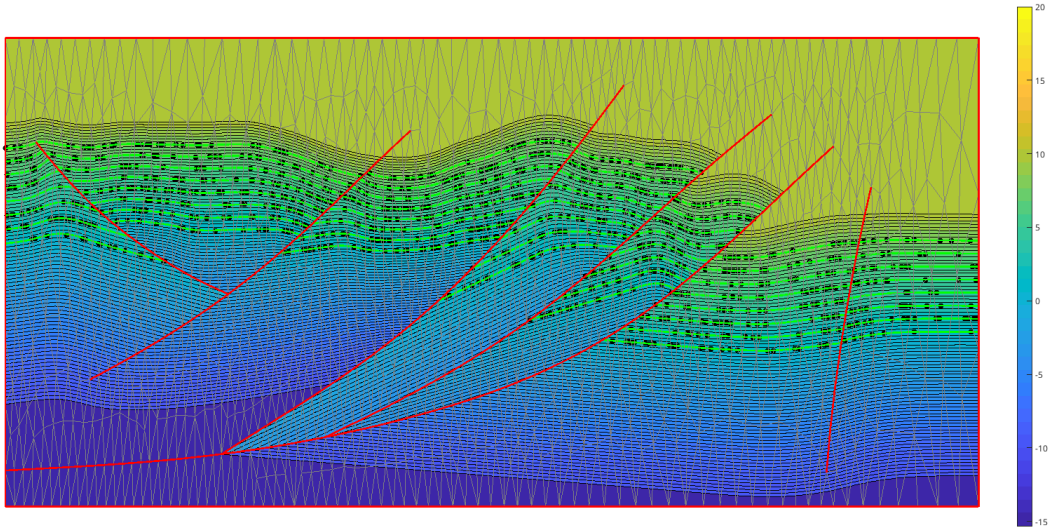

(c)

Figure 5.7: Interpolation of filtered data points. Resulting implicit functions using: (a) Standard Hessian energy with $p = 1$ (Eq. 3.76). (b) Anisotropic diffusion with $\alpha = 0.9$ and $\beta = 1$ (Eq .4.17). (c) Anisotropic bending energy with $p = 1$ (Eq .4.58).

5.4 Handling decimated data

In the Gullfaks model, we extracted a cross-sectional slice. The set of points projected onto this plane exhibits noise and sparsity. Figs. 5.8 shows resulting implicit functions using the Hessian energy, the anisotropic diffusion and the anisotropic bending energy. This model contains five finite faults. The rightmost part of the model contains two horizons, where big parts are decimated because of the projection. In this region, the middle horizon is partially decimated, while the bottom one is severely decimated, particularly in the region after the strong curvature. A desired behaviour in this region is that the contours keep the same trend of data and stay as straight as possible until finishing on the fault. However, all the solutions in this region exhibit oscillations and do not keep the trend of data as shown in Fig. 5.8. On the other hand, in the remaining part of the domain the solutions exhibit a behavior that can be considered reasonable, taking into account the sparsity and noise in the data. This is likely due to the fact that the horizons in this region present similar trends which simplifies the interpolation process.

In Fig. 5.8b, the solution obtained using the diffusion energy presents a superior regularity along the faults compared to the standard Hessian energy and the anisotropic bending energy. The solution of the anisotropic bending energy shown in Fig. 5.8d, with a low regularization weight $p = 0.1$, is better fitting the data. In this case, we observe that the Hessian energy and the anisotropic diffusion when taking a weak regularization weight leads to extremely oscillating solutions.

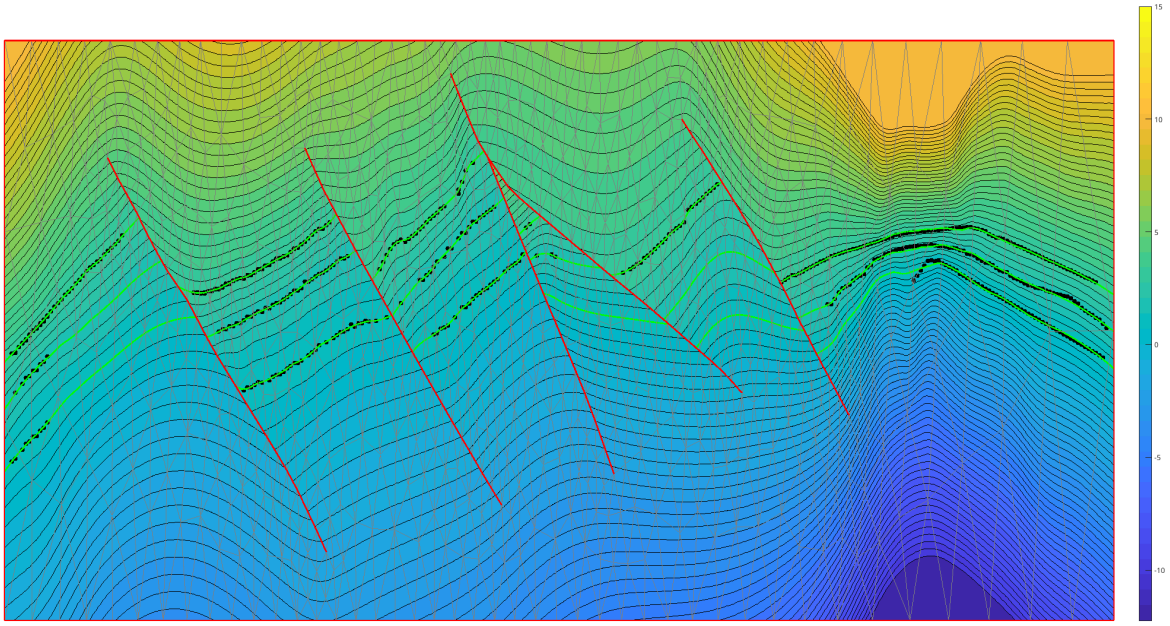

(a)

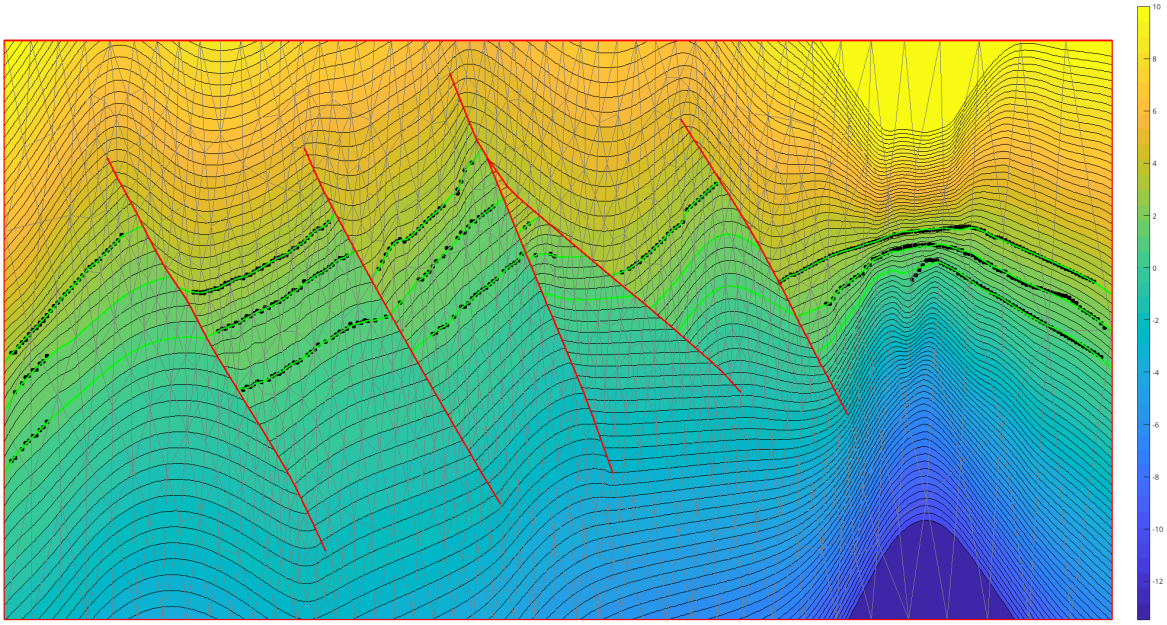

(b)

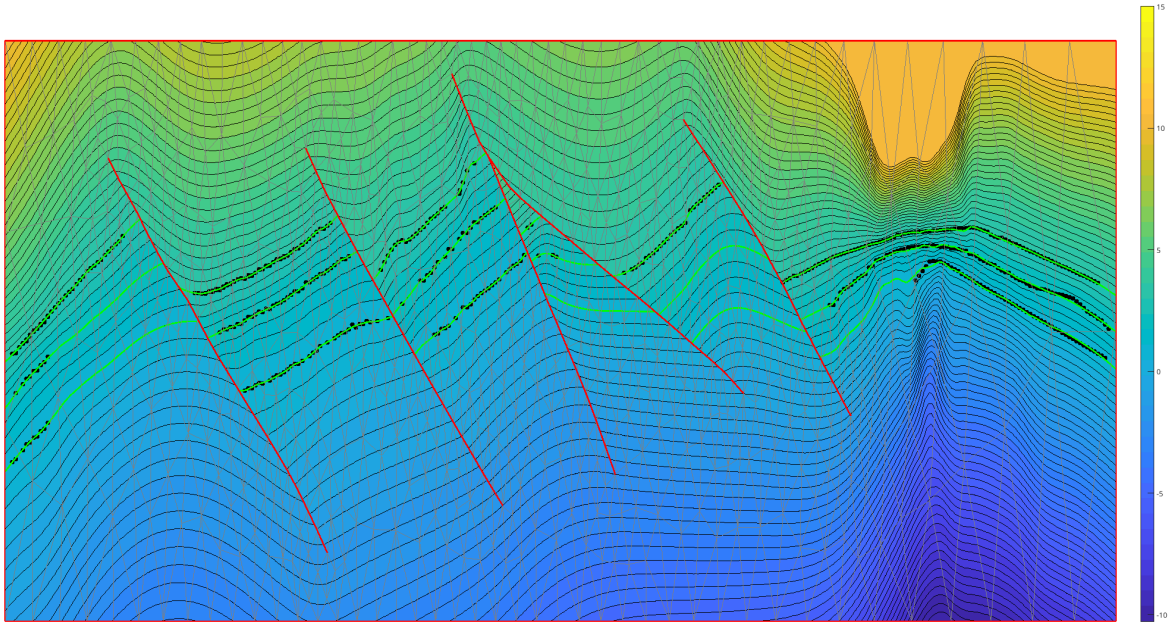

(c)

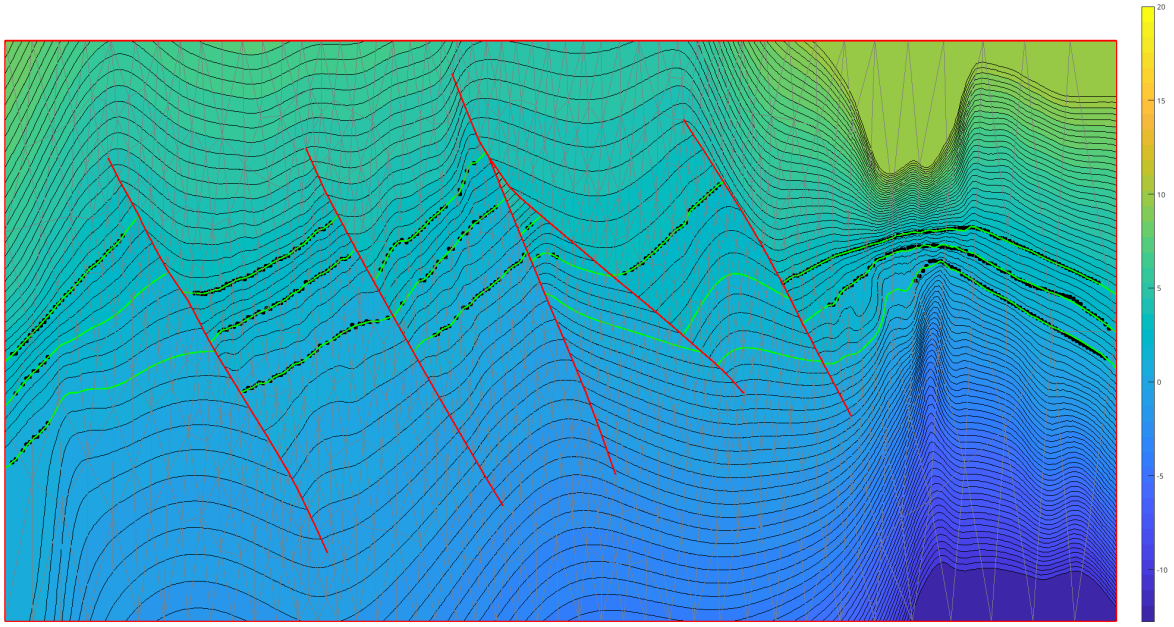

(d)

Figure 5.8: Interpolation of sparse data. Resulting implicit function using: (a) Standard Hessian energy with $p = 1$ (Eq. 3.76). (b) Anisotropic diffusion energy with $\alpha = 0.9$ and $\beta = 1$ (Eq. 4.17). (c) Anisotropic bending energy with $p = 1$ (Eq. 4.58). (c) Anisotropic bending energy with $p = 0.1$ (Eq. 4.58).

Regarding anisotropic diffusion, we observe that for all the models, we converge after three or four iterations. In our experiments, we opt for a parameter $\alpha = 0.5$ for the models exhibiting moderate thickness variations and 0.9 for models with strong thickness variations. The parameter β is typically set equal to one, while we choose small value for the models with sparse density of data points and a very refined mesh. On the other hand, we use higher values to filter noisy data.

Model	**Number of iterations**	α	β
Extracted layers (Fig. 4.7d)	4	0.5	1
Faulted synthetic (Fig. 4.3d)	4	0.5	1
Bell refined (Fig. 4.8)	3	0.9	1
Bell (Fig. 4.7i)	4	0.9	0.1
Rings (Fig. 4.7f)	3	0.9	1
Geo (Fig. 5.1b)	4	0.5	1
Geo refined (Fig. 5.2c)	4	0.9	0.001
Fig. 5.4a	3	0.9	1
Fig. 5.6c	3	0.9	100
Fig. 5.7b	3	0.9	1
Fig. 5.8b	3	0.9	1

Table 5.1: Number of iterations, and the parameters (α,β) per model for the anisotropic diffusion regularization.

Concerning the anisotropic bending energy, we observe that for all the models, we typically converge after two or three iterations. In our experiments, we choose a coefficient $p = 1$ to compute the regularization weights. Only when data is noisy (Fig. 5.6e), we used $p = 10000$.

For the remaining solutions presented in the thesis, the regularization weight is determined using the method described Eq. (4.105), where the coefficient p is set to 1.

The solution $\mathbf{U}$ of Eq. (4.38) is used to evaluate the implicit function all over the domain. In models without faults, we discretize the domain using a regular grid, and the implicit function is evaluated on the grid's nodes. The isovalues are then extracted linearly on each grid element using marching squares. However, in presence of discontinuities, we refine the mesh generated conformal to the faults for interpolation, and we use a marching triangles method for the extraction of the isovalues. It is worth nothing, that the evaluation mesh used for the extraction of the isovalues, is refined up to three times compared to the mesh used for interpolation.

Conclusion and perspectives

In this thesis, we introduced a new definition of the regularity of the stratigraphic function, which are a set of mathematical properties that the implicit function should respect in order to maintain geological coherence. These properties necessitate adequate quantification. Then energies are carefully formulated to measure to what extent these properties are respected. Subsequently, they are integrated into the implicit modeling problem as regularization. Therefore, these criteria are a strong tool to examine to what extent the existing regularization objectives intersect with the desired regularity criteria. Furthermore, they can guide the formulation of new regularization energies that can fulfill these criteria.

We presented new formulations of the regularization that lead to solutions validating all these criteria. The two novel regularization techniques are independent of the choice of the discretization, and can be used with any chosen discretization as long as one is able to discretize first and second partial derivatives. First, an iterative scheme based on the anisotropic diffusion equation. Second, an iterative scheme based on the equation of the bending of an anisotropic thin plate. In both schemes, we tackle nonlinearity by iteratively solving a set of quadratic energies, that are guaranteed to be convex due to the parameterization of diffusion and rigidity tensors. Additionally, the two schemes require only an initial solution, which needs to be regular and not necessarily perfectly fitting the data.

In this thesis, we represented the implicit function using splines, which are piecewise polynomials of high order degree and continuity. The power of splines lies in enabling the use of piecewise polynomials of high order degree and extra inherent degree of continuity for discretization, while the optimization constraints come down simply as linear constraints on the control points of these splines, resulting in a sparse linear system to inverse.

The construction of geological models relies on a diverse set of tools that come from various sciences like statistics, physics, and, more recently, artificial intelligence. This interdisciplinary aspect presents challenges to each scientific discipline, but it also offers an opportunity to create connections among scientists from different backgrounds. As it is the case in this work, where we explored and then introduced new tools coming from image processing, computer graphics, physics and mechanics. Nevertheless, geologists, practitioners, and users of geomodeling tools all demand intuitive and straightforward formulations, while being robust and deals with any arbitrary settings. However, the complexity of geology calls for more complex mathematical equations and formulations. In this context, we proposed technique to estimate the weights associated to the energies associated to the various degrees of freedom of the modeling problem. We simplified the rigidity tensor, using the Voight engineering notation. The methods we presented are autoadaptative and require simply a regular initial solution.

In the following, the contributions of the thesis are summarized and discussed, and some perspectives are given for future developments.

Powell-Sabin splines

In this work, we used Powell-Sabin splines, which has been constructed on triangular meshes discretizing geological domains. These splines have been used for the interpolation of geological data and also for discretizing the regularization energies.

This work might encourage, in the context of structural mesh-based methods, the use of high order interpolants, either on tetrahedral or hexahedral meshes. For instance, the Clough-Tocher cubic C^1 splines on triangulations, can be a notable option. In the case of hexahedral meshes, box splines, Tensor products, hierarchical splines can be used to locally enhance the approximation power of the splines (Giannelli et al. 2012).

Classically, in high-order finite element methods, what is gained on the precision and the regularity of the solution is often lost on the performance. We did not compare the computation time of the method using Powell-Sabin splines with a method using standard linear finite elements. A computational analysis is needed to evaluate the industrial applicability of these splines.

When constructing geological models, it is common to encounter situations where new data become available after the initial model has been computed. In such cases, a local update technique can be employed to enrich specific regions in the model using the new data, without making significant changes to the rest of the model. In this context, PS-splines allow a local editing of the implicit function.

New formulations of the regularization

In the Chap. 4, we introduced a new regularization method based on autoadaptive anisotropic diffusion. Our method is an iterative scheme, where a diffusion tensor is adapted to the variations present in the data. Contrary to existing methods, our approach is data driven and no preprocessing is needed to assign values to geological horizons. Instead, our iterative scheme adapt the diffusion tensor to the anisotropy and thickness variations present in the data to obtain a regular solution.

The iterative scheme we introduced, enables a framework, where many degrees of freedom can be exploited. For example, the ability to impose a specific behaviour of the implicit function near the boundaries. In this scheme, the tensor is parameterized to remain positive semidefinite.

In Chap. 4, we introduced a new regularization method based on autoadaptive anisotropic thin plate energy. Our method is an iterative scheme, where a rigidity tensor is adapted to the variations present in the data. We provided a parameterization of the rigidity tensor ensuring that it remains positive semidefinite. Subsequently, the convexity and the uniqueness of the problem.

In both regularization schemes, the anisotropic behaviour of the implicit function is encoded via a tensor. In the anisotropic diffusion scheme, it is a second order tensor of diffusion, while in the anisotropic bending energy, it is a fourth order tensor that it is reduced using the Voight notation to a second order tensor. We discretized these tensor by representing each of the components of the tensor using basis functions, the PS-splines in this thesis. These tensors are parameterized to remain positive semidefinte. Alternatively, they can be represented using other representations of vector fields or directional fields of any dimension. Various representations, discretizations, and optimization strategies have been developed (Vaxman

et al. 2016). These representations might allow easier discretization of the directional fields, which in turn will allow to express the smoothness energies that are more adapted to directional fields (Pinkall and Polthier 1993). Perhaps also an easier parameterization of the tensors to remain positive semidefinite.

These tensors represent new tools for structural modeling to integrate anisotropy. A further testing in real geological cases, might guide the introduction of criteria that can enhance the stability of these tools. Such criteria might involve prior knowledge of prior directions of anisotropy or bounding of conditioning number of these tensors.

Anisotropic adaptive meshing is a key ingredient in the context of solving anisotropic PDEs. Additionally, the anisotropy tensors that are constructed and discretized can be used to guide an effective adaptive meshing all over the domain.

Open questions

Extending our iterative scheme to three dimensions using Powell-Sabin splines is feasible. Speleers (2013) presented a method for constructing a normalized basis for the multivariate quadratic spline space defined over a generalized Powell-Sabin refinement of a triangulation in $\mathbb{R}^S$, $s \geq 1$. The extension of our new regularization formulations to three dimensions is possible, as well as to other discretizations as long as one as long as one is able to discretize first and second order partial derivatives. However, it is worth noting that we did not conduct experiments in the volumetric context.

In Chap. 1, we highlighted how the values assigned to geological horizons strongly influence the resulting implicit functions. Optimal values associated to these horizons can potentially address the problem of thickness variations. It is worth noting that in this thesis, we did not address this problem, we rather focused on formulating regularization energies that are able to handle geological data with arbitrary assigned values. We believe that optimizing these values to find an optimal distribution of the data points should be aligned with the regularization objectives. For future works, it would be interesting to explore this optimization problem.

In the experiments conducted in Chap. 5, we noticed that when data points are very sparse, the interpolation task becomes challenging. In some regions, we observed that the regularization energies fail to generate reasonable solutions. In similar cases, a solution might involve enriching the model with extra data points. In future research work, we consider it is necessary to investigate these specific cases.

Bibliography

A. H. Abdul Latiff, S. Osman, and S. F. Jamaludin. Seismic data analysis to the converted wave acquisition: A case study in offshore malaysia. *IOP Conference Series: Earth and Environmental Science*, 38:012001, 07 2016. doi: 10.1088/1755-1315/38/1/012001.

E. Albuquerque, P. Sollero, W. Venturini, and M. Aliabadi. Boundary element analysis of anisotropic kirchhoff plates. *International Journal of Solids and Structures*, 43(14): 4029–4046, 2006. ISSN 0020-7683. doi: https://doi.org/10.1016/j.ijsolstr.2006.03.027. URL https://www.sciencedirect.com/science/article/pii/S0020768306001004.

P. Alliez, D. Cohen-Steiner, Y. Tong, and M. Desbrun. Voronoi-based variational reconstruction of unoriented point sets. In *Eurographics Symposium on Geometry Processing*, 2007.

M. Andreux, E. Rodola, M. Aubry, and D. Cremers. Anisotropic laplace-beltrami operators for shape analysis. In *Computer Vision-ECCV 2014 Workshops: Zurich, Switzerland, September 6-7 and 12, 2014, Proceedings, Part IV 13*, pages 299–312. Springer, 2015.

P. Anquez, G. Caumon, J. Pellerin, and B. Levy. Automatic sealing and simplification of 3d geological surface models using topology recovery. 06 2017. doi: 10.3997/2214-4609.201701143.

P. Anquez, J. Pellerin, M. Irakarama, P. Cupillard, B. Lévy, and G. Caumon. Automatic correction and simplification of geological maps and cross-sections for numerical simulations. *Comptes Rendus Geoscience*, 351(1):48–58, 2019. ISSN 1631-0713. doi: https://doi.org/10.1016/j.crte.2018.12.001. URL https://www.sciencedirect.com/science/article/pii/S1631071318301706.

J. Autin, M. Scheck-Wenderoth, H.-J. Götze, C. Reichert, and D. Marchal. Deep structure of the argentine margin inferred from 3d gravity and temperature modelling, colorado basin. *Tectonophysics*, 676, 12 2015. doi: 10.1016/j.tecto.2015.11.023.

D. Barrera, M. Fortes, P. González, and M. Pasadas. Minimal energy surfaces on powell–sabin type triangulations. *Applied Numerical Mathematics*, 58(5):635–645, 2008. ISSN 0168-9274. doi: https://doi.org/10.1016/j.apnum.2007.02.001. URL https://www.sciencedirect.com/science/article/pii/S0168927407000414.

M. Bartoň and J. Kosinka. On numerical quadrature for c1 quadratic powell–sabin 6-split macro-triangles. *Journal of Computational and Applied Mathematics*, 349:239–250, 2019. ISSN 0377-0427. doi: https://doi.org/10.1016/j.cam.2018.07.051. URL https://www.sciencedirect.com/science/article/pii/S0377042718304783.

Y. Bazilevs, V. Calo, J. Cottrell, T. Hughes, A. Reali, and G. Scovazzi. Variational multiscale residual-based turbulence modeling for large eddy simulation of incompressible flows. *Computer Methods in Applied Mechanics and Engineering*, 197(1):173–201,

2007. ISSN 0045-7825. doi: https://doi.org/10.1016/j.cma.2007.07.016. URL https://www.sciencedirect.com/science/article/pii/S0045782507003027.

M. Benning and M. Burger. Modern regularization methods for inverse problems, 2018.

Z. Bi, X. Wu, Z. Li, D. Chang, and X. Yong. Deepismnet: three-dimensional implicit structural modeling with convolutional neural network. *Geoscientific Model Development*, 15(17): 6841–6861, 2022. doi: 10.5194/gmd-15-6841-2022. URL https://gmd.copernicus.org/articles/15/6841/2022/.

A. Buffa and G. Sangalli. *IsoGeometric Analysis: A New Paradigm in the Numerical Approximation of PDEs: Cetraro, Italy 2012*, volume 2161. 01 2016. ISBN 978-3-319-42308-1. doi: 10.1007/978-3-319-42309-8.

F. Calakli and G. Taubin. Ssd: Smooth signed distance surface reconstruction. *Computer Graphics Forum*, 30:1993 – 2002, 11 2011. doi: 10.1111/j.1467-8659.2011.02058.x.

P. Calcagno, J.-P. Chilès, G. Courrioux, and A. Guillen. Geological modelling from field data and geological knowledge - part i. modelling method coupling 3d potential-field interpolation and geological rules. *Physics of The Earth and Planetary Interiors*, 171, 12 2008. doi: 10.1016/j.pepi.2008.06.013.

G. Caumon, F. Lepage, C. H. Sword, and J.-L. Mallet. Building and Editing a Sealed Geological Model. *Mathematical Geology*, 36(4):405 – 424, May 2004. doi: 10.1023/b:matg.0000029297.18098.8a. URL https://hal.univ-lorraine.fr/hal-03029470.

G. Caumon, P. Collon-Drouaillet, C. Le Carlier de Veslud, S. Viseur, and J. Sausse. Surface-based 3d modeling of geological structures. *Mathematical Geosciences*, 41:927–945, 2009.

G. Caumon, G. Gray, C. Antoine, and M.-O. Titeux. Three-dimensional implicit stratigraphic model building from remote sensing data on tetrahedral meshes: Theory and application to a regional model of la popa basin, ne mexico. *Geoscience and Remote Sensing, IEEE Transactions on*, 51:1613–1621, 03 2013.

L. Chen, B. Li, and R. Borst. The use of powell-sabin b-splines in a higher-order phase-field model for crack kinking. *Computational Mechanics*, 67, 01 2021. doi: 10.1007/s00466-020-01923-0.

A. H.-D. Cheng and D. T. Cheng. Heritage and early history of the boundary element method. *Engineering Analysis with Boundary Elements*, 29(3):268–302, 2005. ISSN 0955-7997. doi: https://doi.org/10.1016/j.enganabound.2004.12.001. URL https://www.sciencedirect.com/science/article/pii/S0955799705000020.

J. Chilès, C. Aug, A. Guillen, and T. Lees. Modelling the geometry of geological units and its uncertainty in 3d from structural data: The potential-field method. *Orebody Modelling and Strategic Mine Planning*, 14, 01 2007.

R. Courant. *Dirichlet's Principle, Conformal Mapping, and Minimal Surfaces*. Springer New York, 1977. doi: 10.1007/978-1-4612-9917-2. URL https://doi.org/10.1007/978-1-4612-9917-2.

K. Crane, C. Weischedel, and M. Wardetzky. Geodesics in heat. *ACM Transactions on Graphics*, 32(5):1–11, Sept. 2013. doi: 10.1145/2516971.2516977. URL `https://doi.org/10.1145/2516971.2516977`.

T. Cross and P. Homewood. Amanz gressly's role in founding modern stratigraphy. *Geological Society of America Bulletin*, 109:1617–1630, 12 1997. doi: 10.1130/0016-7606(1997)109<1617:AGSRIF>2.3.CO;2.

P. Dierckx. On calculating normalized powell-sabin b-splines. *Computer Aided Geometric Design*, 15(1):61–78, 1997. doi: https://doi.org/10.1016/S0167-8396(97)81785-2.

P. DIERCKX, S. van LEEMPUT, and T. VERMEIRE. Algorithms for surface fitting using powell-sabin splines. *IMA Journal of Numerical Analysis*, 12(2):271–299, 1992. doi: 10.1093/imanum/12.2.271. URL `https://doi.org/10.1093/imanum/12.2.271`.

C. T. Druyor. *n adaptive hybrid mesh generation method for complex geometries*. PhD thesis, 03 2011.

L. C. Evans. *Partial differential equations*. American Mathematical Society, Providence, R.I., 2010.

M. S. Floater. Mean value coordinates. *Computer Aided Geometric Design*, 20(1):19–27, Mar. 2003. doi: 10.1016/s0167-8396(03)00002-5. URL `https://doi.org/10.1016/s0167-8396(03)00002-5`.

S. Fomel and J. Claerbout. *Three-Dimensional Seismic Data Regularization*. PhD thesis, 07 2001.

T. Frank, A.-L. Tertois, and J.-L. Mallet. 3d-reconstruction of complex geological interfaces from irregularly distributed and noisy point data. *Computers & Geosciences*, 33:932–943, 07 2007.

P. George and H. Borouchaki. *Delaunay Triangulation and Meshing: Application to Finite Elements*. Hermès, 1998. ISBN 9782866016920. URL `https://books.google.fr/books?id=HZGfI61PSUQC`.

P. George, H. Borouchaki, P. Frey, P. Laug, and E. Saltel. *Mesh Generation and Mesh Adaptivity: Theory and Techniques*. 10 2007. ISBN 9780470091357. doi: 10.1002/9780470091357.ecm012.pub2.

C. Giannelli, B. Jüttler, and H. Speleers. Thb-splines: The truncated basis for hierarchical splines. *Computer Aided Geometric Design*, 29(7):485–498, 2012. ISSN 0167-8396. doi: https://doi.org/10.1016/j.cagd.2012.03.025. URL `https://www.sciencedirect.com/science/article/pii/S0167839612000519`. Geometric Modeling and Processing 2012.

G. Giorgiani, H. Guillard, and B. Nkonga. A powell-sabin finite element scheme for partial differential equations. *ESAIM: Proceedings and Surveys*, 53:64–76, 03 2016. doi: 10.1051/proc/201653005.

G. Giorgiani, H. Guillard, B. Nkonga, and E. Serre. A stabilized powell–sabin finite-element method for the 2d euler equations in supersonic regime. *Computer Methods in Applied Mechanics and Engineering*, 340:216–235, 2018. ISSN 0045-7825. doi: https://doi.org/10.1016/j.cma.2018.05.032. URL `https://www.sciencedirect.com/science/article/pii/S0045782518302767`.

G. Giorgiani, H. Bufferand, F. Schwander, E. Serre, and P. Tamain. A high-order non field-aligned approach for the discretization of strongly anisotropic diffusion operators in magnetic fusion. *Computer Physics Communications*, 254:107375, 2020. doi: https://doi.org/10.1016/j.cpc.2020.107375.

H. GJØYSTDAL, J. E. REINHARDSEN, and K. ÅSTEBØL. Computer representation of complex 3-d geological structures using a new "solid modeling" technique*. *Geophysical Prospecting*, 33(8):1195–1211, 1985. doi: https://doi.org/10.1111/j.1365-2478.1985.tb01359.x. URL `https://onlinelibrary.wiley.com/doi/abs/10.1111/j.1365-2478.1985.tb01359.x`.

M. Hillier, E. Schetselaar, E. Dekemp, and G. Perron. Three-dimensional modelling of geological surfaces using generalized interpolation with radial basis functions. *Mathematical geosciences*, 46:931–953, 07 2014.

T. Hughes, J. Cottrell, and Y. Bazilevs. Isogeometric analysis: Cad, finite elements, nurbs, exact geometry and mesh refinement. *Computer Methods in Applied Mechanics and Engineering*, 194(39):4135–4195, 2005. ISSN 0045-7825. doi: https://doi.org/10.1016/j.cma.2004.10.008. URL `https://www.sciencedirect.com/science/article/pii/S0045782504005171`.

M. Irakarama. *Towards Reducing Structural Interpretation Uncertainties Using Seismic Data*. PhD thesis, 2019. URL `http://www.theses.fr/2019LORR0060`. Thèse de doctorat dirigée par Caumon, Guillaume et Cupillard, Paul Géosciences Université de Lorraine 2019.

M. Irakarama, G. Laurent, J. Renaudeau, and G. Caumon. Finite Difference Implicit Structural Modeling of Geological Structures. *Mathematical Geosciences*, 53:785–808, 2021. URL `https://hal.univ-lorraine.fr/hal-02953073`.

M. Irakarama, M. Thierry-Coudon, M. Zakari, and G. Caumon. Finite element implicit 3d subsurface structural modeling. *Computer-Aided Design*, 149:103267, 2022. doi: https://doi.org/10.1016/j.cad.2022.103267.

A. Jacobson, I. Baran, J. Popović, and O. Sorkine. Bounded biharmonic weights for real-time deformation. *ACM Transactions on Graphics*, 30(4):1–8, July 2011. doi: 10.1145/2010324.1964973. URL `https://doi.org/10.1145/2010324.1964973`.

J. Kiendl. *Isogeometric Analysis and Shape Optimal Design of Shell Structures*. PhD thesis, 03 2011.

F. Knöppel, K. Crane, U. Pinkall, and P. Schröder. Globally optimal direction fields. *ACM Trans. Graph.*, 32(4), 2013.

J. Kosinka and T. Cashman. Watertight conversion of trimmed cad surfaces to clough–tocher splines. *Computer Aided Geometric Design*, 90, 06 2015. doi: 10.1016/j.cagd.2015.06.001.

C. Lajaunie, G. Courrioux, and L. Manuel. Foliation fields and 3d cartography in geology: Principles of a method based on potential interpolation. *Mathematical Geology*, 29:571–584, 1997.

G. Laurent. Iterative thickness regularization of stratigraphic layers in discrete implicit modeling. *Mathematical Geosciences*, 48, 06 2016.

C. Legentil, J. Pellerin, M. Raguenel, and G. Caumon. Towards a workflow to evaluate geological layering uncertainty on co2 injection simulation. *Applied Computing and Geosciences*, 18:100118, 2023. ISSN 2590-1974. doi: https://doi.org/10.1016/j.acags.2023.100118. URL https://www.sciencedirect.com/science/article/pii/S2590197423000071.

S. Lekhnitskii, T. Cheron, and S. Tsai. *Anisotropic plates*. Gordon and Breach, 1968. URL https://books.google.fr/books?id=920OzQEACAAJ.

D. Lenz, R. Yeh, V. Mahadevan, I. Grindeanu, and T. Peterka. Adaptive regularization ofnbsp;b-spline models fornbsp;scientific data. In *Computational Science – ICCS 2022: 22nd International Conference, London, UK, June 21–23, 2022, Proceedings, Part I*, page 150–163, Berlin, Heidelberg, 2022. Springer-Verlag. ISBN 978-3-031-08750-9. doi: 10.1007/978-3-031-08751-6_11. URL https://doi.org/10.1007/978-3-031-08751-6_11.

Love. XVI. the small free vibrations and deformation of a thin elastic shell. *Philosophical Transactions of the Royal Society of London. (A.)*, 179:491–546, Dec. 1888. doi: 10.1098/rsta.1888.0016. URL https://doi.org/10.1098/rsta.1888.0016.

B. Lévy and J.-L. Mallet. Constrained discrete fairing for arbitrary meshes. Technical report, GOCAD Consortium, 1999.

R. B. Madsen, A.-S. Høyer, L. T. Andersen, I. Møller, and T. M. Hansen. Geology-driven modeling: A new probabilistic approach for incorporating uncertain geological interpretations in 3d geological modeling. *Engineering Geology*, 309:106833, 2022. ISSN 0013-7952. doi: https://doi.org/10.1016/j.enggeo.2022.106833. URL https://www.sciencedirect.com/science/article/pii/S0013795222003180.

J. Maes and A. Bultheel. Surface compression with hierarchical Powell-Sabin B-splines. *International Journal of Wavelets, Multiresolution and Information Processing*, 4(1):177–196, 2006. doi: 10.1142/S0219691306001154. URL http://nalag.cs.kuleuven.be/papers/ade/pscompres/index.html.

J.-L. Mallet. Discrete smooth interpolation. *ACM Transactions on Graphics*, 8(2):121–144, Apr. 1989. doi: 10.1145/62054.62057. URL https://doi.org/10.1145/62054.62057.

J.-L. Mallet. Discrete smooth interpolation in geometric modelling. *Computer-Aided Design*, 24(4):178–191, 1992. ISSN 0010-4485. doi: https://doi.org/10.1016/0010-4485(92)90054-E. URL https://www.sciencedirect.com/science/article/pii/001044859290054E.

J.-L. Mallet. Discrete modeling for natural objects. *Mathematical Geology*, 29:199–219, 1997.

R. Martin and J. B. Boisvert. Iterative refinement of implicit boundary models for improved geological feature reproduction. *Computers & Geosciences*, 109:1–15, 2017. ISSN 0098-3004. doi: https://doi.org/10.1016/j.cageo.2017.07.003. URL https://www.sciencedirect.com/science/article/pii/S0098300416307555.

S. May, J. Vignollet, and R. Borst. Powell-sabin b-splines and unstructured standard t-splines for the solution of the kirchhoff-love plate theory exploiting bézier extraction. *International Journal for Numerical Methods in Engineering*, 107:n/a–n/a, 12 2015. doi: 10.1002/nme.5163.

K. McClay, P. Whitehouse, T. Dooley, and M. Richards. 3d evolution of fold and thrust belts formed by oblique convergence. *Marine and Petroleum Geology*, 21(7):857–877, 2004. ISSN 0264-8172. doi: https://doi.org/10.1016/j.marpetgeo.2004.03.009. URL https://www.sciencedirect.com/science/article/pii/S026481720400056X. Oil and Gas in Compressional Belts.

S. Merchel, B. Jüttler, and D. Mokriš. Adaptive and local regularization for data fitting by tensor-product spline surfaces. *Adv. Comput. Math.*, 49(4), jul 2023. ISSN 1019-7168. doi: 10.1007/s10444-023-10035-1. URL https://doi.org/10.1007/s10444-023-10035-1.

J. Nieto and T. Susin. *Cage Based Deformations: A Survey*, volume 7, pages 75–99. 01 2013. ISBN 978-94-007-5445-4. doi: 10.1007/978-94-007-5446-1_3.

J. O'Rourke, A. Aggarwal, S. Maddila, and M. Baldwin. An optimal algorithm for finding minimal enclosing triangles. *Journal of Algorithms*, 7(2):258–269, 1986. ISSN 0196-6774. doi: https://doi.org/10.1016/0196-6774(86)90007-6. URL https://www.sciencedirect.com/science/article/pii/0196677486900076.

D. Palmer, O. Stein, and J. Solomon. Frame field operators. *Computer Graphics Forum*, 40(5): 231–245, Aug. 2021. doi: 10.1111/cgf.14370. URL https://doi.org/10.1111/cgf.14370.

P. Perona and J. Malik. Scale-space and edge detection using anisotropic diffusion. *IEEE Transactions on Pattern Analysis and Machine Intelligence*, 12(7):629–639, 1990.

U. Pinkall and K. Polthier. Computing discrete minimal surfaces and their conjugates. *Exp. Math.*, 2:15–36, 1993.

L. Pizzella. *Prise en compte d'une anisotropie variable en modélisation géologique 3D par la méthode implicite du potentiel : application aux structures plissées*. Theses, Université Paris sciences et lettres, Dec. 2020. URL https://pastel.hal.science/tel-03525009.

M. J. D. Powell and M. A. Sabin. Piecewise quadratic approximations on triangles. *ACM Trans. Math. Softw.*, 3(4):316–325, dec 1977. ISSN 0098-3500. doi: 10.1145/355759.355761. URL https://doi.org/10.1145/355759.355761.

E. R and I. Obiadi. Evaluation and prospect identification in the olive field, niger delta basin, nigeria. *Journal of Petroleum Environmental Biotechnology*, 7, 01 2016. doi: 10.4172/2157-7463.1000284.

J. N. Reddy. *Theory and Analysis of Elastic Plates and Shells*. CRC Press, Nov. 2006. doi: 10.1201/9780849384165. URL https://doi.org/10.1201/9780849384165.

J. Renaudeau. *Continuous formulation of implicit structural modeling discretized with mesh reduction methods*. PhD thesis, 2019. URL http://www.theses.fr/2019LORR0075. Thèse de doctorat dirigée par Caumon, GuillaumeLévy, Bruno et Maerten, Frantz Géosciences Université de Lorraine 2019.

D. F. Rogers. An introduction to nurbs: With historical perspective. 2011. URL https://api.semanticscholar.org/CorpusID:117031875.

K. Santosh, N. Das, and S. Ghosh. Chapter 2 - deep learning: a review. In K. Santosh, N. Das, and S. Ghosh, editors, *Deep Learning Models for Medical Imaging*, Primers in Biomedical Imaging Devices and Systems, pages 29–63. Academic Press, 2022. ISBN 978-0-12-823504-1. doi: https://doi.org/10.1016/B978-0-12-823504-1.00012-X. URL https://www.sciencedirect.com/science/article/pii/B978012823504100012X.

D. Sbibih, A. Serghini, and A. Tijini. Normalized trivariate b-splines on worsey-piper split and quasi-interpolants. *BIT Numerical Mathematics*, 52:221–249, 03 2012. doi: 10.1007/s10543-011-0348-y.

L. L. Schumaker and H. Speleers. Nonnegativity preserving macro-element interpolation of scattered data. *Computer Aided Geometric Design*, 27(3):245–261, 2010. ISSN 0167-8396. doi: https://doi.org/10.1016/j.cagd.2009.12.005. URL https://www.sciencedirect.com/science/article/pii/S0167839609001435.

J. R. Shewchuk. Delaunay refinement algorithms for triangular mesh generation. *Computational Geometry*, 22(1):21–74, 2002. ISSN 0925-7721. doi: https://doi.org/10.1016/S0925-7721(01)00047-5. URL https://www.sciencedirect.com/science/article/pii/S0925772101000475. 16th ACM Symposium on Computational Geometry.

W. H. F. Smith and P. Wessel. Gridding with continuous curvature splines in tension. *GEOPHYSICS*, 55(3):293–305, Mar. 1990. doi: 10.1190/1.1442837. URL https://doi.org/10.1190/1.1442837.

T. Snell, N. De Paola, J. van Hunen, S. Nielsen, and C. Collettini. Modelling fluid flow in complex natural fault zones: Implications for natural and human-induced earthquake nucleation. *Earth and Planetary Science Letters*, 530:115869, 2020. ISSN 0012-821X. doi: https://doi.org/10.1016/j.epsl.2019.115869. URL https://www.sciencedirect.com/science/article/pii/S0012821X19305618.

L. Souche, G. Iskenova, F. Lepage, and D. Desmarest. Construction of structurally and stratigraphically consistent structural models using the volume-based modelling technology: Applications to an australian dataset. 12 2014.

H. Speleers. Construction, analysis and application of powell-sabin spline finite elements. 04 2008.

H. Speleers. Multivariate normalized powell–sabin b-splines and quasi-interpolants. *Computer Aided Geometric Design*, 30(1):2–19, 2013. ISSN 0167-8396. doi: https://doi.org/10.1016/j.cagd.2012.07.005. URL https://www.sciencedirect.com/science/article/pii/S0167839612000945. Recent Advances in Applied Geometry.

H. Speleers, C. Manni, F. Pelosi, and M. L. Sampoli. Isogeometric analysis with powell–sabin splines for advection–diffusion–reaction problems. *Computer Methods in Applied Mechanics and Engineering*, 221-222:132–148, 05 2012. doi: 10.1016/j.cma.2012.02.009.

K. Sprague and E. Dekemp. Interpretive tools for 3-d structural geological modelling part ii: Surface design from sparse spatial data. *GeoInformatica*, 9:5–32, 03 2005.

O. Stein. Smoothness energies in geometry processing. 2020. doi: 10.7916/D8-1MB2-PB03. URL https://academiccommons.columbia.edu/doi/10.7916/d8-1mb2-pb03.

O. Stein, E. Grinspun, M. Wardetzky, and A. Jacobson. Natural boundary conditions for smoothing in geometry processing. *ACM Trans. Graph.*, 37(2), May 2018. URL http://doi.acm.org/10.1145/3186564.

O. Stein, E. Grinspun, A. Jacobson, and M. Wardetzky. A mixed finite element method with piecewise linear elements for the biharmonic equation on surfaces, 2022.

structurae. *Gulfaks oil field*, 2023. URL https://structurae.net/en/structures/gullfaks-c.

J. Thornton, G. Mariethoz, and P. Brunner. A 3d geological model of a structurally complex alpine region as a basis for interdisciplinary research. *Scientific Data*, 5:180238, 10 2018. doi: 10.1038/sdata.2018.238.

A. Vaxman, M. Campen, O. Diamanti, D. Panozzo, D. Bommes, K. Hildebrandt, and M. Ben-Chen. Directional field synthesis, design, and processing. *Computer Graphics Forum*, 35 (2):545–572, 2016. doi: https://doi.org/10.1111/cgf.12864. URL https://onlinelibrary.wiley.com/doi/abs/10.1111/cgf.12864.

L. Veiga, T. Hughes, J. Kiendl, C. Lovadina, J. Niiranen, A. Reali, and H. Speleers. A locking-free model for reissner-mindlin plates: Analysis and isogeometric implementation via nurbs and triangular nurps. *Mathematical Models and Methods in Applied Sciences*, 25: 1519–1551, 07 2015. doi: 10.1142/S0218202515500402.

Y. Wang and J. Solomon. Fast quasi-harmonic weights for geometric data interpolation. *ACM Trans. Graph.*, 40(4), jul 2021. URL https://doi.org/10.1145/3450626.3459801.

F. Wellmann and G. Caumon. 3-D Structural geological models: Concepts, methods, and uncertainties. In C. Schmelzbach, editor, *Advances in Geophysics*, volume 59, pages 1–121. Elsevier, Nov. 2018. doi: 10.1016/bs.agph.2018.09.001. URL https://hal.univ-lorraine.fr/hal-01921494.

W. Yang and A. Escalona. Basin modelling and source rock evaluation in the guyana basin. *First Break*, 29, 10 2011. doi: 10.3997/1365-2397.2011030.

,